



**UNIVERSITY**  
*of*  
**GLASGOW**

**MICROMACHINED SENSORS FOR  
SINGLE-CELL SIGNALLING**

**XINXIA CAI**  
B.Sc. M.Sc

A Thesis Submitted to the Faculty of Engineering of  
The University of Glasgow  
For the Degree of Doctor of Philosophy

September 2001

© Xinxia Cai, 2001

ProQuest Number: 13833986

All rights reserved

INFORMATION TO ALL USERS

The quality of this reproduction is dependent upon the quality of the copy submitted.

In the unlikely event that the author did not send a complete manuscript and there are missing pages, these will be noted. Also, if material had to be removed, a note will indicate the deletion.



ProQuest 13833986

Published by ProQuest LLC (2019). Copyright of the Dissertation is held by the Author.

All rights reserved.

This work is protected against unauthorized copying under Title 17, United States Code  
Microform Edition © ProQuest LLC.

ProQuest LLC.  
789 East Eisenhower Parkway  
P.O. Box 1346  
Ann Arbor, MI 48106 – 1346

GLASGOW  
UNIVERSITY  
LIBRARY:

12385

COPY 1

## Abstract

The fabrication of microelectrodes integrated within microtitre chambers for ultra-low volume amperometric determination of lactate continues to be of interest in the subject of cell screening. Devices were fabricated using photolithography to give highly reproducible sensors integrated within high aspect ratio analytical chambers with volumes of between 160 ~ 400 pL. These chambers were either circular or square with a depth of 20  $\mu\text{m}$ , defined using the photoepoxy, SU8. In addition to the 3-microelectrode sensor, a 2-microelectrode sensor was also studied, which consists of a working microelectrode and an internal pseudo-microreference (combined with the counter electrode). The electrochemical characterization of a miniaturized sensor using a model redox compound of FMCA was discussed. Meanwhile, the detection of hydrogen peroxide, the redox enzyme linked electrochemical assay of glucose and the regeneration of the micro planar electrodes were investigated.

'Bulk' and pL-scale lactate measurements were carried out using the micromachined sensors. A microfluidic dispensation system was developed to deliver very low titres (6.5 pL) into a low volume micro-electrochemical cell. The determination of lactate was optimised using an enzyme-linked assay based upon lactate oxidase. This involved the amperometric determination of hydrogen peroxide at 640 mV vs. an internal pseudo Ag|AgCl reference (in the 2 electrode configuration). The system (including the microfluidic device, the microfluidic dispenser) had an observed detection limit of 15-fmol of lactate (as  $3\sigma$  above background). The sensor sensitivity was not limited by the ability of the sensor to resolve the amperometric signal, but rather the capability of the fluidic dispenser to deliver analyte in a reproducible and quantitative fashion at volumes below 6.5 pL. A linear calibration curve of the charge transferred and the amount of injected lactate in the range between 65 and 266 fmol was obtained.

For the study of lactate measurements from single heart cells, the biocompatibility of various materials used in the electrochemical devices was evaluated. The biocompatibility of SU-8 was demonstrated. It was shown that direct contact of the strongly oxidizing AgCl layer with a single myocyte could cause the myocyte to promptly die. Therefore, a two-electrode configuration, with a platinized working electrode and a combined reference and counter platinum electrode, acting as a pseudo-reference electrode, was also used for single-cell measurements. On the

basis of the theory of lactate metabolism and the anoxia model, the dynamic electrochemical measurements of lactate from healthy and anoxic single heart cells were obtained. The lactate content after metabolic inhibition was approximately three times that of the unpoisoned cell. The efflux of high level lactate was measured in real time after the injection of FCCP at high concentration at 150 ~ 200  $\mu\text{M}$ . Whereas, the lactate content of cells poisoned by contact with the AgI/AgCl was similar to that of a healthy cell. The lactate signal produced from cells, inserted using drawn pipettes, was higher for cells with higher metabolic rate than cells that were quiescent and weakly contracting.

In addition to standard photolithography techniques, the use of SU-8 and PDMS, as well as “soft lithography” techniques were explored for microsensor arrays and microfluidics applications. An integrated microfluidic biosensor chip and on-line flow injection analysis (FIA) monitoring system was designed.

In summary, this thesis describes a generic method of fabricating a single cell sensor employing pL-scale volume and based on oxidase-reductase enzymes and microfluidics in a lab-on-a-chip format. The next technological advancement would be the immobilisation of enzymes on the microelectrodes, leading to improve stability and avoiding expensive enzyme strategies as a means to every response in the future. In the future, integration of individual enzyme sensor arrays and fluorescence sensors needs to be performed for the simultaneous detection of various biomolecules from a single cell.

## Acknowledgements

I sincerely wish to thank my supervisor Prof. Jonathan M. Cooper for his invaluable expert supervision, encouragement and enthusiastic support throughout this project.

I am extremely grateful to Dr. Norbert Klauke for his help on microinjection system and cell discussion and I would like to express my sincere gratitude to Dr. Li Cui for her great encouragement, discussion on fabrication and measurements. Many thanks are due to Dr. Andrew Glidle greatly for his patient support. I highly appreciate Dr. Chris Mills's kind help on my thesis corrections.

Likewise, I wish to thank Prof. Godfrey L. Smith for the supply of heart cells and helpful advice. Many thanks are due to Prof. Peter Cobbold for his advice on cell measurements. I am grateful for the help provided by many of the technical staff in this Department and in IBLS (Institute of Biomedical and Life Sciences) at Glasgow University, especially Mrs. Mary Robertson, Mr. Bill Monaghan.

I am grateful to all of my fellow postgraduate students and research assistants who helped to create a friendly and enjoyable atmosphere in the Bioelectronics Research Centre and in this Department. I would like to thank Dr. James Davis, Dr. N. Anicet, Erik A. Johannessen, Scot Mckendry, Charlotte S. Hadyoon, Vincent Benoit, David Holmes, Mairi Sandison, Dr. B. Qiu, Dr. B. Zhang, Dr. Xu Li, Dr. M. Ke and X. Liu for their friendship and help on the project. I am greatly indebted to many people in this Department for their considerable help.

I would like to express my sincere gratitude to the Department and Bioelectronics Research Centre for providing the unique equipment and facilities in a multidisciplinary environment. I would also like to acknowledge the financial support provided by the Overseas Research Students Award Scheme (ORS) and the Faculty of Engineering.

My special thanks are due to my husband Liang Wang, my daughter Yuanyuan and my parents for their love, patience, understanding and support during the three years.

# Contents

|   |            |
|---|------------|
| <b>Abstract</b>   | <b>i</b>   |
| <b>Acknowledgements</b>   | <b>iii</b> |
| <b>Chapter 1: Introduction</b>  | <b>1</b>   |
| <b>1.1 Research Objectives</b>  | <b>1</b>   |
| <b>1.2 Technical Approaches for Single-cell Signalling</b>  | <b>1</b>   |
| 1.2.1 <i>Patch-clamp Technique</i>  | 1          |
| 1.2.2 <i>Fluorescence Assay</i>   | 2          |
| 1.2.3 <i>Electrochemical Measurements and Colour Images for Fast-Scan Cyclic Voltammetry (CV)</i> | 3          |
| 1.2.4 <i>Micromachining Technology</i>  | 4          |
| 1.2.5 <i>Micromachined Sensors for Single Heart Cell Signalling</i>                               | 5          |
| <b>1.3 Advantages of Developing Micromachined Systems</b>   | <b>5</b>   |
| <b>1.4 Significance of a Micromachined Sensor for Single-cell Signalling</b>                      | <b>6</b>   |
| <b>1.5 Thesis Outline</b>   | <b>6</b>   |
| <b>Chapter 2: Device Design and Microfabrication</b>  | <b>8</b>   |
| <b>2.1 Introduction</b>   | <b>8</b>   |
| 2.1.1 <i>Photolithography</i>   | 8          |
| 2.1.2 <i>Electron Beam Lithography</i>  | 9          |
| <b>2.2 Chemicals and Materials</b>  | <b>10</b>  |
| <b>2.3 Methods</b>  | <b>10</b>  |
| 2.3.1 <i>Device Design</i>  | 10         |
| 2.3.1.1 Design of Electrochemical Cell  | 10         |
| 2.3.1.2 Computer Aided Design for Device Patterning   | 11         |
| 2.3.2 <i>Microfabrication</i>   | 13         |
| 2.3.2.1 Electrode Patterning  | 14         |
| 2.3.2.2 Fabrication Using Polyimide   | 16         |
| 2.3.2.3 Fabrication Using SU-8  | 17         |
| 2.3.3 <i>Post Fabrication: Electrochemical Deposition</i>   | 18         |
| 2.3.3.1 Microelectrode Platinisation  | 18         |

|   |   |           |
|---|---|-----------|
| 2.3.3.2   | Microreference Deposition of AgIAgCl  | 20        |
| 2.3.3.3   | Microreference Deposition of AgIAg <sub>3</sub> PO <sub>4</sub>               | 23        |
| <b>2.4</b>  | <b>Results and Discussion</b>   | <b>24</b> |
| 2.4.1   | <i>Evaluation of Polyimide and SU-8</i>                                       | 24        |
| 2.4.1.1   | Processing of Polyimide   | 24        |
| 2.4.1.2   | Processing of SU-8  | 26        |
| 2.4.1.3   | Comparison of Polyimide and SU-8  | 28        |
| 2.4.2   | <i>Evaluation of the Device Fabrication</i>                                   | 30        |
| <b>2.5</b>  | <b>Conclusions</b>  | <b>31</b> |
| <br><b>Chapter 3: Electrochemical System and Devices Characterisation</b> |   | <b>32</b> |
| <b>3.1</b>  | <b>Introduction</b>   | <b>32</b> |
| 3.1.1   | <i>Potentiostatic Measurements</i>  | 32        |
| 3.1.2   | <i>Two-electrode Cell and Three-electrode Cell</i>                            | 33        |
| 3.1.3   | <i>Amperometry and Cyclic Voltammetry</i>                                     | 35        |
| 3.1.4   | <i>Ferrocenemonocarboxylic Acid (FMCA) and Reference Electrode</i>            | 35        |
| 3.1.5   | <i>Clark-type Electrode Reaction via Hydrogen Peroxide</i>                    | 36        |
| 3.1.6   | <i>Ferrocenemonocarboxylic Acid Mediated, Enzyme Catalyzed Reaction</i>       | 37        |
| 3.1.7   | <i>The Butler-Volmer Equation and Tafel Plots</i>                             | 37        |
| 3.1.8   | <i>The Basis of Glucose Oxidase Activity Assay</i>                            | 39        |
| <b>3.2</b>  | <b>Chemicals and Materials</b>  | <b>41</b> |
| <b>3.3</b>  | <b>Methods</b>  | <b>41</b> |
| 3.3.1   | <i>Direct Current (D.C.) Cyclic Voltammetry</i>                               | 41        |
| 3.3.2   | <i>Amperometric Detection</i>   | 42        |
| 3.3.3   | <i>Electrode Regeneration Methods</i>   | 42        |
| 3.3.4   | <i>Assay Procedure of Glucose Oxidase Activity</i>                            | 43        |
| <b>3.4</b>  | <b>Results and Discussion</b>   | <b>43</b> |
| 3.4.1   | <i>Electrochemical Characterisation Using FMCA</i>                            | 43        |
| 3.4.2   | <i>Detection of Hydrogen Peroxide</i>   | 46        |
| 3.4.2.1   | Response at Different Applied Potentials                                      | 46        |
| 3.4.2.2   | Current-time Response to Hydrogen Peroxide                                    | 49        |
| 3.4.2.3   | Calibration Curve and Reproducibility   | 50        |
| 3.4.3   | <i>Detection of Glucose</i>   | 53        |
| 3.4.3.1   | Using the enzyme GOD  | 53        |
| 3.4.3.2   | Using the Mediator FMCA   | 54        |
| 3.4.4   | <i>Pseudo Micro-references of AgIAgCl and AgIAg<sub>3</sub>PO<sub>4</sub></i> | 56        |

|   |  |           |
|---|--|-----------|
| 3.4.4.1   | DC Cyclic Voltammetry  | 56        |
| 3.4.4.2   | Evaluation of Micro Reference of Ag/AgCl                                   | 59        |
| 3.4.5   | <i>Regeneration of the Electrodes</i>                                      | 62        |
| 3.4.5.1   | Passivation of the Electrode   | 62        |
| 3.4.5.2   | Cyclic Voltammetry in Acid   | 63        |
| 3.4.5.2   | Dry Etching  | 65        |
| 3.4.6   | <i>Measurement of Glucose Oxidase Activity</i>                             | 66        |
| <b>3.5</b>  | <b>Conclusions</b>   | <b>66</b> |
| <br><b>Chapter 4: Bulk and Picolitre-scale Detection of Lactate</b> |  | <b>68</b> |
| <b>4.1</b>  | <b>Introduction</b>  | <b>68</b> |
| <b>4.2</b>  | <b>Chemicals and Materials</b>   | <b>69</b> |
| <b>4.3</b>  | <b>Methods</b>   | <b>69</b> |
| 4.3.1   | <i>Reaction Principle</i>  | 69        |
| 4.3.2   | <i>Normal Bulk and "Bulk" Solution Methods For Measurement</i>             | 70        |
| 4.3.3   | <i>Lactate Oxidase Immobilisation on Micromachined Sensors</i>             | 70        |
| 4.3.4   | <i>Microinjection System</i>   | 71        |
| 4.3.4.1   | Experimental Set-up  | 71        |
| 4.3.4.2   | pL-Scale Solution Dispensation   | 73        |
| 4.3.4.3   | Calibration of pL-Scale Solution Dispensation in the Microinjection System | 75        |
| <b>4.4</b>  | <b>Results and Discussion</b>  | <b>79</b> |
| 4.4.1   | <i>Response Using "Bulk" Method</i>  | 79        |
| 4.4.1.1   | The Stability of Lactate   | 79        |
| 4.4.1.2   | Responses to Lactate   | 80        |
| 4.4.2   | <i>pL-scale Detection of Mediators</i>                                     | 83        |
| 4.4.3   | <i>pL-scale Detection of Lactate</i>                                       | 87        |
| 4.4.3.1   | Current-time Responses   | 87        |
| 4.4.3.2   | Calibration Curve against Additions of Lactate                             | 88        |
| 4.4.3.3   | The Non-Faraday Current  | 88        |
| 4.4.4   | <i>Micromachined Sensors with Enzyme Immobilisation</i>                    | 90        |
| 4.4.4.1   | Typical Responses to Successive Additions of Lactate                       | 90        |
| 4.4.4.2   | Stability Testing  | 92        |
| <b>4.5</b>  | <b>Conclusions</b>   | <b>93</b> |

|   |            |
|---|------------|
| <b>Chapter 5: Dynamic Electrochemical Measurements of Lactate from Single Heart Cell</b>  | <b>94</b>  |
| <b>5.1 Introduction</b>   | <b>94</b>  |
| 5.1.1 <i>Lactate Metabolism and Ischaemia</i>   | 94         |
| 5.1.2 <i>The Anoxia Model</i>   | 97         |
| 5.1.3 <i>Biocompatibility of <math>\mu</math>-Analytical Systems</i>  | 98         |
| 5.1.4 <i>Other Designs for Cells Measurements</i>   | 99         |
| <b>5.2 Chemicals and Materials</b>  | <b>99</b>  |
| <b>5.3 Methods</b>  | <b>102</b> |
| 5.3.1 <i>Biocompatibility Measurements</i>  | 102        |
| 5.3.2 <i>Single Heart Cell Experimental Protocol</i>  | 102        |
| <b>5.4 Results and Discussion</b>   | <b>105</b> |
| 5.4.1 <i>Biocompatibility of Various Materials</i>  | 105        |
| 5.4.1.1 Biocompatibility of Conventional Microfabrication Materials   | 105        |
| 5.4.1.2 Poor Biocompatibility of AgI/AgCl Electrode   | 108        |
| 5.4.1.3 Prevention of the Degradation of AgI/AgCl   | 110        |
| 5.4.2 <i>Single Rabbit Heart Cells Permeabilised with Saponin in Bulk Solution</i>  | 110        |
| 5.4.3 <i>Lactate Responses from Single Heart Cells</i>  | 113        |
| 5.4.3.1 Lactate Efflux from Single Heart Cells in Contact with AgI/AgCl   |            |
| References  | 113        |
| 5.4.3.2 Lactate Responses from Healthy Aerobic Cells without FCCP   | 113        |
| 5.4.3.3 Lactate Responses from Anoxia Cells with FCCP   | 117        |
| 5.4.3.4 Summary of Lactate Responses from Single Heart Cells  | 119        |
| <b>5.5 Conclusions</b>  | <b>120</b> |
| <br>  |            |
| <b>Chapter 6: Future Microsensor Arrays, Microstructures and Microfluidics for Microsystems Integration and Miniaturized Analysis Systems (<math>\mu</math>TAS)</b> | <b>122</b> |
| <b>6.1 Introduction</b>   | <b>122</b> |
| <b>6.2 Chemicals and Materials</b>  | <b>122</b> |
| <b>6.3 Methods</b>  | <b>123</b> |
| 6.3.1 <i>Fabrication of Micro Chamber and Micro Flow Channel</i>  | 123        |
| 6.3.2 <i>Fabrication of Microelectrode Array Chip</i>   | 123        |
| 6.3.3 <i>The Rapid Fabrication of Microfluidic Systems in PDMS</i>  | 123        |
| 6.3.3.1 Hydrophobic Modification of the Mold/Substrate Surface  | 125        |

|            |  |            |
|------------|--|------------|
| 6.3.3.2    | Fabricating High-quality Microstructures Using PDMS Replica Molding (REM)  | 125        |
| 6.3.3.3    | Oxidation and Bonding  | 125        |
| <b>6.4</b> | <b>Results and Discussion</b>  | <b>125</b> |
| 6.4.1      | <i>Ultra-Thick Negative SU-8 Resists for Micro Chamber and Micro Flow Channel</i>  | 125        |
| 6.4.2      | <i>Microelectrode Array Chip</i>   | 127        |
| 6.4.3      | <i>The Rapid Fabrication of Microfluidic Systems Using PDMS</i>  | 130        |
| 6.4.4      | <i>Integrated Microfluidic Biosensor Chip and On-line Flow Injection Analysis (FIA) Monitoring of Multi-Biomolecules</i> | 133        |
| <b>6.5</b> | <b>General Conclusions</b>   | <b>135</b> |
|            | <b>Reference</b>   | <b>139</b> |
|            | <b>List of Tables and Figures</b>  | <b>145</b> |
|            | <b>Publications</b>  | <b>159</b> |

# Chapter 1: Introduction

## 1.1 Research Objectives

Lactate is one of the most important cellular metabolites. It is of significant clinical interest as it is produced in small amounts during aerobic respiration, and in large concentrations during ischaemia (e.g. infarction, cell death etc). Lactate oxidase (LOD) catalyses the oxidation of lactate to pyruvate with the production of  $H_2O_2$ , which can be amperometrically, detected at an (oxidising) anode [1-3]. Our interests focus on lactate detection using amperometric micromachined sensors with the aim of dynamic electrochemical measurement of intracellular lactate of a single heart cell. To this end, much fundamental research and engineering development is needed including: device fabrication using novel materials; integration of reference electroplating using different materials; the design and fabrication of a picolitre-scale injection system; the optimisation of sensor response in bulk and low volumes; the study of device material biocompatibility; cellular electrophysiology and single cell dynamic electrochemical measurement.

## 1.2 Technical Approaches for Single-cell Signalling

Several technical approaches for single cell signalling are described, each of which has been used singly or is combined with other approaches for the measurement of single cell signalling [4-7].

### *1.2.1 Patch-clamp Technique [2,6]*

**Production of Single Cell Pipettes:** To measure what is happening in or on a single living cell, scientists use a technique called the patch-clamp, which requires an extremely fine pipette tip to be held tightly against the cell membrane. By carefully heating and pulling a small glass or quartz capillary tube, a very fine pipette can be formed. When pulled by machine, the tip can be much smaller than a human hair and the opening on the end of the pipette may be only 1 micron in diameter.

To measure cell activity, it is necessary to make good electrical contact between the pipette and cell membrane. Sucking the single cell on to the pipette can do this.

Once good contact is made, it is possible to record single events within ion channels potentiometrically.

### *1.2.2 Fluorescence Assay [6,8,9]*

Exocytosis events have been observed using fluorescent microscopic techniques [6]. For molecules without intrinsic fluorescence, immunofluorescence techniques allow qualitative analysis of morphological changes and protein movements associated with exocytosis. For example, the enzyme dopamine  $\beta$ -hydroxylase (DBH) is a major membrane protein in chromaffin cell secretory vesicles. As the DBH appears on the cell surface during exocytosis, the sites of exocytosis can be visualized following the attachment of fluorescently tagged DBH antibodies. The presence of fluorescent spots on the cell surface spatially resolves areas of exocytosis, but temporal information is lost since cell fixation must be used. Real-time observation of exocytotic events and subsequent endocytosis (retrieval of vesicles from the cell membrane) can be accomplished using fluorescent markers such as the styryl dye FM1-43 that selectively labels membrane surfaces [6]. With this dye in the extracellular solution, addition of vesicle membrane to the cell surface during exocytosis results in an increase in cell surface fluorescence.

Intracellular ions, such as calcium can be measured fluorescently using indicator Fura-2/AM [8]. Fura-2/AM is a molecular probe, which can be loaded by incubating islets in solution containing Fura-2/AM. The complex of  $[Ca^{2+}-(Fura-2)]$  is alternately excited at 340 and 380 nm and the resulting fluorescence from individual islets was collected. The ratio of the emission intensities after excitation at 340 and 380 nm was used as a normalised measure of  $[Ca^{2+}]_i$  in the islet.

Recently a nanosensor equipped with an antibody-based nanoprobe capable of monitoring biochemicals of single cells has been developed [9]. After chemical treatment of single cells with benzo  $[\alpha]$  pyrene tetrol (BPT), a nanoprobe (10 ~ 100 nm in diameter) quartz optical fibre is coated with silver, so as to prevent light from emerging anywhere along the length of the fibre except the tip, where antibodies were attached. The nanoprobe was then moved inside the cell membrane and extending a short way into the cytoplasm, the fluorescence of BPT molecules binding to antibodies at the fibre tip has been recorded by using bright field microscopic illumination. Laser light was allowed to illuminate the optical fibre and readings were taken as a function of

time that the nanoprobe was inside the cell. Such an “irreversible” nanosensor device could lead to the development of nanosensing systems with the capability to monitor biochemical processes in single cells.

### 1.2.3 *Electrochemical Measurements and Colour Images for Fast-Scan Cyclic Voltammetry (CV)*

There are a variety of chemical messengers that relay information between biological cells, which can be electrochemically oxidized, either directly [7,10,11], or by using an enzyme linked assay [12-14]. Amperometry and cyclic voltammetry are the two primary techniques that have been used to non-invasively monitor exocytosis from single cell. In amperometry, the electrode potential is held constant, whereas in cyclic voltammetry it is periodically scanned in a triangular waveform. The advantage of amperometry is that it provides exquisite time resolution. Cyclic voltammetry, while having lower temporal resolution, provides a current-voltage curve whose characteristics depend on the particular molecule present at the electrode surface.

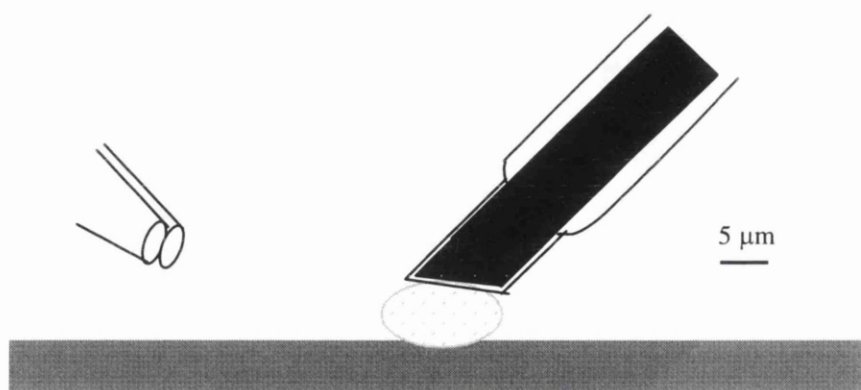


**Figure 1.1** Schematic of the experimental arrangement for single-cell measurements using the dual microsensor. The cylindrical microsensor was positioned touching a chromaffin cell that is attached to the floor of a Petri dish. A double-barrel microinjector was placed approximately 50  $\mu\text{m}$  from the cell to introduce reagents onto it. (Reproduced from reference [7])

Initial work in this area has involved the use of handcrafted carbon fibres, placed in a pulled glass capillary as microelectrodes. These can be located proximally to cells in culture, and used to measure presence of messengers, most notably catecholamines such as the neurotransmitter dopamine [7,10]. Such microelectrodes

can also be readily integrated with a second analytical method to provide improved levels of information. For example, carbon microelectrodes have been integrated with an optical sensor (e.g. a fibre) and combined with patch-clamp technique to simultaneously measure ion flux (using a fluorescence dye), whilst determining the presence of an electroactive cell messenger (see Figure 1.1) [7]. Alternatively, electrochemical carbon fibre electrodes have been integrated with microcolumn liquid chromatography (MLC) or capillary electrophoresis (CE) for single cell analysis [15]. Injection volumes as small as 270 fL have been obtained by use of CE sample preparation.

Fast-scan cyclic voltammetry (CV) is particularly useful because it has sufficient temporal resolution so that individual secretory processes can be observed. Each cyclic voltammogram contains information on the instantaneous chemical composition of the local environment at the electrode tip. In just a few seconds, information on the detected species and any temporal changes in concentration can be obtained. This information is crucial to interpreting the complex and dynamic chemical environment of the extracellular space around biological cells. A colour representation/image of the large amounts of data obtained with fast-scan CV is particularly useful, especially when contour plots are superimposed on the graphs [16]. The variables for repetitive CV are electrode potential, current, and time. In the three-dimensional plots, time increases along the abscissa whereas electrode potential is plotted along the ordinate. Current is encoded according to the colour bar. A colour image was produced revealing the exocytotic response of an isolated mast cell stimulated with  $\text{Ca}^{2+}$  ionophore. Traces for histamine and 5-hydroxytryptamine were obtained from the average voltammetric current around the respective peak potentials. The colour image allows rapid inspection of all the data and clearly reveals that both analytes come from the same exocytotic secretory event.

#### *1.2.4 Micromachining Technology*

Recently, microtechnology has been used to produce low volume structures. For example, handcrafted microelectrodes have been placed within embossed nano-arrays of picoliter-scale polystyrene vials for electrochemical investigation [17]. Although, in general, the use of a microelectrode provides the ability to determine new analytes from cells, either in culture, or in vivo, the nature of the experiment dictates that the

distance between the sensor and the cell (and hence the absolute magnitude of the response) can be varied.

Micromachining technology (most commonly including photolithography) has enabled the production of a wide variety of two-dimensional (planar) electrode arrays, microchambers and microchannels [14]. The flexibility of both the computer-aided design (CAD) process and fabrication methods has resulted in a wide variety of different sensor geometries and sizes ( $> 1 \mu\text{m}$ ). In an attempt to develop this integrated sensor technology, 600 pL-sized electrochemical cells have been fabricated previously [18-19]. These devices contain electrodes of fixed surface area and geometry. Single heart cells had been analysed in the electrochemical cells using a cascade of enzyme-linked assays to measure femtomole amounts of purines, including adenosine and inosine, during simulated ischaemia [12]. Further miniaturisation of both the microelectrodes and microchambers, reduced in size from those previously reported [12, 18, 19], to geometric volumes as small as 160 pL has been completed during the course of this research.

### *1.2.5 Micromachined Sensors for Single Heart Cell Signalling*

As a biological system to study, the mammalian cardiac myocyte has a number of advantages, being at least an order of magnitude larger than many other cells types. For example, when cells have a volume of  $10 \mu\text{m}^3$  (or 0.01 pL), whilst the heart cell volume used in this research may be as large as 20 pL. If all the cells common analytes are present in the same concentration (e.g. glucose, lactate), then there are 2000 $\times$  as many molecules available, for measurement. It has now become apparent that if the technology of using glass/metal/polymer electroanalytical systems is to become more widespread in single cell measurement, there is a need to further decrease the volume of measurement and hence decrease the volume of the measuring device (see below). This is an exercise that puts increasing demands, both on the skill of the fabricator, and on the successful implementation of experiment. As the volumes of such devices are decreased, so for a given analytical sensitivity, the dilution of the analyte into the chamber decreases and therefore the physiological (not "absolute") sensitivity of the device increases.

## **1.3 Advantages of Developing Micromachined Systems**

The advantages of developing such miniaturised systems are already documented [12,18,19]. They can provide the possibility of implementing new single cell assays (using enzyme-linked oxidase reaction) and the devices can be fabricated in batch with potential reductions in costs. In addition, within the structures, there is a more efficient transport of analyte to the microelectrode (as a consequence of the particular diffusion profiles for a given geometry), which will often result in relatively higher fluxes of redox species. Higher signal-to-noise ratios as well as faster steady-state responses could also be achieved (due to shorter diffusion distances). Under these circumstances, when using microanalytical chambers, none of the analyte within the analytical chamber is "lost" to bulk solution, enabling an "absolute" determination of the "response". As the analytical volume is very small (typically less than a nanolitre), the amount of reagents used in an assay is reduced, with decreased costs.

Finally, the techniques described provide a generic method to produce a wide range single cell sensor of a pL-scale, based on oxidoreductase enzymes (including, for example, the determination of glucose, superoxide radicals, dopamine and glutamate). The analytical platforms may be integrated with microfluidics to produce apparatus with a lab-on-a-chip format.

#### **1.4 Significance of a Micromachined Sensor for Single-cell Signalling**

This work is relevant to the fields of cellular engineering, biosensors and bionanotechnology. The traditional single cell measurement (patch clamp or fluorescence) range can be augmented through this method. This is particularly noticeable in the fields of biotechnology and drug discovery, where a number of potential benefits are evident, including improved throughput.

Studies on cardiomyocytes (heart cells) are helpful in understanding how anoxia and ischaemia perturbs cytoplasmic lactate levels and in understanding the cellular pathology of heart attacks (currently the largest cause of mortality and morbidity, in the western world) [20].

#### **1.5 Thesis Outline**

Chapter 2 addresses the design and fabrication of devices using both two and three microelectrode configurations (the former with a combined counter and reference

electrode). The use of polyimide and SU-8 (both negative photoresists) as two polymeric surface micromachining systems were also explored and compared. Further, post fabrication was attempted.

In Chapter 3, an investigation into the ferrocene monocarboxylic acid redox couple, and the subsequent enzymatic determination of glucose with glucose oxidase either using a mediator or, directly, via electro-oxidation of hydrogen peroxide was completed. In addition, sensitivity, time response and calibration curves were studied for the lactate amperometric bioanalytical sensor. The reproducibility, which is a key problem for this application, was optimised.

Chapter 4 presents the fabrication of an in house picolitre-scale microinjection system and the optimisation of a lactate assay using this platform. In Chapter 5, the biocompatibility study on different materials has been described and the lactate quantitative measurement of single heart cell response to physiological stimulation/inhibition was achieved. In Chapter 6, microsensor arrays device, microstructure and microfluidics for microsystem integration or miniaturized analysis systems ( $\mu$ TAS) are described.

## Chapter 2: Device Design and Microfabrication

### 2.1 Introduction

In this chapter, the design and fabrication of 2-electrode and 3-electrode devices are reviewed. This is followed by post fabrication electrochemical deposition including platinisation and AgI/AgCl. The evaluation of polyimide, SU-8 and the fabricated devices are then presented.

Lithographic techniques are the most commonly used for microelectronics fabrication. In this chapter, two lithographic patterning techniques, photolithography and electron beam (E-beam) lithography, have been used. Here, the basic principles of lithographic patterning and the relative advantages of photolithography and E-beam lithography processes are introduced.

#### 2.1.1 Photolithography

Photolithography is the basic tool of microelectronics fabrication providing a technique to allow high throughput and adequate registration with device feature spacing of about 1.5  $\mu\text{m}$  [21]. The use of positive resists can give rather better resolution than negative resists since they do not swell or expand during development. The theoretical resolution of an optical projection aligner is given by [22]:

$$\omega = \kappa\lambda/(\text{NA}) \quad (2.1)$$

where  $\omega$  is the minimum feature size,  $\kappa$  is an empirically determined process dependent constant between 0.5 and 1.0,  $\lambda$  is the wavelength of the exposure light and NA is the numerical aperture of the aligner's optics, is the sine of its half acceptance angle between 0 and 1. Therefore, diffraction of the exposing light (in the visible or near-ultraviolet wavelength range, 200 ~ 500 nm) around the edge of the mask puts a fundamental limit on the resolution of photolithography at about 0.2  $\mu\text{m}$  (i.e.  $0.5 \times 200\text{nm} \div 1 = 200 \text{ nm}$ )

In photolithography, a substrate, spin-coated with a thin layer of photosensitive polymer (photoresist), is exposed to an UV light source through a photomask. The photomask is typically a quartz plate with patterned microstructures of an opaque material (usually chromium). The photoresist exposed to UV light becomes either more (positive resist) or less (negative resist) soluble in a developing solution. In either case, the pattern on the photo-mask is transferred into the film of photoresist. The patterned photoresist can subsequently be used as the mask in metal electrodes patterning, doping or etching the substrate.

### *2.1.2 Electron Beam Lithography*

Electron beam lithography is an advanced imaging technique which is used when very fine device features are required and for mask making, but the method is rather slow (i.e. it is serial, rather than parallel). Electron beam lithography can produce devices where the feature size and separation is less than 1  $\mu\text{m}$ , due to the use of exposing radiation with shorter wavelengths ( $\lambda \sim 10^{-12}$  m) to overcome the diffraction limit on resolution [21].

Large-area sources of electrons are not currently available and so a finely focused electron beam must be 'written' across the wafer surface to define each device feature individually. This has the advantage that no mask is required in Electron beam lithography, but the processing of a single wafer takes a longer time so that throughput is low. However registration is excellent because the Electron beam can be used to recognise previously patterned features on the wafer surface, whilst defining a pattern in the overlying resist. The major limitation to the resolution available arises from the scattering of the electrons in the resist and back from the underlying material. The EBPG5 (beamwriter, B3) within the Department of Electronics and Electrical Engineering of Glasgow University is a commercial electron beam lithography tool capable of writing features down to 20 nm over areas up to 126 mm. The modified Jeol TEM lithography tool (B3) is used for exploring the limits of electron beam lithography and is routinely capable of 10 nm features.

## 2.2 Chemicals and Materials

All solutions were prepared with high-purity deionized water (Millipore Elix 10) and analytical reagent grade chemicals, without further purification. Probimide 7020 (Cat. No. 851338), QZ 3501 polyimide developer (Cat. No. 850973) and QZ 3512 polyimide rinse (Cat. No. 850979) were obtained from Olin Microelectronics Materials Company (Coventry, UK). SU-8 (SM 1060) was obtained from SOTEC Microsystems (Renens, Switzerland). SU-8 (10) was supplied by MicroChem Corp (Newton, MA02464-1418, USA). SU-8 developer (Microposit EC-solvent: propylene glycol monomethyl ether acetate) was obtained from Shipley Europe Limited (Coventry, UK). Platinic chloride (Cat. No. P-5775), L(+)-Lactic acid (sodium salt, Cat. No. L-7022), Silver nitrate (Cat. No. S-0139), Sodium thiosulfate (Cat. No. S-7143) and Lead acetate (Cat. No. L-3396) were obtained from Sigma (Dorset, England). Potassium iodide (Cat. No. 20796-9) was obtained from Aldrich Chemical Co. (Dorset, England). Isopropyl alcohol (Cat. No.10224BQ) and glass slides (Cat. No. 406/0183/04, 76×26×1.0-1.2 mm) were from BDH Laboratory Supplies (Poole, England).

## 2.3 Methods

### 2.3.1 Device Design

#### 2.3.1.1 Design of Electrochemical Cell

The electrochemical cell consists of an enclosed volume incorporating electrodes and containing electrolyte, comprising the container or “chamber”. Three electrodes are commonly employed: a working electrode (WE) which defines the interface under study, a reference electrode (RE) which maintains a constant reference potential, and a counter electrode (CE) which completes the electrochemical current by supplying the current. When the current demanded by the experiment is only a few microamperes [23], the reference electrode can also act as the counter electrode, and measurements can be made with a two-electrode configuration without a significant shift in the potential at the WE. The use of the two-electrode configuration provides the potential to reduce the size of the electrochemical cell and simplify the fabrication and measurement.

Designs for working electrodes are diverse. The working electrode can be a small sphere or disc, or a short wire, but it could also be a metal foil or an evaporated thin film. An essential feature of the working electrode is that the electrode material should not react chemically with the solvent or solution components. In principle, in order to decrease the double layer capacitance of the electrode, which is the major noise generator, the electrode should be relatively small. Moreover it should preferably be smooth, so the geometry and mass transport can be better defined. It is desirable to have a uniform current and potential distribution and hence there is a need for the electrochemical cell to be designed so that all points on the working electrode surface are geometrically equivalent with respect to the counter electrode. In practice achieving, this latter stipulation is difficult.

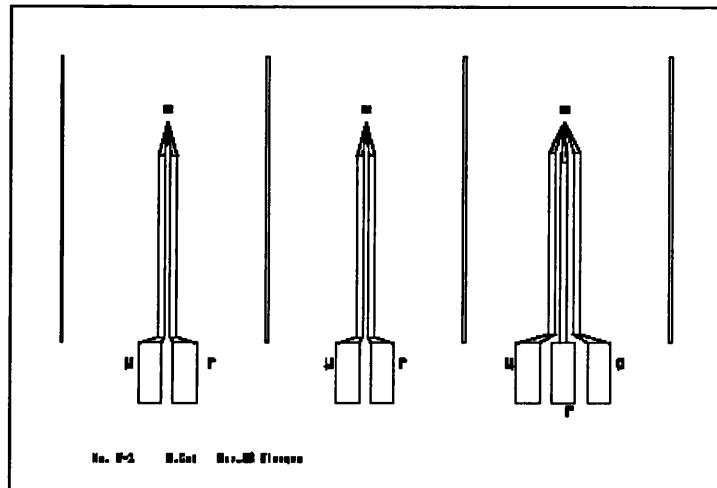
The purpose of the counter electrode is to supply the current required by the working electrode without in any way limiting the measured response of the electrochemical cell. It is essential that the electrode process is oxidation/reduction of a component of the electrolyte so that the current flows readily without the need for a large overpotential. As noted above, the counter electrode should have a large area compared to the working electrode so that the reaction at the working electrode is not limited. Moreover, the counter electrode's shape and position are important since these determine whether the working electrode is an equipotential surface. The role of the reference electrode is to provide a fixed potential that does not vary during the experiment (e.g. it should be independent of current density). It is advantageous to have the working and counter electrodes close together as this minimizes the cell resistance and maximizes the current which may be driven through the electrochemical cell by the potentiostat.

The electrolyte solution is the medium between the electrodes in the electrochemical cell. The solution consists of a solvent in which dissolved a high concentration of an ionized salt as well as the electroactive species; it may also contain other materials like buffers, etc.

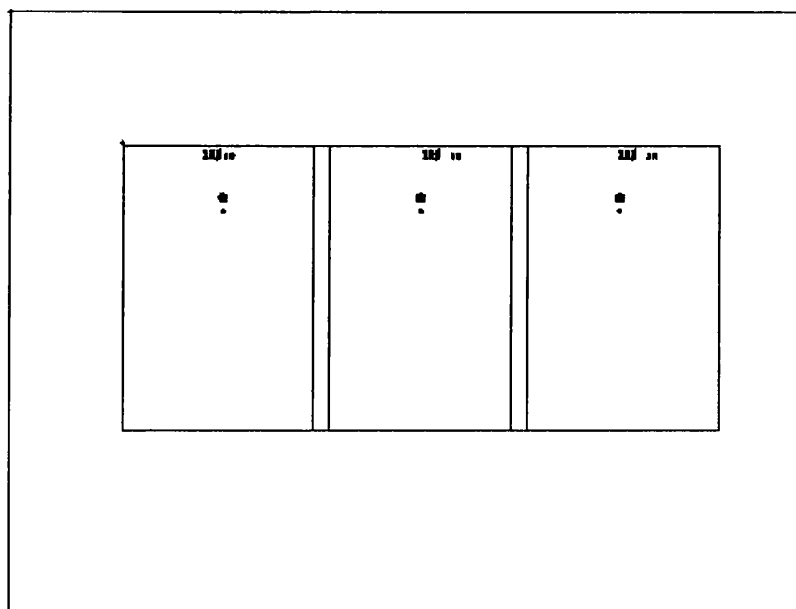
### 2.3.1.2 Computer Aided Design for Device Patterning

The proposed device pattern was designed using a PC-based design package 'WAM' (WaveMaker V3.8, Barnard Microsystems Limited) to create the photolithographic masks on an electron beam lithography system. The beamwriter

(Leica EBP5-5, HR) 'draws' the desired design onto a quartz plate as a master (covered by the polymer (polymethyl methacrylate, PMMA)). This master could then be copied to either a ferric oxide mask or a NiCr mask.



(a)



(b)

**Figure 2.1** Diagrams of the two layers in a WAM file used to producing two masks for the electrochemical devices (scale, 2:1): (a) the electrode layer including contact bands; (b) the chambers/channels layer.

In this research, there were two CAD layers in one file for producing two masks. The first of them is the layer for electrodes patterning and the second is for chambers/channels patterning. Figure 2.1 shows the examples of the two layers: (a) is the electrode layer and (b) is the chambers/channels layer.

### 2.3.2 Microfabrication

A flow chart for device fabrication is shown in Figure 2.2 and the major steps involved in the device fabrication are illustrated in Figure 2.3. Whereas many of the procedures followed standard lithographic methods, some of the steps were modified and optimized for this particular application (see following sections). Devices were constructed onto standard microscope slides, to enable observation of the titre volume under a microscope (in future applications).

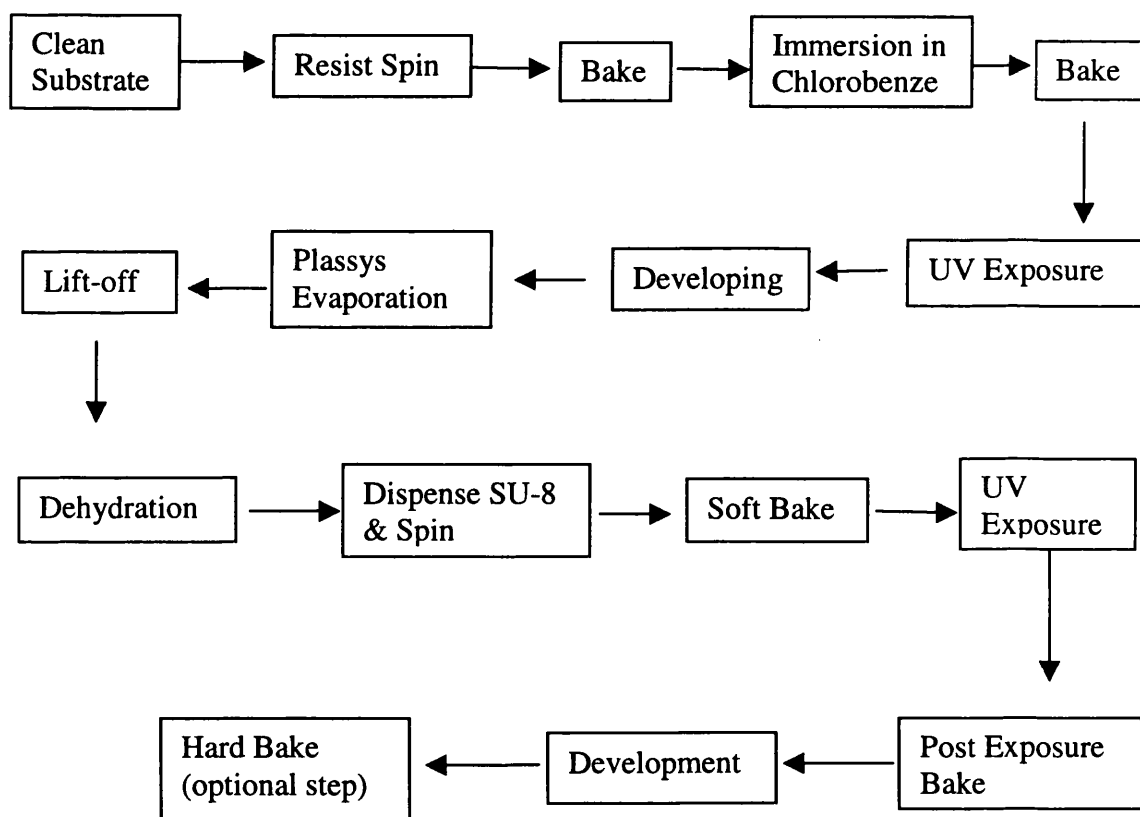


**Figure 2.2** Flow diagram briefly showing 16 steps for the fabrication of microelectrochemical cell (using SU-8) devices. The figure aims to show the complexity of the fabrication, which should be considered in the context of overall yield (90%).

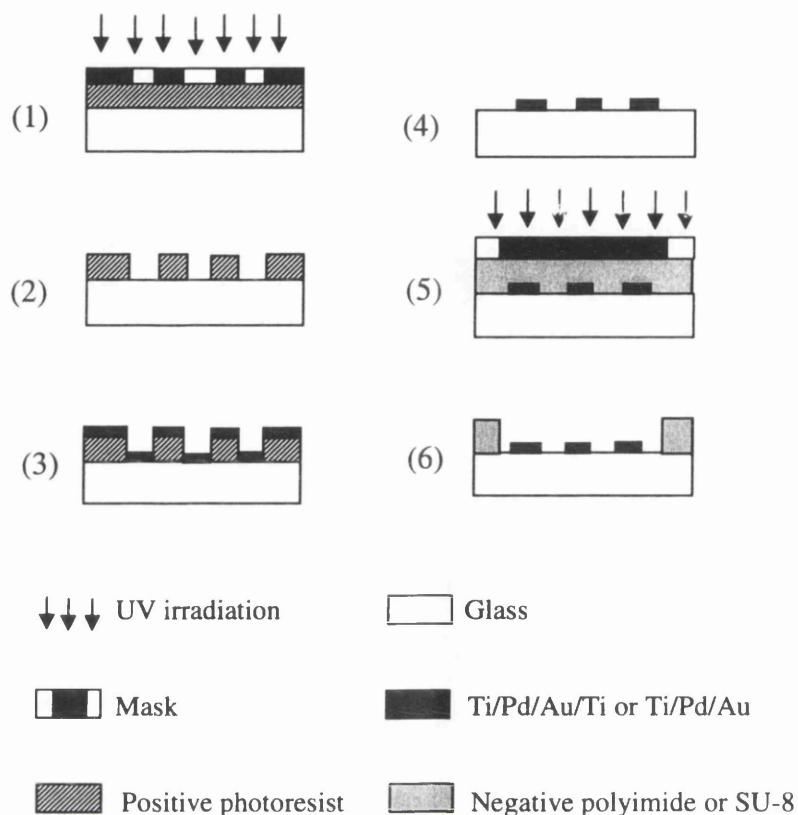


**Figure 2.3** Schematic diagram of major fabrication steps: (1) exposure of positive photoresist through a mask, in order to define the template for microelectrode deposition; (2) development of exposed photoresist followed by; (3) evaporation of multilayers of metals to form the microsensor array; (4) lift off reveals the microsensor configuration; (5) deposition of the negative photoresist (e.g. polyimide or SU-8) and exposure through a mask; (6) development of the exposed resist to reveal the microelectrodes within an analytical chamber.

### 2.3.2.1 Electrode Patterning

The microelectrodes were first patterned onto the slide, as a common step in the fabrication (regardless of which negative resist was used to define the microchamber). This involved a process in which the glass slide was first cleaned, dried and spun with an appropriate primer (in this case, hexamethyldisilazane). The slide was then spin-coated with positive photoresist (S1818) at 4000 rpm for 30 seconds. The photoresist was baked for 15 minutes at 90°C prior to a 15 minutes

immersion in chlorobenzene. The chlorobenzene soak was used to ease the final “lift-off” stage and to help define electrodes with clean and sharp edges. The slide was then rebaked for 15 min at 90°C and exposed to UV light ( $4 \text{ mW cm}^{-2}$ , 350-450 nm) for 12 seconds through the ferric oxide mask of the electrode pattern, and then developed, leaving the pattern for producing the microelectrodes and contact leads.

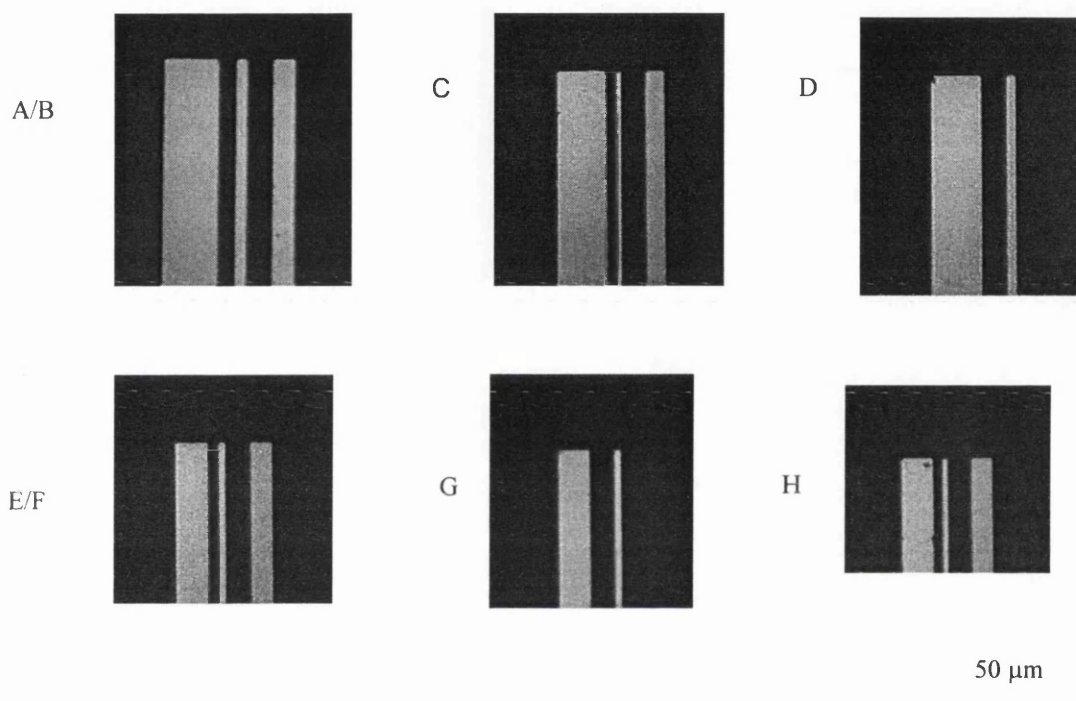


**Figure 2.4.** Photographs of 2-electrode or 3-electrode microelectrodes prior to the fabrication of the chambers, which sizes are shown in Table 2.1. The minimum width of the above microelectrodes is  $2 \mu\text{m}$ . “A ~ B” are the label of the devices refer to Table 2.1.

Metals were deposited by automated electron-beam evaporation (Plassys QD1) as Ti/Pd/Au/Ti (10/10/100/20 nm, for polyimide microchambers) or Ti/Pd/Au (10/10/100 nm, for SU-8 microchambers) multilayer structures. This recipe provides excellent adhesion of the metal to the glass substrate and good electrochemical stability. In this respect, the Ti underlayer acts as an adhesive layer to the glass (being highly diffusive), whilst the Pd layer forms a barrier, preventing the occurrence of Ti-mediated electrochemistry in the gold sensor. The 20 nm of Ti used, as the overlayer for the polyimide system, was deposited as a sacrificial layer, which stops the gold electrodes becoming fouled by polymer residues which persisted after the microchamber had been formed. It is important to note that this additional step is not

required for the SU-8 system (described below), due to the relative ease with which the three-dimensional chambers can be formed without unwanted residues (this may be a significant factor if using a less-sophisticated evaporator).

After metal deposition, the remaining photoresist was gently removed by a one-hour dissolution in acetone, causing the metal to “lift-off” and leaving patterns of microelectrodes and contact leads. Photographs of the microelectrodes used in this project are shown in Figure 2.4. The microelectrodes were produced in batches of 3 with a 100% yield. The minimum microelectrode width was 2  $\mu\text{m}$ . The sizes of them are illustrated in Table 2.1.

**Table 2.1** The sizes of the devices in Figure 2.4, where, CE: counter electrode; WE: working electrode; RE: reference electrode.

| Device<br>(see<br>Figure 2.4) | CE<br>Width<br>( $\mu\text{m}$ )<br>/Area<br>( $\mu\text{m}^2$ ) | Gap<br>between<br>CE & WE<br>( $\mu\text{m}$ ) | WE<br>Width<br>( $\mu\text{m}$ )<br>/Area<br>( $\mu\text{m}^2$ ) | Gap<br>between<br>WE &<br>RE<br>( $\mu\text{m}$ ) | RE<br>( $\mu\text{m}^2$ ) | Chamber<br>( $\mu\text{m}^3$ ) | Volume<br>( $\mu\text{L}$ ) |
|-------------------------------|--|--|--|---|---------------------------|--------------------------------|-----------------------------|
| A/B (3E)                      | 25/2500  | 8  | 5/500  | 12  | 10/1000                   | 140×140<br>×20                 | 390                         |
| C (3E)                        | 25/2500  | 5  | 2/200  | 12  | 10/1000                   | 140×140<br>×20                 | 390                         |
| D (2E)                        |  |  | 5/500  | 12  | 25/2500                   | 140×140<br>×20                 | 390                         |
| E/F (3E)                      | 15/1125  | 5  | 3/225  | 12  | 10/750                    | 100×100<br>×20                 | 200                         |
| G (2E)                        |  |  | 3/225  | 12  | 15/1125                   | 100×100<br>×20                 | 200                         |
| H (3E)                        | 12/660   | 5  | 2/110  | 12  | 10/550                    | 80×100<br>×20                  | 160                         |

### 2.3.2.2 Fabrication Using Polyimide

Using the Ti/Pa/Au/Ti electrodes described previously, the electrochemical cell container, i.e. microchamber, was completed using polyimide.

After drying for 10 min at 180°C to drive off surface moisture, the slide was spin-coated (2000 rpm for 9 secs) with photopolymerizable polyimide. The polyimide was soft-baked in two steps on hot plate, first at 60°C and subsequently at 90°C. The

layer was photopolymerised by exposure to UV light (4 mW cm<sup>-2</sup>, 350 ~ 450 nm, System 3 Series, HTG) for 11 seconds through a NiCr mask. The polyimide was then developed with polyimide developer for 4 minutes and rinsed for 10 seconds in with polyimide rinse to expose an  $\mu\text{m}$ -scale titre chamber over the microelectrodes, with large rectangles over the bonding pads. The samples were hard-baked at 300°C in a nitrogen-purged oven for 1 hour, in order to convert polyimide precursors into the final durable polyimide.

During the curing process, a weight loss occurs which is associated with a film thickness reduction of 40-50%. Finally, in order to remove the polyimide residue, the Ti sacrificial layer was removed using a reactive ion etching (RIE). The RIE occurred in 30 sccm (standard cubic centimeters per minute) pure oxygen at 20 mTorr and 100 W RF power for 3 minutes followed by 10 sccm SF<sub>6</sub> at 13 mTorr and 100 W for 9 minutes. The thickness of the polyimide film was about 20 ~ 25  $\mu\text{m}$ . The fabrication yield using polyimide is about 60%.

### 2.3.2.3 Fabrication Using SU-8

Using the Ti/Pd/Au electrodes described previously, the electrochemical cell container, i.e. microchamber, was also completed using SU-8.

SU-8 primer (hexamethyldisilazane) was spun at 2000 rpm for 40 seconds on a dried glass slide onto which the electrode configuration had already been patterned (optional). SU-8 resist was initially spun at 500 rpm for 5 sec, to a final spin speed of 1300 rpm for 30 seconds, via incremental 5 seconds steps. The resist was then pre-baked on a flat hot plate at 90 ~ 95 °C for 10 min. Microlithography was performed using a contact aligner (4 mW, 350 ~ 450 nm, System 3 Series, HTG) with a 23 sec exposure time. The exposed resist was then subjected to a 15 min post exposure bake on the hot plate at 90 ~ 95°C, then developed for 1 ~ 1.5 min and rinsed for 10 sec. An optional hardbake was then performed in an oven at 120°C for 30 min. In order to ensure a clean microelectrode surface, the samples were finally etched using 30 sccm pure oxygen at 20 mTorr and 100 W RF power for 1 to 2 min. If desired, Pt was electrodeposited after step 6 (see Figure 2.3) or sputtered to a thickness of 100 nm after step 3 (Figure 2.3). The SU-8 film thickness obtained was about 20 ~ 25  $\mu\text{m}$ . The fabrication yield using SU-8 is about 90%.

### 2.3.3 Post Fabrication: Electrochemical Deposition

Prior to electrochemical deposition, the devices were cleaned using dry etching method as described in Section 3.3.3. Chronopotentiometry was used for platinisation, electrochemical deposition of Ag or AgCl, when a current density was set at a value (see below). Also chronoamperometry was used for Pt-black or AgI/AgCl electrochemical deposition. The microelectrode, either for the working electrode platinisation or for the reference/counter electrode deposition, was biased at between  $-1.00$  V and  $-0.15$  V, using a coil of platinum wire as both the counter and the reference electrodes. The potentiostat used was either a potentiostat/galvanostat model 273A (EG&G Princeton Applied Research) or a CV-37 (BAS).

#### 2.3.3.1 Microelectrode Platinisation

Pt was deposited from 24 mM hexachloroplatinate in the presence of 2.1 mM lead acetate either by chronopotentiometry or by chronoamperometry methods. Figure 2.5 shows a representative response of platinisation on microelectrodes. The chronopotentiometry responses of platinisation on a  $1000 \mu\text{m}^2$  microelectrode are shown in Figure 2.5 (a). A uniform greyish white platinum planar layer was prepared at a current density of  $-45 \text{ mA cm}^{-2}$  in curve (i). A dense platinum black layer was prepared at a current density of  $-70 \text{ mA cm}^{-2}$  in curve (ii). Note the potentials in curve (i) and curve (ii) are about  $-0.6$  V and  $-1.0$  V respectively. The chronoamperometry responses of platinisation on microelectrodes were shown in Figure 2.5 (b). Dense black particular layer (Figure 2.6) were deposited on the microelectrodes with different area, at a biased voltage of  $-1.0$  V vs. a pseudo reference (using a coil of platinum wire as both the counter and the reference).

The equation describing the reduction of platinum at the microelectrode is,



Chronoamperometry was more reliable than chronopotentiometry for the platinum black deposition as less control is needed for the exact conditions required. For chronoamperometry, only the deposition time needed to be fixed depending on the electrode area, at a potential of approximately  $-1.0$  V. However, in chronopotentiometry, not only must the deposition time be fixed, but the current density must be carefully controlled. If the current density was too high to produce a

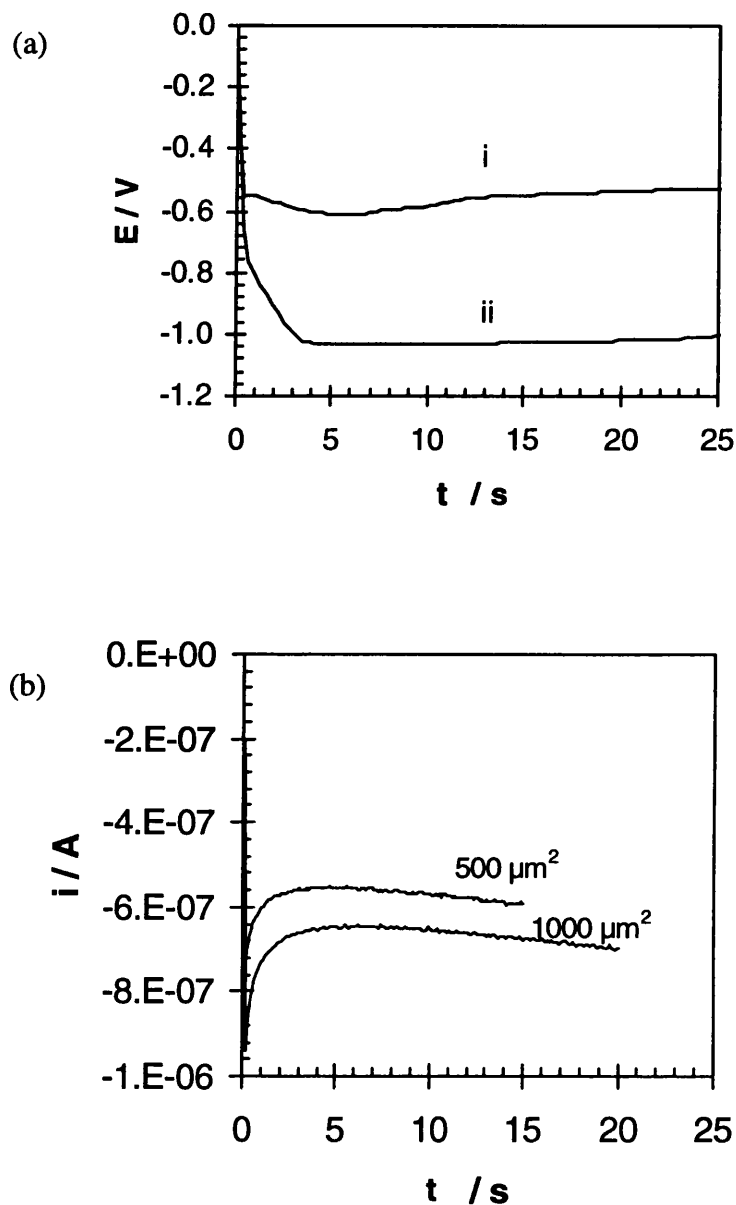


**Figure 2.5** Chronopotentialmetric and chronoamperometric curves for microelectrode platinisation. (a) Chronopotentiometry response to platinisation on a  $1000 \mu\text{m}^2$  microelectrode. The current density was fixed at  $-45 \text{ mA cm}^{-2}$  in curve (i) (producing an uniform greyish white platinum planar layer) and  $-70 \text{ mA cm}^{-2}$  in curve (ii) (producing platinum black layer). (b) Chronoamperometry response to platinisation on microelectrodes of two different areas ( $500 \mu\text{m}^2$  and  $1000 \mu\text{m}^2$ ). The applied potential was held at  $-1.00 \text{ V}$ .

potential of  $-1.0$  V, an electrode short can form between the microelectrodes because platinum black formed at high-speed. If the current density was too low to produce a potential of approximately  $-1.0$  V, the platinum black layer can not be formed. In this later case, nothing formed or only a thin grey/white platinum layer formed. This suggests both that the working potential for platinum black deposition on the microelectrode is about  $-1.0$  V, and chronoamperometry is the preferred deposition method.

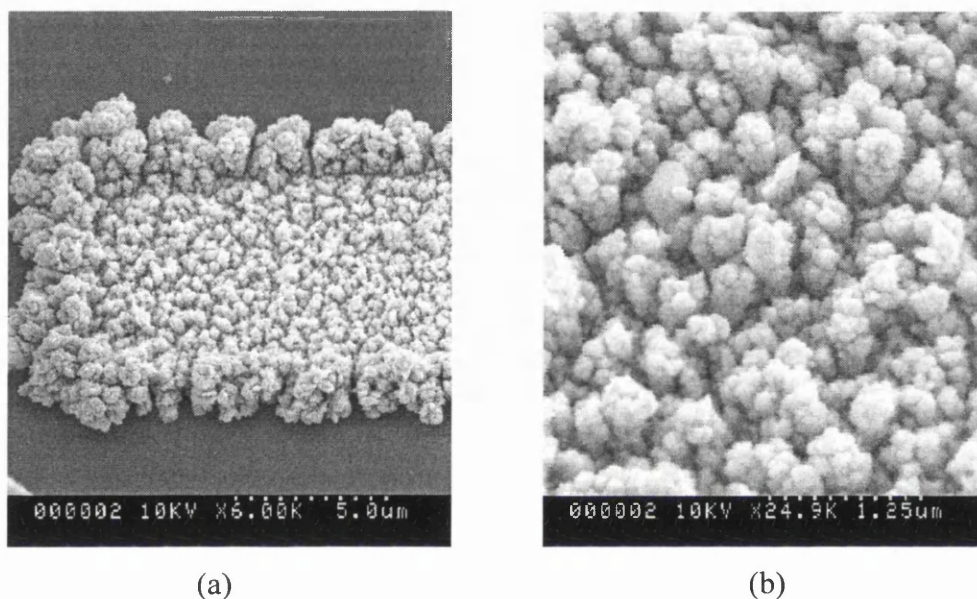


**Figure 2.6** SEM micrographs of platinisation morphology: (a) micrograph of the platinized electrode; (b) magnified area of (a) to highlight platinum black morphology.

### 2.3.3.2 Microreference Deposition of Ag|AgCl

Similarly, silver was deposited either by chronopotentiometry or by chronoamperometry on larger reference microelectrode ( $1200 \sim 3125 \mu m^2$ ) by connecting this to the working electrode lead and using a coil of platinum wire as both the counter and the reference electrodes. The silver layer was deposited from  $0.2$  M  $AgNO_3$  /  $2$  M  $KI$  /  $0.5$  mM  $Na_2S_2O_3$  whereas  $AgCl$  was prepared in  $0.1$  M  $HCl$ . The silver deposition solution was prepared as below:

$3.38$  g of  $AgNO_3$ ,  $33.2$  g  $KI$  and  $0.0124$ g  $Na_2S_2O_3$  were dissolved in about  $33$  ml of reverse osmosis (R.O.) water separately, the total solution was made up to  $100$  ml.  $AgNO_3$  solution was dropped into the stirred mixture of  $Na_2S_2O_3$  solution and  $KI$  solution.

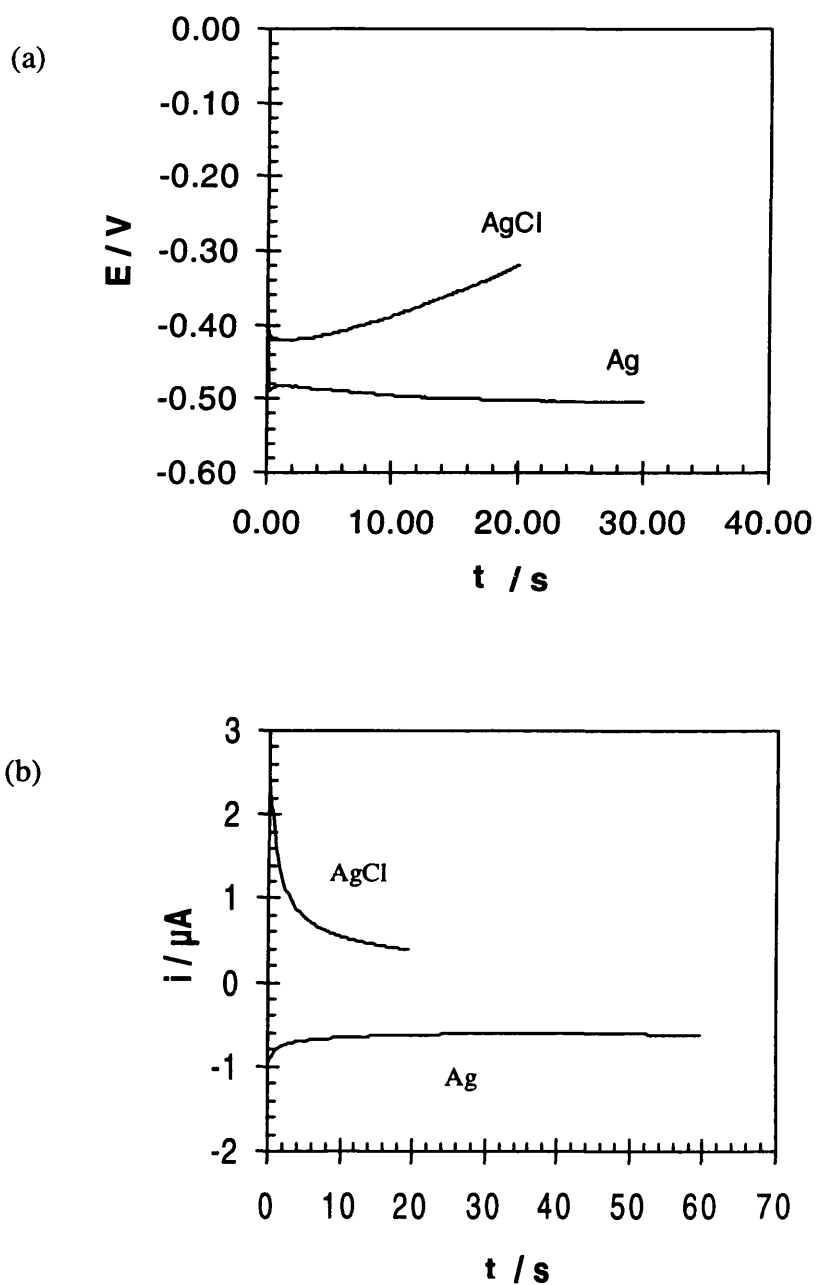


**Figure 2.7** Chronopotentiometric and chronoamperometric curves for Ag|AgCl deposition on microelectrodes: (a) chronopotentiometry responses to Ag deposition (at  $-40 \text{ mA cm}^{-2}$ ) and subsequent AgCl formation (at  $40 \text{ mA cm}^{-2}$ ) on a  $1200 \mu\text{m}^2$  microelectrode; (b) chronoamperometry curves using a  $3125 \mu\text{m}^2$  microelectrode. The potential was biased at  $-0.48 \text{ V}$  and  $-0.15 \text{ V}$ , for Ag and AgCl deposition respectively.

Equations are given below describing reduction (2.3) and oxidation (2.4) at the microelectrode and reduction at the platinum wire (2.5).

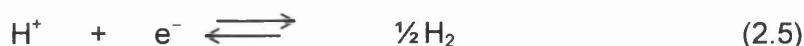
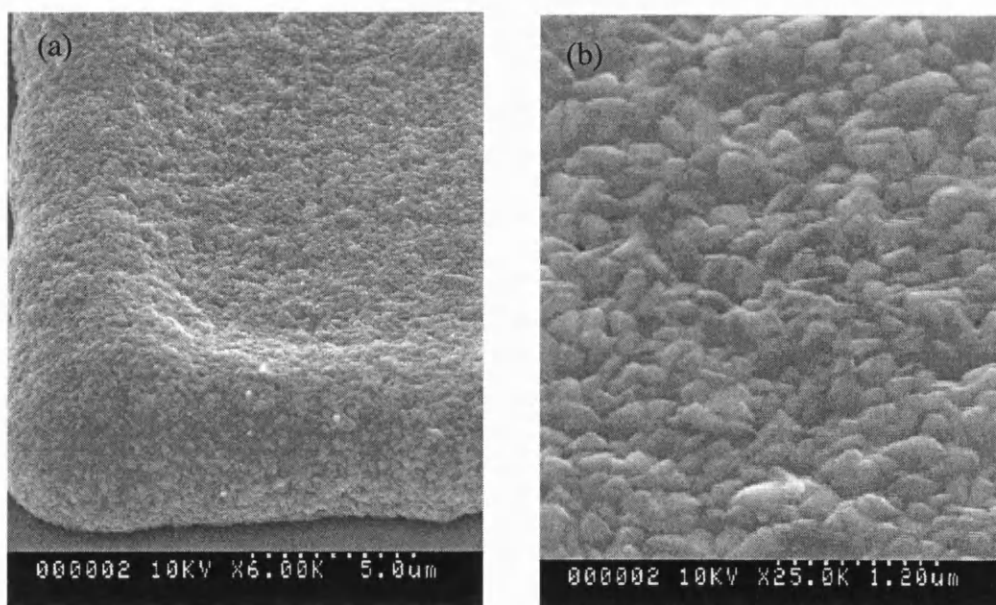


Figure 2.7 recorded the deposition of Ag|AgCl with time, on the microelectrodes. Chronopotentiometry using a  $1200 \mu\text{m}^2$  microelectrode is shown in Figure 2.7 (a). A silver layer was deposited at a current density of  $-40 \text{ mA cm}^{-2}$  and the AgCl layer was subsequently formed by anodizing the silver layer at a current density of  $40 \text{ mA cm}^{-2}$ . Chronoamperometry using a  $3125 \mu\text{m}^2$  microelectrode were shown in Figure 2.7 (b). A silver layer was deposited on the microelectrode, biased at  $-0.48 \text{ V}$ , then a AgCl layer was subsequently formed by anodizing the deposited silver layer at  $-0.15 \text{ V}$  for  $20 \sim 30 \text{ s}$ . During this period, the current decayed slowly from  $1.8$  to about  $0.25 \mu\text{A}$ . Both methods produced a shiny, uniform underlayer of silver prior to formation of a dense, coherent red/brown silver chloride layer (Figure 2.8).



**Figure 2.8** SEM micrographs of Ag|AgCl morphology: (a) micrograph of the Ag|AgCl reference electrode; (b) magnified area of (a) to highlight the AgCl morphology.

As it is difficult to control the current density for deposition of Ag|AgCl on different size electrodes, chronoamperometry is recommended for the deposition. The preferred applied potential was  $-0.48$  V and  $-0.15$  V for Ag and AgCl respectively, and the deposition time is set depending on the area of the microelectrodes.

### 2.3.3.2 Microreference Deposition of Ag|Ag<sub>3</sub>PO<sub>4</sub>

The deposition of Ag|Ag<sub>3</sub>PO<sub>4</sub> was also explored for the production of a possible reference electrode. Such a system would have the advantage of providing a suitable electrochemical cell for biological measurements in phosphate buffers, e.g. cell culture. In addition, it is established that Ag<sub>3</sub>PO<sub>4</sub> has a low solubility in aqueous solution, and should therefore provide a stable system.

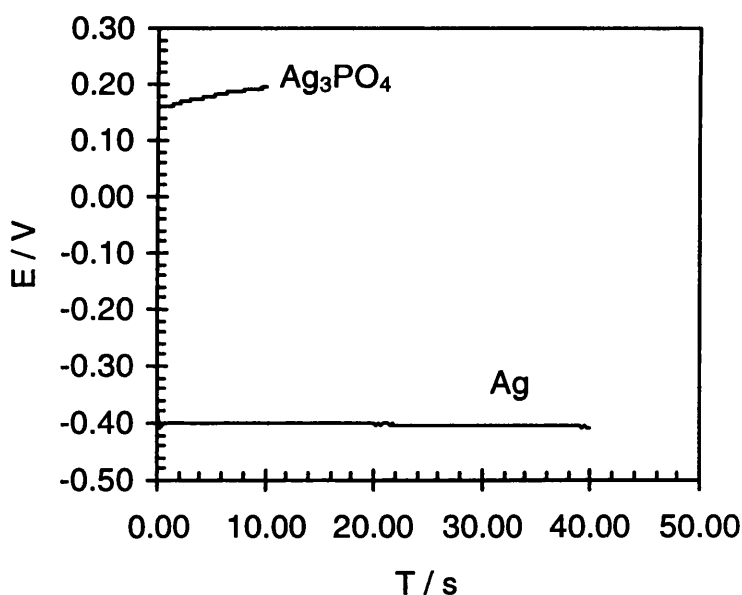


**Figure 2.9** Chronopotentiometry response for time dependent deposition of Ag on a  $1200 \mu\text{m}^2$  microelectrode from a solution of AgNO<sub>3</sub>/KI/Na<sub>2</sub>S<sub>2</sub>O<sub>3</sub> (0.2/2.0/0.5 M), and subsequent formation of Ag<sub>3</sub>PO<sub>4</sub> at a current density of  $33 \text{ mA cm}^{-2}$  in a solution of 0.1 M H<sub>3</sub>PO<sub>4</sub>.

AgIAg<sub>3</sub>PO<sub>4</sub> were deposited electrochemically onto a microelectrode for use as an internal reference. Alternatively a larger external reference was used, to corroborate these results (see Section 3.4.4). The Ag layer was prepared at current density of -30 ~ -40 mA cm<sup>-2</sup> for 30 ~ 45 seconds using 0.2M AgNO<sub>3</sub>, 2.0M KI and 0.5 mM Na<sub>2</sub>S<sub>2</sub>O<sub>3</sub>. The silver phosphate layer was formed by anodizing the deposited silver layer in 0.1 M or 0.03 M H<sub>3</sub>PO<sub>4</sub> at current density of 10 ~ 40 mA cm<sup>-2</sup> for 7 ~ 10 seconds (Figure 2.9).

The equations for reduction (2.2) at the microelectrode and reduction (2.4) at the platinum wire have been given above; The oxidation (2.5) at the microelectrode is given below.



## 2.4 Results and Discussion

### 2.4.1 The Evaluation of Polyimide and SU8

There are a number of considerations when deciding upon a microfabrication or micromachining protocol for hybrid electroanalytical devices, not least the material's chemical resistance, electrical and electrochemical properties of the metals and the mechanical properties of the polymer. Further issues concern the biocompatibility of the materials used (see Section 5.4.1) as well as the compatibility of the proposed methods with microfabrication protocols.

Using both polyimide and SU-8 with depths between 20 ~ 25 μm, circular chambers with diameters in the range 100 ~ 160 μm and square chambers with geometries of 80 × 100 μm<sup>2</sup> and 140 × 140 μm<sup>2</sup> have been fabricated. Geometric volumes vary between 160 pL and 490 pL, as a function of the device size, geometry and thickness of the polymer (Table 2.1).

#### 2.4.1.1 Processing of Polyimide

It is important to note that polyimide is almost impossible to dissolve in common solvents and it can be considered insoluble for all practical purposes. The fabrication

technique described in this work involves the application of a 'polyimide precursor' coating to the glass surface, which is subsequently converted to the polymer by "curing" (*i.e.* heating to affect the chemical reaction), which produces the final polyimide bond. When the "curing" temperature was set at 300°C, there was a gentle peak in the wall of the chamber and the polyimide color was light translucent brown. When the curing temperature was set at 350°C, as suggested by the product company (Olin Microelectronics Materials), the peak in the wall became very sharp and the wall deformed to varying degrees; likewise the polyimide colour was dark opaque brown. In order to control the structure of the chamber accurately and monitor the microelectrode more easily, a curing temperature of 300°C was chosen.

In addition, examination using an SEM, or by surface profilometry revealed residue on the microelectrodes after processing. This was found to severely inhibit subsequent electrochemical studies, giving large device to device response variability (see later). Two methods were used to remove residual polyimide, both involving a sacrificial layer. Previously, a wet etch was chosen to remove a NiCr layer [18], thereby freeing the Au surface from the residue. However, the acid etch solution removed the NiCr under the polyimide surface, undercutting the polymer. As an alternative method, a dry etch, using a Ti sacrificial layer was developed (O<sub>2</sub> followed by SF<sub>6</sub>, O<sub>2</sub> is used for polyimide residue etching and SF<sub>6</sub> is used for Ti etching).

The problem subsequently encountered is that of over-etching the polyimide. In an attempt to remove the residue over-etching, could cause the residue become resistant to the etching gases. The resistant residue is based on the formation of metallo-organic compounds from reactions between RIE products and metal sputtered from the electrode structures [24]. Methods optimised to reduce the amount of etch residue include the reduction of the etching power and careful controls of etch depth/time (see later).

Figure 2.10 shows a representative sample of devices fabricated with polyimide microchambers. Figures 2.10 (a-c) show, respectively, examples of 3 microband electrode device, 2-electrode device and a device with polyimide residue at the bottom of the chamber.

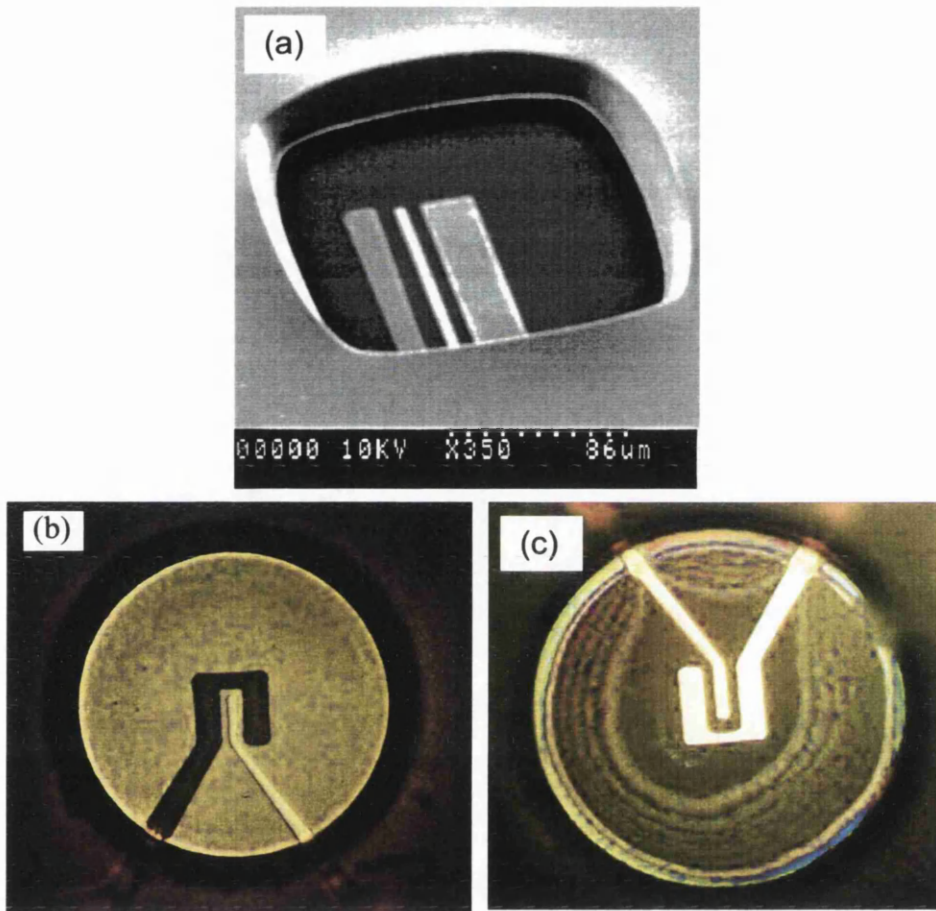


**Figure 2.10** SEM Image (a) and photographs (b-c) of the devices fabricated with polyimide microchambers: (a) a 3-microelectrode with a polyimide microchamber ( $140 \times 140 \mu\text{m}^2$ ); (b) a 2-microelectrode with a polyimide microchamber (diameter:  $160 \mu\text{m}$ ); (c) a device with polyimide residue in its chamber bottom (diameter:  $160 \mu\text{m}$ ).

#### 2.4.1.2 Processing of SU-8

SU-8 is an epoxy based, chemically amplified resist system with excellent sensitivity and a demonstrated ability to produce surface microstructures with high aspect ratios. For example, it has previously been used in producing microfabricated mechanical structures and other microsystems, such as sensors, actuators,

microfluidic components and molds for electroplating [25,26]. As well as being cheaper than comparable polyimide resists, it has a better exposure sensitivity, which coupled with the excellent adhesion of epoxy derivatives, makes it very suitable for defining microchambers for the applications described in this work.

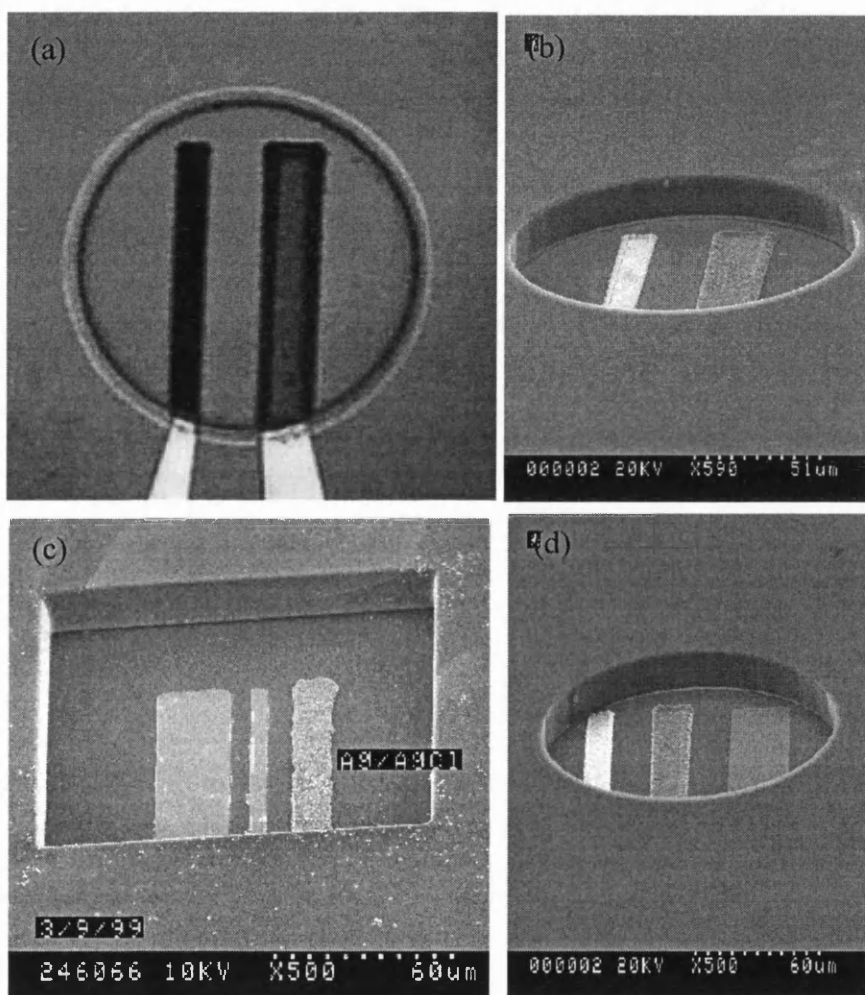


**Figure 2.11** Photograph (a) and SEM images (b-d) of the devices fabricated using SU-8: (a) a 2-microelectrode device (microchamber diameter: 150  $\mu\text{m}$ ); (b) a 2-microelectrode device (microchamber diameter: 150  $\mu\text{m}$ ); (c) a 2-microelectrode device (microchamber: 140  $\times$  140  $\mu\text{m}^2$ ); (d) a 3-microelectrode device (microchamber diameter: 150  $\mu\text{m}$ ).

SU-8 offers an attractive alternative to polyimide as a photoactive polymer for machining such electroanalytical structures. The material has a very low optical absorption in the near-UV and this high transparency means that high aspect ratio structures can be obtained when the polymer is exposed using a standard UV aligner. There are other advantages in the use of SU-8 in this application. For example, due to its aromatic functionality, with its highly cross-linked matrix, the exposed resist is both thermally and chemically stable. Additionally, a number of thicknesses can be obtained with a single deposition, ranging from 750 nm to 450  $\mu\text{m}$  with a conventional spin coating [25].

However, SU-8 is a high stress material, and exhibits surface cracking caused by incomplete cross-linking when the exposure dose is too low. Some care must be taken in optimising the exposure protocols. Exposures of 92  $\text{mJ cm}^{-2}$  for the film with 20 ~ 25  $\mu\text{m}$  thickness were found to give films with good integrities (as evidenced by examination under SEM). Any surface aberrations can be removed by annealing the polymer at 120  $^{\circ}\text{C}$  for 30 mins. Figure 2.11 shows photograph and SEM images of representative samples of devices fabricated with SU-8 microchambers.

#### 2.4.1.3 Comparison of Polyimide and SU-8

Comparison of the devices fabricated from polyimide (Figure 2.10) and SU-8 (Figure 2.11) reveal that the completed lower surface of the chamber is cleaner for the SU-8 device, with virtually no polymer residue present. The sizes of the devices are illustrated in Table 2.2.

**Table 2.2** The sizes of the devices in Figure 2.11 (b,d), where, CE: counter electrode; WE: working electrode; RE: reference electrode.

| Device (see Figure 2.11) | CE Width ( $\mu\text{m}$ ) /Area ( $\mu\text{m}^2$ ) | Gap between CE & RE ( $\mu\text{m}$ ) | WE Width ( $\mu\text{m}$ ) /Area ( $\mu\text{m}^2$ ) | Gap between WE & RE ( $\mu\text{m}$ ) | RE ( $\mu\text{m}^2$ ) | Volume of Chamber (with depth of 20 $\mu\text{m}$ ) (pL) |
|--------------------------|--|---------------------------------------|--|---------------------------------------|------------------------|--|
| 2E (Fig 2.11b)           |  |                                       | 10/1250  | 30                                    | 25/3125                | 353  |
| 3E (Fig 2.11d)           | 30/3450  | 22                                    | 20/1125  | 24                                    | 14/1820                | 353  |

Additional physical characterisation of the devices was performed using surface profilometry as shown in Figure 2.12 (a) and (b). The profile of the devices were obtained using Dektak surface profiler (Veeco Sloan Technology). The microelectrodes can be clearly identified in the bottom of the fabricated SU-8 chamber (Figure 2.12(a)). Comparison of the surface profiles shows that the sidewalls of the SU-8 chamber have higher aspect ratios, than for polyimide, leading to chambers with reduced surface to volume ratios. Figure 2.12(b) shows that when fabricating devices using polyimide, there was a gentle peak in the lip of the chamber (where due to its thinness, the polyimide is a light translucent brown). In contrast with polyimide, almost no lip was seen on the SU-8 chamber sidewalls. This is important when considering the acute angle of the microcapillary, when accessing the microchamber, required upon microinjections is being performed under the microscope.

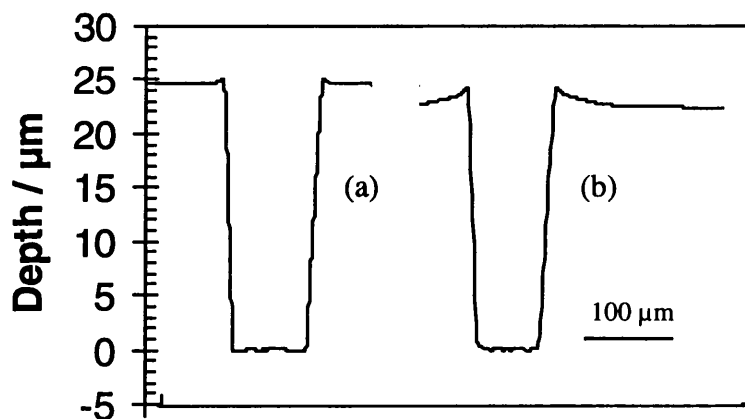


**Figure 2.12** Typical profiles of microchambers fabricated using (a) SU-8 and (b) polyimide, obtained using surface profilometry. The electrode can be seen in the bottom of both chambers, whilst the lipped polyimide can be seen in Figure 2.12 (b). This latter feature can make micro-pipetting of cells into the chamber more problematical.

### 2.4.2 Evaluation of the Device Fabrication

Sub-nanovolume electrochemical cells could be produced reliably and reproducibly. Figure 2.13 gives examples of devices with two-electrode and three-electrode configurations. High aspect ratio in thick SU-8 film with smooth vertical sidewalls is possible to be obtained using photo lithography technique as shown

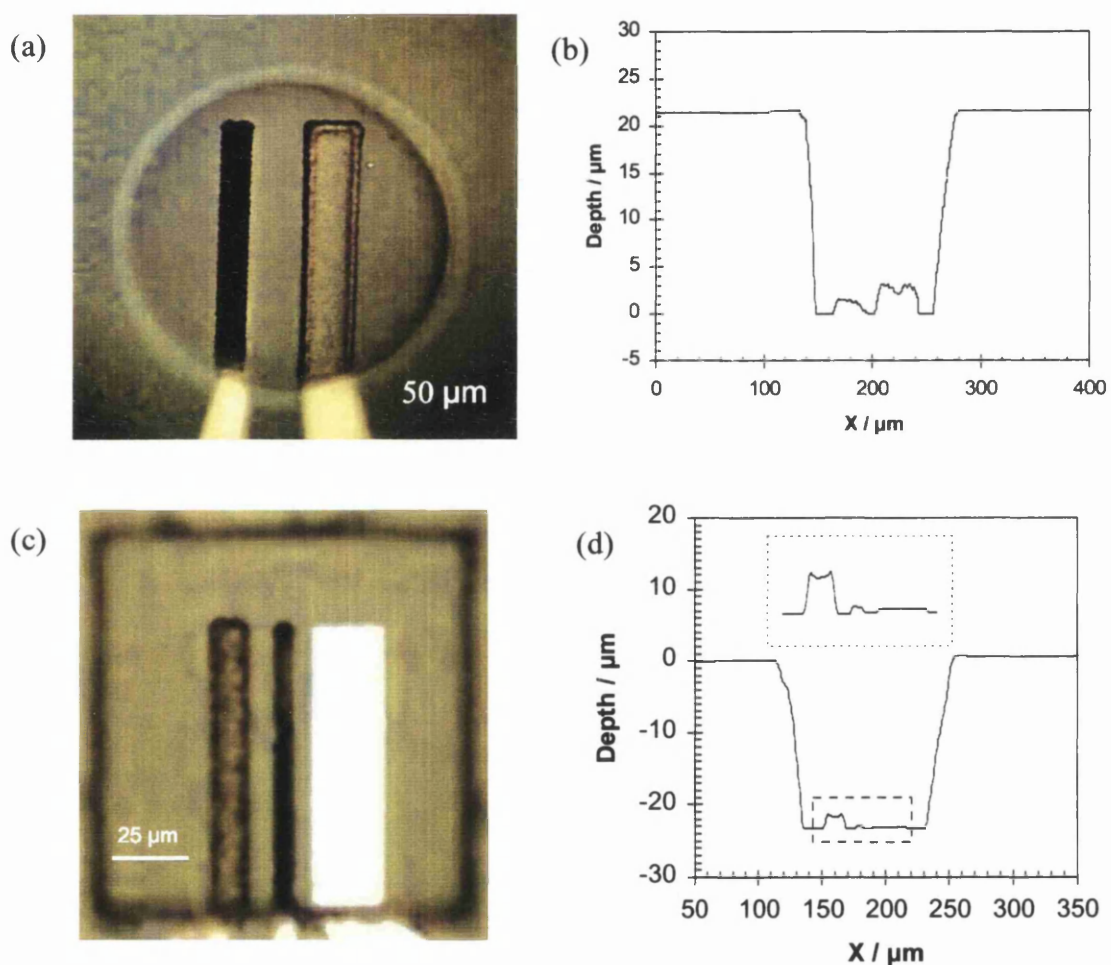


**Figure 2.13** shows some representative device: (a) the photograph of a typical two-microelectrode (left, working electrode; right, reference electrode) within SU-8 microchamber ( $150\ \mu\text{m}$  diameter); (b) the profile of the device in (a); (c) the photograph of a typical three-electrode (left, reference electrode; middle, working electrode; right, counter electrode) within SU-8 microchamber ( $140 \times 140\ \mu\text{m}^2$ ); (d) the profile of the device in (c).

by the SEM micrographs in Figure 2.11 (b-d). Black functionalised microparticles of platinum were seen on the working electrode and a dense coherent red-brown silver chloride layer was seen on the large reference electrode (Figure 2.13 (a, c)). Using surface profilometry, the thickness of the Ag|AgCl reference electrode in Figure 2.13(b) was measured as between 2.0 ~ 3.0  $\mu\text{m}$ , whilst the thickness of the platinised working electrode in Figure 2.13 (b) was between 0.3 ~ 1.5  $\mu\text{m}$ .

The platinized microelectrodes, comprising porous platinum microparticles (platinum black), possess a large surface area and are highly catalytic for electrochemical detection processes (with a reduced overpotential for the oxidation of  $\text{H}_2\text{O}_2$ , for example). This enhanced surface area was found to increase the signal/noise ratio significantly. Whereas a planar platinum surface was easily fouled, the sensitivity and lifespan of biosensors, where the detection takes place on planar platinum surface can be improved by making the surface porous (see Section 3.4.5).

## 2.5 Conclusions

Micromachined sensors were fabricated using photolithography to give a high aspect ratio 'well' (as the analytical chamber) with microelectrodes (consisting layers of Ti/Pd/Au/Pt) positioned within it. As well as a 3-microelectrode sensor, 2-microelectrode sensor was also studied, containing a working microelectrode and an internal microreference Ag|AgCl or Ag|Ag<sub>3</sub>PO<sub>4</sub> (also act as the counter electrode). Chronoamperometry is more reliable than the chronopotentiometry for the deposition of platinum black and Ag|AgCl.

Photopolymerizable polyimide and SU-8 photoepoxy were used to form the micorchambers (having a depth of 20 ~ 25  $\mu\text{m}$ ) with either a circular (diameter 100-160  $\mu\text{m}$ ) or rectangle/square (80 $\times$ 100  $\mu\text{m}^2$  ~140 $\times$ 140  $\mu\text{m}^2$ ) geometry. The smallest width achieved for the microband electrode was 2  $\mu\text{m}$  and the lowest volume of the micorchambers was 160 pL. Comparison of the two materials revealed that SU-8 was found to be more promising than polyimide for this micromachining application.

## Chapter 3: Electrochemical System and Device Characterisation

### 3.1 Introduction

This chapter describes the use of ferrocenemonocarboxylic acid (FMCA) as a model redox compound for investigating the electrochemical characterization of the integrated sensors. Hydrogen peroxide and glucose detection were also demonstrated. Ferrocene and its derivatives can be used as mediators for glucose sensors to eliminate the dependence of the sensors on oxygen tension and remove  $[H^+]$  interference, as well as reducing the working potential [27]. The use of FMCA as a mediator in the presence of the enzyme glucose oxidase and glucose as a substrate was also described. Previously, Pt (platinum black) has been deposited onto Au microelectrodes to reduce the required over-potential for hydrogen peroxide detection [12]. In order to simplify this procedure, and to implement a less time consuming protocol, the use of 100 nm of sputtered Pt was investigated (after step 3 in Figure 2.3). As a consequence, all the subsequent experiments described in this chapter involving bioelectrochemical analyses, with the exception of those in Section 3.4.5, were carried out with a 100 nm thick sputtered Pt ad-layer over the Au microelectrodes. Finally, the working electrode of sputtered Pt was found to be easily fouled and was compared with platinum black electrode.

The opening sections of this chapter (Section 3.1.1 ~ 3.1.7) provide a brief synopsis of some of the underlying theory and practicalities that govern the electrochemical techniques used in Chapters 3 ~ 5.

#### 3.1.1 *Potentiostatic Measurements*

Measurements are made using a potentiostat, an instrument that compares the potential difference between the working electrode and reference electrode with a 'desired' input potential. If these two potentials are different, a feedback loop causes current to flow between the counter electrode and working electrode. Thus an electrochemical process at the working electrode causes the potential to change (bringing the potential difference between the reference and working electrodes closer to the 'desired' potential).

The current flowing into or out of the working electrode is equal to that flowing through the counter electrode. If the same electroactive species are determining the counter and working electrode potentials and the oxidised and reduced forms are present in equal amounts, then the potentials of these electrodes will differ from the reference electrode potential by equal and opposite amounts. If different electroactive species are involved at the two electrodes, then expressions such as the Tafel relationship (Section 3.1.7) determine the potential of the counter and working electrodes with respect to the reference electrode.

### 3.1.2 Two-electrode Cell and Three-electrode Cell [28,29]

A simple two-electrode cell (Figure 3.1(a)) is perfectly acceptable for the measurement of current/voltage curves where only a small current density is passed. For example, it is ideal for microelectrode studies (where  $i < \mu\text{A}$ ). However, for larger electrodes a difficulty arises. Consider an applied potential difference,  $E$ , applied between a large working electrode and a reference and assume that a finite current is flowing between them. Then,

$$E = (\phi_m - \phi_s) + iR + (\phi_s - \phi_{\text{REF}}) \quad (3.1)$$

Notice that the potential is split into three terms. The first of these,  $(\phi_m - \phi_s)$ , is the driving force for electrolysis at the working electrode/solution interface. The second describes the voltage drop,  $iR$ , in solution due to passage of current between the two electrodes ( $R$  is the electrical resistance of the intervening solution). The third term,  $(\phi_s - \phi_{\text{REF}})$  is the potential drop at the reference electrode/solution interface and is fixed by the chemical composition of the chosen reference electrode.

The aim of any voltammetry experiment is to measure  $i$  as a function of changes in the quantity  $(\phi_m - \phi_s)$ . For microelectrode experiments the term  $iR$  ( $i < 10 \mu\text{A}$ ,  $R < 100 \Omega$ ,  $iR < 1 \text{ mV}$ ) can be neglected and since  $(\phi_s - \phi_{\text{REF}})$  is fixed, eqn (3.1) simply reduces to

$$E = (\phi_m - \phi_s) + \text{constant} \quad (3.2)$$

Consequently, changes in the applied potential are directly reflected in the driving force,  $(\phi_m - \phi_s)$ , as desired, and voltammetry is meaningful with two electrodes.

With large electrodes, however,  $iR$  is no longer negligible and so changes in the applied potential are not confined to changes in  $(\phi_m - \phi_s)$ . In particular, the  $iR$  term is altered since the current flowing through the cell will also be induced to change. Moreover, the passage of large currents through the reference electrode can cause a change of the reference's chemical composition and so the third term,  $(\phi_s - \phi_{REF})$ , may no

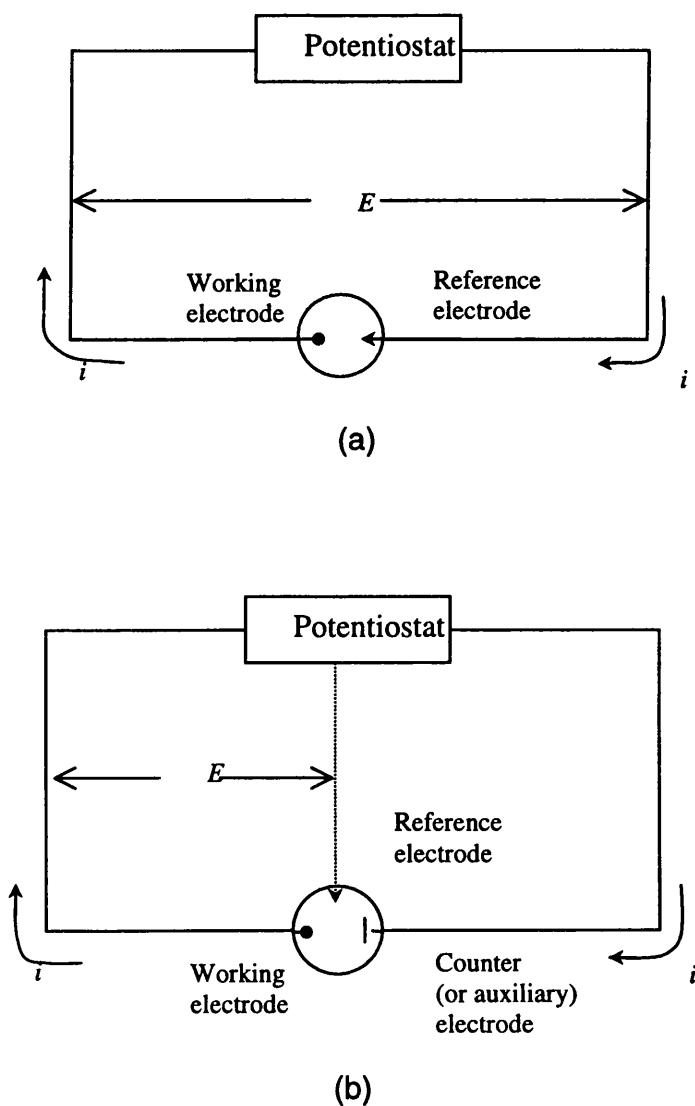


Figure 3.1 Schematic diagrams of (a) a two-electrode cell and (b) a three-electrode cell.

longer be constant.

To circumvent this problem it is usual to conduct voltammetric experiments using a three-electrode cell (see Figure 3.1(b)) in which an auxiliary or counter electrode is used, in addition to the other two. The three-electrode cells are controlled by a potentiostat, which ensures the current only flows between the working and counter electrode. The potential of the working electrode is held relative to the stable reference electrode and the potentiostat ensures that no current passes through the reference arm of the circuit.

### 3.1.3 Amperometry and Cyclic Voltammetry

Amperometry and cyclic voltammetry are two primary electroanalytical methods used in this study. In amperometry, the electrode potential is held constant, whereas in cyclic voltammetry it is periodically scanned with respect to time in a triangular waveform. The advantage of amperometry is that it provides sensitive time resolution. However it provides no information on the chemical nature of the species detected. Cyclic voltammetry, while having lower temporal resolution, provides a current-voltage curve whose characteristics depend on the particular molecule present at the electrode surface. Thus the two techniques provide complementary information.

### 3.1.4 Ferrocenemonocarboxylic Acid (FMCA) and Reference Electrode

FMCA has a “well-behaved”, reversible or Nernstian electrochemical redox couple ferrocene/ferrocenium (FMCA/FMCA<sup>+</sup>). As shown in eqn. (3.3), a molecule of FMCA<sup>+</sup> in solution may accept an electron from the electrode and become reduced. Alternatively, an electron can be removed from the molecule by the electrode causing the molecule being oxidized due to its “well behaved” redox properties. FMCA can be used as a model redox compound for investigating the electrochemical characterization of the integrated sensors.



Potentials are often measured and quoted with respect to reference electrodes, which is very convenient from an experimental standpoint. A common reference is the saturated calomel electrode (SCE), which can be described as,



The SCE has a potential of +0.242 V vs. normal hydrogen electrode (NHE) [30]. Another common reference electrode is the silver-silver chloride electrode,



with a potential of +0.197 V vs. NHE [30]. The Ag|AgCl electrode has a smaller temperature coefficient of potential than the SCE and can be built more compactly. Because of the difficulty in finding a reference electrode for a nonaqueous solvent that does not contaminate the test solution with undesirable species, a quasi-reference electrode (QRE), i.e. pseudoreference electrode, is often employed. In this work, an integrated pseudo-microreference electrode using Ag|AgCl is explored.

Each redox couple has different potential under different conditions. For example, Ferrocene|Ferrocenium has potential of +0.31 V vs. SCE in aprotic solvents (MeCN, 0.2 M LiClO<sub>4</sub>) [30]; Fe(II)|Fe(III) has a formal potential of +0.7 V vs. NHE in 1 M HCl [30] and Fe(CN)<sub>6</sub><sup>3-</sup>|Fe(CN)<sub>6</sub><sup>4-</sup> has a formal potential of +0.71 V vs. NHE in 1M HCl [30]. The ferrocene/ferrocenium (FMCA|FMCA<sup>+</sup>) couple was used in this work. Its formal potential (i.e. measured potential)  $E^0(\text{FMCA}/\text{FMCA}^+)$  can be determined vs. a true reference. This couple could be recommended as a calibrating redox couple, since both forms are soluble and stable in many solvents, and the couple normally displays nernstian behaviour [30]. Voltammograms for FMCA oxidation might be recorded to establish the value of the FMCA|FMCA<sup>+</sup> formal potential vs. a QRE, so that the potentials of the QRE can be reported against a true reference electrode.

### 3.1.5 Clark-type Electrode Reaction via Hydrogen Peroxide

The classic example of enzyme electrodes is the glucose sensor proposed by Clark and Lyons [31]. Glucose oxidase (GOD) catalyses the oxidation of glucose to gluconolactone in the presence of molecular oxygen:



The amount of glucose can be determined by the rate at which hydrogen peroxide is produced. Hydrogen peroxide can be electrochemically oxidized on a platinum electrode, which is polarized at +0.64 V vs. an Ag/AgCl reference electrode:



### 3.1.6 Ferrocenemonocarboxylic Acid Mediated, Enzyme Catalyzed Reaction

A second generation biosensor system has been developed [27,32], in which the enzyme performs the first redox reaction with its substrate, but is then reoxidized by a mediator as opposed to oxygen; the mediator in its turn is oxidized by the electrode. FMCA (FeCpCp', where Cp': C<sub>5</sub>H<sub>4</sub>COOH) is such a mediator, acting as a low molecular weight redox couple, which shuttles electrons from the redox centre of the enzyme (GOD) to the surface of the electrode. During the catalytic cycle the mediator first reacts with the reduced enzyme and then diffuses to the electrode surface where it undergoes rapid charge transfer. The following scheme describes the reaction sequence:



### 3.1.7 The Butler-Volmer Equation and Tafel Plots [33]

The Butler-Volmer equation for a one-step, one-electron process is described as

$$i = i_0 [e^{-\alpha f\eta} - e^{(1-\alpha)f\eta}] \quad (3.12)$$

Where  $i_0$  is the *exchange current*;  $\alpha$  is the transfer coefficient;  $\eta = E - E_{\text{eq}}$ , i.e. the overpotential,  $E_{\text{eq}}$  is the equilibrium potential;  $f = F/RT$ ,  $F$  is the Faraday constant,  $R$  is the gas constant and  $T$  is the absolute temperature. For small values of  $x$ , the exponential  $e^x$  can be approximated as  $1 + x$ , hence for sufficiently small  $\eta$ , equation (3.12) can be reexpressed as

$$i = -i_0 f \eta \quad (3.13)$$

Which shows that the net current is linearly related to overpotential in a narrow potential range near  $E_{\text{eq}}$ . For large values of  $\eta$  (either negative or positive), one of the bracketed terms in (3.12) becomes negligible. For example, at large negative overpotentials,  $\exp(-\alpha f\eta) \gg \exp[(1-\alpha)f\eta]$  and (3.12) becomes

$$i = i_0 e^{-\alpha f\eta} \quad (3.14)$$

Meanwhile, at large positive overpotentials,  $\exp(-\alpha f\eta) \ll \exp[(1-\alpha)f\eta]$  and (3.12) becomes

$$i = -i_0 e^{(1-\alpha)f\eta} \quad (3.15)$$

A plot of  $\log i$  vs.  $\eta$ , known as a *Tafel plot*, can be obtained from equation (3.12). It is a useful device for evaluating electroanalytical kinetic parameters, such as  $\alpha$  and  $i_0$ . In general, there is an anodic branch with slope  $(1-\alpha)F/2.3RT$  and a cathodic branch with slope  $-\alpha F/2.3RT$ . As shown in Figure 3.2, both linear segments extrapolate to an intercept of  $\log i_0$ . The plots deviate sharply from linear behaviour as  $\eta$  approaches zero, because the back reactions can no longer be regarded as negligible. The transfer

coefficient,  $\alpha$ , and the exchange current,  $i_0$ , are obviously readily accessible from this kind of presentation, when it can be applied.

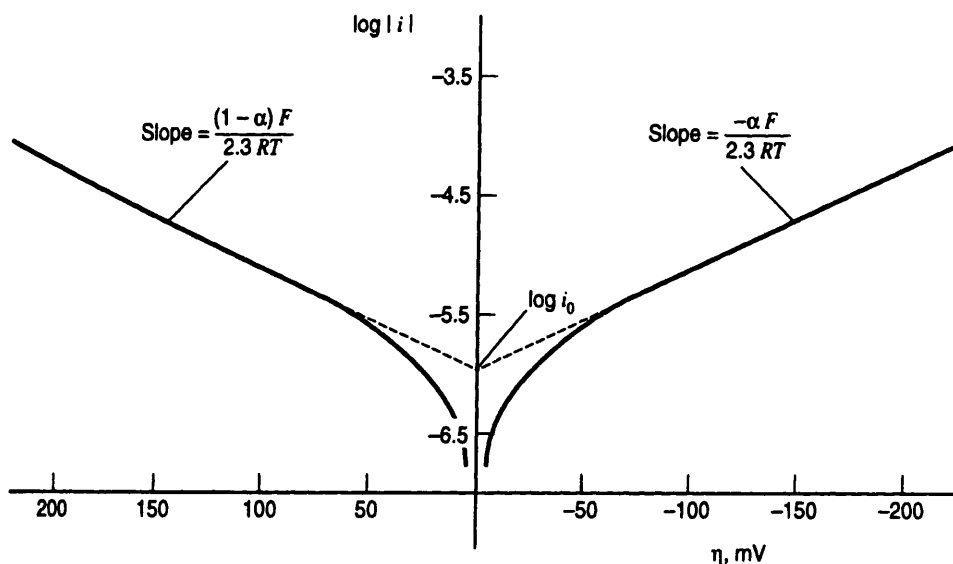
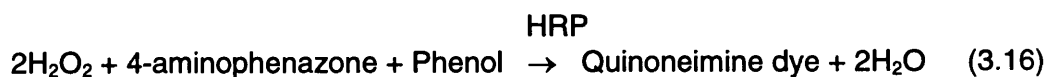


**Figure 3.2** Tafel plots for anodic and cathodic branches of the current-overpotential curve for  $\text{O} + \text{e}^- \rightleftharpoons \text{R}$  with  $\alpha = 0.5$ ,  $T = 298 \text{ K}$ , and  $i_0 = 10^{-6} \text{ A/cm}^2$ . (Reproduced from reference [33])

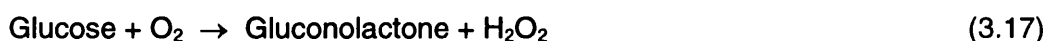
### 3.1.8 The Basis of Glucose Oxidase Activity Assay

The basis of this particular assay is the oxidative coupling of hydrogen peroxide with 4-aminophenazone and a phenol, in the presence of horseradish peroxidase (HRP), to yield a chromogen (a quinoneimine dye) with a maximum absorption at 520 nm:



Glucose oxidase is a flavincontaining glycoprotein which catalyses the oxidation of glucose to gluconolactone:

GOD



Note that 2 moles of glucose are required to yield 2 moles of  $\text{H}_2\text{O}_2$ , which further yields 1 mole of the dye according to equations (3.17, 3.18). The concentration of glucose consumed over one minute is expressed as

$$[\text{GLU}] = 2 \times [\text{DYE}] \quad (3.18)$$

$$\text{Beer's law can be described as } A = \epsilon lc \quad (3.19)$$

Where,  $A$  is absorbance (no units);  $\epsilon$  is the molar absorptivity (*i.e.* the extinction coefficient) with units of  $\text{L mol}^{-1} \text{cm}^{-1}$ ;  $l$  is the path length of the sample, *i.e.* the path length of the cuvette in which the sample is contained and is expressed in centimetres;  $c$  is the concentration of the compound in solution, expressed in  $\text{mol L}^{-1}$ .

According to equation (3.19), and assuming the extinction coefficient of the dye is  $13300 \text{ M}^{-1} \text{cm}^{-1}$ , the concentration of dye yielded per minute is

$$\begin{aligned} [\text{DYE}] &= \Delta A \div (13300 \text{ M}^{-1} \text{cm}^{-1} \times 1 \text{ cm}) \div 2 \text{ min} \\ &= \Delta A \times 10^{-3} \div 26.6 \text{ } \mu\text{M min}^{-1} \end{aligned} \quad (3.20)$$

Substitution of equation (3.20) into (3.18) yields the concentration of glucose over one minute, described as

$$[\text{GLU}] = \Delta A \times 10^{-3} \div 13.3 \text{ } \mu\text{M min}^{-1} \quad (3.21)$$

The enzyme activity in units in 2.05 ml composite sample (where 1 unit is defined as the amount of enzyme that cause the oxidation of 1  $\mu\text{mole}$  of glucose per minute under the given conditions) can be calculated as follows:

$$\begin{aligned} 2.05 \times 10^{-3} (\text{L}) \times [\text{GLU}] &= 2.05 \Delta A \div 13.3 (\mu\text{mol min}^{-1}) \\ &= 0.154 \Delta A (\text{unit}) \end{aligned} \quad (3.22)$$

0.05 ml GOD has the above enzyme activity, so the GOD activity in unit/ml is described as

$$\begin{aligned} \text{GOD activity} &= 0.154\Delta A \text{ (unit)} \div 0.05 \text{ (ml)} \\ &= 3.08 \Delta A \text{ (unit/ml)} \end{aligned} \tag{3.23}$$

## 3.2 Chemicals and Materials

All solutions were prepared with high-purity deionized water (Millipore Elix 10) and analytical reagent grade chemicals, without further purification. Glucose oxidase was from Sigma (GOD, Cat. No.G-6641, Dorset, England) or Medisense. Ferrocene monocarboxylic acid (FMCA, Cat. No. F-2641), hydrogen peroxide (Cat. No. H-0904), D-(+)-glucose (Cat. No. G-7528), Ethylenediaminetetraacetic acid (EDTA) (disodium salt: dihydrate,  $\text{C}_{10}\text{H}_{14}\text{N}_2\text{O}_8\text{Na}_2\cdot\text{H}_2\text{O}$ ), 4-aminoantipyrine (or 4-aminophenazone, or ampyrone,  $\text{C}_{11}\text{H}_{13}\text{N}_3\text{O}$ ), 3,5-dichloro-2-hydroxy-benzenesulphonic acid ( $\text{C}_6\text{H}_3\text{Cl}_2\text{O}_4\text{SNa}$ ), hydrogen peroxide ( $\text{H}_2\text{O}_2$ ) and horseradish peroxidase (HRP) were from Sigma (Dorset, England). Di-sodium hydrogen orthophosphate ( $\text{Na}_2\text{HPO}_4$ ) was from BDH. Sodium dihydrogen orthophosphate dihydrate ( $\text{NaH}_2\text{PO}_4\cdot\text{H}_2\text{O}$ ) was from FSA. Sodium hydroxide (NaOH) was from Fluka. Supporting electrolyte was either 10 mM PBS (10 mM phosphate buffer, 2.7 mM KCl and 137 mM NaCl; pH 7.4) or Krebs-Ringer buffer (KRB) of the following composition (mM): 120 NaCl, 20 Hepes, 5.4 KCl, 0.52  $\text{NaH}_2\text{PO}_4$ , 3.5  $\text{MgCl}_2$ , 1  $\text{CaCl}_2$ ; pH 7.4 with NaOH.

## 3.3 Methods

### 3.3.1 Direct Current (D.C.) Cyclic Voltammetry

D.C. cyclic voltammetry experiments were carried out between 0 V and 0.6 V and at the appropriate scan rates in a bulk solution with working volume of 5 ml at 23°C. The two-electrode or three-electrode devices were cleaned as previously described in Section 3.3.3. D.C. cyclic voltammetry was carried out using a BAS potentiostat (CV-37, UK) with a triangular wave generator and a PC for data collection. Water insoluble FMCA was dissolved in methanol first and then dropped into the stirred electrolyte and it was solubilised by the addition of 1% methanol. Reagents were made up freshly prior to their use.

### *3.3.2 Amperometric Detection*

For the detection of hydrogen peroxide, the working electrode was held at +640 mV (vs. integrated Ag|AgCl pseudo-microreference). When using a mediator, FMCA, the working electrode potential was reduced to +320 mV (vs. integrated Ag|AgCl pseudo-microreference). In all cases, amperometric detection was carried out in ~10  $\mu\text{L}$  "bulk" solution (macro-volume) at 23°C, a constant background current was allowed to stabilise and the reaction was then initiated by the addition of hydrogen or glucose.

### *3.3.3 Electrode Regeneration Methods*

Activation (regeneration) of the electrode surface can sometimes be obtained by proceeding an experiment with a program of potential steps to values where desorption of impurities occurs or where oxide films are formed and then reduced. The probe electrode can be first cleaned with alumina slurry, then re-cleaned using the above program of electrochemical regeneration. Unfortunately, a planar microelectrode can not be cleaned using traditional mechanical (polishing) methods, as the metal will typically have thickness of < 150 nm, and will be removed by physical abrasion. Two methods to regenerate the passivated electrode for a planar microelectrode device were investigated, which involved electrochemical cycling and dry etching. Firstly, cycling in acid [1], where the microelectrode was cycled in 0.5M  $\text{H}_2\text{SO}_4$  between -0.2 V and +1.2 V, until a steady-state voltammogram was observed; and secondly, dry etching was used to remove surface contamination from lithographically patterned microelectrodes (e.g. prior to the electrodeposition of metals) and to regenerate passivated electrodes after experimentation. This was performed using a ET Plasmofab 505 Barrel Asher (Electrontech) for 30 ~ 60 s with 2  $\text{L min}^{-1}$  oxygen, 5 psi nitrogen, 30 mT base pressure and 70 W RF power. The extent of electrode regeneration, after cellular or enzymic assays was characterised through a series of detailed experiments involving the model redox compound FMCA.

### *3.3.4 Assay Procedure of Glucose Oxidase Activity*

0.53 g of 3,5-dichloro-2-hydroxy-benzenesulphonic acid was dissolved in distilled water and the pH was adjusted to 7 by addition of 1 M NaOH. 30 mg of horseradish

peroxidase was added and the final volume was made up to 100 ml (**Reagent 1**). This solution is stable for 4 weeks at 4 °C. 162 mg of 4-aminophenazone was dissolved in 100 ml of distilled water (**Reagent 2**). 0.133 M sodium phosphate buffer was prepared containing 7 mM EDTA (**Reagent 3**) by dissolving the following in 1 litre of distilled water: 14 g of sodium dihydrogen orthophosphate dihydrate, 8 g of di-sodium hydrogen orthophosphate and 0.372 g of EDTA. The pH of the solution was in the range pH 6.9 – 7.1 and was stored as for reagent 1. 18 g of glucose was dissolved in 100 ml of distilled water (**Reagent 4**) and again, was stored as for reagent 1.

A sufficient quantity of a composite assay reagent (**Reagent 5**) was prepared. For each measurement 1.95 ml was required and had the following composition: 1.55 ml of reagent 3; 0.20 ml of reagent 4; 0.2 ml of reagent 1. This composite was prepared on the day of measurement. 1.95 ml of the combined reagent solution was placed in a 3 ml cuvette (1cm pathlength) and 0.05 ml of reagent 2 added. The background absorbance at 520 nm was measured, then 0.05 ml of an appropriately diluted solution of glucose oxidase (GOD) added and the change in absorbance ( $\Delta A$ ) was measured at 520 nm over the initial 2 min.

### 3.4 Results and Discussion

#### 3.4.1 Electrochemical Characterisation Using FMCA

FMCA was used as a model redox compound in order to investigate the electrochemical characterisation of the sensor. The DC cyclic voltammograms of 2-microelectrode ((a) working electrode area: 500  $\mu\text{m}^2$ ) and 3-microelectrode (working electrode area: (b) 200, (c) 500  $\mu\text{m}^2$ ) devices with 0.5 mM FMCA at 100 mV/s are shown in Figure 3.3. Both the voltammograms for the 3-electrode devices describe a steady state curve where the reverse tracks almost coincides with the forward one. However, the 2-electrode device voltammogram reveals redox peaks and the charge associated with the cathodic process was low compared to the forward oxidation process.

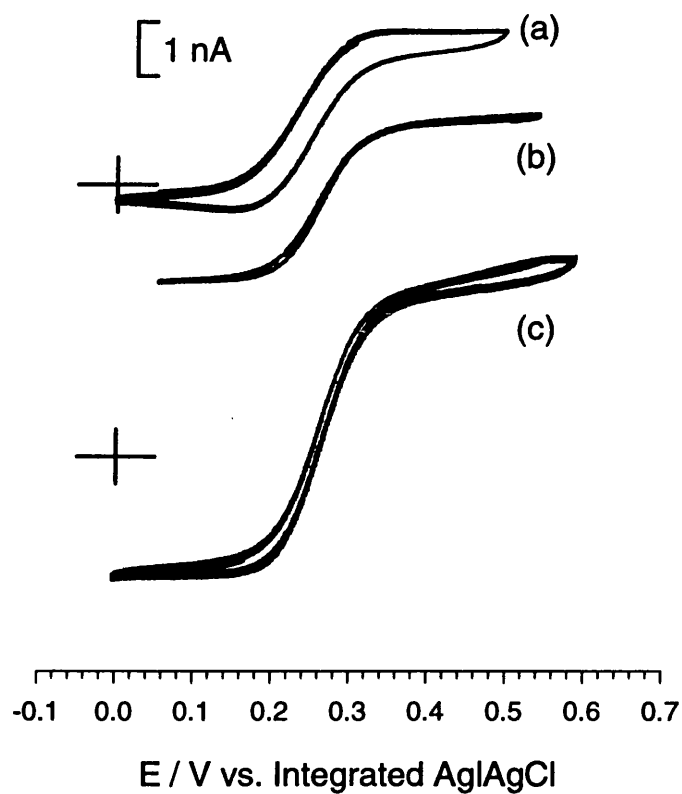


**Figure 3.3** DC cyclic voltammograms for 0.5 mM FMCA cycled at  $100 \text{ mV sec}^{-1}$ , for different microanalytical devices, respectively: (a) a 2-microelectrode device with a  $500 \mu\text{m}^2$  working electrode area; (b) a 3-microelectrode device with a  $200 \mu\text{m}^2$  working electrode area; (c) a 3-microelectrode device with a  $500 \mu\text{m}^2$  working electrode area. Peak currents scale according to the area of the working electrode.

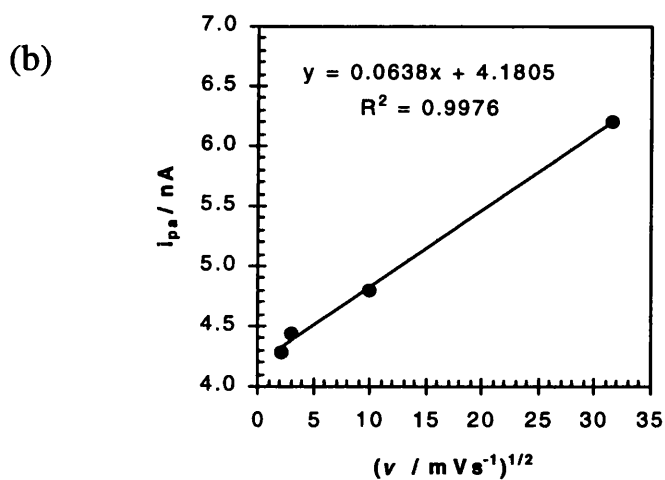
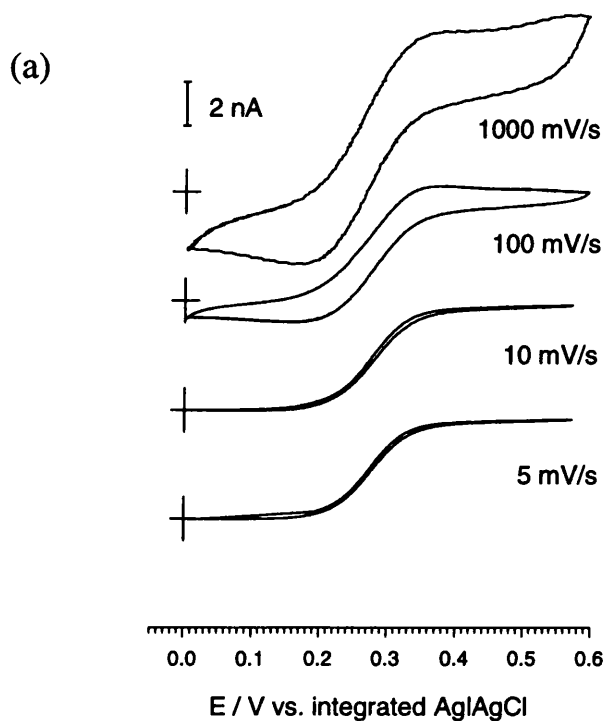


**Figure 3.4** Response of a two-electrode device to 1.0 mM FMCA in 10 mM PBS bulk solution: (a) the DC cyclic voltammograms at scan rates between 5 ~ 1000 mV sec<sup>-1</sup>; (b) the relationship between the peak current  $i_{pa}$  and  $v^{1/2}$  in (a), where  $v$  is the potential scan rate, indicating diffusion limited reactions. The surface area of the working electrode was 500  $\mu\text{m}^2$ .

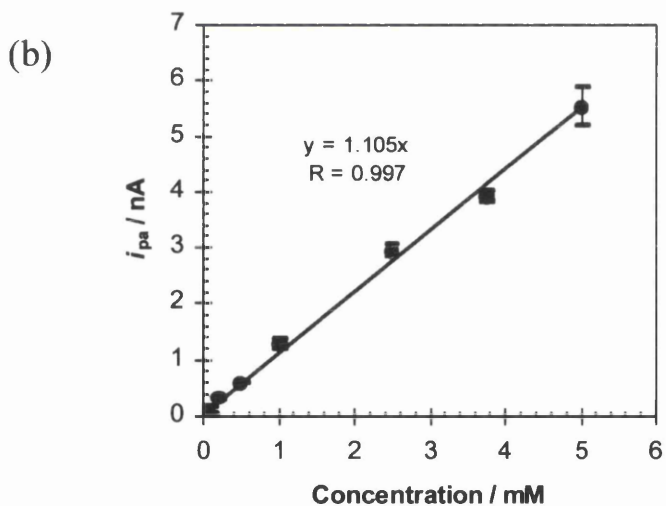
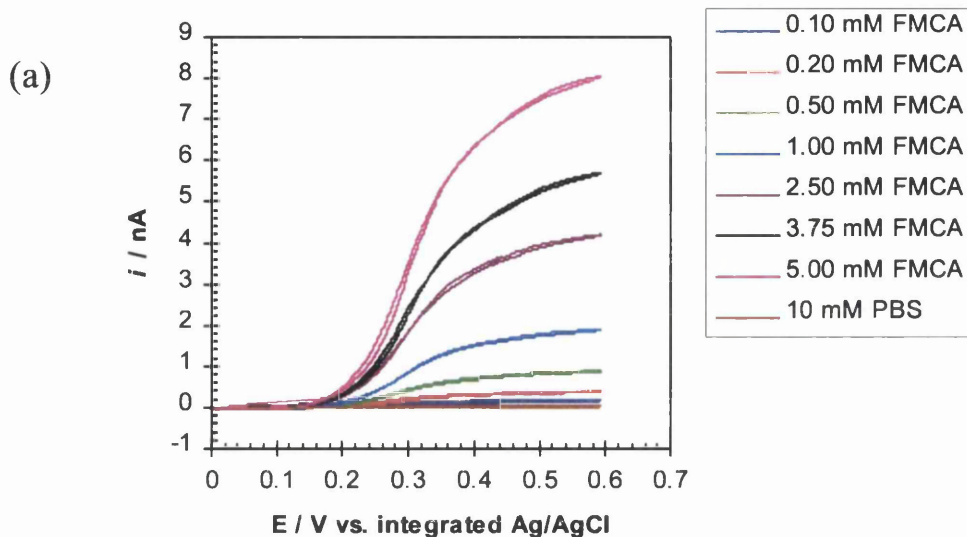
Figure 3.4(a) shows cyclic voltammetry (CV) responses to FMCA at varied scan rates from the 2-electrode sensor with an integrated (in situ) Ag|AgCl microreference. Under the experimental conditions used in this study and over the range of potential scan rate ( $\nu=5-1000 \text{ mVs}^{-1}$ ), FMCA gave voltammograms consistent with a reversible one-electron redox agent at the working microelectrode.  $E_{pa}$  is independent of scan rate and  $|i_{pa}| = |i_{pc}|$ . The peak current  $i_p$  as a function of  $\nu^{1/2}$  is linear (Figure 3.4(b)) with a correlation coefficient R of 0.9988.  $E_{1/2}$  for the redox couple was 265 mV. At slow scan rates, steady-state current persisted up to a scan rate of  $10 \text{ mVs}^{-1}$  and a plateau current was present. At faster scan rates, the CV responses showed peaked behaviour.

Figure 3.5(a) shows DC cyclic voltammograms of the response to different concentrations of FMCA in 10 mM PBS, at a scan rate of  $10 \text{ mVs}^{-1}$ . All of the voltammograms recorded appeared as steady state  $i$  &  $E$  curves at the slow scan rate. Note that the baseline of supporting electrolyte PBS is a flat curve around  $E = 0$ . Figure 3.5(b) shows the plot of  $i_{pa}$  against concentrations of FMCA in 10 mM PBS at a scan rate of  $10 \text{ mVs}^{-1}$ . Each point was measured in triplicate and the mean was taken, with error bars as shown. The linear range of FMCA detected varied from 0.1 to 5.0 mM with a correlation coefficient (R) of 0.997.

### 3.4.2 Detection of Hydrogen Peroxide

#### 3.4.2.1 Response at Different Applied Potentials

The response to hydrogen peroxide at different applied potentials was investigated. 'Macro-volumetric' test of microelectrode response to hydrogen peroxide at different applied potentials is shown in Figure 3.6. The Pt-working electrode was held at the potentials indicated vs. internal Ag|AgCl reference. The microwell of the device was filled with  $10 \mu\text{l}$  of 2 mM PBS (pH7.4), and then  $1.2 \mu\text{l}$  of 5 mM  $\text{H}_2\text{O}_2$  was injected. Figure 3.6(a) shows the plot of current against time.



**Figure 3.5** 2-electrode sensor responses to FMCA in 10 mM PBS bulk solution, at the scan rate of  $10 \text{ mVs}^{-1}$ : (a) DC cyclic voltammograms response to different concentrations of FMCA; (b) the plot of  $i_{pa}$  against concentrations of FMCA, each point was measured in triplet and the mean was taken, with error bars shown. The surface area of the working electrode was  $500 \mu\text{m}^2$ .

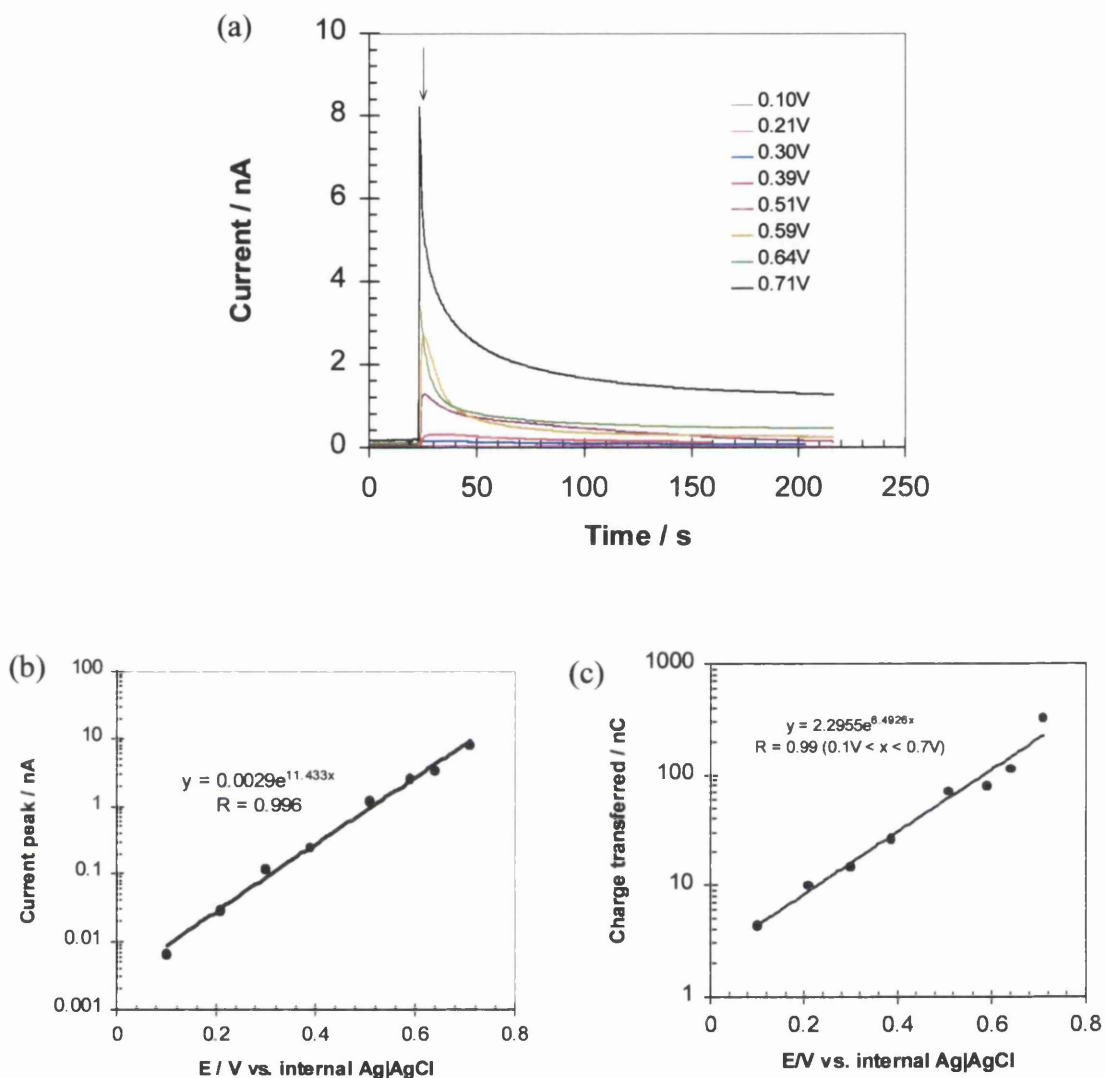


**Figure 3.6** “Macro-volumetric” test of microelectrode response to hydrogen peroxide at different applied potentials. A Pt-working electrode was held at the potentials indicated vs. internal Ag|AgCl reference. The microwell of the device was filled with 10  $\mu$ l of 2 mM PBS (pH7.4), and then 1.2  $\mu$ l of 5 mM H<sub>2</sub>O<sub>2</sub> was injected: (a) Plot of current against time; (b) Tafel plot of current peak against applied potential, obtained from the data of (a); (c) Plot of charge transferred against applied potentials over 150 sec., obtained from the data of (a). The surface area of the working electrode was 500  $\mu$ m<sup>2</sup>.

Figure 3.6(b) shows the real Tafel plot of current peak against applied potential, obtained from the data of Figure 3.6(a). With a correlation coefficient R of 0.97, the trendline can be expressed by,

$$y = 0.0029e^{11.433x} \quad (3.24)$$

Comparing (3.24) with (3.15), we obtain the exchange current,  $i_0 = 0.0029$  nA, and

$$11.433 = (1-\alpha)f \quad (3.25)$$

in which,  $f = F/RT = 38.9 \text{ V}^{-1}$  at 25 °C (*i.e.* 298.15 K) [33]. The transfer coefficient  $\alpha$  is then calculated as 0.71.

The  $i-t$  responses are integrated (for 150s) to give a plot of the charge transferred against the same concentration hydrogen peroxide at different potentials (Figure 3.6(c)). The trendline can be expressed by an exponential growth equation,

$$y = 2.2955e^{6.4926x}$$

The correlation coefficient (R) is about 0.99. The applied potential can be estimated at +640 mV vs. internal Ag|AgCl from the plot.

#### 3.4.2.2 Current-time Response to Hydrogen Peroxide

Detection of hydrogen peroxide was recorded in Figure 3.7 using “macro-volumetric” test. 10  $\mu\text{l}$  supporting electrolyte of 10 mM PBS was injected over the microchamber of the device, and then (i) 1 nmol, (ii) 2 nmol, (iii) 4 nmol, (iv) 6 nmol, (v) 8 nmol and (vi) 10 nmol  $\text{H}_2\text{O}_2$  was injected into the microchamber. The current increased incrementally as the quantity of  $\text{H}_2\text{O}_2$  was increased.

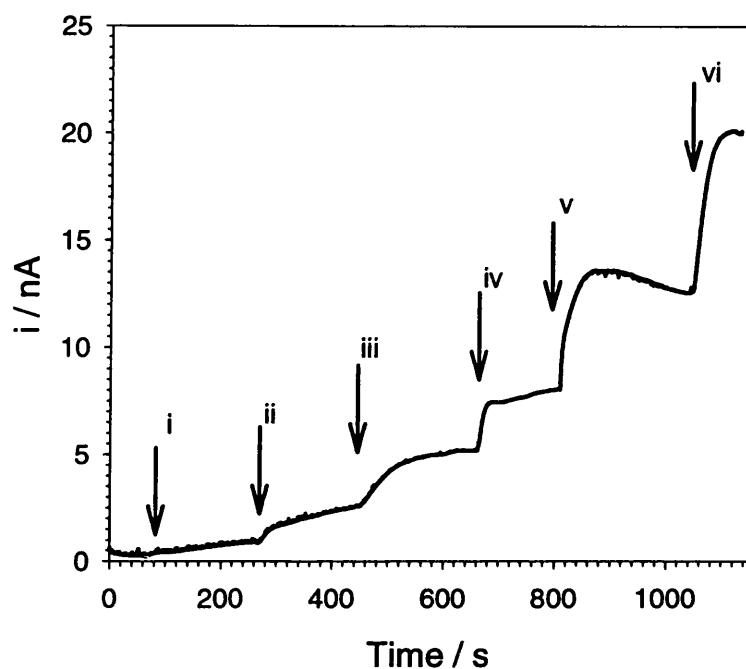


**Figure 3.7** shows representative “macro-volumetric” responses of the 2-microelectrode sensor to hydrogen. 10  $\mu\text{l}$  supporting electrolyte of 10 mM PBS was injected over the microchamber of the device, and then: (i) 1 nmol; (ii) 2 nmol; (iii) 4 nmol; (iv) 6 nmol; (v) 8 nmol; and (vi) 10 nmol  $\text{H}_2\text{O}_2$  was injected into the microchamber. The potential was held at +640 mV vs. internal Ag|AgCl. The surface area of the working electrode was  $500 \mu\text{m}^2$ .

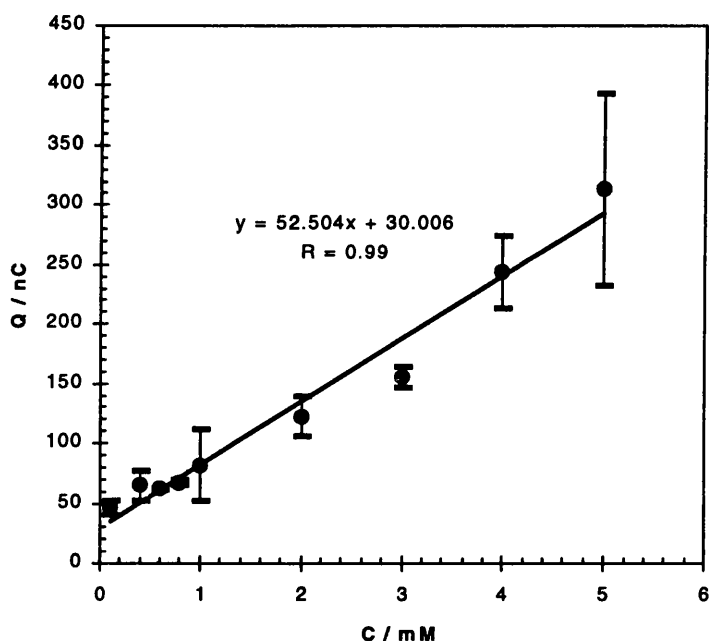
### 3.4.2.3 Calibration Curve and Reproducibility

Figure 3.8 shows the linear calibration curve for the charge (Q) transferred as a consequence of the oxidation of hydrogen peroxide, over a range of final concentrations between 0.1 ~ 5 mM at a potential of +640 mV vs. internal Ag|AgCl microreference. The reported values are means from three test results. The response sensitivity and correlation coefficient (R) were 61.5 nC/mM and 0.96 respectively.

The major contributions to the errors were the position of the micropipette and speed with which the fluid was dispensed. Further work in this subject involves the

implementation of microfluidic methods to deliver analytes and cells to the microchambers (Chapter 4 & 5).

The representative repeated responses of a 2-electrode sensor “macro-volumetric test” to 0.1, 0.6, 3, 4 mM H<sub>2</sub>O<sub>2</sub>, (the raw data of Figure 3.8, are given in Figure 3.9). The tests were completed continuously on same day. The graphs indicate that the responses could display greater reproducibility if the injection position, quantity and speed were carefully controlled.



**Figure 3.8** Calibration curve of a 2-electrode sensor “macro-volumetric test” for the charge generated (Q) as a consequence of hydrogen peroxide, over a range of concentrations between 0.1 and 5 mM. Each point is measured as a mean of three readings.

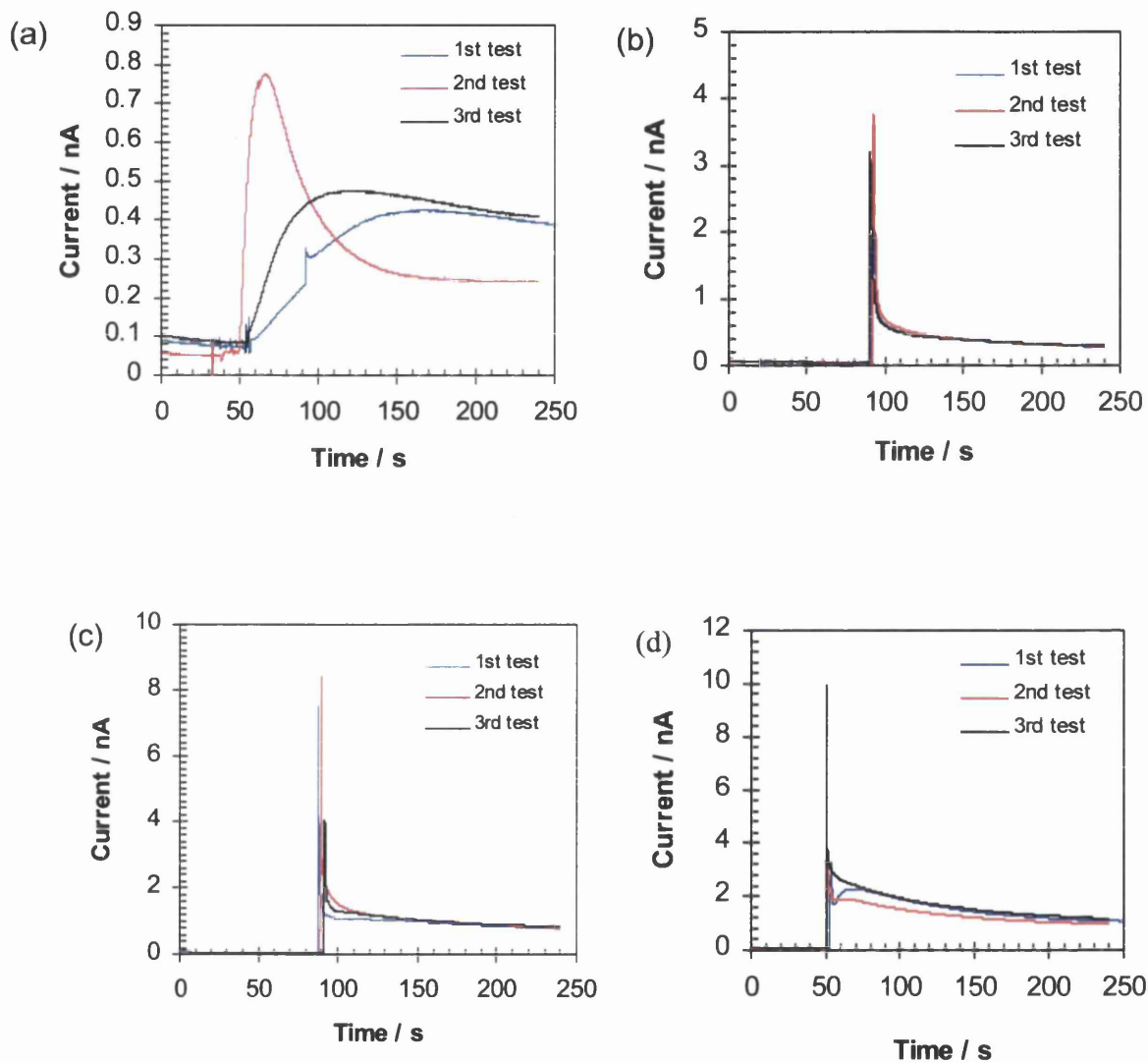
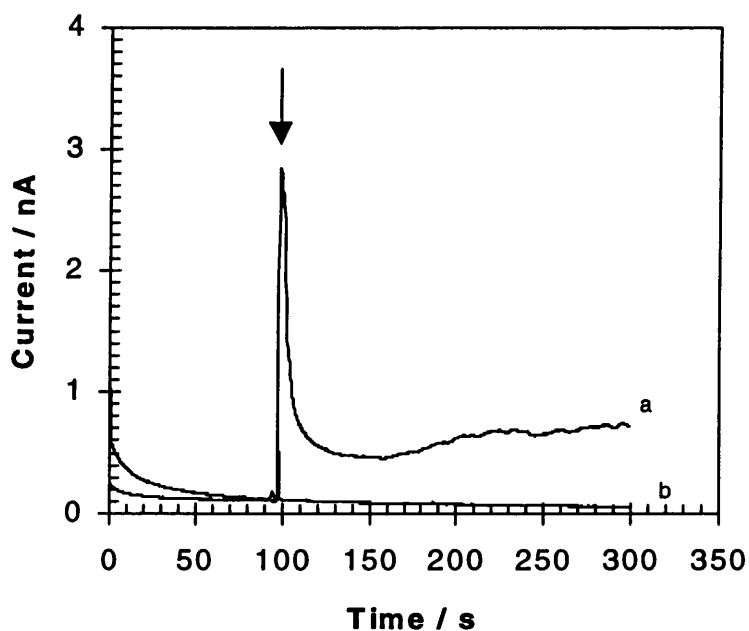


**Figure 3.9** Repeated responses of 2-electrode sensor “macro-volumetric test” to (a) 0.1 mM, (b) 0.6 mM, (c) 3 mM and (d) 4 mM  $\text{H}_2\text{O}_2$ . The surface area of the working electrode was  $500 \mu\text{m}^2$ . (Raw data of Figure 3.8)

### 3.4.3 Detection of Glucose

#### 3.4.3.1 Using the Enzyme GOD

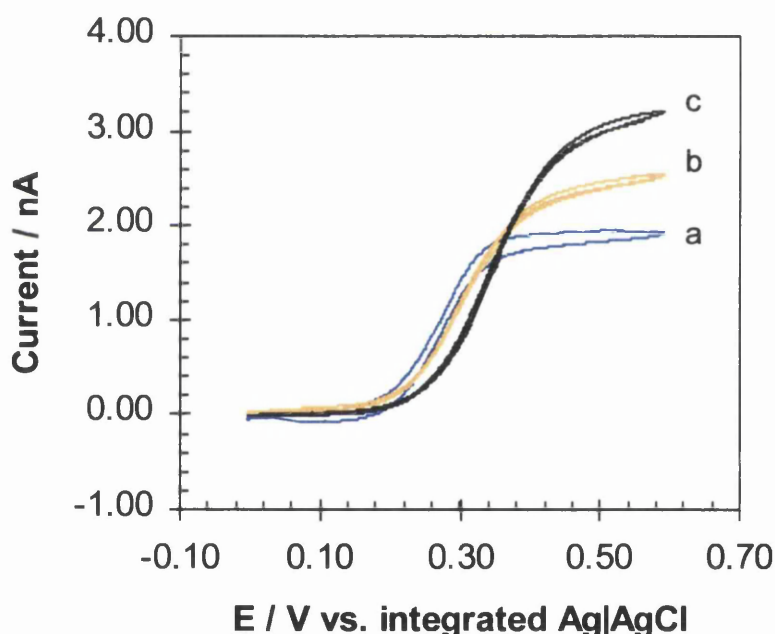
In Equations (3.6), (3.7) and (3.8), GOD catalyzes the oxidation of glucose by oxygen to produce gluconolactone (product) and  $\text{H}_2\text{O}_2$  (coproduct).  $\text{H}_2\text{O}_2$  is subsequently detected electrochemically to produce a glucose dependent current. This was demonstrated as shown in Figure 3.10. There is an obvious anodic response upon addition of glucose added (Figure 3.10a), but no response to the supporting electrolyte except the small narrow peak (Figure 3.10b) which is caused by the vibration of sample addition.



**Figure 3.10** 'Macro-volumetric' test of microelectrode response to glucose via the production of hydrogen peroxide. The sputtered Pt working electrode was held at 0.64 V vs. internal Ag/AgCl reference. At first, the microchamber was filled with 8  $\mu\text{l}$  244  $\text{Uml}^{-1}$  GOD in 2 mM PBS at pH7.4. Current values were then recorded upon addition of (a) 1  $\mu\text{l}$  50 mM glucose in 2 mM PBS to get the final 5 mM glucose; or (b) 2  $\mu\text{l}$  2 mM PBS. The surface area of the working electrode was 500  $\mu\text{m}^2$ .

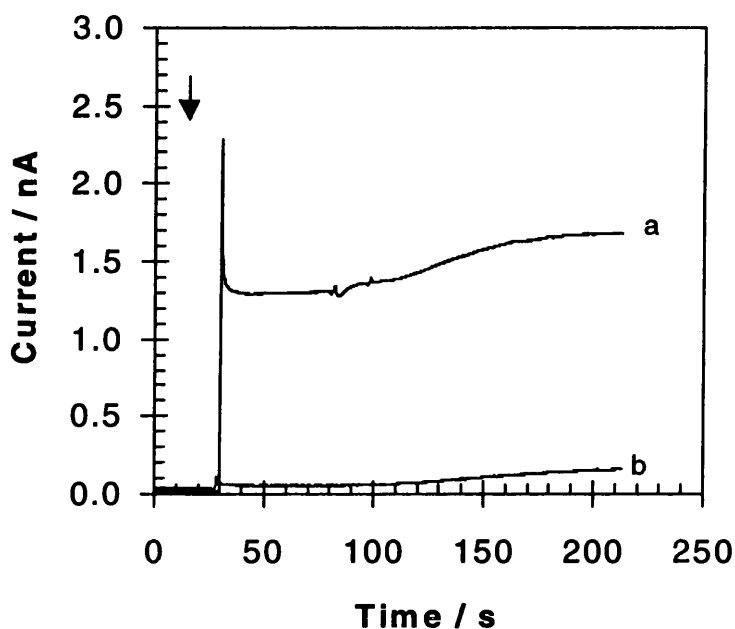
### 3.4.3.2 Using the Mediator FMCA

Figure 3.11(a) shows a voltammogram of FMCA in the presence of glucose alone at 10 mV/s vs. integrated Ag|AgCl. Upon duplicate addition of glucose oxide (GOD) to the solution, changes in the voltammogram could be seen (Figure 3.11 (b) and (c)) with less peak-shaped sigmoidal behaviors. Large catalytic currents flow at oxidizing potentials. It is indicative of the regeneration of ferrocene from the ferricinium ion by the enzyme GOD in its reduced form. The latter is maintained in this reduced state by the presence of substrate (equations (3.9) to (3.11)). The ratio of the kinetically controlled currents to the diffusion-controlled current,  $i_k/i_d$ , can be measured from Figure 3.11, which is 1.3 for curve b and 1.7 for curve c.



**Figure 3.11** DC cyclic voltammograms, for a 2-microelectrode sensor, of 0.5 mM FMCA at a scan rate of 10 mV/s at pH 7.4 with 10 mM PBS. (a) Addition of 50 mM Glucose to the solution, then further addition of (b) 200 unit ml<sup>-1</sup> GOD ( $i_k/i_d = 1.3$ ) or (c) 10 mg ml<sup>-1</sup> (i.e. 781 unit ml<sup>-1</sup>) GOD ( $i_k/i_d = 1.7$ ). The surface area of the working electrode was 500  $\mu\text{m}^2$ .

Equations (3.9) to (3.11) also show that it is possible to replace the natural electron acceptor (oxygen) by an artificial electron acceptor, such as the mediator FMCA, reducing the working potential to +320 mV vs. the integrated Ag|AgCl. Such an assay could be used to eliminate the dependence of the sensors on oxygen tension as well as to reduce interference from  $H^+$ . Figure 3.12 illustrates this point for the ferrocene mediated reaction (at 0.32 V vs. Ag|AgCl).



**Figure 3.12** Response to glucose via reaction involving ferrocene monocarboxylic acid. (a) Sensor response, when the microchamber was filled with 0.5 mM FMCA and 12.5 mg/ml (*i.e.* 977  $U\text{ml}^{-1}$ ) GOD in the supporting electrolyte, upon addition of 10 mM glucose. The potential was held at 0.32 V vs. internal Ag|AgCl microreference. (b) Response using the same conditions as for (a), but without the addition of FMCA. The surface area of the working electrode was  $500\ \mu\text{m}^2$ .

### 3.4.4 Pseudo Micro-references of Ag|AgCl and Ag|Ag<sub>3</sub>PO<sub>4</sub>

Besides a micro-reference of Ag|AgCl, a micro-reference of Ag|Ag<sub>3</sub>PO<sub>4</sub> was also explored as a possible reference electrode. Such a system would have the advantage of providing a suitable electrochemical cell for biological measurements in phosphate buffers, e.g. cell culture. In addition, it is established that Ag<sub>3</sub>PO<sub>4</sub> has a lower solubility in aqueous solution ("solubility product"  $K_{sp} (= [Ag^+]^3 [PO_4^{3-}])$  is about  $1 \times 10^{-14} \text{ M}^2$ ) [34] than AgCl ( $K_{sp} ([Ag^+][Cl^-])$  is about  $1.8 \times 10^{-10} \text{ M}^2$ ) [35], and should therefore provide a stable material system. Here, the Ag|Ag<sub>3</sub>PO<sub>4</sub> microreference is compared with the Ag|AgCl microreference electrode.

#### 3.4.4.1 DC Cyclic Voltammetry

Figure 3.13 shows DC voltammograms of the devices for both the Ag|AgCl and Ag|Ag<sub>3</sub>PO<sub>4</sub> references. The potential of the Ag|AgCl microreference electrode was relatively stable, with results repeated seven times (i.e. every 3 days over a period of 21 days). Figure 3.13 (a) shows minimal drift in either peak oxidation and reduction potentials. The device was stored in a dry box between testing.

Ag|Ag<sub>3</sub>PO<sub>4</sub> was first deposited on a  $0.09 \text{ cm}^2$  Au from  $0.03 \text{ M H}_3\text{PO}_4$  at a current density of  $10 \text{ mA cm}^{-2}$  for 7 seconds. Devices were stored in  $50 \text{ mM}$  phosphate buffer at  $4 \text{ }^\circ\text{C}$ . Figure 3.13 (b, (i) and (ii)) show how the  $E_{1/2}$  for  $1.0 \text{ mM}$  ferrocene monocarboxylic acid drifts from  $0.14 \text{ V}$  to  $0.35 \text{ V}$  during 10 mins of repeated cycling, tested at 4-day intervals over 21 days.

In Figure 3.13(c), the integrated Ag|Ag<sub>3</sub>PO<sub>4</sub> was prepared using  $0.1 \text{ M H}_3\text{PO}_4$  at a current density of  $33 \text{ mA cm}^{-2}$  for 10 seconds, and the device was stored in a dry box at room temperature. There was significant drift with time from curve (i) to (iv), and finally, after 21 days, the redox peaks disappeared due to the peaks moved to higher potentials than are being measured. In Figure 3.13 (d), the integrated Ag|Ag<sub>3</sub>PO<sub>4</sub> was prepared using  $0.03 \text{ M H}_3\text{PO}_4$  at a current density of  $10 \text{ mA cm}^{-2}$  for 12 seconds and was stored in a dry box at the room temperature. Again there is significant drift in the FMCA half-potential, prior to the complete disappearance of the redox couple curve (v).

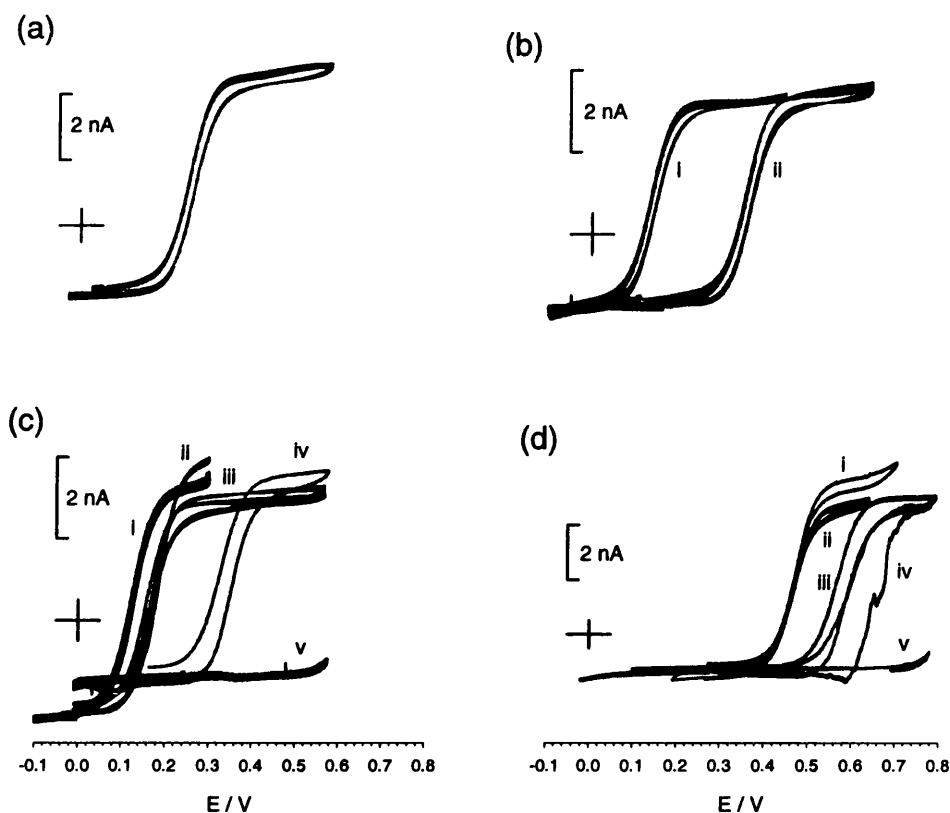


**Figure 3.13** DC cyclic voltammograms of 1.0 mM FMCA at  $100 \text{ mV sec}^{-1}$  (The surface area of the working electrode was  $500 \mu\text{m}^2$ ), using either AgI/AgCl or AgI/Ag<sub>3</sub>PO<sub>4</sub> as a reference:

- (a) Stable electrochemistry of the microanalytical devices using an integrated AgI/AgCl reference.
- (b) Electrochemistry of FMCA, where the working potential was controlled with respect to an external AgI/Ag<sub>3</sub>PO<sub>4</sub> reference electrode. Ag<sub>3</sub>PO<sub>4</sub> was deposited onto an Au electrode using 0.03 M H<sub>3</sub>PO<sub>4</sub> at a current density of  $10 \text{ mA cm}^{-2}$  for 7 seconds: (i) and (ii) describe a shift in the  $E_{1/2}$  values upon repeated cycling over 10 mins.
- (c) Working potential was controlled with respect to an integrated AgI/Ag<sub>3</sub>PO<sub>4</sub> within the microchamber. Ag<sub>3</sub>PO<sub>4</sub> was prepared using 0.1 M H<sub>3</sub>PO<sub>4</sub> at a current density of  $33 \text{ mA cm}^{-2}$  for 10 seconds: scans (i) to (v) show the instability of the reference with respect to time.
- (d) Working potential was controlled with respect to an integrated AgI/Ag<sub>3</sub>PO<sub>4</sub>. Ag<sub>3</sub>PO<sub>4</sub> was prepared using 0.03 M H<sub>3</sub>PO<sub>4</sub> at a current density of  $10 \text{ mA cm}^{-2}$  for 12 seconds: scans (i) to (v) show the instability of the reference with respect to time.

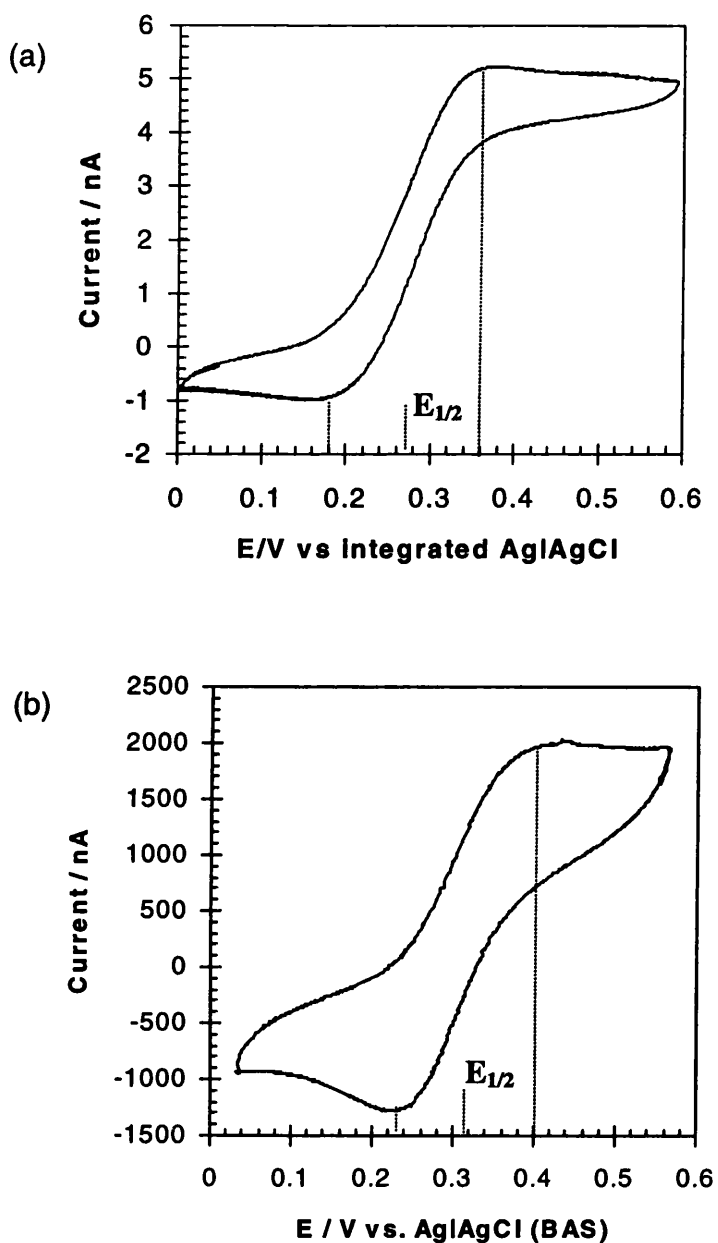


Figure 3.14 D.C. cyclic voltammetry for 1mM FMCA in 10 mM PBS (pH 7.4), ionic/compositions were equivalent in both experiments: (a) a micro working electrode's potential was scanned with reference to a micro integrated Ag|AgCl. The formal redox potential,  $E^{\circ}(\text{FMCA}/\text{FMCA}^+)$ , is estimated to be +270 mV vs. the micro quasireference; (b) a micro working electrode's potential was scanned with reference to a true reference electrode of Ag|AgCl (BAS),  $E^{\circ}(\text{FMCA}/\text{FMCA}^+)$  is estimated to be +315 mV vs. Ag|AgCl (BAS).

#### 3.4.4.2 Evaluation of Micro Reference of Ag|AgCl

The Ag|AgCl electrode is a reference electrodes which has widespread use in electrochemical experiments and in the development of various biochemical sensors [1,36-38]. Besides meeting the basic requirements which a reference must satisfy (stability, reversibility and reproducibility), it is superior to the other types of reference electrode in its compatibility with the current microfabrication techniques [36-38]. A microreference of Ag|AgCl, referred as 'quasi-' or 'pseudo-' reference electrode, is an Ag|AgCl film in direct contact with a test solution.

From Figure 3.14, the actual potential of the microquasireference vs. a true reference electrode, Ag|AgCl (BAS) was be calibrated, in order to report potentials with reference to the microquasireference in the applications (at known ionic compositions). The calibration was achieved simply by measuring (e.g., by voltammetry) the formal redox potential of FMCA/FMCA<sup>+</sup>,  $E^0(\text{FMCA}/\text{FMCA}^+)$  vs. the micro quasireference Ag|AgCl electrode. The FMCA/FMCA<sup>+</sup> couple's formal potential was known vs. Ag|AgCl (BAS) under the same conditions. An approximation to the formal redox potential of FMCA,  $E^0(\text{FMCA}/\text{FMCA}^+)$ , was derived by measuring the mid-point potential,  $E_{1/2}$ , of the anodic and cathodic peaks. From the data obtained from Figure 3.14,  $E^0(\text{FMCA}/\text{FMCA}^+)$  was estimated to be +270 mV vs. the microquasireference of Ag|AgCl and +315 mV vs. the true reference of Ag|AgCl (BAS), therefore the actual potential of the microquasireference Ag|AgCl vs. Ag|AgCl (BAS) was about +45 mV (Figure 3.15).

Section 3.4.4.1 states that the potential stability of the Ag|AgCl microreference is satisfactory compared with Ag|Ag<sub>3</sub>PO<sub>4</sub>. The most influential factor of the durability and potential stability is the dissolution ( $K_{sp}$  in aqueous media is about  $1.8 \times 10^{-10} \text{ M}^2$ ) [35] of the AgCl layer [36-38]. To test the durability, variation of the DC voltammographs of the microelectrode vs. the micro reference of Ag|AgCl (25  $\mu\text{m}$   $\times$  125  $\mu\text{m}$   $\times$  2 ~ 3  $\mu\text{m}$ ) was examined for 1 mM FMCA whilst the device was immersed in the supporting electrolyte of KRB with 129 mM Cl<sup>-</sup> (Figure 3.16). A slight decrease in the redox currents response with time were observed from curve (a) to curve (g), which was ascribed to a built-up of adsorbed impurities on the working microelectrode surface by their diffusion from the bulk

solution. Curve (h) showed the redox characteristic of recovery with a larger DC cyclic voltammogram after dry etching.

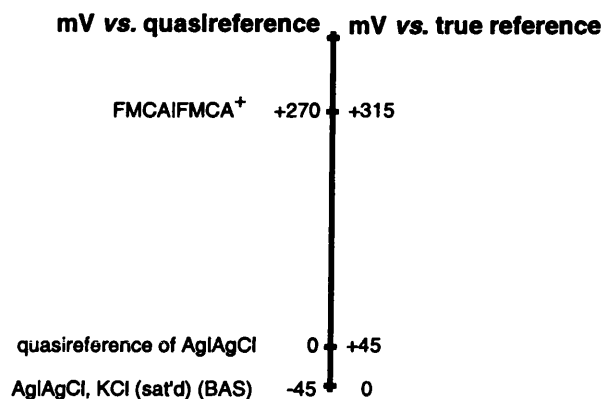


**Figure 3.15** Potentials of redox couple FMCAIFMCA<sup>+</sup> and reference electrodes in 10 mM PBS (pH 7.4 at 23°C). Potentials obtained vs. an integrated micro quasireference of Ag|AgCl are plotted on the left and potentials obtained vs. a true reference of Ag|AgCl electrode (BAS) are on the right.

Stable half-wave potential ( $E_{1/2}$ ) vs. micro reference of Ag|AgCl was obtained from Figure 3.16 for each test during 17.6 hours storage in KRB (Figure 3.17). This confirmed that the potential of the Ag|AgCl microreference maintained a stable and reproducible potential after at least 17.6 hours storage in KRB. Normally, devices with Ag|AgCl micro references with stable potential were stored in dry boxes and every test, including for mammalian cells measurements, was completed within 2 hours. Therefore this micro reference of Ag|AgCl can be applied to this research and has opened a way to the development of a miniature reference electrode for general use.

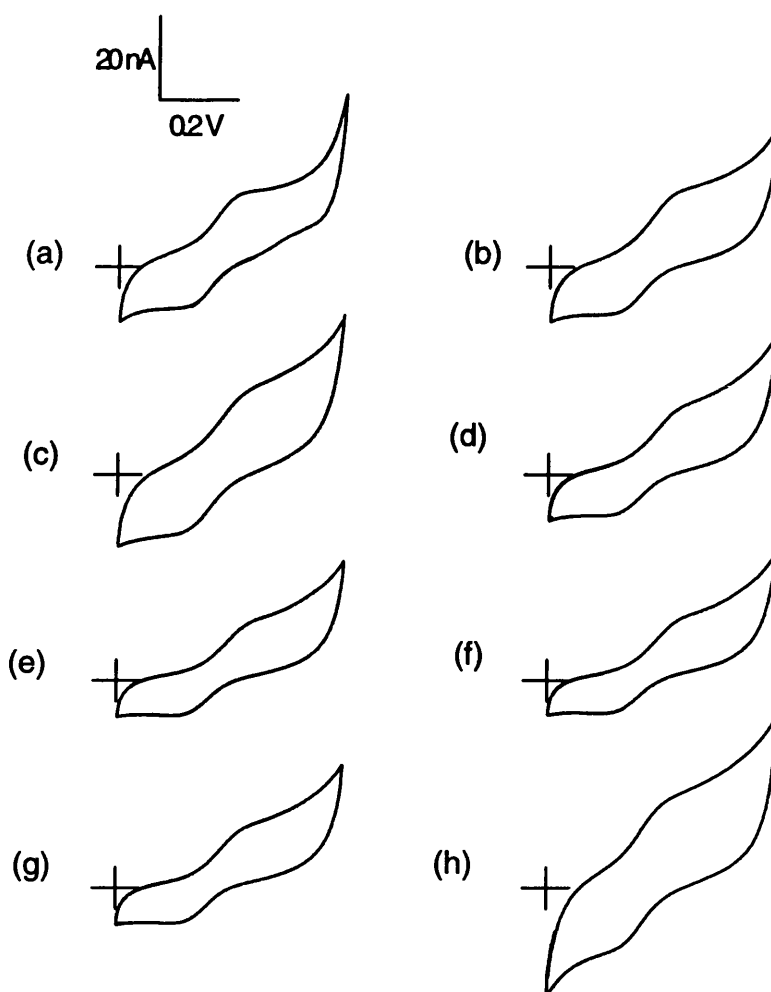


**Figure 3.16** Variation of the DC voltammogram to 1 mM FMCA while the device was immersed in a supporting electrolyte of KRB with 129 mM  $\text{Cl}^-$  for 17.6 hours. The voltammograms were measured using microelectrodes vs. a microreference of Ag/AgCl ( $2 \sim 3 \mu\text{m}$  thickness) with a scan rate of  $100 \text{ mVs}^{-1}$ . Scans (a) to (h) show the responses with after 0, 0.3, 0.75, 1.08, 2.08, 3.08, 3.41, 17.6 hours. Curve (h) showed the redox characteristic of recovery with a larger DC cyclic voltammogram after dry etching.

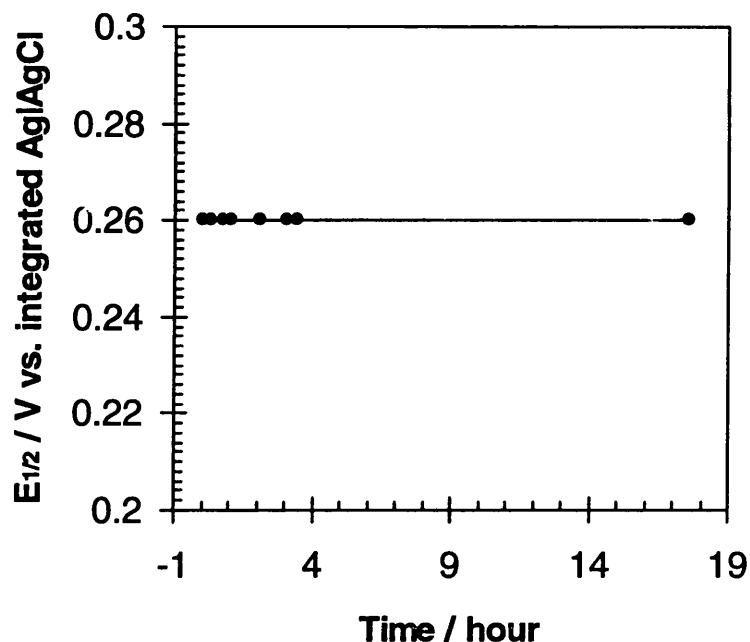


**Figure 3.17** Stable half-wave potential ( $E_{1/2}$ ) vs. a micro reference of AgI/AgCl, obtained from Figure 3.17 for each test during 17.6 hours storage in KRB.

### 3.4.5 Regeneration of the Electrodes

#### 3.4.5.1 Passivation of the Electrode

The adsorption of electroinactive species (some times referred to as the 'formation of a film of foreign substance') on an electrode surface occurs frequently [39]. Such adsorption can inhibit (or poison) an electrode reaction (e.g., by formation of an impervious layer that blocks a portion of the electrode surface). Indeed, a slow change in the electrochemical response with time is observed, which can be ascribed by the built-up of adsorbed impurities on the electrode surface by their diffusion from the bulk solution or from the air.

The sputtered platinum electrode is more easily inhibited/passivated than the platinized electrode (porous platinum black). Compared with the sputtered platinum

electrodes, much greater current densities can be obtained per external unit area on porous platinum black electrodes, which can be attributed simply to the greater available internal surface area per external geometric area.

### 3.4.5.2 Cyclic Voltammetry in Acid

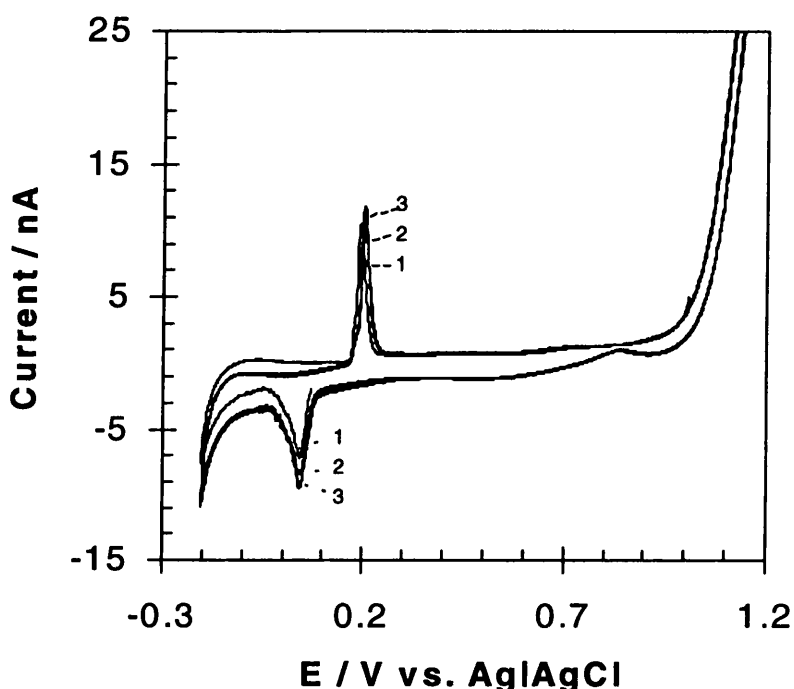


**Figure 3.18** Regeneration of a passivated sputtered Pt microelectrode swept successively in 0.5M  $\text{H}_2\text{SO}_4$  (the sweep number is given for each curve).

Figure 3.18 is a set of curves displaying the reaction of a passivated, sputtered Pt microelectrode swept successively in 0.5 M  $\text{H}_2\text{SO}_4$  (the sweep number is given for each curve). The DC cyclic voltammograms at 100 mV/s with 1mM FMCA was shown in Figure 3.19. Curve (i) was obtained from a new device with a reference of electrodeposited Ag|AgCl. Curve (ii) was obtained from the same device with a passivated working electrode in which the redox currents decrease. Curve (iii) was obtained from the device with regenerated working electrode after cycling in acid (Figure

3.17). Note the redox characteristic of FMCA on the electrode “recovered” to larger DC cyclic currents (see curves (i) & (iii)). The results can be explained as the recovered working electrode surface is cleaner than in the new device, and as the latter was slightly passivated after the reference deposition of AgI/AgCl.

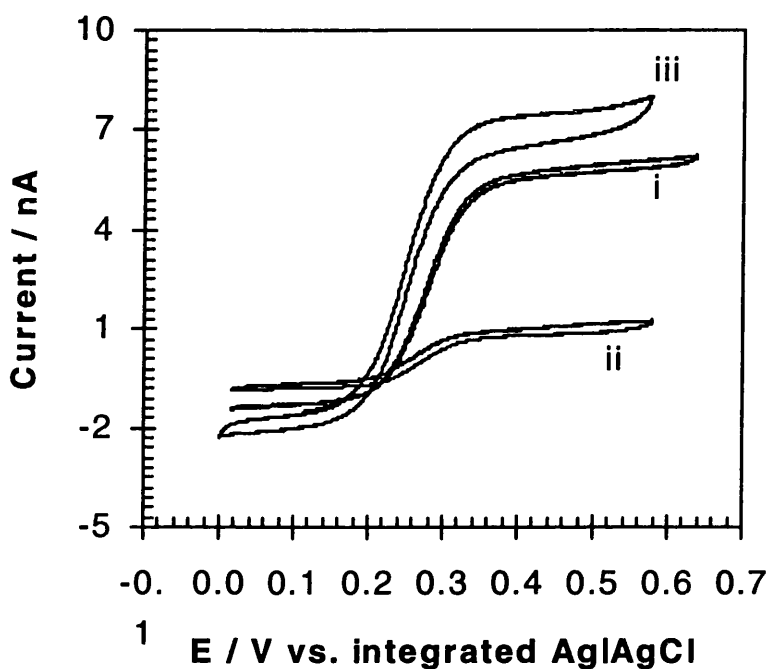


**Figure 3.19** DC cyclic voltammograms at 100mV/s with 1mM FMCA before and after regeneration of the working microelectrode using cycling in acid method: (i) voltammogram of a device immediately after reference deposition of AgI/AgCl; (ii) voltammogram of the same device with a passivated working electrode showing decreased redox currents; (iii) voltammogram of the same device with a regenerated working electrode after cycling in acid.

### 3.4.5.3 Dry Etching

Figure 3.20 is a typical comparison of the device DC cyclic voltammograms, at 100mV/s with 1mM FMCA, before and after a dry etching process. Prior to the etch, the device has been used for extensive cell tests and was completely passivated by oil and debris. Even when it was cleaned using ethanol or diethyl ether, the device was still heavily passivated as shown in curve (i). After dry etching, its DC cyclic voltammogram returned to a normal response, showing increased currents (ii) and indicating that the microelectrode in the device was “regenerated” completely. This device regeneration has been repeated successfully more than 6 times for assays including the determination of lactate, such that the regenerated device can respond repeatedly to substrate whilst the passivate device failed to responded to lactate.

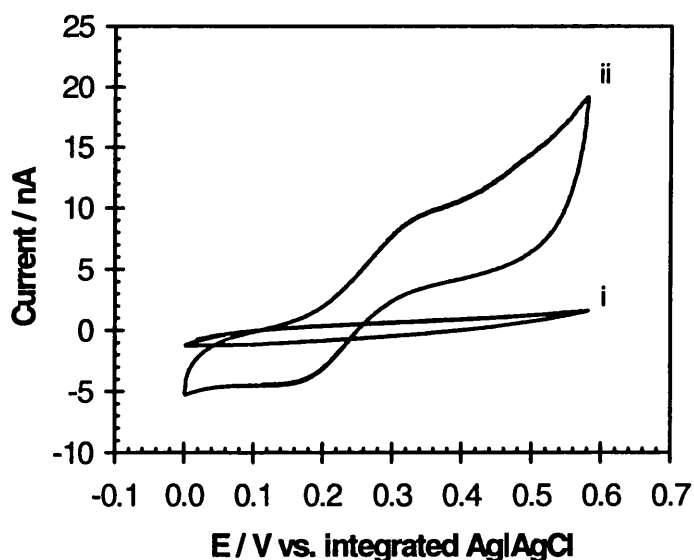


**Figure 3.20** A typical comparison of the device DC cyclic voltammogram, at 100 mVs<sup>-1</sup> in a solution containing 1 mM FMCA in 10 mM PBS, before (i) and after (ii) dry etching process. Prior to dry etching, the electrode had been “fouled” in cell culture medium.

Microelectrodes can be regenerated using both the methods of cycling in acid and dry etching. However, the microelectrodes and microreference of Ag|AgCl can be partly destroyed in the 0.5 M H<sub>2</sub>SO<sub>4</sub> during the process of cycling in acid. This does not occur during the process of dry etching. Not only was the electrode surface absolutely cleaned (as viewed by SEM, data not shown), but also the SU-8 thickness was only etched by 0.2 μm after 1 min dry etching process. Dry etching was therefore used routinely for regeneration in this work.

Reproducibility after electrode regeneration, which presents a key challenge, was optimised using a dry etch technology to give devices with a coefficient of variation of < 10% for measurement of 1 mM FMCA. This gave an average  $i_{pa}$  of 6.8 nA ( $n = 4$ ;  $\sigma = 0.64$  nA;  $cv < 10\%$ ). The regeneration protocol enabled individual devices to be used more than 4 times (normally 5 ~ 10 times), thereby greatly reducing the amount of fabrication required.

#### *3.4.6 Measurement of Glucose Oxidase Activity*

12.5 mg/ml GOD was measured using the method in Section 3.3.4. 0.05 ml of the diluted solution of 0.125 mg/ml GOD was added for the sample and the change in absorbance at 520 nm over the initial 2 min was measured to be about 3.173 using spectrophotometer (Hitachi U-2000).

Substituting  $\Delta A = 3.173$  into equation (3.23), the GOD activity of the diluted solution is found to be about 9.77 unit/ml, indicating that the sample of 12.5 mg/ml GOD is about 977 unit/ml.

### **3.5 Conclusions**

In this chapter, The basic concepts and measurement theory of electrochemical system have been introduced. The electrochemical characterization of miniaturized two-electrode or three-electrode sensor using a model redox compound of FMCA has been discussed. The detection of hydrogen peroxide, the redox enzyme linked electrochemical assay of glucose has been reviewed. It has been found that the response to hydrogen peroxide shows the Tafel plot of current peak against applied potential. Microreferences

of Ag|AgCl and Ag|Ag<sub>3</sub>PO<sub>4</sub> were compared and evaluated and the potential of the Ag|AgCl microreference was relatively stable whereas the potential of Ag|Ag<sub>3</sub>PO<sub>4</sub> showed the instability with respect to time. By using FMCA/FMCA<sup>+</sup> as a calibrating redox couple, the actual potential of the micro pseudoreference Ag|AgCl vs. the true reference of Ag|AgCl (BAS) was determined to be +45 mV. A novel regeneration methods for micro planar electrodes have been explored and optimised. The glucose oxidase activity has been measured using spectrophotometer technique. All these research methods will be applied to the single cell measurements in this work (Chapter 5).

## Chapter 4: Bulk and Picolitre-Scale Detection of Lactate

### 4.1 Introduction

L-Lactate is one of the most important cellular metabolites and is of significant clinical interest, for which a reliable, sensitive and fast detection method is required in clinical, food and bioprocess analysis [40-42]. Amperometric L-lactate sensors are becoming increasingly important as inexpensive, miniaturizable, and sensitive detectors for possible in vivo and flow analysis [43,44].

Lactate, pyruvate and the ketone bodies (acetoacetate and acetate) are important fuels for the heart under aerobic conditions and must be transported into the cell. In contrast, under hypoxia conditions, the heart uses glycolysis in its attempt to maintain the production of ATP required for ionic homeostasis and contraction. The resulting lactic acid must be transported out of the cell, to prevent its intracellular accumulation and consequent decrease in pH [45-47], i.e. there is increased lactate effluxing from the heart cell during hypoxia or ischaemia (e.g. infarction or cell death). Lactate oxidase (LOD) catalyses the oxidation of lactate in the presence of oxygen to pyruvate with the production of  $H_2O_2$ , which can be detected amperometrically [1,2,43].

In this chapter, our interests focus on developing thin film amperometric sensors, which in future will be applied to the dynamic electrochemical measurement of lactate within very low volumes (including e.g. the determination of intra- and extracellular metabolites from mammalian and bacterial cells). The sensitivity, response times and calibration curves were studied for the resulting lactate amperometric bioanalytical sensor using “bulk” and normal bulk methods. We also describe an automated dispensation technology, which we have coupled to the detection system and used to deliver extremely low volume ( $\geq 6.5$  pL)-aliquots of lactate to the analytical system. It is necessary that the micromachined sensors would include enzyme immobilisation for flow injection analysis or continuous monitoring in vivo application, so the sensors with enzyme immobilisation were also developed.

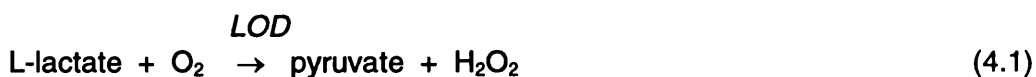
## 4.2 Chemicals and Materials

All solutions were prepared with high-purity deionized water (Millipore Elix 10) and analytical reagent grade chemicals, without further purification. Lactate oxidase from *Aerococcus viridans* (LOD, EC 1.1.3.2, 39.1 U $\text{mg}^{-1}$ , Cat. No. 1381) was purchased from Genzyme Biochemicals (Kent, England). Ferrocene monocarboxylic acid (FMCA, Cat. No. F-2641), L(+)-Lactate acid (sodium salt, Cat. No. L-7022) and mineral oil (Cat. No. M-3516), Bovine albumin (Cat. No. A-2153), Glutaraldehyde (Cat.No. G-5882) and Ethanolamine (Cat. No. E-9608) were from Sigma (Dorset, England). Supporting electrolyte was either 10 mM PBS (10 mM phosphate buffer, 2.7 mM KCl and 137 mM NaCl; pH 7.4) or Krebs-Ringer buffer (KRB) of the following composition : 120 mM NaCl, 20 mM Hepes, 5.4 mM KCl, 0.52 mM NaH<sub>2</sub>PO<sub>4</sub>, 3.5 mM MgCl<sub>2</sub>, 1 mM CaCl<sub>2</sub>; equilibrated to pH 7.4 with 1 mM NaOH. Lactate solutions were prepared immediately prior to their use. Sodalime glass capillaries were supplied by Hilgenberg (Germany).

## 4.3 Methods

### 4.3.1 Reaction Principle

The amperometric approach to L-lactate is based on the enzymatic oxidation of the analytes with the lactate oxidase (LOD) according to the reaction:



The hydrogen peroxide generated in this reaction is electrochemically oxidized on a platinum electrode, which was polarized at +0.64 V vs. an Ag/AgCl microreference electrode:



### ***4.3.2 Normal Bulk solution and “Bulk” Solution Methods For Measurements***

For a normal bulk solution method, the device with (or without) enzyme immobilisation was soaked in ~5 ml, stirred PBS (10 mM) without LOD (or with 50 units ml<sup>-1</sup> LOD) within a 5 ml beaker. After the residual current reached a steady state value, 50 µL aliquots of lactate were successively injected into the solution and the final lactate concentrations were calculated. Note, lactate in a bulk LOD solution can be consumed quicker than in a bulk PBS without LOD. In the later case, lactate is consumed only in the immobilized enzyme membrane.

In order to preserve the biochemical reagents and save time, besides normal bulk solution, a ~10 µL drop of solution was used to model the bulk solution for measurement, this method was called a “bulk” solution method or “macro-volumetric-test” method. For example, a drop of 9 µL LOD in supporting electrolyte was used to cover the microchamber of the device. After the residual current became constant, 1 µL of *C* mM Lactate was injected into the solution to give a final lactate concentration of about 0.1*C* mM.

### ***4.3.3 Lactate Oxidase Immobilization on Micromachined Sensor [48-50]***

Prior to immobilisation, the device was cleaned using dry etching (Section 3.8). To a 2 µl aliquot of bovine albumin, 100 mg ml<sup>-1</sup>, 2 µl LOD, 6 KU ml<sup>-1</sup>, and 2 µl glutaraldehyde, 0.5% v/v in 10 mM PBS was added. 0.5 µl of the mixed solution was coated onto microchambers with hydrophilic surfaces. The protein molecules were crosslinked (Figure 4.1) and the gel membrane was allowed to dry at room temperature for 5 min. The treated device was then rinsed with PBS and immersed in 0.2 M ethanolamine for 5 min to block the unreacted aldehyde groups, preventing extensive cross-linking which can affect biomolecule (LOD) function. The final device was rinsed thoroughly with distilled water and immersed in PBS.

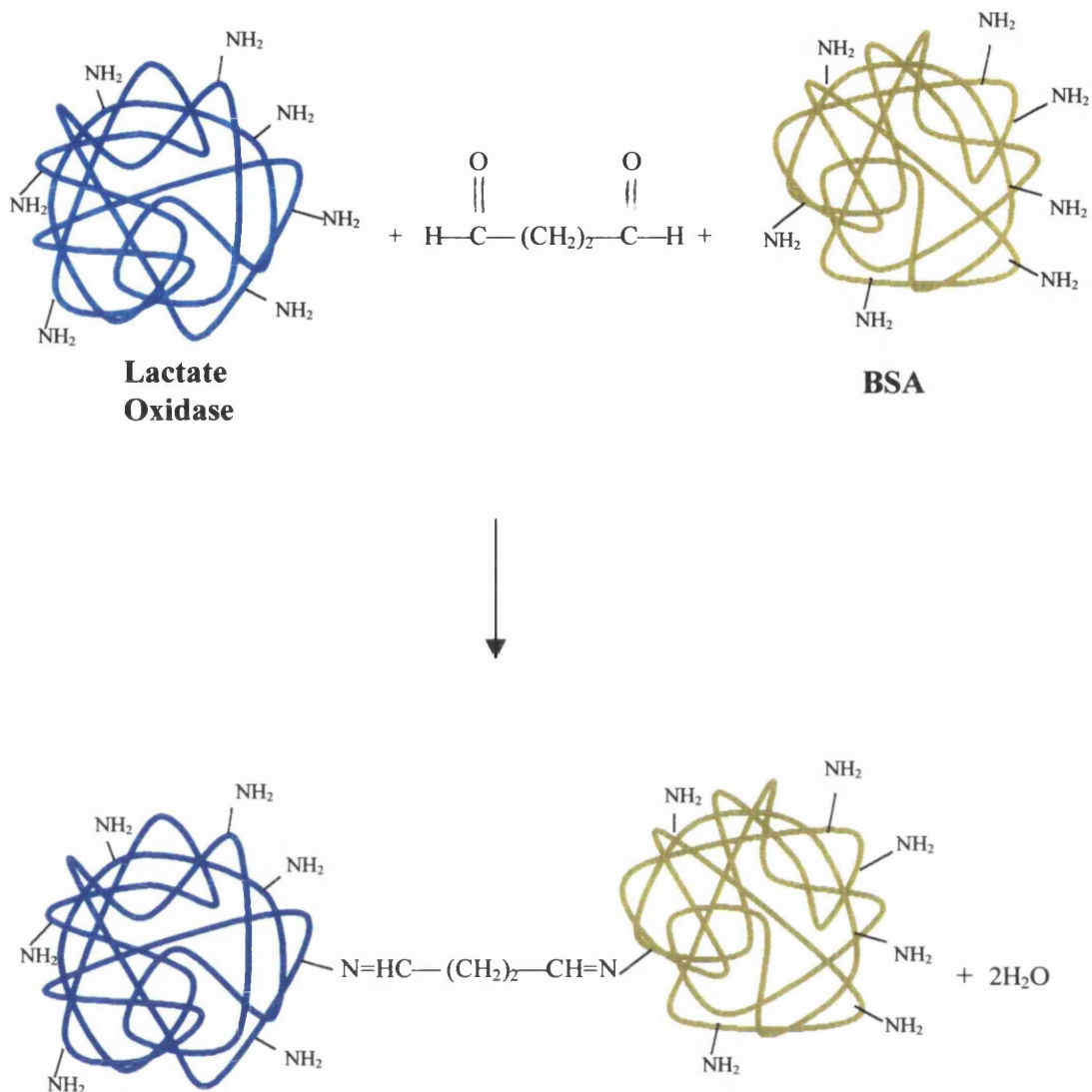


**Figure 4.1** Schematic of the crosslinking of lactate oxidase to bovine serum albumin (BSA) using glutaraldehyde.

#### 4.3.4 Microinjection System

##### 4.3.4.1 Experimental Set-up

A schematic representation of the analytical set-up is given in Figure 4.2 comprising a low current potentiostat (CV-37, BAS, UK), with data collected on a PC, an inverted microscope and a microfluidic dispensation system. Data was collected from the device housed inside a small Faraday cage. Throughout experimentation, the

titre chamber and fluid dispensation were monitored using a microscope with a CCD video camera.

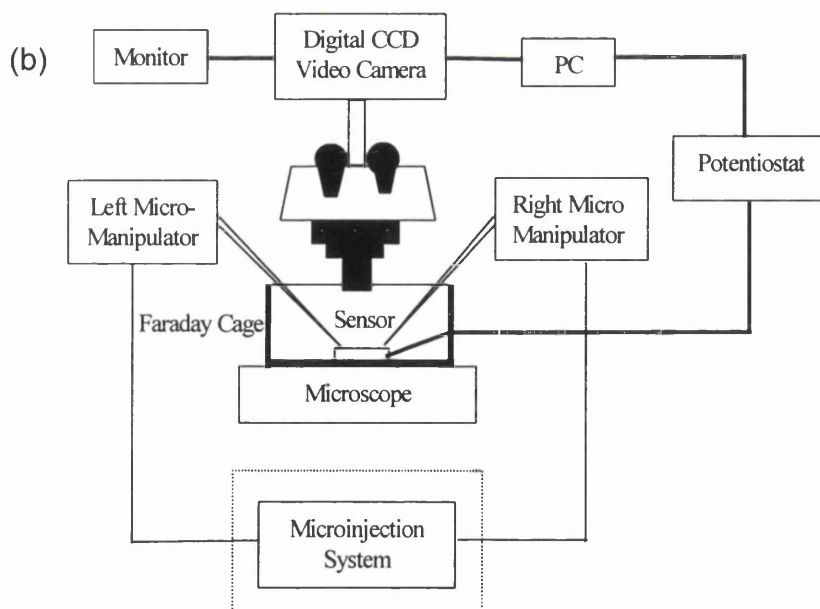
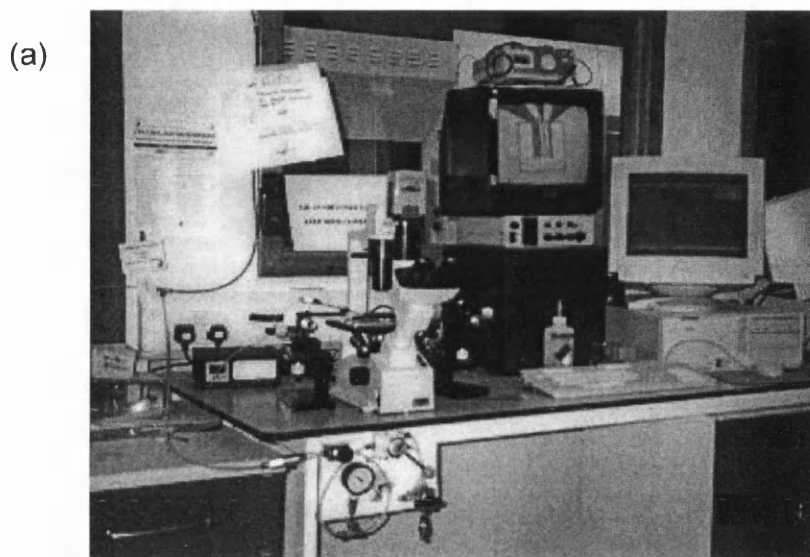


**Figure 4.2** Showing the measurement apparatus: (a) photograph of the measurement set-up; (b) a schematic diagram of the measurement set-up.

The in-house pL-microinjection system (Figure 4.3a) was developed for the reproducible dispensing of pL-scale volumes of fluid into the chamber. Micropipettes of sodalime glass capillaries (1.2 mm outer diameter, 0.96 mm inner diameter, with an inner filament; Hilgenberg, Germany) were pulled (PC-10, Narishige) to a tip with a bore of about 700 nm (Figure 4.3b) and were manually maneuvered into the chamber for low volume injection. Glass micropipettes were subsequently fixed onto left and right three-axis micromanipulators (Intracel, UK) and connected to either the balanced pressure or the injection pressure from the dispenser (the balanced pressure prevented capillary action enabling very low volume injections to be made), see Figure 4.3 legend.

#### 4.3.4.2 pL-Scale Solution Dispensation

Prior to performing low volume liquid dispensation, the microchamber was first cleaned by dry etching as described in Section 3.3.3. Evaporation was prevented using dispensation of a thin film of mineral oil [12]. A 0.3  $\mu\text{l}$  droplet of solution was placed directly onto the microchamber area (which has a hydrophilic surface), and was immediately covered with 30  $\mu\text{l}$  mineral oil constrained within an epoxy ring wall (ring diameter 8-10 mm, wall width 2 mm and wall height 1 mm) for preventing bulk evaporation of the droplet. The pipette (end bore between 5 to 10  $\mu\text{m}$ , without filament) was then inserted manually through the mineral oil layer into the droplet and allowed to fill by capillary action. The rate of filling was slow, so that, by viewing the chamber under the microscope (Nikon TMS, 10 $\times$  eyepiece, 10 $\times$  or 20 $\times$  objective) and carefully inserting and removing the pipette, the volume of the medium could be reduced to the volume of the chamber.

The filament pipette with a fine tip (bore diameter: 500 ~ 700 nm) was then back filled with lactate solution (Figure 4.4) and an injection pressure of 15 psi was used for dispensation of pL volumes. A “one shot” timer (Figure 4.3) can be set between 0.01 s. to 99.99 s to enable the volume of fluid to be determined (assuming a constant flow rate).

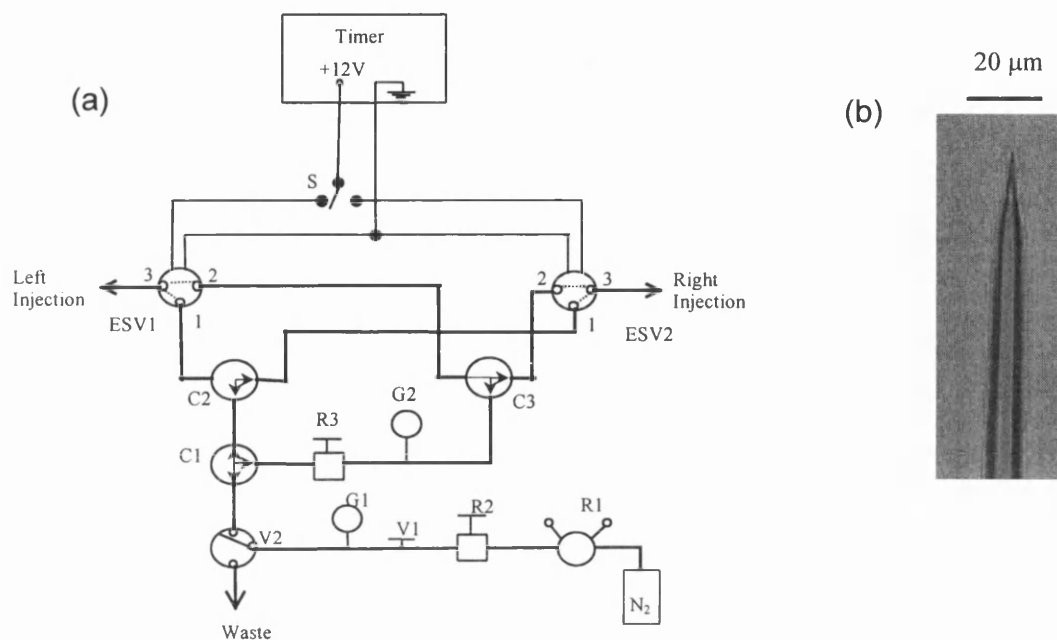


**Figure 4.3** Showing the microinjection system as a schematic diagram:

- (a) The microinjection system assembly, in which, R1 is the gas cylinder regulator assembly; R2 is a 0-60 psi pressure regulator; R3 is a 0-10 psi pressure regulator; V1 is a needle valve; V2 is a SMC 3-port valve that allows flow across selected ports; G1 is 0-60 psi pressure gauge; G2 is a 0-10 psi pressure gauge; C1 is a 3-way connector (which allows flow across 3 ports); C2 and C3 are 3-way connectors allowing flow across selected ports; S is a switch; ESV1 is an electric solenoid valve for left injection (timer pulse on: 1 ↔ 3) and balance (off: 2 ↔ 3); ESV2 is electric solenoid valve for right injection (timer pulse on: 1 ↔ 3) and balance (off: 2 ↔ 3). Port 1 and port 3 of electric solenoid valve (ESV1 or ESV2) are open for dispensation when timer pulse was set on; port 2 and port 3 of ESV1 or ESV2 are open for balance process when timer pulse was switched off. The left or right process was controlled by selecting left or right ports of C2 (for left or right dispensation) and C3 (for left or right balance), as well as left or right of S.
- (b) a photograph of the glass micropipette with fine tip for microinjection.

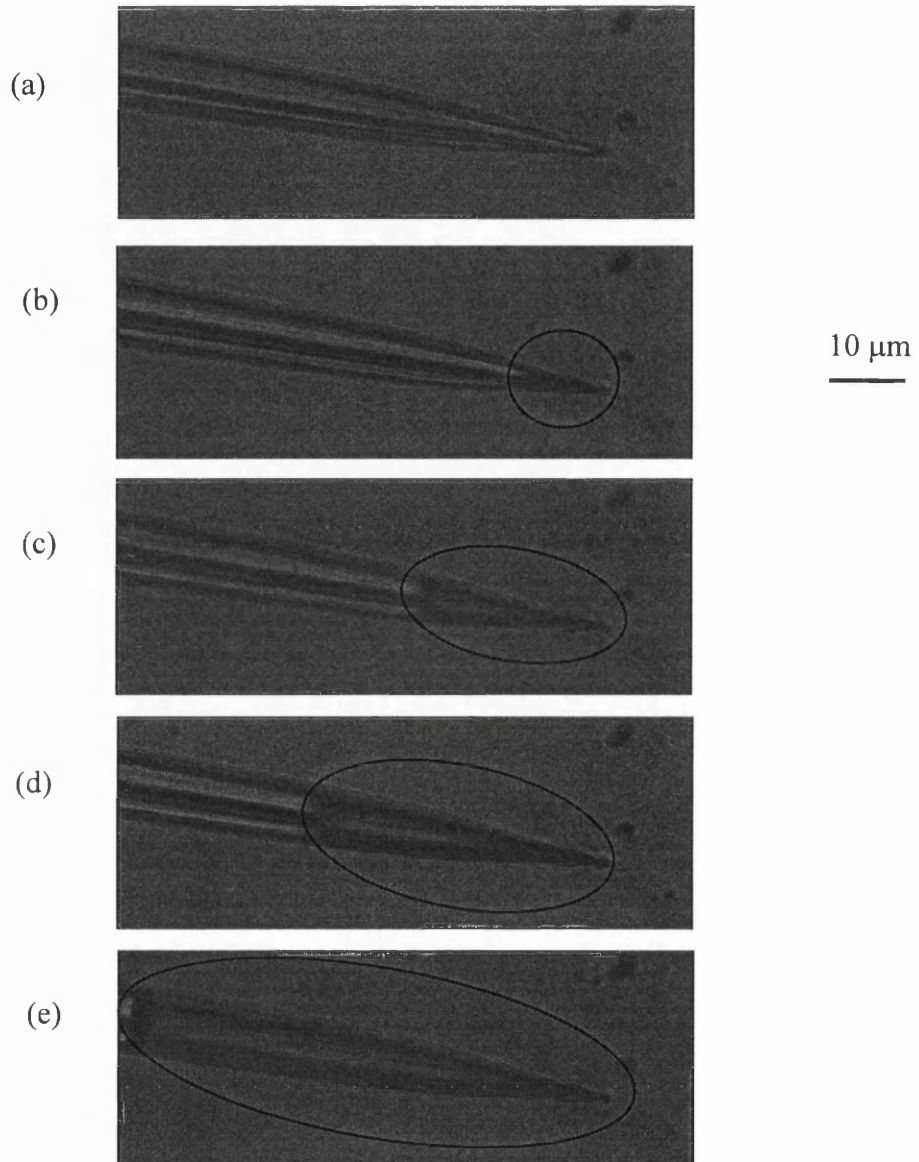


**Figure 4.4** Fluid moving (from a to e) in the fine tip of a filament pipette while it was being back filled with solution. The frame rate is  $10 \text{ frames sec}^{-1}$ .

#### 4.3.4.1 Calibration of pL-Scale Solution Dispensation in the Microinjection System

Using the method above, a low volume of the KRB was placed in the microchamber. The filament pipette with a fine tip was then soaked in KRB for a short time, fixed in the manipulator at a low angle ( $\alpha = 25^\circ$ ) to the horizontal plane (Figure

4.5a). The tip was inserted manually through the mineral oil layer into the droplet and allowed to fill by capillary action. Typically it stopped filling when the solution length was about 500  $\mu\text{m}$ . Throughout the experimentation, the fluid change for dispensation in the tip was observed using a microscope (eyepiece 10 $\times$ , objective 10 $\times$ ) with a monitor (Panasonic). The system magnification of the pattern in the monitor is about 450 $\times$ . The length change ( $\Delta L$ ) of the fluid for dispensation was thus measured in the system, where 1 mm on the monitor screen corresponded to 2.22  $\mu\text{m}$  of the sample.

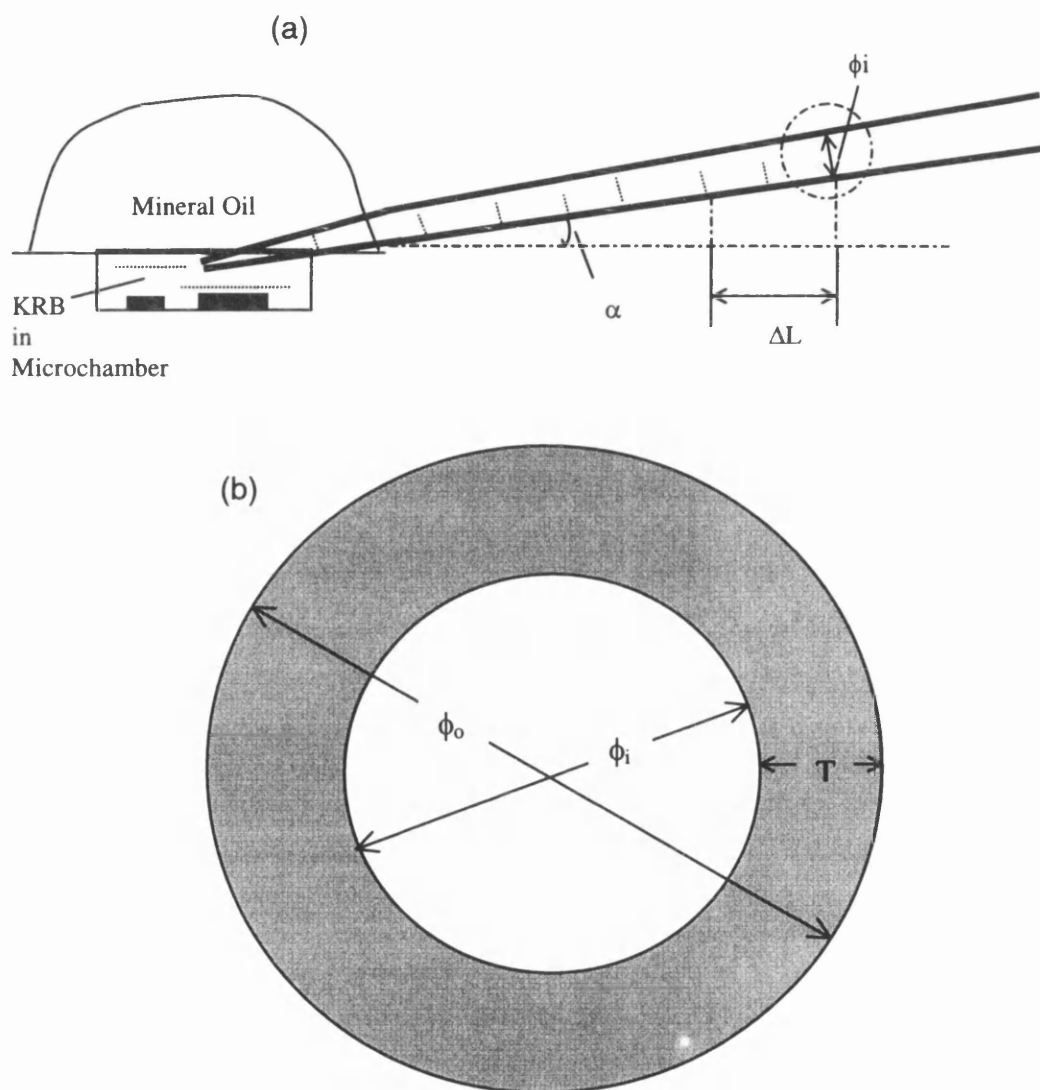


**Figure 4.5** A pulled pipette in the microinjection system for calibration of picolitre scale solutions: (a) insertion of a drawn micropipette into KRB in a microchamber covered with mineral oil, allowing the pipette to fill by capillary action, where,  $\alpha = 25^\circ\text{C}$ ,  $\Delta L =$  length change,  $\phi_i =$  inner diameter; (b) section diagram of the pipette tip at the position circled with the dotted line in (a).

As shown in Figure 4.5(b), using a microscope (Nikon, objective piece 20×) with an eye-piece graticule (10×), the outer diameter ( $\phi_o$ ) of a pulled pipette was measured 20.7  $\mu\text{m}$  at the position of 500  $\mu\text{m}$  length from its tip end. The thickness (T) of the pulled pipette wall was measured to be 2.95  $\mu\text{m}$  with an outer diameter of 30.0  $\mu\text{m}$ . Considering the tip to be an uniform cone up to 2 mm and the thickness of the pulled pipette wall to change uniformly over the tapered length of the pipette, the thickness of the pipette wall with at an outer diameter of 20.7  $\mu\text{m}$  is calculated to be 1.97  $\mu\text{m}$ .

This technique assumes that the sides of the micropipette are parallel in a short length, i.e. the diameter change in the dispensed solution length is close to zero (Figure 4.3b), the volume dispensed ( $\Delta V_{inj}$ ) by the microinjection system is estimated using the following equations:

$$\Delta V_{inj} = \pi (\phi/2)^2 \Delta L \div \text{Cos}\alpha \quad (4.3)$$

$$\phi_i = \phi_o - 2T \quad (4.4)$$

in which,  $\phi_i$  is the inner diameter (Figure 4.5b). At 500  $\mu\text{m}$  from the tip,  $\phi_o = 20.7$   $\mu\text{m}$ ;  $T=1.97$   $\mu\text{m}$ . Substitution of  $\phi_o$  and T into equation (4.4) gives  $\phi_i = 8.4$   $\mu\text{m}$ .

Further substitution of  $\phi_i = 8.4$   $\mu\text{m}$  and  $\alpha = 25^\circ\text{C}$  into equation (4.3) gives,

$$\Delta V_{inj} = 244.55 \Delta L (\mu\text{m}^3) \quad (4.5)$$

The shot time ( $\Delta T_{inj}$ ) of the “one shot” timer was set to 100, 200 and 300 ms to enable the volume of fluid to be determined (assuming a constant flow rate) for calibration. As shown in Table 4.1, the length change ( $\Delta L$ ) of the fluid for dispensation was measured with three times ( $n=3$ ). Substitution of the values of  $\Delta L$  into (4.5) enabled a calibration plot of the injection volume vs. the shot time to be obtained (Figure 4.6). The plot equation is described as

$$\Delta V_{inj} = 0.0667 \Delta T_{inj} - 0.3889 \quad (4.6)$$

A calibration table (Table 4.2) can be easily obtained from equation (4.6) for different shot time dispensations.

**Table 4.1** The length change ( $\Delta L$ ) of the fluid for dispensation ( $n=3$ ) with different shot time ( $\Delta T_{inj}$ ).

| $\Delta T_{inj}$<br>(ms) | $\Delta L1$ of Tip1<br>( $\mu m$ ) | $\Delta L2$ of Tip2<br>( $\mu m$ ) | $\Delta L3$ of Tip3<br>( $\mu m$ ) |
|--------------------------|------------------------------------|------------------------------------|------------------------------------|
| 100                      | 26.6                               | 24.4                               | 26.6                               |
| 200                      | 53.3                               | 53.3                               | 51.1                               |
| 300                      | 79.9                               | 82.1                               | 79.9                               |

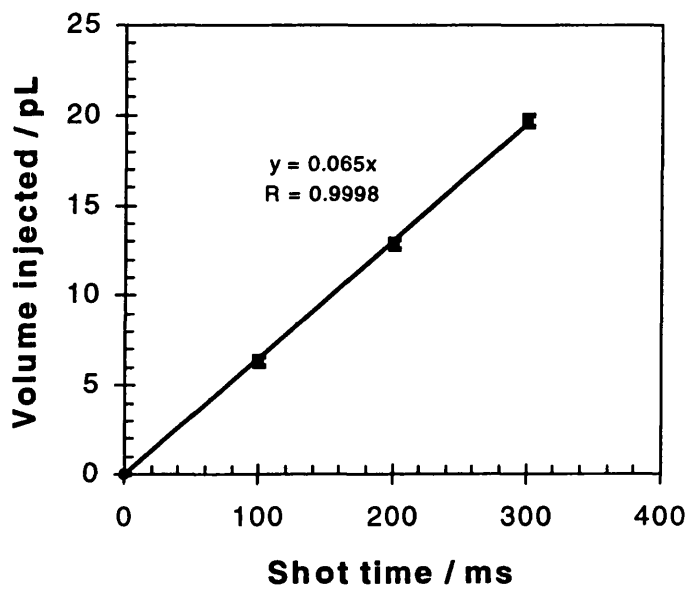


**Figure 4.6** Calibration plot of injection volume vs. the shot time (calculated using the raw data in Table 4.1)

**Table 4.2** Calibration table for different shot time dispensations, where,  $\Delta V_{inj}$  is the injection volume and  $\Delta T_{inj}$  is the shot time.

|                          |     |     |     |     |      |      |      |
|--------------------------|-----|-----|-----|-----|------|------|------|
| $\Delta T_{inj}$<br>(ms) | 20  | 30  | 60  | 100 | 200  | 300  | 400  |
| $\Delta V_{inj}$<br>(pL) | 1.3 | 2.0 | 3.9 | 6.5 | 13.0 | 19.5 | 26.0 |

## 4.4 Results and Discussion

### 4.4.1 Response Using “Bulk” Method

#### 4.4.1.1 The Stability of Lactate

As the stability of lactate solution may be affected by ionic association with  $\text{Ca}^{2+}$  and  $\text{Mg}^{2+}$ , the responses to the fresh lactate (prepared immediately prior to their use) and the lactate stored at  $4^\circ\text{C}$  for 3 days are compared in Figure 4.7. The response to 1 mM lactate stored for 3 days decreased to zero (Figure 4.17 (a)), meanwhile the response to the fresh 1 mM lactate produced an output of about 14 nA (Figure 4.7(b)). Lactate was thus always prepared immediately prior to its use during this work.

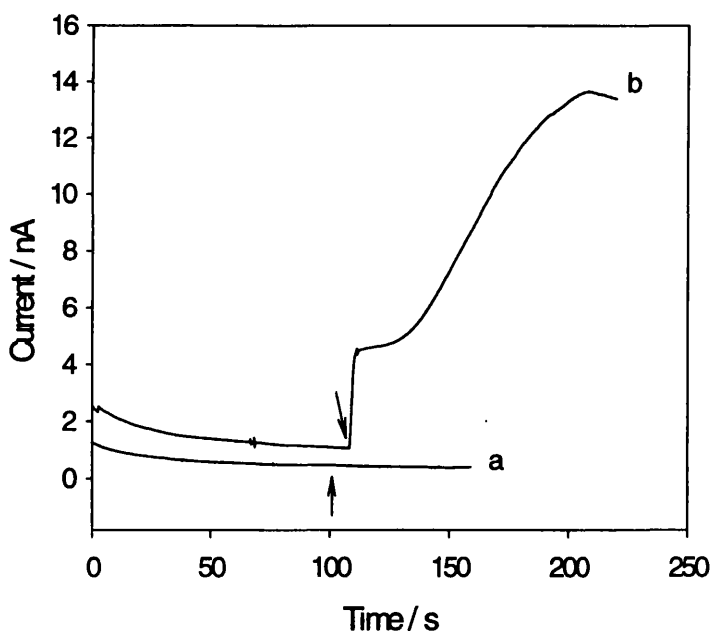


**Figure 4.7** Responses to fresh lactate and stored lactate. 20  $\mu\text{L}$  lactate (1 mM) was used to cover on the microchamber, then 2  $\mu\text{L}$  120  $\text{U ml}^{-1}$  LOD was added to the solution from the time labelled by the arrow: (a) the response to lactate stored at  $4^\circ\text{C}$  for 3 days; (b) the response to fresh lactate prepared immediately prior to its use. The surface area of the working electrode was  $1250 \mu\text{m}^2$ .

#### 4.4.1.2 Responses to Lactate

The microwell device was filled with 9  $\mu\text{l}$  200 unit/ml LOD in 10mM PBS (pH 7.4). After the residual current became a constant value, each lactate sample was injected. The output current increased promptly after the injections for final concentrations of 10  $\mu\text{M}$ , 100  $\mu\text{M}$  and 1 mM as illustrated in Figure 4.8. For the final low concentrations of 2, 4, 6, 8, 10  $\mu\text{M}$ , the current-time response is shown in Figure 4.9(a). The increase in the oxidising current was caused by oxidation of the hydrogen.

The charge transferred on the working electrode (for 120s) was obtained by calculating the integral of current-time. The normalization of charge transferred on the working electrode vs. lactate concentration is shown in Figure 4.9(b). Each point was measured in triplicate using three 3-electrode devices and the mean was taken.

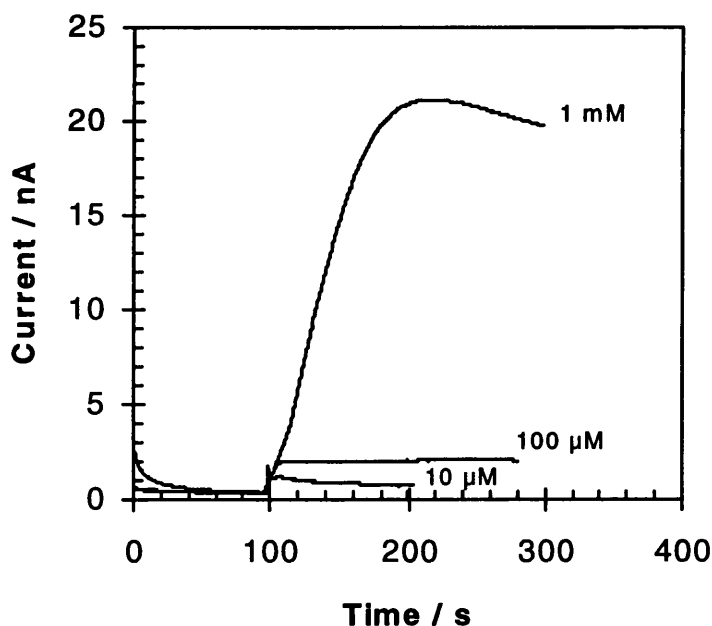


**Figure 4.8** Typical current-time responses to 10  $\mu\text{M}$ , 100  $\mu\text{M}$  and 1 mM lactate using a platinized electrode within the 3-electrode microstructure. The working potential was held at +0.64 V vs. internal Ag|AgCl reference. The microwell device was filled with 9  $\mu\text{l}$  200 unit  $\text{ml}^{-1}$  LOD in 10mM PBS (pH 7.4) before each addition of lactate. The surface area of the working electrode was 500  $\mu\text{m}^2$ .

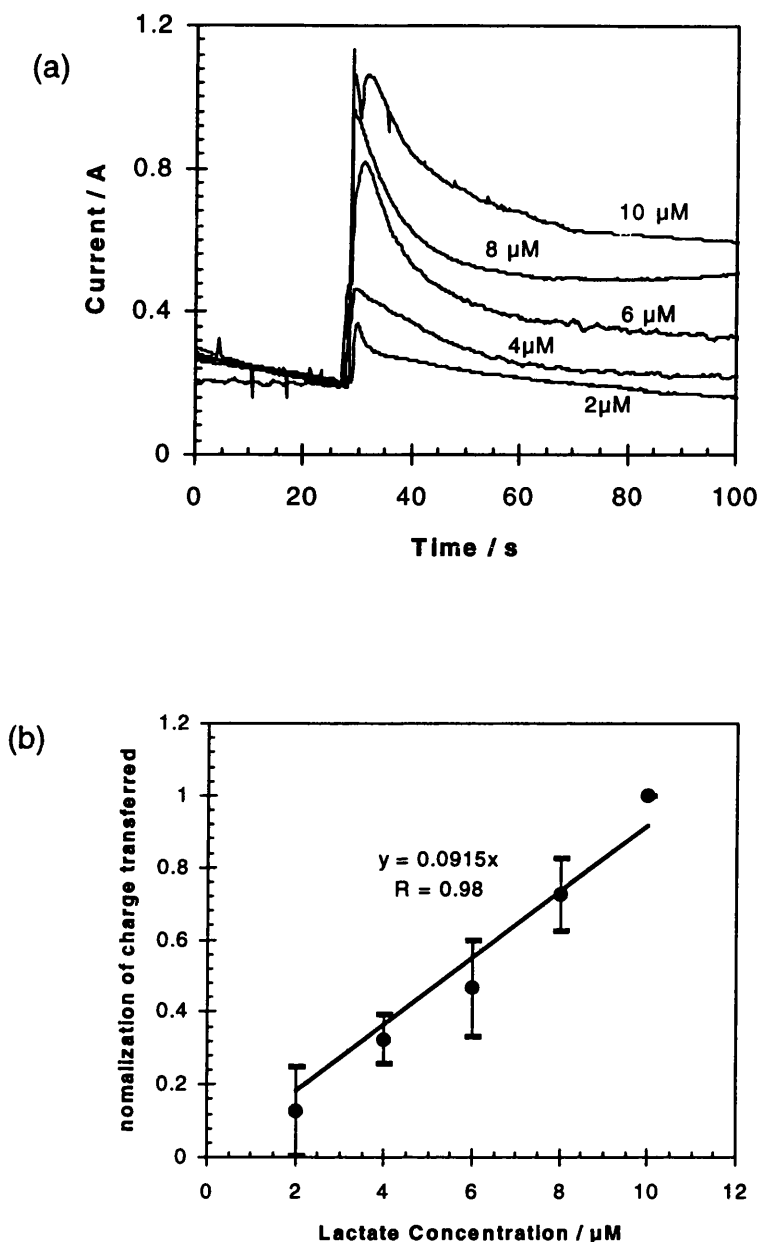


**Figure 4.9** Typical response to 2 ~ 10  $\mu\text{M}$  lactate using a platinized electrode within the 3-electrode microstructure. The working potential was held at +0.64 V vs. an internal Ag/AgCl reference. The microwell device was filled with 9  $\mu\text{l}$  200 units/ml LOD in 10mM PBS (pH7.4) before each addition of lactate: (a) the  $i-t$  response to lactate; (b) the normalization of charge transferred on the working electrode (for 70 sec) vs. lactate concentration, each point was measured in triplet and the mean was taken, with error bars shown. The surface area of the working electrodes was 500  $\mu\text{m}^2$ .

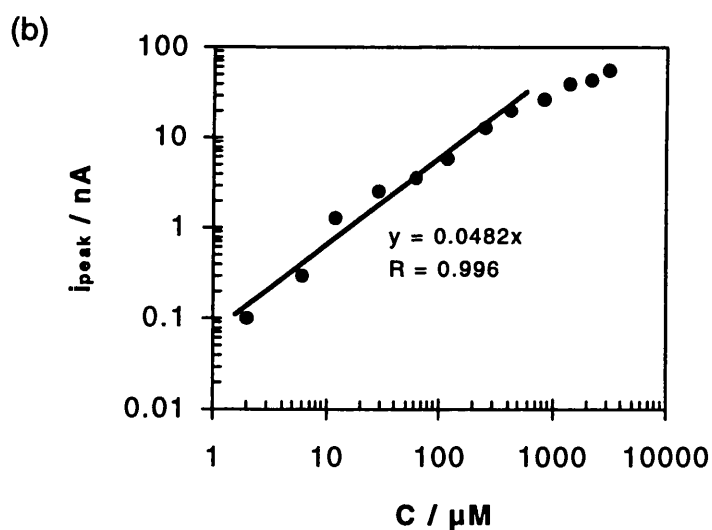
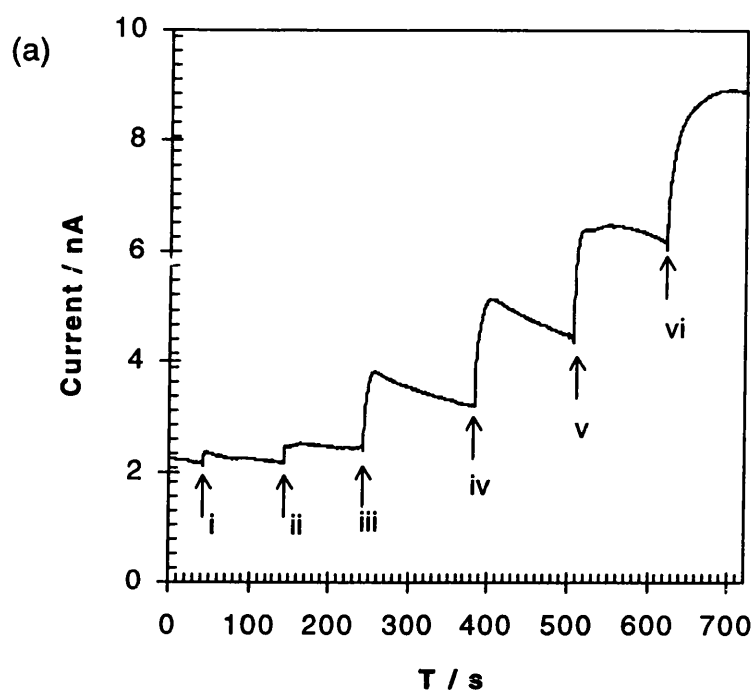


**Figure 4.10** Typical response to successive additions of lactate using a ‘bulk’ solution method. The working potential was held at +0.64 V vs. an internal Ag|AgCl reference. The micro well device was filled with 126 units ml<sup>-1</sup> LOD in 10mM PBS (pH 7.4), then 1 μl aliquots of lactate were successively injected into it: (a) the current-time behaviour of additions of lactate made at points (i) to (vi) for 2, 6, 10, 29, 63, 116 μM; (b) current peak output of the lactate sensor as a function of lactate concentration. The surface area of the working electrode was 1000 μm<sup>2</sup>.

A typical response to successive additions of lactate using a 'bulk' method is shown in Figure 4.10. Figure 4.10(a) shows the current-time plot for successive additions of lactate made at points (i) to (vi) for 2, 6, 10, 29, 63, 116  $\mu\text{M}$ . The correlation of the current peak with lactate concentration is illustrated in Figure 4.10(b). It has a linear relationship between 2 ~ 429  $\mu\text{M}$  of lactate. The response sensitivity and correlation coefficient were 0.048  $\text{nA } \mu\text{M}^{-1}$  and 0.996 respectively.

A typical response to successive additions of lactate using the normal bulk method is shown in Figure 4.11. The device was soaked in 50  $\text{U ml}^{-1}$  LOD in 4.5 ml 10mM PBS (pH7.4) stirred in a beaker, then 50  $\mu\text{l}$  aliquots of lactate were successively injected into it. Figure 4.11(a) shows the current-time behaviour of additions of lactate made at points (i) to (xi) for 4.4, 6.5, 8.6, 14.9, 27.0, 56.4, 122.4, 201.9, 368.6, 738.3, 1322.3  $\mu\text{M}$ . Figure 4.11(b) shows current peak output of the lactate sensor as a function of lactate concentration with the conditions as for (a). The relationship was linear between 4.4 ~ 202  $\mu\text{M}$  of lactate, and the response sensitivity and correlation coefficient  $R$  were 0.046  $\text{nA}/\mu\text{M}$  and 0.999 respectively. Comparing the model 'bulk' method and the real bulk method, it can be seen that the correlation of the real bulk (with stirring) method ( $R=0.999$ ) is slightly better than the model 'bulk' method ( $R=0.996$ ). With 50  $\text{U ml}^{-1}$ , the sensitivity is slight lower and the linear range is narrower than with 126  $\text{U ml}^{-1}$ .

#### 4.4.2 *pL-scale Detection of Mediators*

FMCA was used as a model one-electron redox compound in order to investigate the low volume electrochemical characterization of the sensor using an integrated (in situ) Ag|AgCl microreference. The cyclic voltammetry of 400 pL FMCA (1 mM) of the 2-electrode sensor is shown in Figure 4.12(a). The slow scan rate voltammogram ( $10 \text{ mV s}^{-1}$ ) was peak-shaped, with a large increase in current on the reverse wave of the cyclic voltammetry. This response was substantially different from the bulk response shown in Figure 4.12(b), in which cyclic voltammetric response followed that expected for a microelectrode: steady-state behaviour at slow scan rates. The slow scan rate response in low volumes support the simple physical model

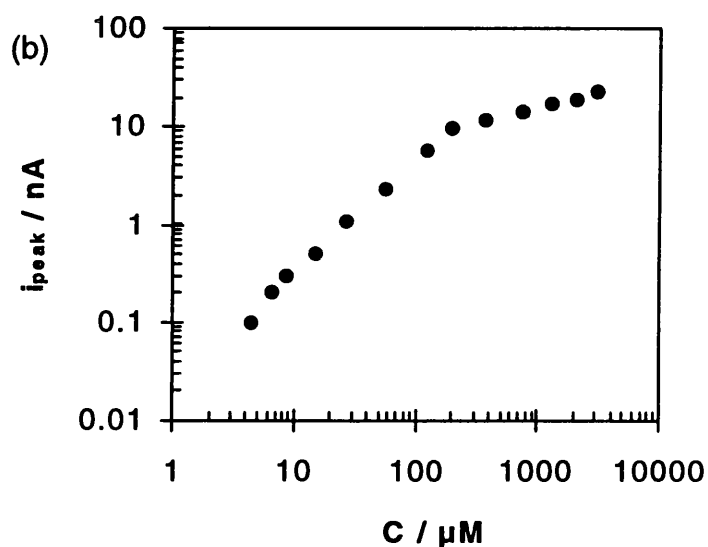
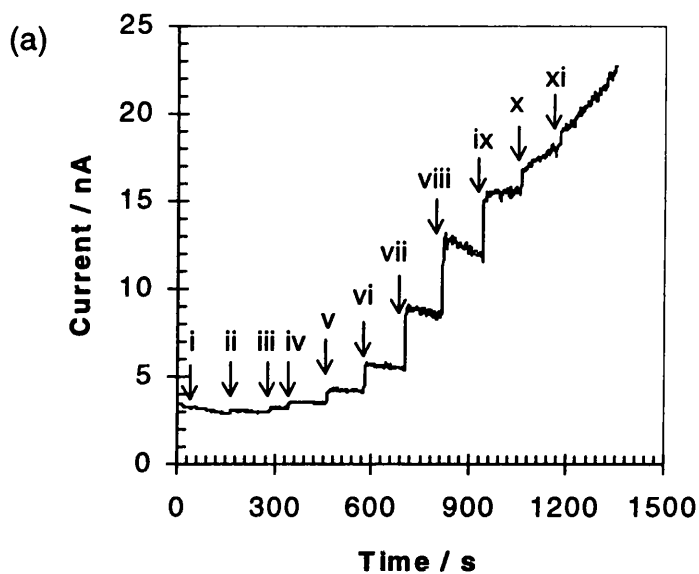


**Figure 4.11** Typical response to successive additions of lactate using the bulk method. The working potential was held at +0.64 V vs. an internal Ag/AgCl reference. The device was soaked in 50 units/ml LOD in 4.5 ml 10mM PBS (pH 7.4), then 50  $\mu\text{l}$  aliquots of lactate were successively injected into it: (a) the current-time behaviour of additions of lactate made at points (i) to (xi) for 4.4, 6.5, 8.6, 14.9, 27.0, 56.4, 122.4, 201.9, 368.6, 738.3, 1322.3  $\mu\text{M}$ ; (b) current peak output of the lactate sensor as a function of lactate concentration. The surface area of the working electrode was 1000  $\mu\text{m}^2$ .

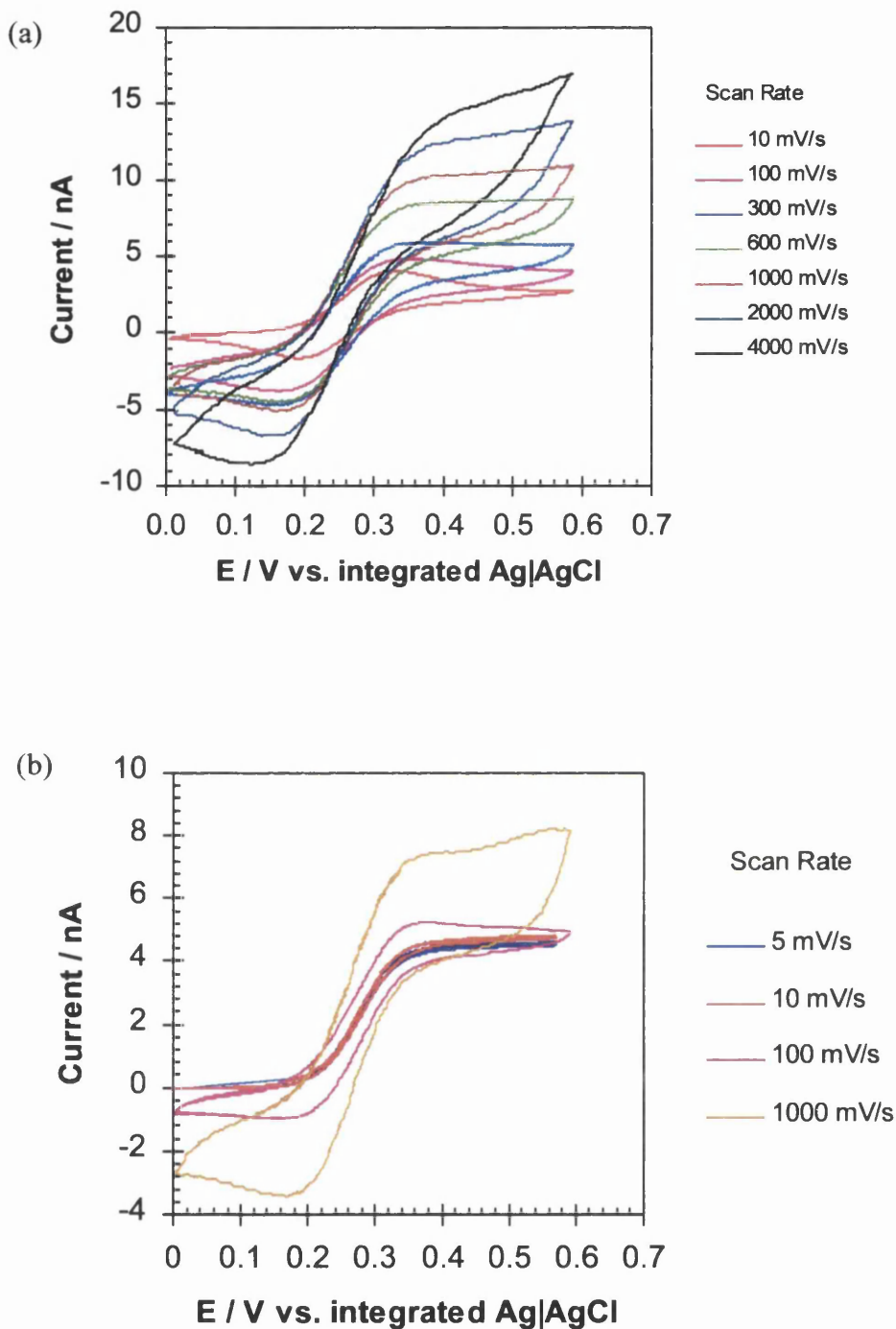


**Figure 4.12** Comparison of a 2-electrode sensor cyclic voltammograms of 1 mM FMCA in a low volume and a 'bulk' drop. The electrolyte is 10 mM PBS at pH 7.4: (a) in a 400 pL microchamber; (b) in a 'bulk' drop. The surface area of the working electrode was  $500 \mu\text{m}^2$ .

described by Ewing [51]. This model explains the voltammetric response in the microvial centres around restriction of analyte in the microenvironment of picolitre vials. The oxidized analyte attempts to diffuse away from the microelectrode as in normal bulk solutions, except that in the microvials the distance that the analyte travels is minimal. On the reverse scan, the material that is close to the electrode surface is reduced, and then additional oxidised material in the restricted environment can diffuse to the electrode to be reduced, thus contributing to the current past the normal reduction peak (peak broadening).

This effect is quasi-reversible at higher sweep rates (100 ~ 4000 mV/s) as shown in Figure 4.13. In this quasi-reversible region,  $i_p$  increases with  $v^{1/2}$  but is not proportional to it,  $\Delta E_p (= E_p^A - E_p^C)$  is greater than 59 mV. This quasi-reversibility occurred when the relative rate of the electron transfer with respect to that of mass transport was insufficient to maintain Nernstian equilibrium at the working electrode surface.

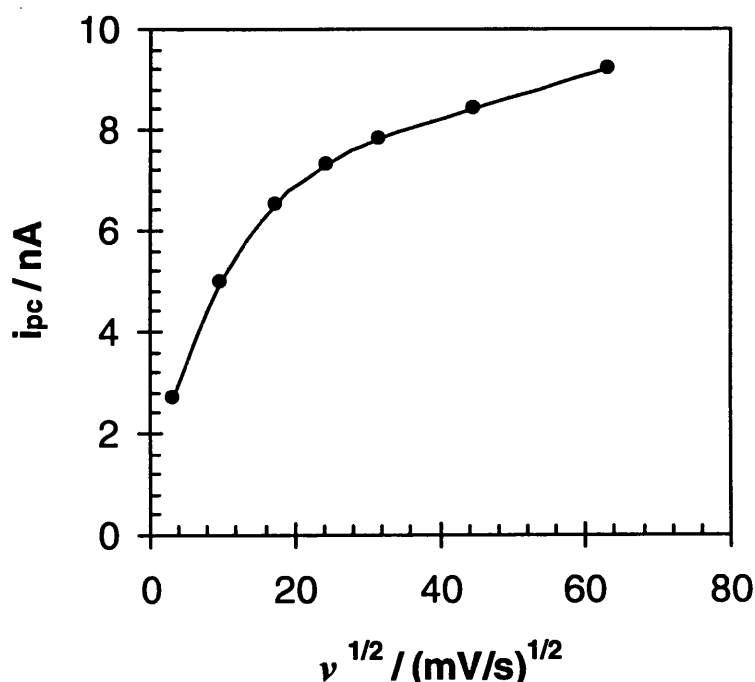


**Figure 4.13** Plot of the dependence of the peak current on the square root of the potential sweep rate according to Fig. 4.12(a).

### 4.4.3 pL-scale Detection of Lactate

#### 4.4.3.1 Current-time Responses

Results of lactate microinjection peaks using pL-scale detection are given in Figure 4.14. The microchamber was filled with 112 U/ml LOD in KRB, then 10 mM lactate in KRB was injected in 1.5, 3.7, 6.5, 6.5, 13.0, 20.0 and 26.6 pL amounts. The signal from each addition was allowed to return to baseline after each addition. As illustrated in Figure 4.14, all of the injected lactate was oxidized with LOD within 50 sec. In contrast to bulk/macro detection, the response was fast (about 10 sec to arrive at peak current) with no indication of current saturation for any of the quantities of lactate injected. The increase in speed of response for the bioanalytical system is a consequence of the reduced diffusion length to the sensor.

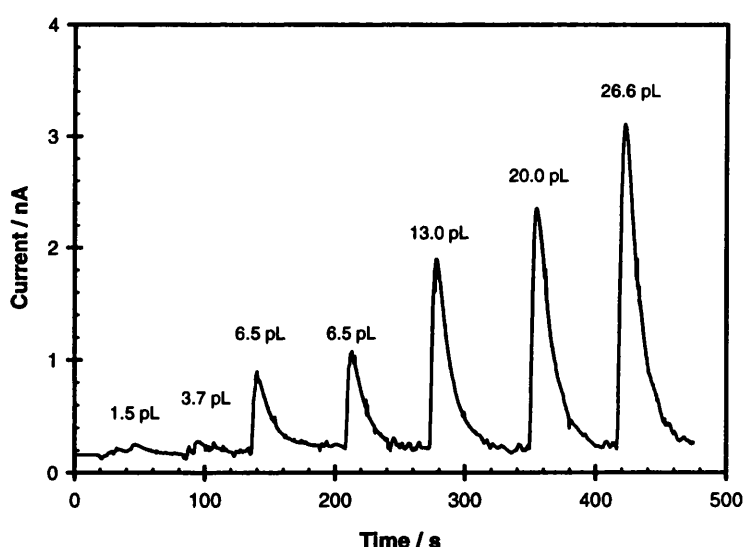


**Figure 4.14** Injection of pL-scale lactate. The device microchamber was filled with 360 pL KRB containing 112 U/ml LOD. 1.5, 3.7, 6.5, 13.0, 20.0 and 26.6 pL volume aliquots of stock solutions of 10 mM lactate were injected and their responses recorded. The surface area of the working electrode was 1000  $\mu\text{m}^2$ .

#### 4.4.3.2 Calibration Curve against Additions of Lactate

A linear calibration plot between the charge transferred on the working electrode and the injected lactate quantity is shown in Figure 4.15, with amounts of lactate being injected in 15, 37, 65, 65, 130, 200 and 266 fmol amounts. Each point was measured as a mean of three readings giving a linear correlation coefficient of 0.99.

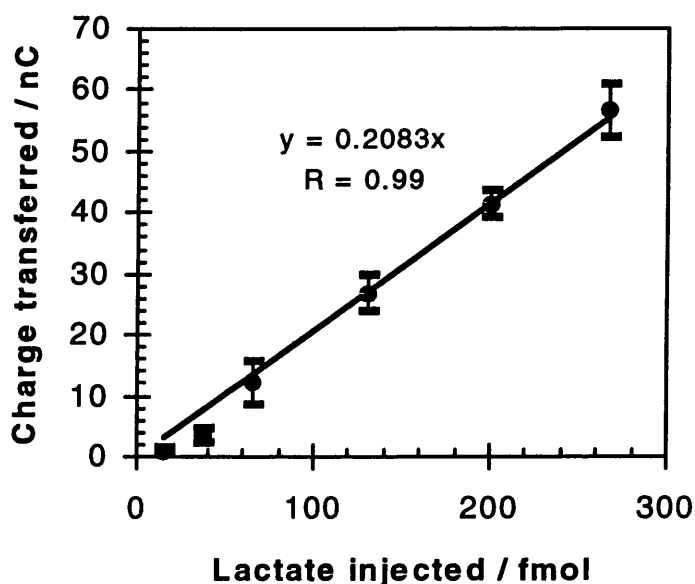


**Figure 4.15** Lactate calibration plot for the charge transferred vs. the injected lactate quantity. Each point was measured as a mean of three readings.

#### 4.4.3.3 The Non-Faraday Current

To account for the non-Faradic current, caused by injection pulse and perturbation of the electrode double layer, measurements were carried out by injection different volumes of lactate or just supporting electrolyte (buffer) into the pL volume well, under identical conditions (Figure 4.16). The background current was dependent on the volume injected, however the integral of the  $i/t$  curve was always less than 3% of the equivalent titre of lactate.

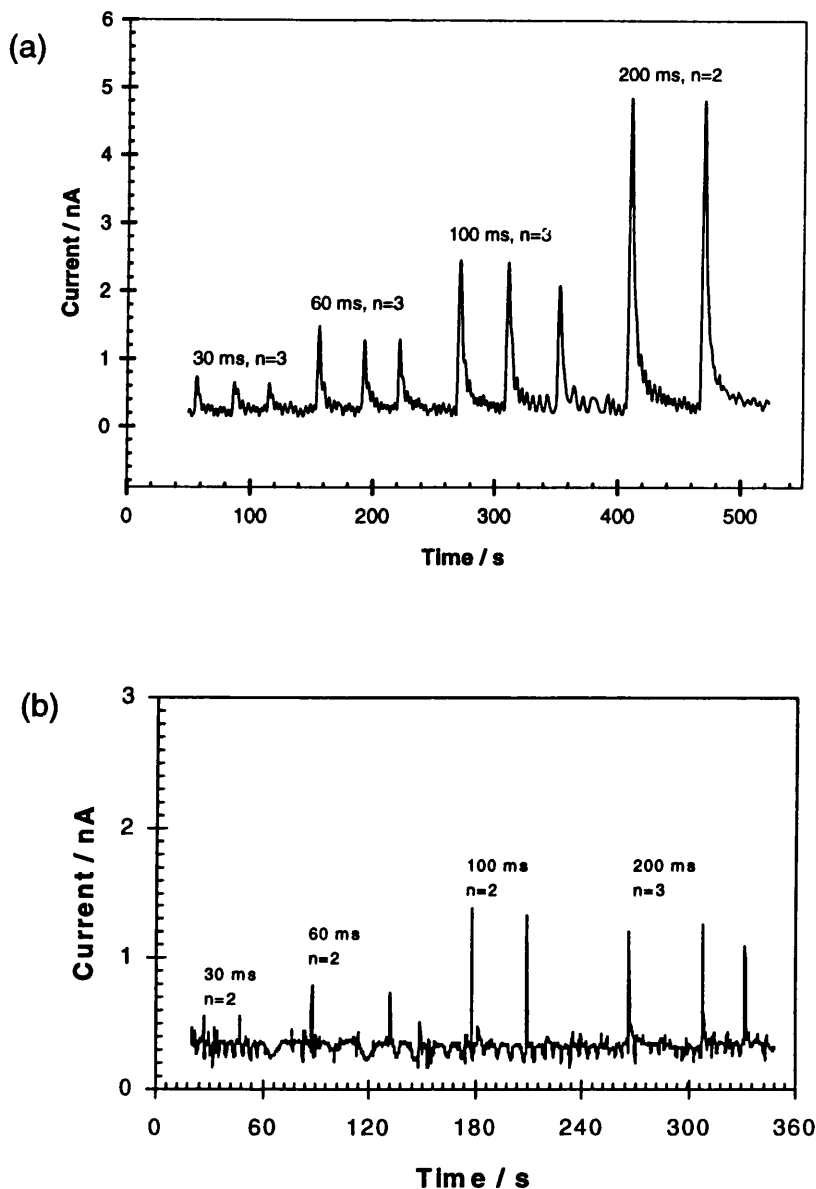


**Figure 4.16** Comparison of the response to lactate and the non-Faradic current, caused by injection pulse and perturbation of the electrode double layer. The device microchamber was filled with 360 pL KRB containing  $112 \text{ U ml}^{-1}$  LOD: (a) response to the injection of pL-scale lactate. 10 mM lactate was injected for 30 ms (1.5 pL,  $n=3$ ), 60 ms (3.7 pL,  $n=3$ ), 100 ms (6.5 pL,  $n=3$ ) and 200 ms (13.0 pL,  $n=2$ ); (b) response to the injection of supporting electrolyte (buffer) under identical conditions. The surface area of the working electrode was  $1250 \mu\text{m}^2$ .

#### 4.4.4 Micromachined Sensors with Enzyme Immobilisation

As depicted in Figure 4.17, the LOD/BSA biological membrane formed on the surface of the microelectrode confers both selectivity and protection from fouling. The membrane is transparent and mechanically rigid, adhered to the platinum black electrode. The thickness of the membrane was measured as between 2.0 ~ 3.0  $\mu\text{m}$  using a Dektak surface profiler. Additionally, a membrane system is able to improve the linearity and increase the biocompatibility of an enzyme electrode for blood lactate detection [48].

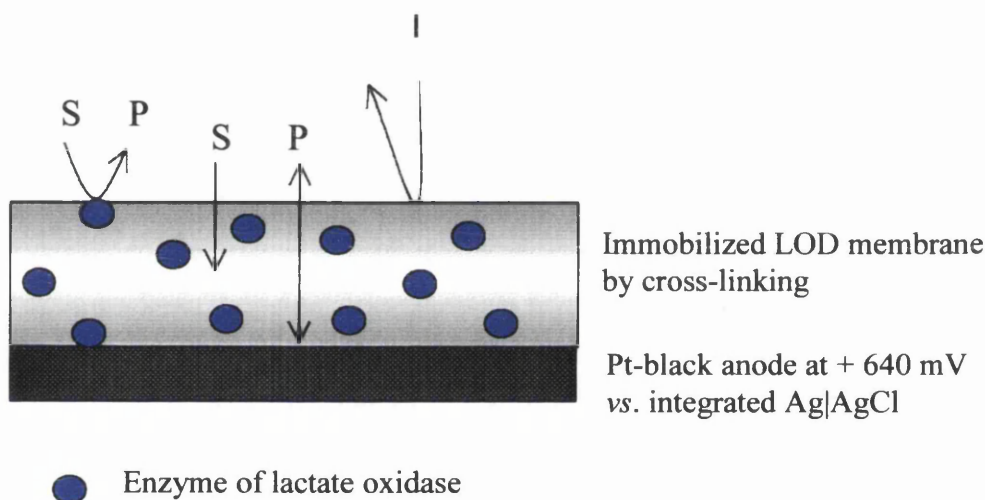


**Figure 4.17** Location of lactate oxidase covalently linked in a bovine albumin gel membrane, indicating the rejection of interference (I) and the conversion of substrate (S) of lactate to electro-active product (P) of  $\text{H}_2\text{O}_2$ .

##### 4.4.4.1 Typical Responses to Successive Additions of Lactate

A typical response of a device with an immobilised LOD membrane is shown in Figure 4.18. The working potential was held at +0.64 V vs. an internal Ag|AgCl reference. The device was soaked in 4.95 ml 10 mM stirring PBS (pH 7.4), then 50  $\mu\text{L}$  aliquots of lactate were successively injected into it. Figure 4.18 (a) shows the current-time behaviour of additions of lactate made at points (I) to (ix) for final lactate

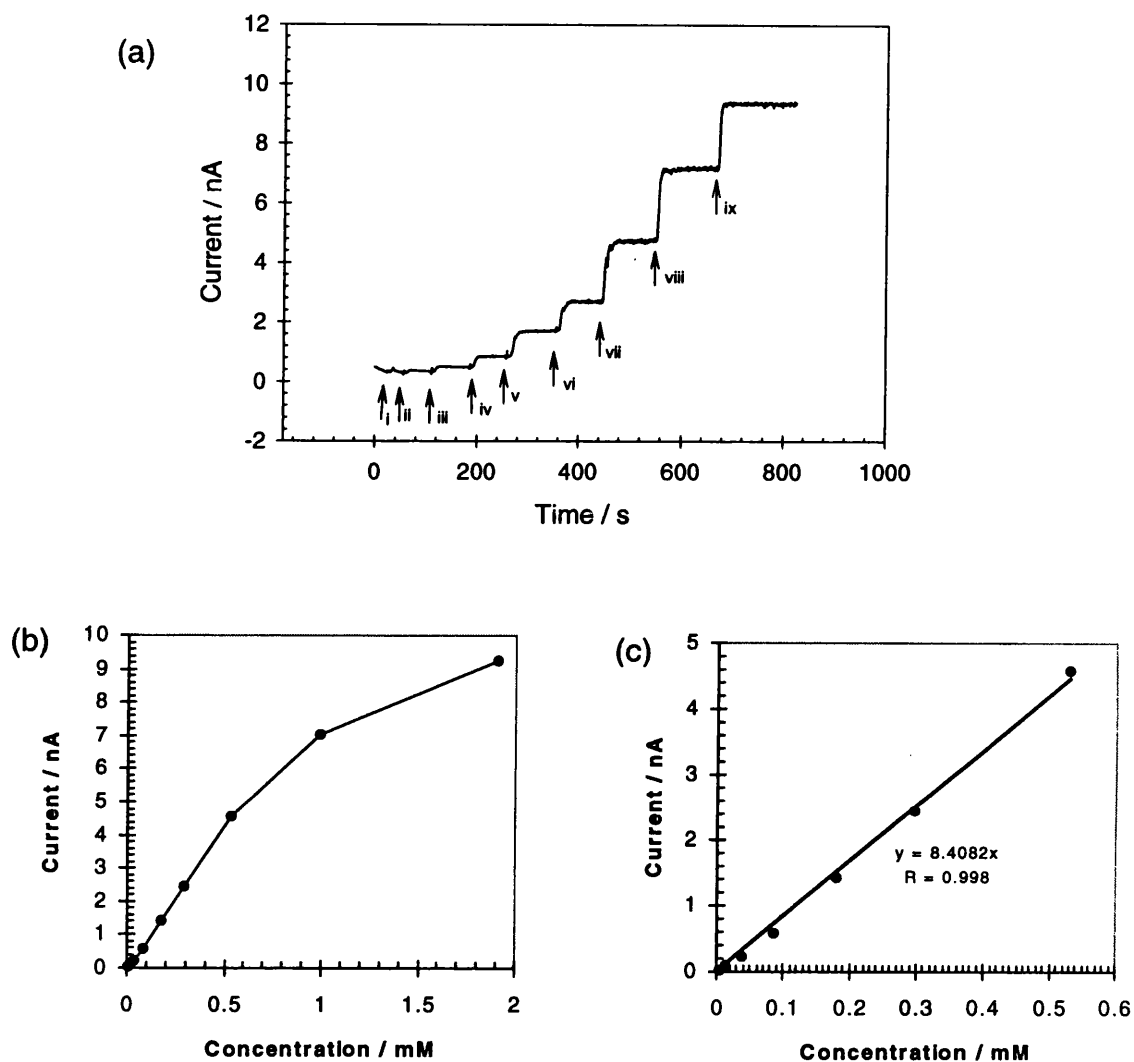


**Figure 4.18** Typical responses of a device with an immobilised LOD membrane. The working potential was held at +0.64 V vs. an internal Ag|AgCl reference. The device was soaked in 4.95 ml 10 mM stirring PBS (pH 7.4), then 50  $\mu$ L aliquots of lactate were successively injected into it: (a) the current-time behaviour of additions of lactate made at points (i) to (ix) for final lactate concentrations of 5  $\mu$ M, 13  $\mu$ M, 37  $\mu$ M, 85  $\mu$ M, 181  $\mu$ M, 298  $\mu$ M, 531  $\mu$ M, 994  $\mu$ M and 1.910 mM; (b) calibration curve of lactate detection. conditions as for (a); (c) linear plot in the concentration range between 5  $\mu$ M and 531  $\mu$ M lactate, obtained from (b). The surface area of the working electrode was 1250  $\mu$ m<sup>2</sup>.

concentrations of 5  $\mu\text{M}$ , 13  $\mu\text{M}$ , 37  $\mu\text{M}$ , 85  $\mu\text{M}$ , 181  $\mu\text{M}$ , 298  $\mu\text{M}$ , 531  $\mu\text{M}$ , 994  $\mu\text{M}$  and 1.910 mM. A steady current was obtained after each addition within 10 sec. The response time is almost same as the sensor without an LOD immobilised membrane. It can be seen that the LOD/BSA membranes (2 ~ 3  $\mu\text{m}$ ) had good permeability for lactate and  $\text{H}_2\text{O}_2$ . A calibration curve of the lactate detection is given in Figure 4.18 (b). In the concentration range between 5  $\mu\text{M}$  and 531  $\mu\text{M}$ , the plot is linear with correlation coefficient R of 0.998 and sensitivity of 8.4  $\text{nA mM}^{-1}$  (Figure 4.18(c)).

#### 4.4.4.2 Stability Testing

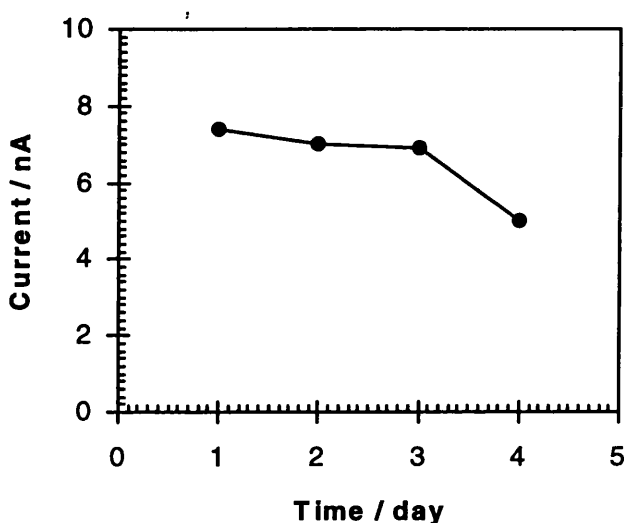


**Figure 4.19** shows the longevity study of a device with LOD immobilisation for 1 mM lactate measurement using normal bulk method. The surface area of the working electrode was 1250  $\mu\text{m}^2$ .

Stability testing, to assess the activity of both the immobilised enzyme and the working electrode, was carried out using the device with immobilised LOD membrane for lactate detection in PBS. The device was stored dry at 4  $^{\circ}\text{C}$  between testing. The temporal study for 1 mM lactate measurement using normal bulk method is represented in Figure 4.19. During the 4 days, the device was tested for different

concentrations of lactate in total about 16 times using normal bulk, “bulk” or low volume injection methods. The initial activity (or response) of the device was slightly higher when the immobilisation was just finished. The device remained active for at least 4 days. Interestingly, after cell testing on the 3<sup>rd</sup> day, the device retained the activity shown on the 2<sup>nd</sup> day. Clearly, the lysed cell and mineral oil did not foul the device, however the bare platinum black electrodes were completely fouled after cell experiments. The LOD/BSA membrane on the sensor seems promising for the future applications, such as flow injection analysis measurements and in vivo monitoring etc.

#### **4.5 Conclusions**

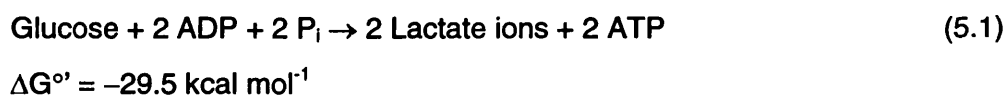
“Bulk” and pL-scale lactate measurements using the micromachined sensors has been carried out. The sensor was found to have an observed detection limit of 2  $\mu\text{M}$  with a model ‘bulk’ method and 4.4  $\mu\text{M}$  with a real bulk method. The resulting sensor, in 400 pL volume of FMCA, shows a different cyclic voltammogram at slow scan rates compared to a bulk response. The lactate sensor was characterised using a micro-injection system to dispense volumes as low as 1.5 pL producing a linear calibration curve for the charge transferred vs. the amount of injected lactate in the range, 15 to 266 fmol. This work will be relevant to the fields of cellular engineering and biosensors, and will be focus on the measurement of lactate in cell based assays. The methods described provide a generic method to make a wide range single cell sensors in pL-scale volumes based on oxidase-reductase enzymes and microfluidics to produce a lab-on-a-chip format. The LOD immobilised sensors had improved stability and prompt response, avoiding expensive enzyme strategies as a means to every measurement.

## Chapter 5: Dynamic Electrochemical Measurements of Lactate from Single Heart Cell

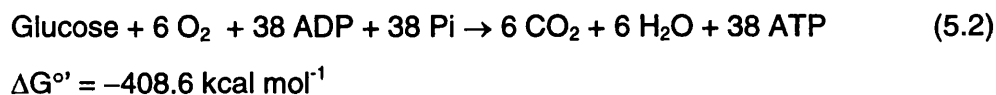
### 5.1 Introduction

#### 5.1.1 Lactate Metabolism and Ischaemia

The activities of a live cell demand both compounds of high-energy chemical potential, which can release energy quickly for performing work in the cell, and a pool of reduced compounds for synthesis of the compounds necessary for life (required for oxidation). Cellular oxidoreductions, through anaerobic and aerobic respiration, supply both these needs using cell nutrients [52]. The multi-step conversion of glucose to lactate ions is an exergonic and anaerobic process [53], described diagrammatically as pathway (a) in Figure 5.1. Two molecules of ADP are phosphorylated to ATP for each molecule of glucose metabolised. The overall reaction is expressed as follows,



in which,  $\text{P}_i$  is phosphate ion. The breakdown of glucose under aerobic conditions proceeds to a greater extent than under anaerobic conditions [53]. Pathway (b) in Figure 5.1 and Equation 5.2 show that the end products of aerobic oxidation are six molecules of carbon dioxide and six molecules of water for each molecule of glucose. Up to 38 molecules of ADP can be phosphorylated to ATP when one molecule of glucose is broken down completely to carbon dioxide and water. The net exergonic reaction for the complete oxidation of glucose and phosphorylation is shown below,



Note that more ATP is produced in aerobic oxidation of glucose than in anaerobic oxidation. The hydrolysis of ATP produced by breakdown (aerobic and anaerobic) of glucose can be coupled to endergonic processes, such as muscle contraction. This example process is central to the function of the myocyte.

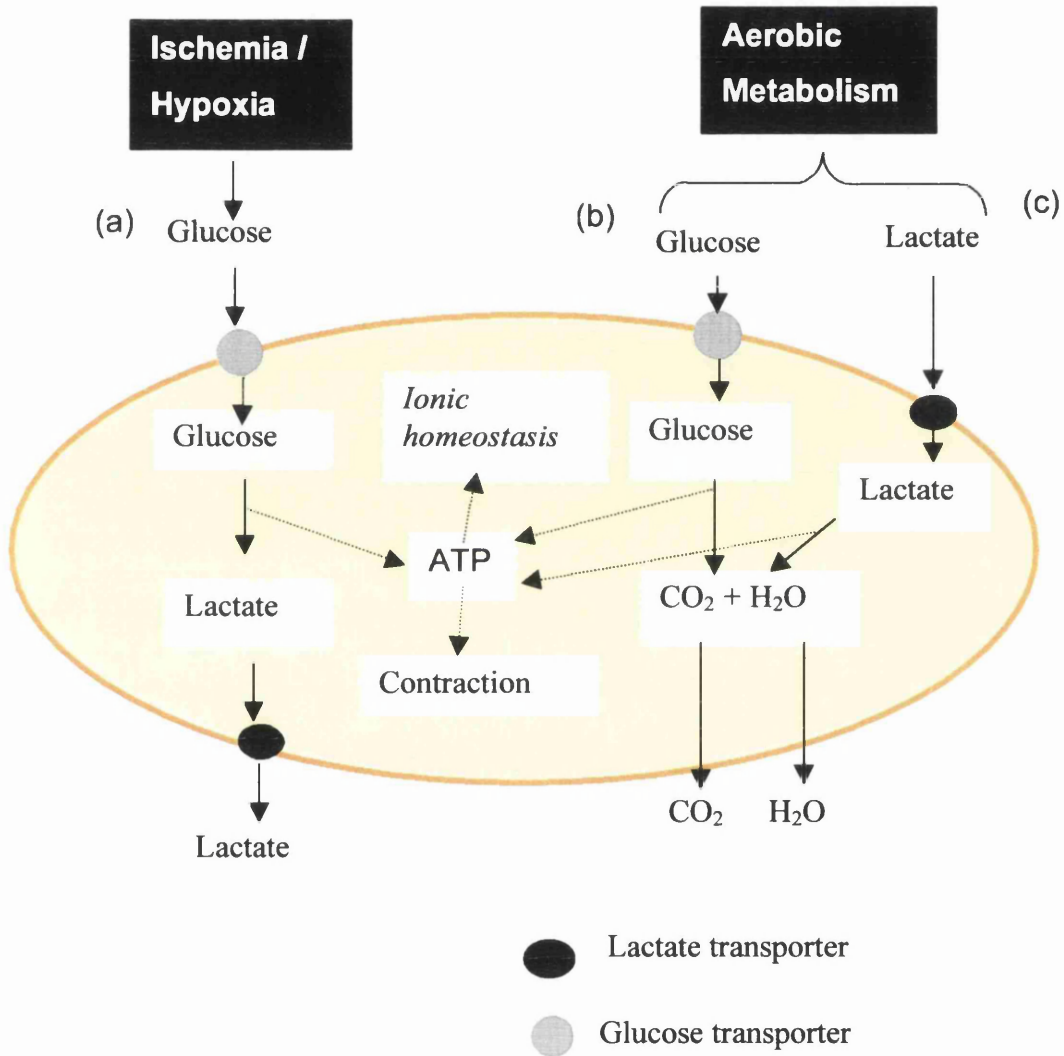


**Figure 5.1** Main metabolic pathways (a, b & c) of a muscle cell involving lactate transport across the plasma membranes.

Lactate has two established functions in the metabolism of the heart [46,54], one during aerobic metabolism and the other during anaerobic metabolism. First, during aerobic metabolism lactate is a normal myocardial fuel, which during certain conditions (such as, exercise) can account for the major part of the myocardial oxygen consumption. A supply of lactate appears to depend on competition with other myocardial fuels, especially free fatty acids. In this case, lactic acid must be rapidly transported into the cardiac myocytes for oxidation, as shown in pathway (c) in Figure 5.1. Secondly, during anaerobic metabolism or ischaemia, two molecules of lactate are produced for every glucose molecule consumed. The lactate must be transported out the cell if high rates of glycolysis are to be maintained. If efflux of lactic acid from the cell does not keep pace with production, intracellular concentrations increase and cause the pH of the cytosol to decrease. This leads to inhibition of both glycolysis and contraction [46,55,56]. In both instances lactate transport across the cardiac sarcolemma membrane is catalysed by a specific monocarboxylate/proton cotransporter (MCT) such as is found in the plasma membrane of a wide variety of cells [55]. Rates of efflux of lactate from a normoxic working heart may attain rates as high as  $5 \mu\text{mol min}^{-1} \text{g}^{-1}$  (dry wt) at an intracellular lactate concentration of  $\sim 2 \text{ mM}$ , whereas under hypoxia conditions these rates increase to  $60 \sim 70 \mu\text{mol min}^{-1} \text{g}^{-1}$  (dry wt) at an intracellular [lactate] of  $5 \sim 6 \text{ mM}$  [47].

Myocardial ischaemia, a condition in which for one of a variety of reasons coronary blood supply is insufficient to meet cellular energy demand, initiates a sequence of cellular changes that progresses through reversible damage and irreversible damage to cell death and tissue necrosis. The rate at which this process of evolving myocardial infarction occurs will be determined by the duration and severity of the ischaemia, and the size of the final infarct will be determined by the number of cells that become irreversibly damaged.

An increased lactate concentration in venous return from working muscle is considered a sign of cellular ischaemia [57]. In peripheral arterial disease, muscles are working under ischaemic conditions. Carlson and Pernow have compared arterial and venous lactate concentration in normal subjects and in patients with peripheral arterial

occlusive disease at rest and after different degrees of works [58]. There was no difference at rest between the subjects, the arterial and venous lactate concentrations at rest were about 1 mM in healthy subjects and in patients. After different degrees of work at 90 ~ 145 beats min<sup>-1</sup>, the arterial and venous lactate concentration increased to 2 ~ 4 mM in healthy subjects. In patients, the arterial lactate concentration increased to 3.5 ~ 5.5 mM and the venous lactate concentration increased to 4.5 ~ 7 mM.

In a second set of experiments, the coronary sinus of pigs was catheterized to monitor the effects of ischemia by coronary artery obstruction [59]. The lactate concentration rose sharply during reperfusion for a few minutes, reaching a maximum of 2.80 mM (from 2.3 mM) at 1 min after 5 min of ischaemia, 9.27 mM (from 1.43 mM) at 3 min after 15 min of ischaemia and 6.11 mM (from 1.14 mM) at 3 min after 45 min of ischaemia.

Both sets of test values [58,59] provide a guide to the expected level of intracellular lactate concentration (namely 1 ~ 2 mM during aerobic conditions and 2 ~ 10 mM after work in anaerobic conditions).

### 5.1.2 *The Anoxia Model*

As a model for anoxia, a single cell was poisoned by microinjecting carbonylcyanide *p*-(trifluoromethoxy)-phenylhydrazone (FCCP), cyanide or azide into the chamber. These substances inhibit aerobic glycolysis. The anaerobic system will then be used to generate ATP with the net production of lactate. Lactate production will be in proportion to the metabolic rate of the cell, i.e. quiescent cells will have a lower lactate output than cells that are actively contracting.

After a single injection of 50 μM FCCP and 10 mM 2-deoxyglucose for a metabolic poisoning protocol, single cell was allowed to contract to 50 ~ 70% of its original length, maintaining its rod-shaped morphology. This rigor-mediated contracture has been shown to occur simultaneously with a sudden lowering of cytosolic ATP levels [60]. Cell shape did not change after injection of saponin, which confirmed that

the cell was mostly or completely depleted of ATP [61]. ATP is required both to relax and contract the actin-myosin complex [62], and severe depletion of cytosolic ATP has been shown to accompany rigor-contraction [60].

### 5.1.3 Biocompatibility of $\mu$ -Analytical Systems

Before any molecules, materials, or devices can be used in conjunction with a biological system, whether cells or organisms, their effect on the system must be tested. Any substance which has no effect (at least in the time-scale tested) is termed biocompatible. Biocompatibility is a complex phenomenon: many substances are immediately toxic to all cells or organisms; some are toxic only to specific animals; other are harmful in the long-term (e.g. carcinogens - cancer causing); others, whilst not toxic, may cause marked changes in the normal behaviour of the system. The techniques of cell culture or tissue culture allow cells to be maintained outside the body. An enormous variety of plant and animal cells can be maintained *in vitro*.

Considering the device materials' biocompatibility for cell experiments, glass [63] and platinum [64,65] are in general considered to be biocompatible materials. For the biocompatibility of Ag|AgCl reference electrode, several studies have been reported [66,67]. Studies of Ag and AgCl implants in the brain of cats demonstrated local toxicity problems and a significant inflammatory response [67]. Ag|AgCl electrodes provoked loss of vascular smooth muscle contractility and a rapid dissolution of AgCl in the body fluids was suggested as the cause of these phenomena [66]. In those studies there was no work performed on assessing the stability of the potential of Ag|AgCl reference.

Velho et al. has studied the *in vitro* and *in vivo* stability of various reference electrodes [68]. They demonstrated that the Ag|AgCl electrode was the most successful in retaining a stable potential *in vivo* amongst the electrodes tested. Due to the importance of the reference electrode stability for long-term testing, the behaviour of the Ag|AgCl electrode coated with polyurethane or Nafion was examined [66,69]. Moatti-Sirat *et al.* reported a 10-day implantation of a glucose sensor using a polyurethane-coated Ag|AgCl reference with no apparent degradation of the reference

electrode [69]. The unprotected Ag|AgCl reference electrodes were rapidly degraded after subcutaneous implantation in rats, resulting a very significant shift in potential. However, these electrodes can be protected using polyurethane or thermally cured Nafion coatings [66]. This suggests that low-permeability membranes will reduce the dissolution of the AgCl layer.

#### *5.1.4 Other Designs for Cells Measurements*

An enzyme electrode for operation in a complex medium such as whole blood and cell media demands device biocompatibility and lifespan of both the working and the reference electrodes. The sensor surface will be a target for proteins, which will begin to adsorb within seconds after the initial contact with the medium [48]. Protein adsorption will decrease the activity of the electrode. In most cases, an enzyme electrode surface is made up of a mechanically protective biocompatible polymeric membrane to reduce, or preferably eliminate, its susceptibility to biofouling [66,8,48,70].

A two-electrode configuration, with a platinized working electrode and a combined reference and counter platinum electrode acting as a pseudo-reference electrode was used for hydrogen peroxide, purine detection and all single cell measurements [71]. This configuration without Ag|AgI or Ag|AgCl is simple, readily fabricated and also does not poison the cells. The main problem is its polarisation, which affects the potential stability of the pseudo reference and also introduces severe interference noise. Reducing the applied potential can help attenuate polarisation problems in the two-electrode configuration and using differential output methods allow the signal to be obtained. This configuration was also used for single cell measurements here.

## **5.2 Chemicals and Materials**

Lactate oxidase from *Aerococcus viridans* (LOD, EC 1.1.3.2, 39.1 Units/mg, Cat. No. 1381) was purchased from Genzyme Biochemicals (Kent, England). L(+)-Lactate

acid (sodium salt, Cat. No. L-7022), carbonylcyanide-*p*-(trifluoromethoxy)-phenylhydrazone (FCCP, Cat. No. C-2920), Saponin (Cat. No. S-4521) and Bovine Serum Albumin (BSA, Cat. No. A-4503) were obtained from Sigma (Dorset, England). Sodalime glass capillaries were supplied by Hilgenberg (Germany). SU-8 (SM 1060) was from SOTEC Microsystems (Renens, Switzerland).

BHKC13 cells (baby hamster kidney cells clone 13) were used as a model system for biocompatibility testing. The cells and cell culture solutions (Growth Medium, Hepes-Saline, Trypsin-Versene) and the various materials samples (silicon, germanium, gallium arsenide, gold sputtered onto glass, tissue culture plastic) were obtained from the Bioelectronics Undergraduate Laboratory [72] at the University of Glasgow.

The single heart cells measurement solution was Krebs-Ringer buffer (KRB) with the following composition: 120 mM NaCl, 20 mM Hepes, 5.4 mM KCl, 0.52 mM NaH<sub>2</sub>PO<sub>4</sub>, 3.5 mM MgCl<sub>2</sub>, 1 mM CaCl<sub>2</sub>, 11.1 mM glucose (add on day); titrated to a pH of 7.4 with 1 M NaOH. The single heart cells and cells media (Krebs solution) were from Institute of Biomedical and Life Sciences (IBLS) of Glasgow University and used within 28 hours of isolation. The Krebs solution was made of the following compositions: 120 mM NaCl, 20 mM Hepes, 5.4 mM KCl, 0.52 mM NaH<sub>2</sub>PO<sub>4</sub>, 3.5 mM MgCl<sub>2</sub>, 1 mM CaCl<sub>2</sub>, 11.1 mM Glucose, 20 mM Taurine, 10 mM Creatine and 0.1%BSA (weight ratio); titrated to a pH of 7.4 with 1 M NaOH. At all times, the Cl<sup>-1</sup> concentration was maintained at 138.9 mM. The Lactate solutions were made in KRB and were prepared immediately prior to their use.

Rabbit heart cells, called cardiocytes, are rod-shaped with a single central nucleus and fine elongate contractile striated fibrillates. Figure 5.2 shows that the cells are diverse in size. The myocyte volume was calculated by assuming a cell thickness of 10 μm and using the dimension of each cell. The mean cell volume was about 21 pL, ranging from 9 pL to 31 pL (mean = 21 pL, Sd = 6 pL, n = 8). In the media, many of the dispersed cells were “dormant”, healthy and attached to the substrate. Some of them were capable of spontaneous contraction.

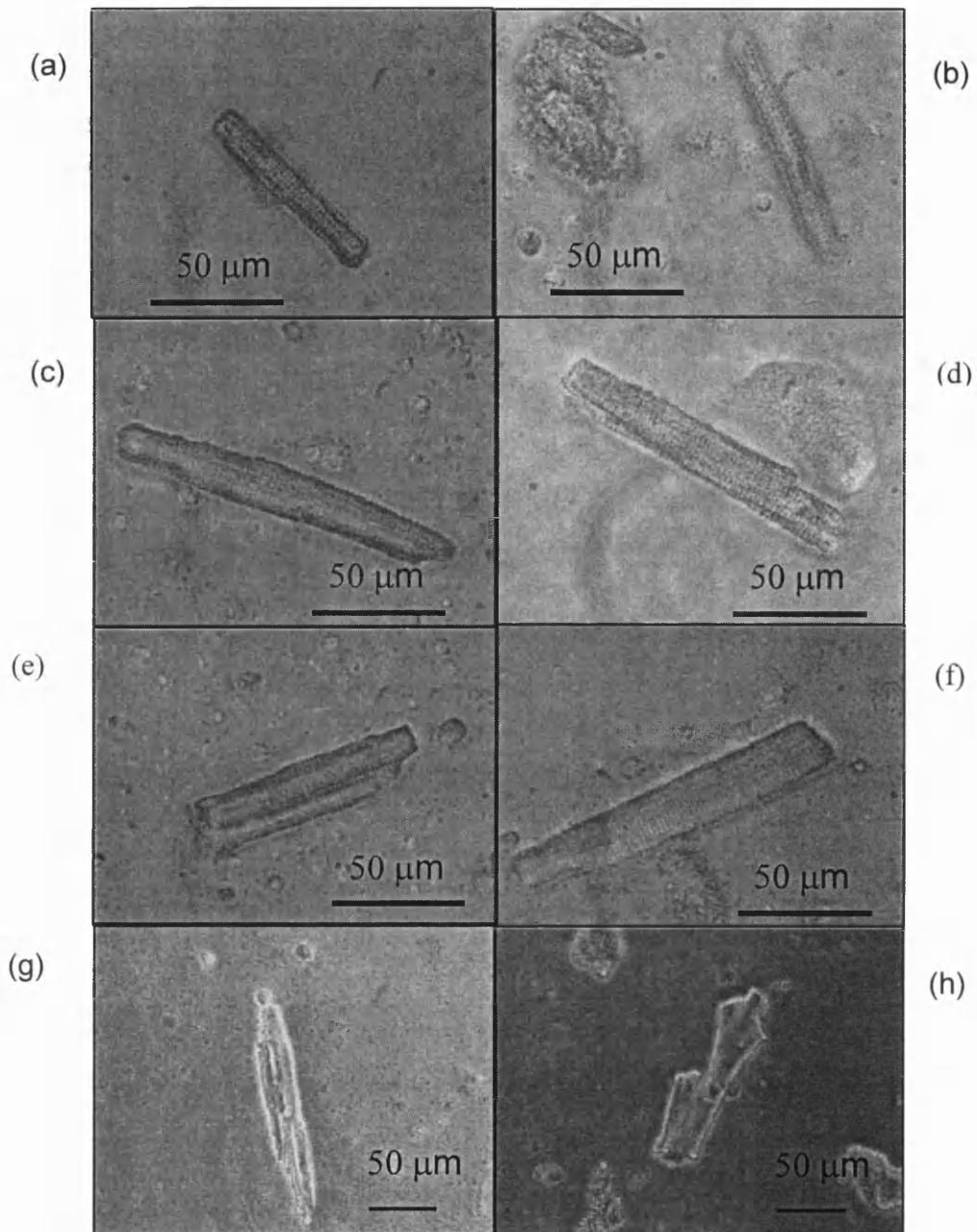


**Figure 5.2** Photographs of various different shapes of rabbit single heart cells. Sizes (mean = 21 pL, Sd = 6 pL, n=8) vary accordingly: (a) volume = 9 pL; (b) volume = 11 pL; (c) volume = 24 pL; (d) volume = 22 pL; (e) volume = 19 pL; (f) volume = 25 pL; (g) volume = 30 pL; (h) volume = 31 pL.

## 5.3 Methods

### 5.3.1 *Biocompatibility Measurements*

The biocompatibility of materials was tested simply, by observing whether the surfaces were suitable substrates for the attachment, spread and growth of cultured cells. The BHKC13 cells were isolated from embryos or from cell cultures. Under correct conditions, not only the BHKC 13 cells could survive, but also they can grow and multiply. However, the single heart cells isolated from the tissues of adult rabbit heart organism could not multiply except only survive for one or two days. Therefore, the BHKC13 cells were used for cell culture under the correct conditions, and their compatibility was tested. The necessary conditions were as follows:

The sample materials were first sterilised in a flow hood with ethanol to ensure that no bacteria or fungi were present. The samples were placed into petri dishes and covered with 1 ~ 2 ml of ethanol for 5 min. The ethanol was then decanted off and any excess ethanol allowed to evaporate. The sample materials were then washed with 1 ~ 2 ml of Hepes-Saline.

100 000 BHKC13 cells in 2 ml of growth medium were added to each petri dish. The cell growth medium, containing the nutrients (the correct balance of salts, an energy source, vitamins, amino acids and animal serum) necessary for cell growth, covered the sample materials. The petri dishes were then placed in a plastic box with a piece of damp tissue (preventing the medium drying out) and maintained at 37°C in an incubator for 48 ~ 161 hours. Cells growth was examined under a microscope (Nikon microscope, objective 10×, eyepiece 10×) for opaque samples or an inverted microscope (Nikon TMS, objective 10×, eyepiece 10×) for transparent samples.

### 5.3.2 *Single Heart Cell Experimental Protocol*

The protocol used to investigate the formation of lactate by single heart cells is described as follows:

After dry etching (Section 3.3.3), approximately 0.3  $\mu\text{l}$  of 200 U/ml LOD in fresh KRB was placed over the microchamber, then immediately covered with 30  $\mu\text{l}$  mineral oil, constrained within an epoxy ring wall (ring diameter 8-10 mm, wall width 2 mm and wall height 1 mm) to prevent bulk evaporation of the droplet.

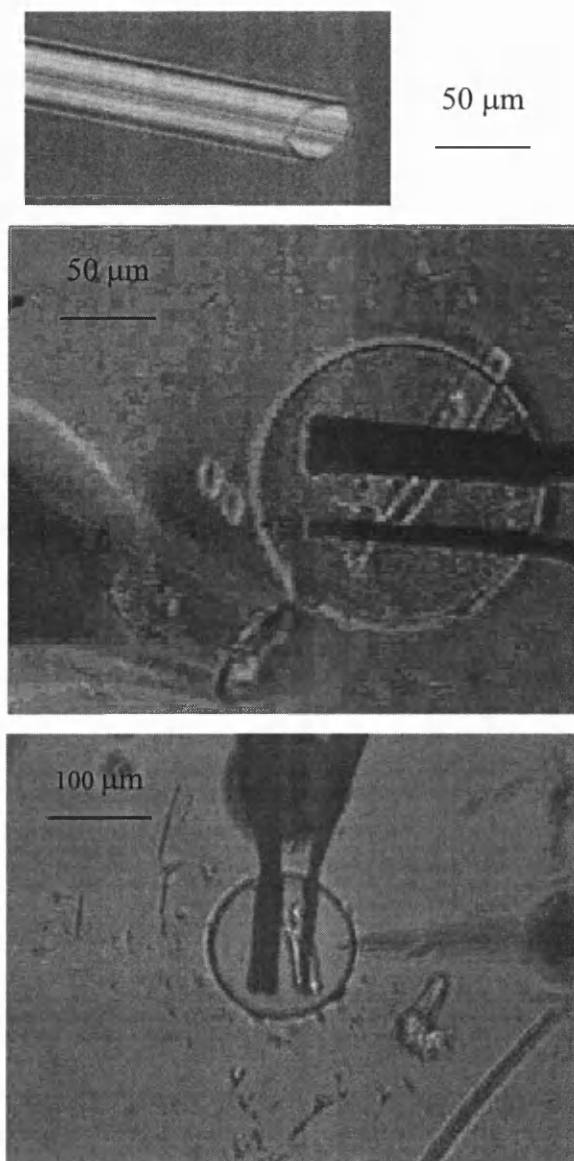


**Figure 5.3** Experimental myocyte manipulation: (a) photograph of the glass micropipette with a 30 ~ 40  $\mu\text{m}$  diameter tip for cell injection; (b) a single myocyte expelled from a pipette into the droplet over a device; (c) a fine tip pipette for drug microinjection positioned over a device microchamber, in which a myocyte is attached. Care was taken to avoid contact between the cell and the reference/counter electrode.

A sodalime glass pipette with a tip bore of approximately 30 ~ 40  $\mu\text{m}$  (Figure 5.3a), was soaked in 200 U  $\text{ml}^{-1}$  LOD in KRB and some media was sucked into the tapered region (ca. 1 cm length). This media slowed the rate of capillary filling when the pipette was placed into aqueous media for cell pipetting. The pipette holding the media was connected to one output port of the microinjection system (Section 4.3.3, Figure 4.1 & 4.2) and was positioned close to the end of a rod-shaped cell. As shown in Figure 5.3 (b), the myocyte was then ejected at 5 psi for 20 or 30 ms into the droplet over a device. Once the cell was inserted into the droplet, it was manoeuvred over the chamber by gently “sucking” with the pipette, and then allowed to sink to the bottom of the chamber. It was a distinct advantage to keep the cell moving continuously whilst positioning it into the microchamber in order to prevent cell attachment to the other parts of the device. The volume of the media was then reduced to the chamber volume by “sucking” with the same pipette. Finally, the working potential was applied to the working electrode.

A filament pipette (fabricated immediately prior to their use) with a fine tip (700 nm in diameter, Figure 4.2b) was then back filled with the reagent and an injection pressure of 15 psi was used for dispensation of pL volumes. The pipette, connected to the second output port was used to deliver aliquots of reagent in picolitres (Figure 5.3c). All output pressures and shot times were regulated. Injection was triggered using a foot switch. When required, metabolic inhibition was imposed by injecting a freshly prepared carbonyl cyanide-*p*-(trifluoromethoxy)-phenylhydrazone (FCCP, dissolved in ethanol as 40 mM stock solution and stored at 4 °C, then diluted in aqueous media at 1:40 for 1 mM) to a concentration of 15  $\mu\text{M}$ . After 10 ~ 15 min, the membrane of the cell was then permeabilised using saponin at a concentration of ~ 80  $\mu\text{g/ml}$  to release the intracellular contents. After the lactate response had returned to a nominal baseline current, a calibration of 65 fmol (100 ms, 15 psi, 10 mM) lactate was injected. In order to eliminate the injection noise from the measurements (*i.e.* the effect from double layer, electrode polarization and injection pulse), FCCP or/and saponin were injected again using the same conditions after the cell balled and died. This was then subtracted from the measurement to give a measurement termed “differential output analysis”.

At the end of the experiment, the chamber and device surface was washed using reverse osmosis (R.O.) water and ethanol, the cell debris was removed and the device

dried using nitrogen gas. The electrodes were subsequently cleaned by the RIE process. The measurements were performed at  $23 \pm 0.5$  °C.

## 5.4 Results and Discussion

### 5.4.2 Biocompatibility of Various Materials

#### 5.4.2.1 Biocompatibility of Conventional Microfabrication Materials

Gold [63,65], glass [63], silicon [65,73], silicon nitride [64], platinum [64,65] and platinized platinum [67] are, in general, considered to be biocompatible materials. Meanwhile, copper [65], iron [65] and silver [65] are considered as toxic materials. The devices used here have an SU-8 chamber wall, a glass bottom with 2 electrodes (a platinized platinum working electrode and a Ag/AgCl reference electrode), or with 3-electrodes (a platinized platinum working electrode, a Ag/AgCl reference electrode and a gold/platinum counter electrode). Much less is known about SU-8's biocompatibility. A culture test was therefore carried out to test the biocompatibility of SU-8 device (processed using dry etching) and compared with the biocompatibility of conventional microfabrication materials, i.e. gold (Au), silicon (Si), indium-tin oxide (ITO), germanium (Ge), gallium arsenide (GaAs) and tissue culture plastic (a specially treated polystyrene).

Figure 5.4 shows the results cell growth on the different samples after 48 hours in culture. Cells attached and spread on most substrates except GaAs, which is toxic for cell culture. Figure 5.4(a) shows the cells were dead and "balled". The cells grew to a higher density on tissue culture plastic (Figure 5.4b), which was specially treated using dry etch (oxygen). The surface of the polystyrene is more active as it has a more hydrophilic character after etching. Gold, silicon, germanium and indium-tin oxide and SU-8 were suitable for cell culture growth (Figure 5.4(c)-(g)). After 105 hours in culture, the cells multiplied, attached and spread on SU-8 substrate (Figure 5.5a). The cells achieved confluence both on SU-8 and gold after 161 hours in culture, i.e. the cells have filled the available space and the rate of cell division decreased (Figure 5.5(b) and (c)). Therefore it could be concluded that SU-8 is suitable for use with this type of cultured cells and could be considered biocompatible in the context of experiments, which last only 1 or 2 hours.

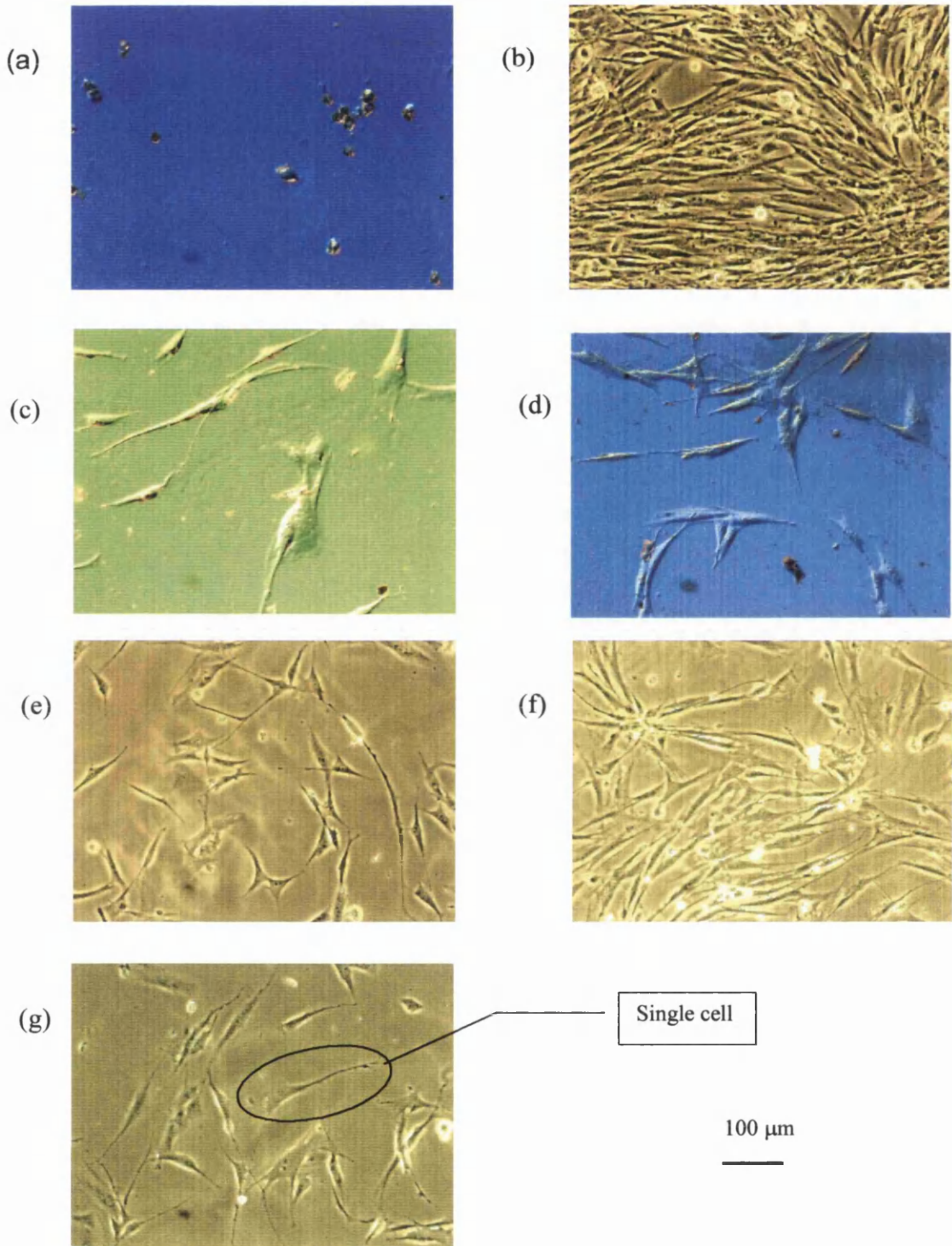


**Figure 5.4** shows BHKC13 cells attached and spreaded onto different substrate materials after 48 hours incubation at 37°C. (a) GaAs; (b) specially-treated polystyrene, *i.e.* tissue culture plastic; (c) gold; (d) silicon; (e) germanium; (f) indium-tin oxide; (g) SU-8.

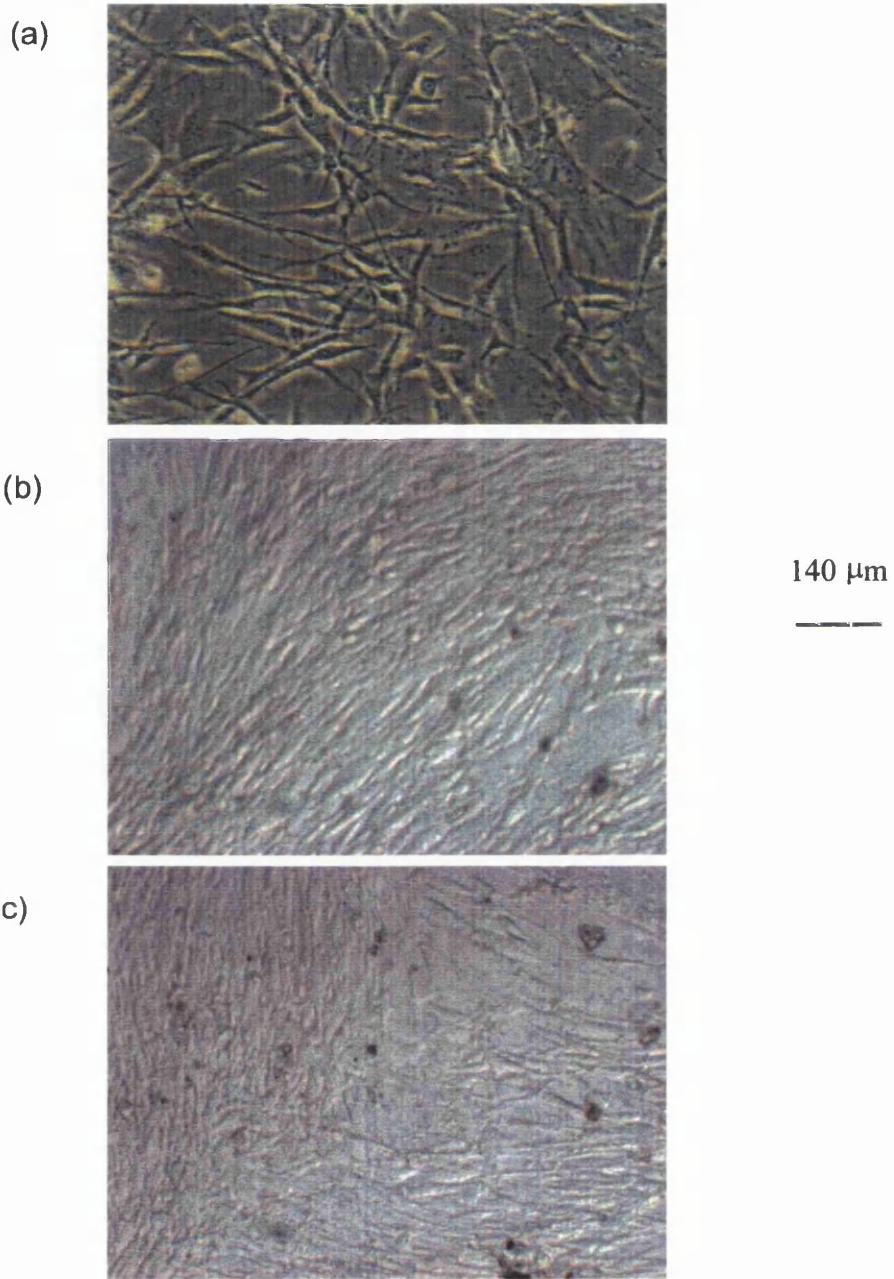


**Figure 5.5** BHKC13 cell growth on different substrate materials after incubation at 37°C. Accordingly on: (a) SU-8 for 105 hours; (b) SU-8 for 161 hours; (c) gold for 161 hours.

#### 5.4.1.2 Poor Biocompatibility of Ag|AgCl Electrode

Optical microscopy of a single myocyte poisoned directly in contact with an Ag|AgCl pseudo reference inside a microchamber device is shown in Figure 5.6. This situation provoked fast beating and contractility causing the cell to die within 2 min 30 sec. A healthy rod shaped myocyte was injected at 5 psi for 20 msec onto the Ag|AgCl reference electrode, causing fast beating and contracture (Figure 5.6(a)). Figure 5.6(b) and (c) then show shortening of the cell over a period of two minutes, until finally, Figure 5.6(d) shows the myocyte balled up rapidly after 2 min 30 sec beating and contracture. This severe reaction is consistent with the poor biocompatibility of the Ag|AgCl electrode.

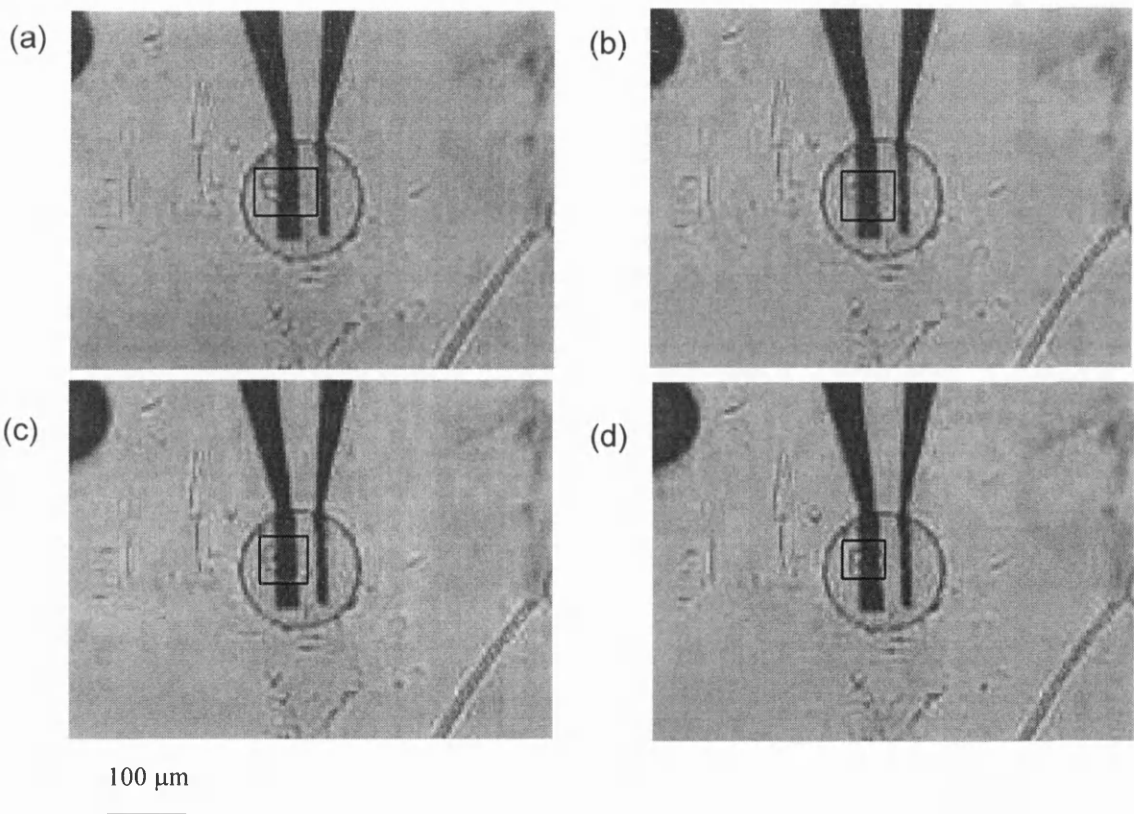


**Figure 5.6** Optical microscope images of a single myocyte in contact with a Ag|AgCl pseudo reference within a microchamber, filled with 400 pL KRB solution (with 11 mM glucose): (a) a healthy rod shaped myocyte was just injected onto the Ag|AgCl reference electrode. This resulted in a fast beating and contracture; (b) the same myocyte, after 1 min beating and contracture, with a shortened length; (c) the same myocyte, after 2 min beating and contracture, with a further shortened length; (d) after 2 min 30 sec beating and contracture, the myocyte balled up rapidly.

Direct contact of the strongly oxidizing AgCl layer with a single myocyte causes the myocyte die promptly. Meanwhile, the dissolution of AgCl into the microchamber can also cause a local toxicity problem with a slower reaction compared with the direct contact. Figure 5.7 shows optical microscope images of single myocytes inside a microchamber with 400 pL KRB solution (containing 11.1 mM glucose). A healthy rod shaped myocyte was injected (at 5 psi for 20 ms) onto the platinum black electrode and then lay “dormant” for 8 min after the injection. As AgCl dissolution into the microchamber continued, the cell started beating slowly at 8 min and moved onto the Ag|AgCl reference at 11 min, here, it started a faster beating and contracture due to the direct contact with the Ag|AgCl electrode. The myocyte balled up rapidly after 14 min.

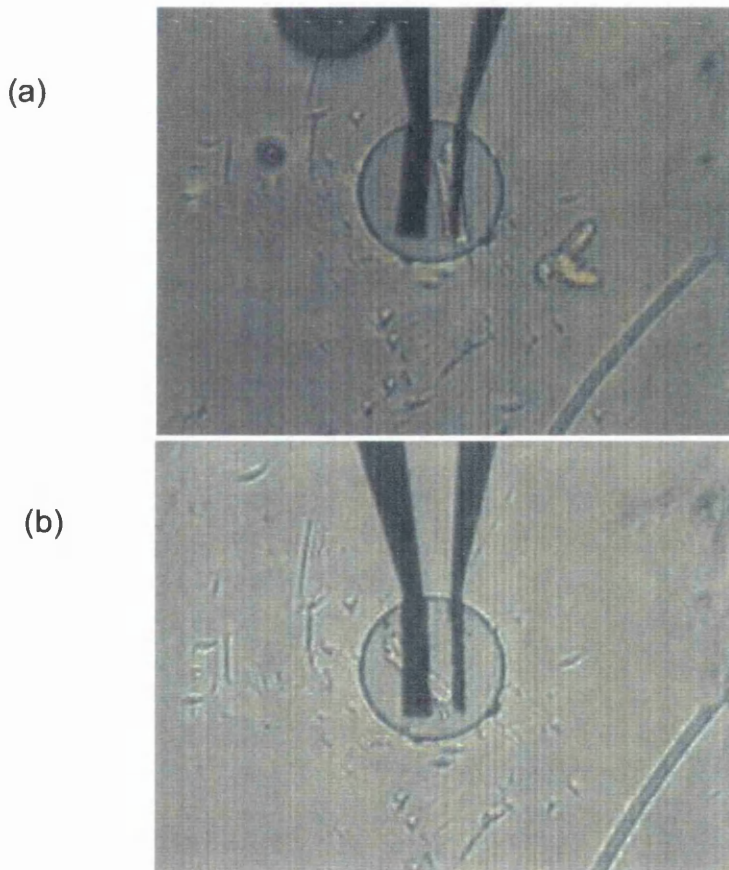


**Figure 5.7** Optical microscope images of single myocyte cells inside a microchamber device, filled with 400 pL KRB solution (with 11 mM glucose): (a) a healthy rod shaped myocyte injected onto the platinum black electrode. After lying “dormant” for 8 min, it started a slow beating; (b) the same myocyte after slow beating for a further 3 minutes, moved onto the Ag|AgCl reference and started beating more quickly and contracture. The myocyte “balled-up” rapidly after 14 min.

#### 5.4.1.3 Prevention of the degradation of AgI/AgCl

A LOD/BSA membrane was coated on the microelectrodes in order to reduce the dissolution of the AgCl layer, similar to the procedure used to coat a lactate oxidase–bovine serum albumin (LOD/BSA) membrane onto microelectrodes described in Section 4.3.3. This prevented reference polarization and direct contact of the AgI/AgCl electrode with a myocyte. The lifespan of a myocyte in microchamber with such a membrane was examined. A healthy rod shaped myocyte was injected (at 5 psi for 20 ms) across the modified AgI/AgCl reference electrode within the chamber of the device. The cell lay “dormant” as a healthy myocyte for 40 min. Subsequently it started beating slowly but kept an unchanged length until after 1.5 hours. Compared with the uncoated device, the myocyte reaction to AgI/AgCl decreased and the lifespan of the cell in the modified device increased, indicating an improved biocompatibility of the coated device.

#### 5.4.2 *Single Rabbit Heart Cells Permeabilised with Saponin in Bulk Solution*

The rod-shaped cell membrane integrity could be breached by permeabilization with saponin, which caused the cell to contract and round up quickly, for lactate to be released from the cell (Figure 5.8 and Figure 5.9). Saponin was injected into the myocytes Krebs solution to a final concentration of 80 µg/ml. The duration from the addition of saponin to cell balling up was variable for different cells. The duration for the “dormant” cell in Figure 5.8 was approximately 52 sec, and the duration for a slow beating cell in Figure 5.9 was approximately 81 sec.

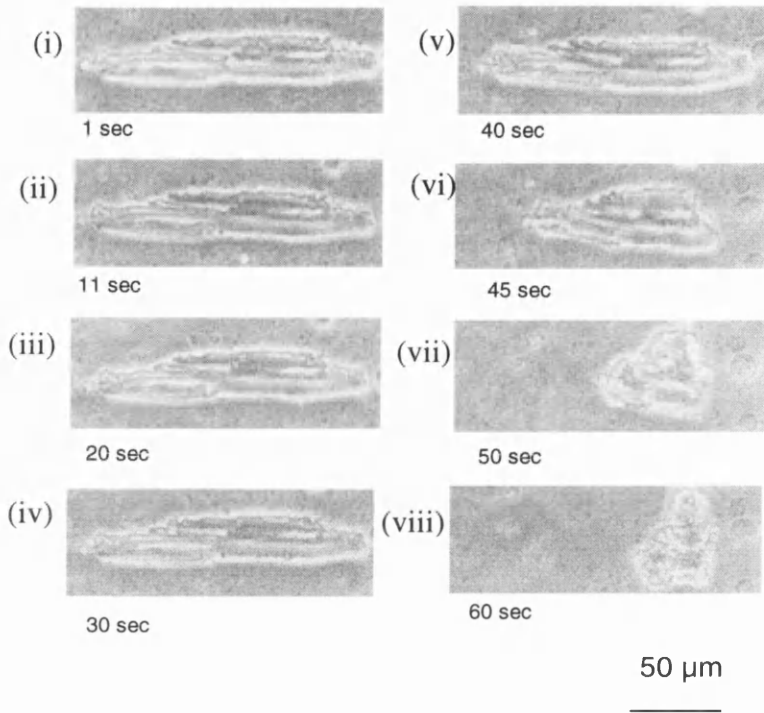


**Figure 5.8** A healthy “dormant” myocyte was permeabilised with saponin. The images show the length of the initially rod-shaped myocyte (i) prior to (ii) ~ (viii) after injection of the saponin (after 8 secs to a concentration of 80  $\mu\text{g/ml}$ ).

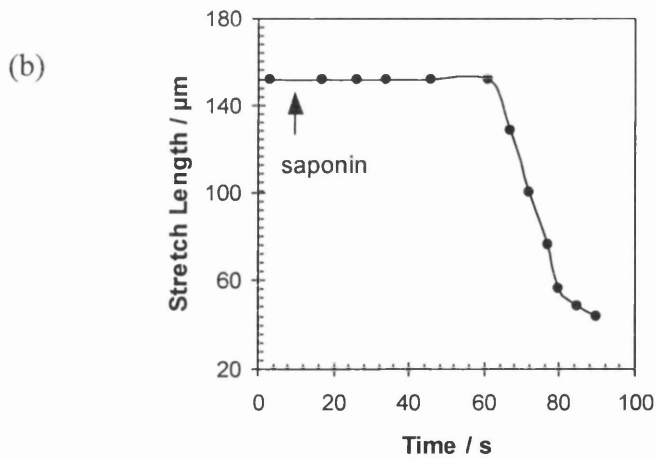
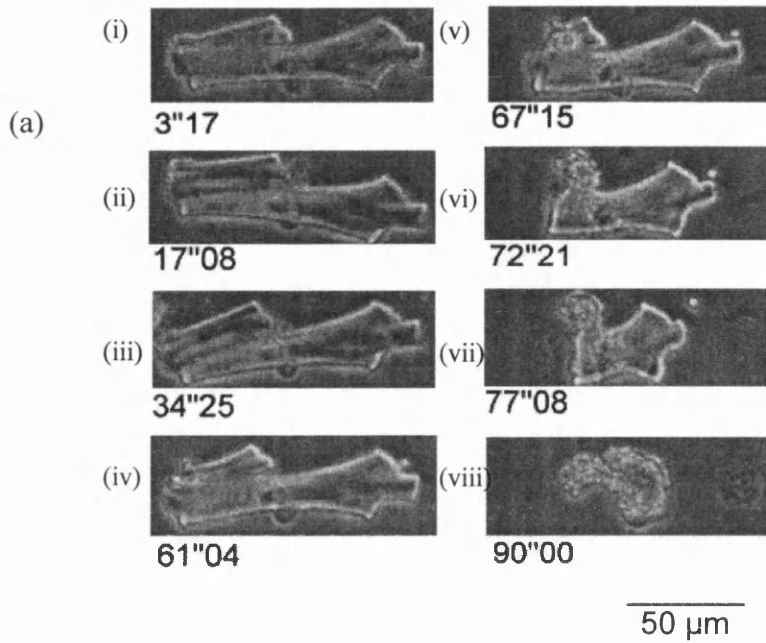


**Figure 5.9** A healthy beating single myocyte was permeabilised with saponin: (a) images showing the length of the myocyte (i) before and (ii) ~ (viii) after the addition of saponin (at 9 sec to a concentration of 80  $\mu\text{g/ml}$ ); (b) cell length is shown as a function of time.

### 5.4.3 Lactate Responses From Single Heart Cells

#### 5.4.3.1 Lactate Efflux from Single Heart Cells in Contact with AgI/AgCl References

As demonstrated in Section 5.4.1.2, direct contact of the AgI/AgCl reference with a single myocyte can cause the myocyte to die promptly, due to the poor biocompatibility of AgI/AgCl electrode. A myocyte was placed in contact with the AgI/AgCl reference directly and was provoked into fast beating and high contractility. The cell shortened and balled up rapidly releasing lactate (Figure 5.10), giving rise to a lactate signal corresponding to a mean content of 36.0 fmol, at a mean intracellular concentration of 1.8 mM ( $36.0 \pm 7.5$ ,  $n=3$ ; concentration  $1.8 \pm 0.3$  mM). The signal obtained at the onset of shortening, increased gradually until the cell balled up and decreased gradually as lactate was consumed.

#### 5.4.3.2 Lactate Responses from Healthy Aerobic Cells without FCCP

The lactate response from healthy cells without FCCP was evaluated using two methods. Firstly, lactate release from a single myocyte during cell shortening and balling up after the cell was punctured by the tip (outer diameter  $< 1 \mu\text{m}$ ) of a glass micropipette. Secondly, lactate release from a single myocyte was measured after the cell was permeabilised by the detergent saponin. As the cells can be easily poisoned by the reference electrode of AgI/AgCl, a platinum pseudo reference/counter was also used in the second method.

Figure 5.11 shows the electrochemical response when lactate was released from a myocyte after piercing the cell wall with the extruded tip of glass micropipette. Meanwhile, the cell was provoked into actively contracting and fast beating, which may introduce a higher lactate output due to the higher metabolic rate of the cell in this state when compared to that of a quiescent or weakly contracting cell. The lactate signal corresponds to a mean content of 60.0 fmol, at a mean intracellular concentration of 2.4 mM ( $60.0 \pm 17.1$  fmol,  $n=2$ ; concentration  $2.4 \pm 0.7$  mM).

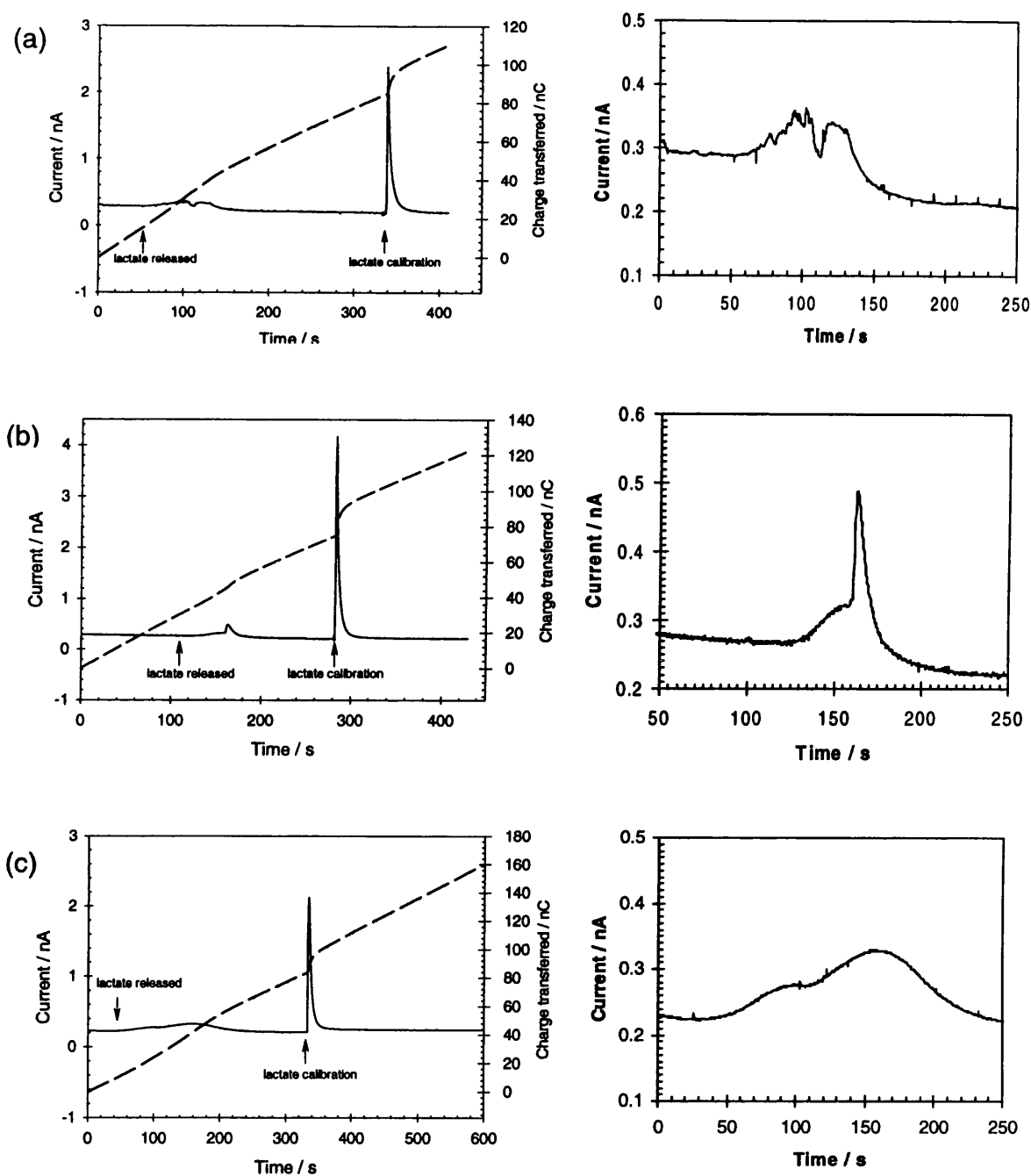


**Figure 5.10** Lactate released from a single myocyte after direct contact with an Ag|AgCl reference electrode, provoked fast beating and contractility. Current response was shown in solid line (left axis) and the related charge transferred was shown in short dash line (right axis). Chamber was filled with 400  $\mu\text{L}$  200 U/ml LOD in fresh KRB. Lactate calibration signal was obtained by injection of  $\sim 6.5 \mu\text{L}$  of 10 mM lactate. Platinised working electrode was poised at 0.64 V vs. an integrated Ag|AgCl pseudo-reference/counter. (a) to (c) are repeats of the same protocol (left) with the area of the graph around the lactate release magnified (right). The surface area of the working electrode was  $1250 \mu\text{m}^2$ .

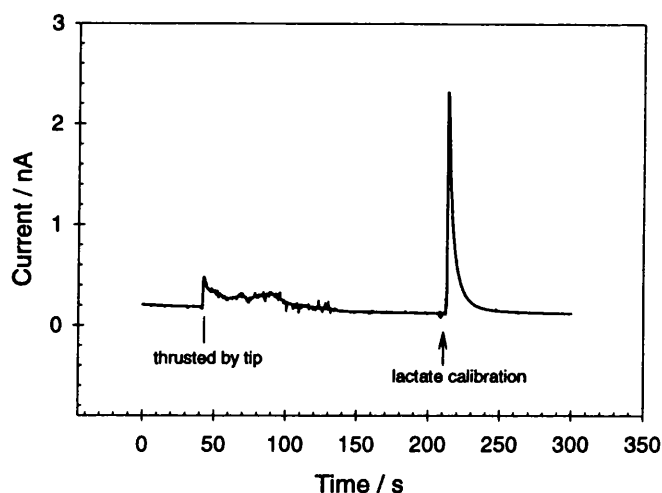


**Figure 5.11** Lactate released from a single myocyte in a 400 pL chamber during cell shortening and balling up after piercing of the cell wall using the extruded tip (outer diameter <math>< 1 \mu\text{m}</math>) of a glass micropipette. A lactate calibration signal was obtained by injection of  $\sim 6.5$  pL of 10 mM lactate. The platinised working electrode was held at 0.64 V vs. an integrated Ag|AgCl pseudo-reference electrode. The surface area of the working electrode was  $1250 \mu\text{m}^2$ .

Figure 5.12 shows the differential output of lactate released from a single myocyte after the cell was permeabilised by the detergent saponin. Here, the platinised working electrode was held at 0.64 V vs. an integrated Ag|AgCl pseudo-reference electrode. The chamber was filled with 400 pL 200 U/ml LOD in fresh KRB. Saponin was injected to concentration of  $\sim 80 \mu\text{g ml}^{-1}$ , upon which the cell immediately shortened and balled. A lactate calibration signal was obtained by injection of  $\sim 6.5$  pL of lactate (10 mM). The lactate signals by saponin obtained correspond to a mean content of 34.0 fmol, at a mean intracellular concentration of 1.6 mM ( $34.0 \pm 8.0$ ,  $n=4$ ; concentration =  $1.6 \pm 0.3$  mM).

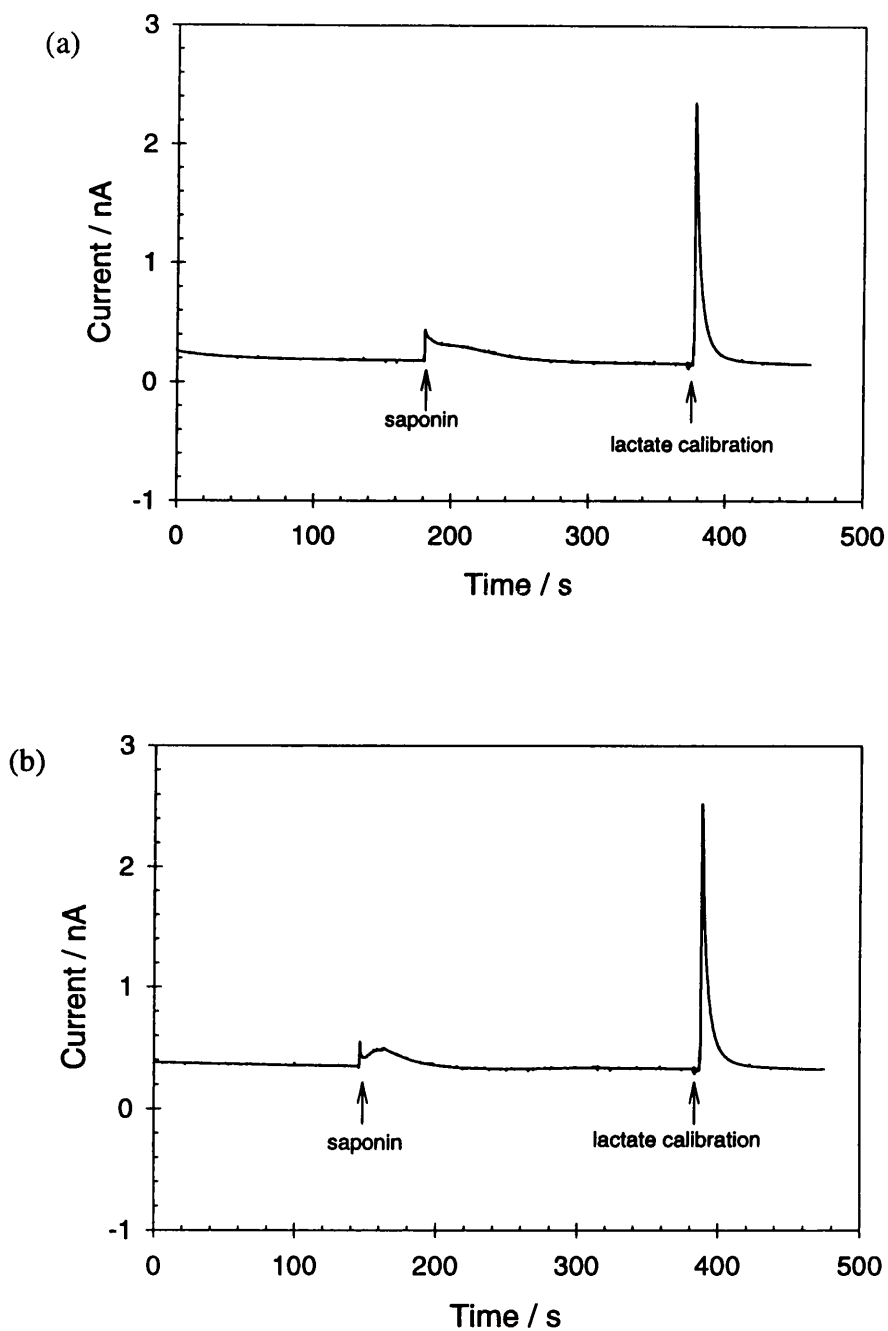
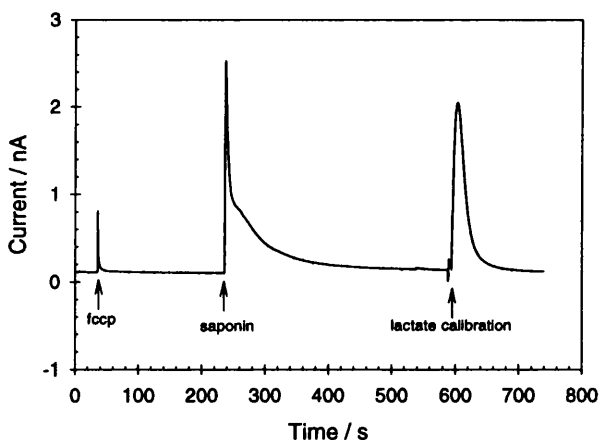


**Figure 5.12** Differential output of lactate released from a single myocyte after the cell was permeabilised by the detergent saponin. The platinised working electrode was held at 0.64 V vs. integrated Ag|AgCl pseudo-reference electrode. Saponin was injected to  $\sim 80 \mu\text{g ml}^{-1}$ , at which the cell immediately shortened and balled. Lactate calibration signal was obtained by injection of  $\sim 6.5 \text{ pL}$  of 10 mM lactate. (a), (b) are repeats of the same protocol. The surface area of the working electrode was  $1250 \mu\text{m}^2$ .

### 5.4.3.3 Lactate Responses from Anoxic Cells with FCCP

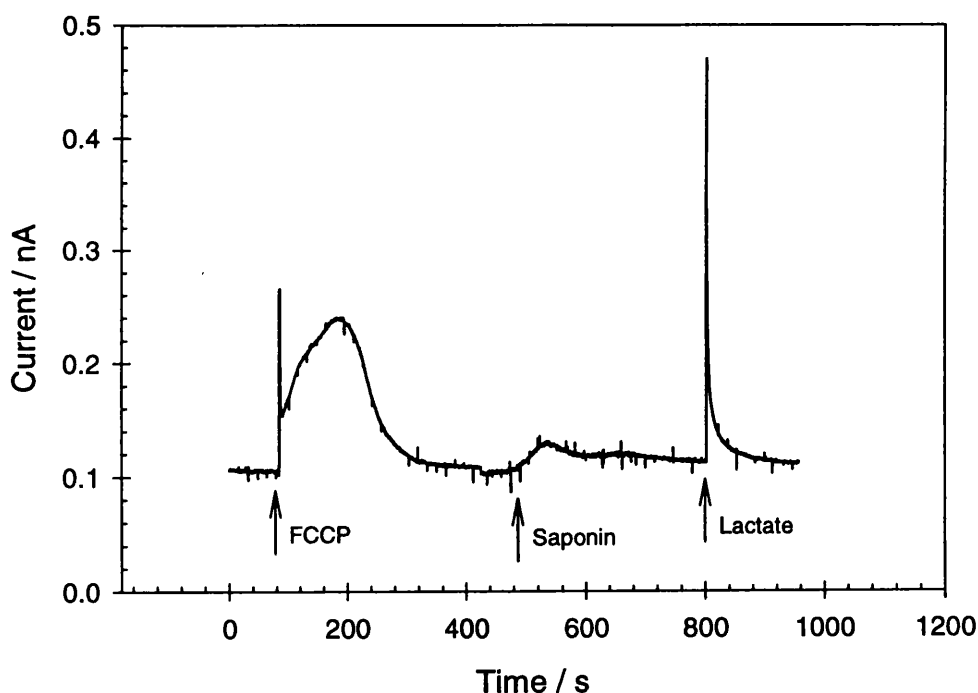
In order to produce a model for anoxia, a single cell was poisoned by microinjecting carbonylcyanide *p*-(trifluoromethoxy)-phenylhydrazone (FCCP) into the chamber, inhibiting aerobic glycolysis. The anaerobic system will then be used to generate ATP with the net production of lactate.

Figure 5.13 shows the differential output of lactate generation by a single rabbit myocyte, (in a 400 pL chamber), permeabilised after metabolic inhibition, imposed by injecting FCCP (to  $\sim 15 \mu\text{M}$ ). The platinised working electrode was held at 0.64 V vs. an integrated Ag|AgCl pseudo-reference electrode. During the metabolic inhibition, the cell contracted only slightly, however, lactate efflux was not observed. The cell membrane was then permeabilised using saponin to a final concentration of  $\sim 80 \mu\text{g ml}^{-1}$ , at which the cell immediately shortened and balled. A lactate calibration signal was obtained by injection of  $\sim 6.5 \text{ pL}$  of 10 mM lactate. The lactate signals after the addition of saponin correspond to a mean content of 106.7 fmol, at a mean intracellular concentration of 5.0 mM ( $106.7 \pm 17.0$ ,  $n=3$ ; concentration  $5.0 \pm 1.1 \text{ mM}$ ).



**Figure 5.13** Electrochemical detection of lactate generation by a single rabbit myocyte ( $\sim 25 \text{ pL}$ ) (in a 400 pL chamber) permeabilised after metabolic inhibition, imposed by injecting FCCP to  $\sim 15 \mu\text{M}$ . A platinised working electrode was poised at 0.64 V vs. an integrated Ag|AgCl pseudo-reference electrode. During the metabolic inhibition, which lasted 200 sec, the cell contracted a little. The cell membrane was then permeabilised using saponin to a final concentration of  $\sim 80 \mu\text{g ml}^{-1}$ , upon which the cell immediately shortened and balled. Lactate calibration signal was obtained by injection of  $\sim 6.5 \text{ pL}$  of 10 mM lactate. The surface area of the working electrode was  $1250 \mu\text{m}^2$ .

As the cells can be easily poisoned by the reference electrode of Ag/AgCl, a platinum pseudo-reference/counter was also used allowing time for metabolic inhibition. The applied potential was reduced to 0.15 V in an attempt to decrease the amount of polarisation [12]. Figure 5.14 shows the efflux of lactate measured in real time after injecting FCCP at high concentration of 150  $\mu\text{M}$ . During the metabolic inhibition the shape of the cell did not alter significantly and the efflux lactate level increased to a peak and no further lactate generated as the severe depletion of ATP, which is too low to prime the first steps in glycolysis. The total lactate efflux is about 658 fmol in 7 min and the efflux rate is 97  $\text{fmol min}^{-1}\text{cell}^{-1}$ . A higher efflux of lactate was also measured at higher FCCP concentration of about 200  $\mu\text{M}$ , with a total lactate efflux of 3738 fmol in 15 min, i.e. 252  $\text{fmol min}^{-1}\text{cell}^{-1}$ .



**Figure 5.14** Lactate efflux from a single rabbit myocyte (25 pL) in a 400 pL chamber after metabolic inhibition, imposed by injecting FCCP to 150  $\mu\text{M}$ . A platinised working electrode ( $1250 \mu\text{m}^2$ ) was poised at 0.15 V vs. a Pt pseudo-reference/counter. Saponin was injected to a concentration of 0.3  $\text{mg ml}^{-1}$ , at which point the cell shortened and balled. A lactate calibration signal was obtained by injection of 65 fmol lactate.

#### 5.4.3.4 Summary of Lactate Response from Single Heart Cells

The results of lactate response from single heart cells are summarised in Figures 5.15 and 5.16. The signal recorded upon permeabilisation of a healthy aerobic cell showed a higher basal content of intracellular lactate of  $33.9 \pm 8.0$  fmol (C, n=4), corresponding to an intracellular concentration of  $1.6 \pm 0.4$  mM. The lactate content of cells poisoned by AgI/AgCl was close to the content of a healthy cell at  $36.0 \pm 7.5$  fmol (A, n=3), corresponding to an intracellular concentration of  $1.8 \pm 0.3$  mM. However, the signal recorded for cells punctured by pipette tips showed a larger content of intracellular lactate of  $60.0 \pm 17.1$  fmol (B, n=2), corresponding to an intracellular concentration of  $2.4 \pm 0.7$  mM. The lactate content after metabolic inhibition by injection of FCCP at  $15 \mu\text{M}$  was considerably larger than the content of a healthy cell at  $106.7 \pm 17$  fmol (D, n=3), which corresponds to an intracellular concentration of  $5.1 \pm 0.8$  mM. After injection of FCCP at  $150 \sim 200 \mu\text{M}$ , the efflux of lactate was measured in real time with a total of  $21987 \pm 17$  fmol (E, n=2).

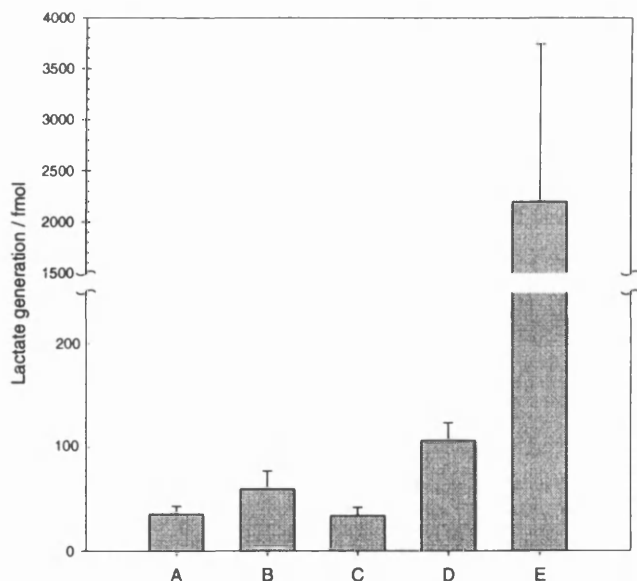


**Figure 5.15** Summary of data for the electrochemical detection of lactate generation by single isolated rabbit ventricular myocytes: (A) cells poisoned by AgI/AgCl ( $36.0 \pm 7.5$  fmol, n=3); (B) cells inserted by tips ( $60.0 \pm 17.1$  fmol, n=2); (C) permeabilisation of healthy rod-shaped cells ( $33.9 \pm 8.0$  fmol, n=4); (D) cells after metabolic inhibition by FCCP at  $15 \mu\text{M}$  ( $106.7 \pm 17$  fmol, n=3); (E) cells after metabolic inhibition by FCCP at  $150 \sim 200 \mu\text{M}$  ( $2198 \pm 1540$  fmol, n=2).

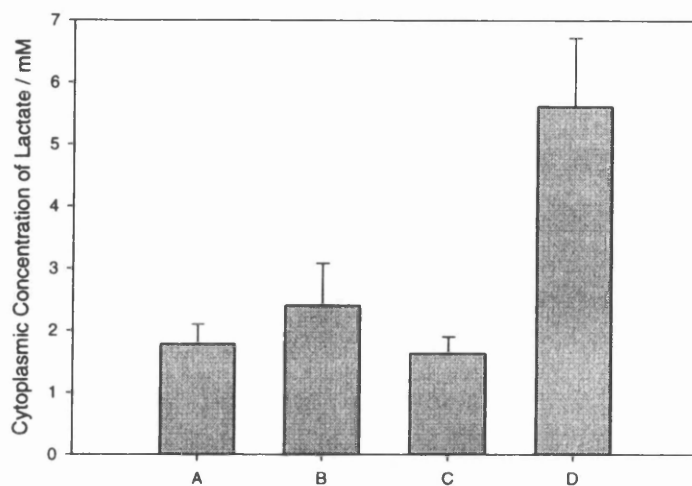


**Figure 5.16** Summary of cytoplasmic concentrations calculated from the data values and the individual cell volumes. (A) Cells poisoned by AgI/AgCl ( $1.8 \pm 0.3$  mM,  $n=3$ ); (B) cells inserted by tips ( $2.4 \pm 0.7$  mM,  $n=2$ ); (C) healthy rod-shaped cells permeabilised by saponin ( $1.6 \pm 0.4$  mM,  $n=4$ ); (D) cells after metabolic inhibition by FCCP ( $5.0 \pm 0.8$  mM,  $n=3$ ).

## 5.5 Conclusions

The study of lactate measurements from single heart cells has been described in this chapter. The biocompatibility of various materials of the electrochemical devices has been evaluated. A new material, SU-8, has been studied and considered as biocompatible with the system used in this work. The cell's response with a AgI/AgCl reference has been examined. Lactate effluxed from a single heart cell upon contacting AgI/AgCl in the microchamber. As the AgI/AgCl electrode was the most successful in retaining a stable potential, *in vivo*, amongst the tested electrodes [68], a biological membrane of LOD and BSA was coated on the microelectrodes to reduce the dissolution of the AgCl layer and to prevent direct contact with the single cell. Comparison of the effects of the raw and modified AgI/AgCl electrodes on the lifetime of the cell revealed that direct contact of the strongly oxidizing AgCl layer with a single myocyte can cause the myocyte to die promptly. Therefore, biocompatibility of the electrode is much improved using a coating film of LOD/BSA.

On the basis of the theory of lactate metabolism and the anoxic model, dynamic electrochemical measurement of lactate from healthy and anoxic single heart cells have been obtained. The lactate content after metabolic inhibition by injection FCCP at 15  $\mu\text{M}$  was approximately three times that in the unpoisoned cell. The efflux of high level lactate was measured in real time after the injection of FCCP at high concentration at 150 ~ 200  $\mu\text{M}$ . The lactate content of cells poisoned by AgI/AgCl was close to the content of a healthy cell. The signal recorded from cells punctured by extruded pipette tips revealed a higher lactate output with active contracting as the cell achieved a higher metabolic rate than that for a quiescent and weakly contracting cell. In conclusion, both biocompatibility and elimination of polarisation should be considered in any future work.

# **Chapter 6: Future Microsensor Arrays, Microstructures and Microfluidics for Microsystems Integration and Miniaturized Analysis Systems ( $\mu$ TAS)**

## **6.1 Introduction**

Photolithography is the most commonly used technique for the fabrication of microelectronic circuits, microelectromechanical systems, microanalytical devices and micro-optics [74]. Recently, a set of non-photolithographic techniques for microfabrication based on the printing of self-assembled monolayers (SAMs) and molding of organic polymers have been developed and can be called “soft lithographs” [74,75]. This chapter gives a brief introduction to such soft microlithographic techniques, non-traditional materials and replica molding (REM) for microfabrication of high-resolution microsensor arrays, microstructures and microfluidics. It also describes how the new materials and methods can yield simple, cost effective routes to microsystems and presage the potential for application of microsystems integration and miniaturized analysis systems ( $\mu$ TAS) [76,77].

## **6.2 Chemicals and Materials**

SU-8 (SM 1060) was obtained from SOTEC Microsystems (Renens, Switzerland). SU-8 (500) was supplied by MicroChem Corp (Newton, MA02464-1418, USA). SU-8 developer (Microposit EC-solvent: propylennglycol monomethylether acetate) was from Shipley Europe Limited (Conventry, UK). Isopropyl alcohol (Cat. No.10224BQ) and glass slides (Cat. No. 406/0183/04, 76 mm  $\times$  26 mm  $\times$  1.0 ~ 1.2 mm) were obtained from BDH Laboratory Supplies (Poole, England). Dimethyldichlorosilane (Cat. No. 44027-2) was from Aldrich (Dorset, England). Poly(dimethylsiloxane) (PDMS) (Silicon elastomer clear, Cat. No. RS494-966) was obtained from RS Components (Northants, UK). Square glass plates (50 mm  $\times$  50 mm  $\times$  1.1 mm) were generously provided from Dr. T. Haruyama, Tokyo Institute of Technology.

## 6.3 Methods

### 6.3.1 Fabrication of Micro Chamber and Micro Flow Channel

The preparation of SM 1060 for 21  $\mu\text{m}$  thick SU-8 microchannels was performed as described in Section 2.4.2.3. For 60  $\mu\text{m}$  thick SU-8 microchambers, SU-8(500) resist was spun at 500 rpm for 10 sec and then ramped over 10 sec to 3000 rpm at which it was maintained for 30 sec. The resist was baked on a hot plate at 90 ~ 95°C for 15 min. Lithography was carried out on a contact aligner (4 mW, 350 ~ 450 nm, System 3 Series, HTG) with a 50 sec exposure time. The exposed resist was subjected to a 15 min post-exposure bake on a hotplate at 90~95°C and then developed in propylennglycol monomethylether acetate for 2 min.

### 6.3.2 Fabrication of Microelectrode Array Chip

4 pairs of microelectrodes and contact leads with Ti/Pd/Au (10/10/100 nm) multilayer structures were first patterned onto a square glass plate (50 mm  $\times$  50 mm  $\times$  1.1 mm), similar to the fabrication process described in Section 2.4.2.1. SU-8(5) resist was spun at 500 rpm for 5 sec and then ramped over 5 sec to 1400 rpm, at which it was maintained for 30 sec. The resist was baked on a hot plate at 90 ~ 95°C for 10 min. Lithography was carried out on a contact aligner (4 mW, 350 ~ 450 nm, System 3 Series, HTG) with a 14 sec exposure time. The exposed resist was subjected to a 20 min post-exposure bake on a hotplate at 90~95°C and then developed in propylennglycol monomethylether acetate for 1.5 min. The thickness of the SU8 layer obtained was approximately 9  $\mu\text{m}$ .

### 6.3.3 Rapid Fabrication of Microfluidic Systems in PDMS

The Fabrication of microfluidic systems in PDMS was completed by a simple rapid method illustrated in Figure 6.1, which is described as follows.

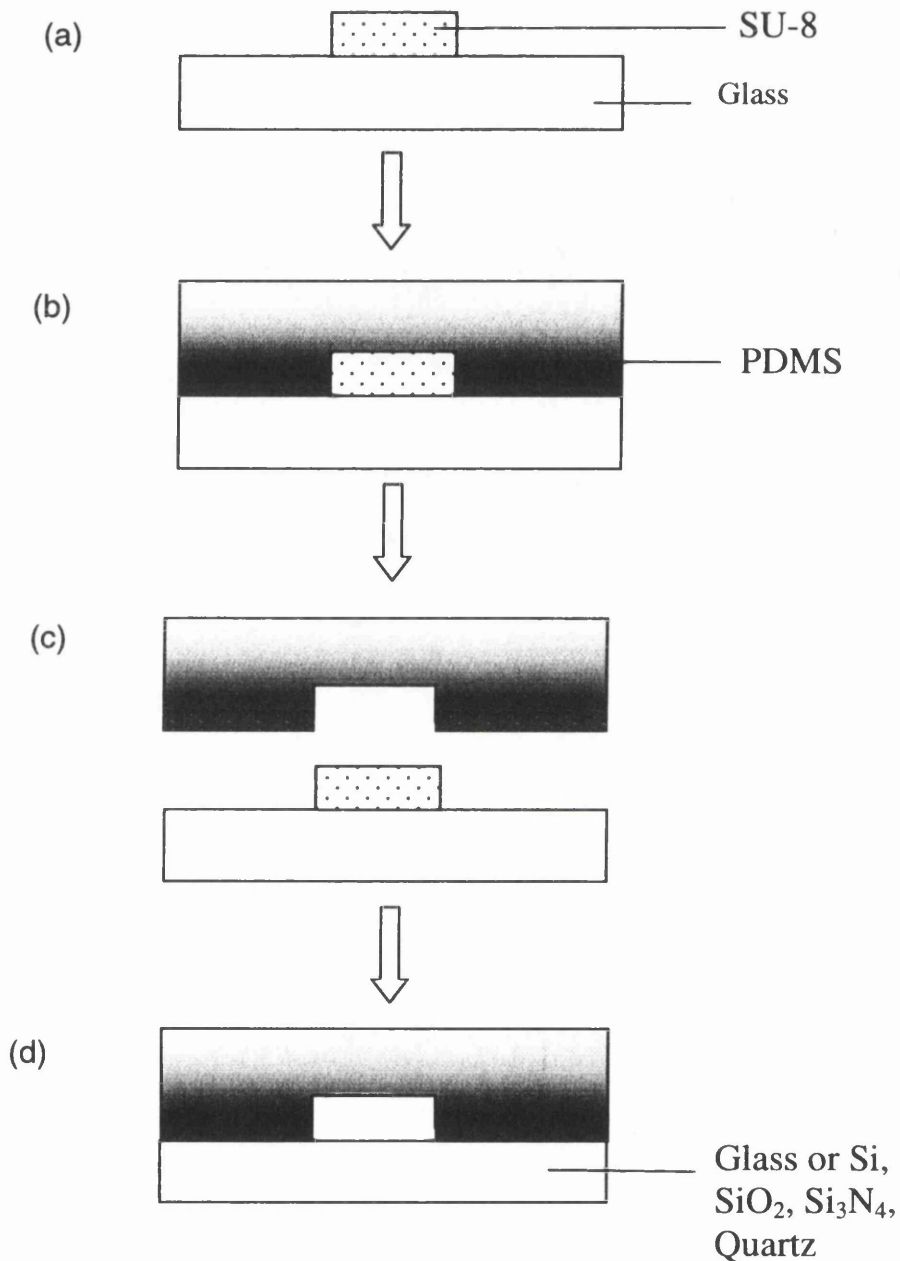


**Figure 6.1** Schematic diagram describing the fabrication of an enclosed microscopic channel in oxidised PDMS. (a) An SU-8 mold was modified to produce a hydrophobic surface. (b) A prepolymer of PDMS was cast onto the mold and cured at 75°C for 1 hour. (c) The PDMS replica containing a negative relief of the channels was peeled away from the mold. (d) The PDMS replica and glass (or Si, SiO<sub>2</sub>, Si<sub>3</sub>N<sub>4</sub>, quartz) substrate were oxidized in a oxygen plasma discharge for 1 min and then were immediately brought into conformal press contact.

### 6.3.3.1 Hydrophobic Modification of the Molds/Substrate Surfaces

For easy removal of PDMS from SU-8 pattern mold (or silicon wafers, or glass slides substrates), the mold or substrates were modified by dimethyldichlorosilane to produce hydrophobic surfaces (Figure 6.1a). The mold or substrates were immersed in 2% (v/v) solution of dimethyldichlorosilane, in chlorobenzene, for 5 min. They were then rinsed several times in ethanol, drained and carefully blown dry to remove any remaining ethanol.

### 6.3.3.2 Fabrication of High-quality Microstructures Using PDMS Replica Molding (REM)

The two components of PDMS prepolymer were thoroughly mixed using a volume ration of 10 ml of base (A) to 1 ml of curing agent (B). After half-hour, any entrapped air bubbles disappeared from the catalysed material. The mixed product was then cast onto the master with or without a frame to hold the solution (Figure 6.1b). The former method produced a thicker PDMS film whereas the later one gave a polymer thickness of about 700  $\mu\text{m}$ . The sample was then cured in an oven at 75°C for 60 min. After curing, the PDMS containing the inlaid pattern was peeled from the mold (Figure 6.1c).

### 6.3.3.3 Oxidation and Bonding

A glass slide was rinsed in ethanol and water, blown dry in nitrogen gas and baked in 110°C oven for 10 min. The glass slide and a fresh PDMS replica were then placed in an oxygen plasma cleaner (ET Plasmofab 505 Barrel Asher, Electrontech) for 60 sec with 2 L  $\text{min}^{-1}$  oxygen, 5 psi nitrogen, 30 mT base pressure and 70 W RF power. Immediately after removal from the plasma cleaner, the substrates were brought into conformal press contact, spontaneously producing an irreversible bond (Figure 6.1d).

## 6.4 Results and Discussion

### 6.4.1 Ultra Thick Negative SU-8 Resists for Micro Chambers and Micro Flow Channels

Many MEMS (Micro-Electro Mechanical Systems) devices require processing of thick photoresist films for their novel microstructures. SU-8 is a negative epoxy based resin photoresist for microstructures with high aspect ratios. SU-8 resist has two important properties suited for ultra thick applications. First, its low molecular weight allows dissolution in a variety of organic solvents to form mixtures of very high concentrations (72%~85% solids by weight), thus permitting coatings from 750 nm to well over 450  $\mu\text{m}$  in a single coat [25]. Second, the layer has very low optical absorption in the visible and near-UV spectrum. At 350 nm and 360 nm, UV transmissions through a 60  $\mu\text{m}$  thick layer are approximately 63% and 79% (after subtract the absorbance of the glass slide substrate) respectively (Figure 6.2). As stated in Chapter 2, in the exposure region of 350 ~ 450 nm, the material has a very low optical absorption with high transparency, so that nearly vertical sidewall profiles can be obtained when the polymer is exposed using a standard UV aligner. Features fabricated using SU-8 included a deep hole (as a microchamber), a corner with sidewalls and microchannels (height 21  $\mu\text{m}$ , width 20  $\mu\text{m}$ ) are depicted in Figure 6.3. The floor and sidewalls of the microstructures are clean with the sidewalls being smooth and practically vertical. These structures can therefore be applied for use in microfluidics.

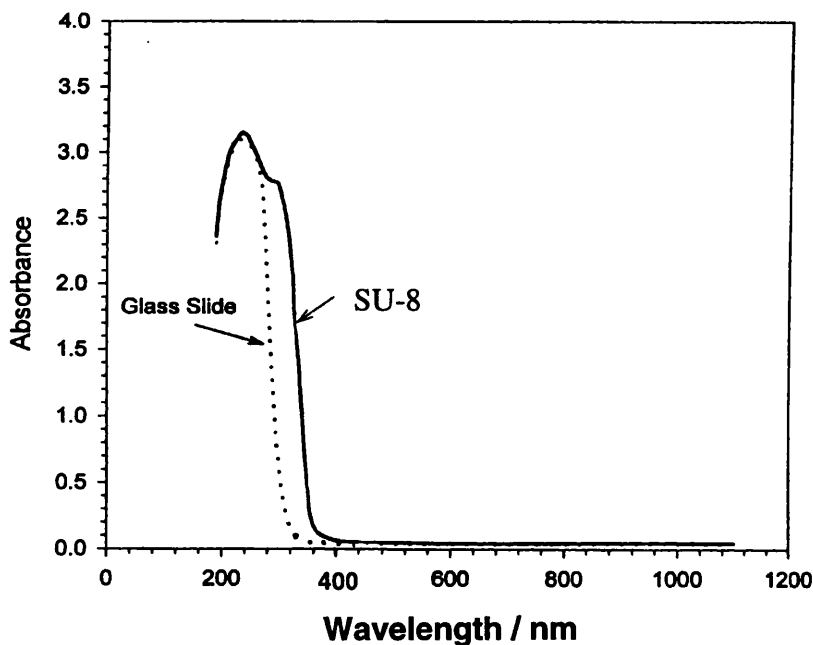


**Figure 6.2** UV absorption spectrum for a 60  $\mu\text{m}$  thick SU-8 film on a glass slide. Transmission ( $T$ ) =  $10^{-A}$ , where,  $A$ : absorbance.

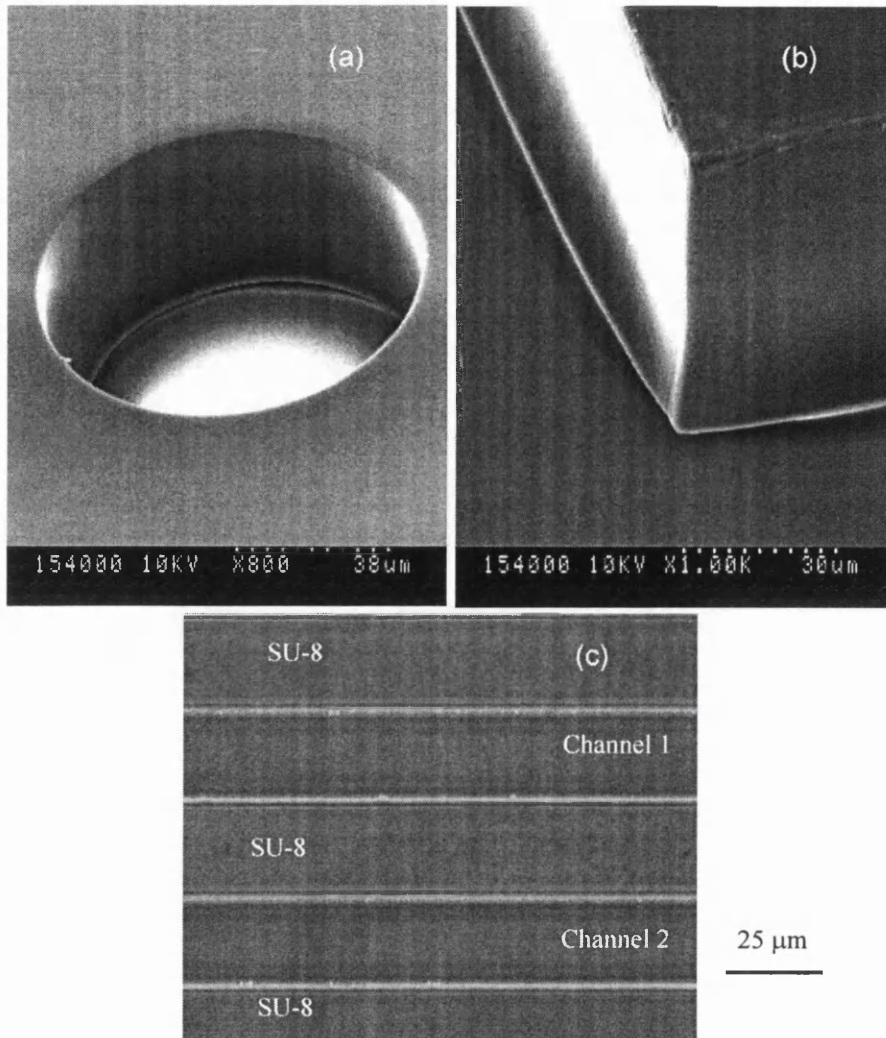


**Figure 6.3** SEM and optical microscope images of SU-8 micromachined structures. (a) SEM of SU-8 (500) microchamber with diameter of 100  $\mu\text{m}$  and depth of 60  $\mu\text{m}$ ; (b) SEM of SU-8 (500) corner with straight walls; (c) an optical microscope image of an SU-8 (SM1060) multi-channel with a channel width of 20  $\mu\text{m}$  and depth of 21  $\mu\text{m}$ .

#### 6.4.2 Microelectrode Array Chip

A planar microelectrode array chip has been designed and fabricated in a joint project with the Department of Biological Information of Tokyo Institute of Technology (TIT). The microelectrode array chips have been sent to TIT and will be applied to monitor the real extracellular membrane potential of single or multi-cells. Compatibility

with the measuring and controlling system of MED8™ (Panasonic) was a stipulation. Four pairs of microelectrode array within microchambers and microchannels (with 9 μm depth) were developed as shown in Figure 6.4. Each pair consisted of a working electrode and a reference electrode in a microchamber/microchannel configuration (Table 6.1).

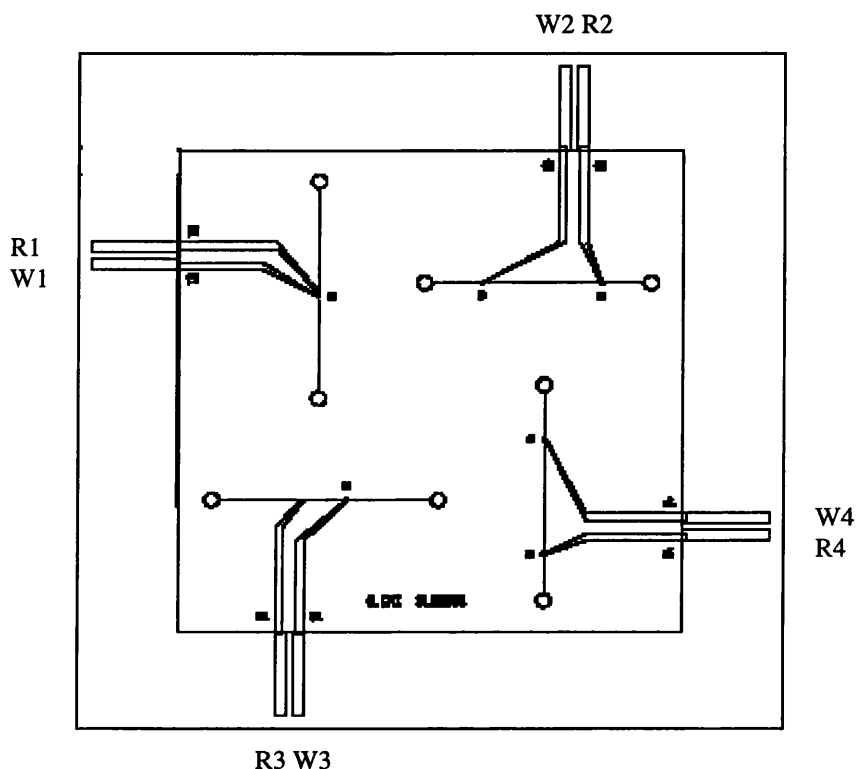


**Figure 6.4** Four pairs of microelectrodes within four microchamber and microchannel systems.

**Table 6.1** The sizes of the microelectrodes(in Figure 6.4), where, WE: working electrode; RE: reference electrode.

| Electrode Pair-Number & Chamber Type | Channel Width (μm) | WE Diameter (μm) | Chamber Diameter of WE (μm) | Distance between WE & RE | RE Size (μm) | Chamber Diameter of RE (μm) |
|--------------------------------------|--------------------|------------------|-----------------------------|--------------------------|--------------|-----------------------------|
| 1, single-cell                       | 12                 | 35               | 35                          | >200 μm                  | 12×200       | —                           |
| 2, single-cell                       | 10                 | 35               | 35                          | 9 mm                     | Ø150         | 150                         |
| 3, multi-cell                        | 12                 | 200              | 200                         | >200 μm                  | 12×5000      | —                           |
| 4, multi-cell                        | 10                 | 200              | 200                         | 9 mm                     | Ø300         | 300                         |

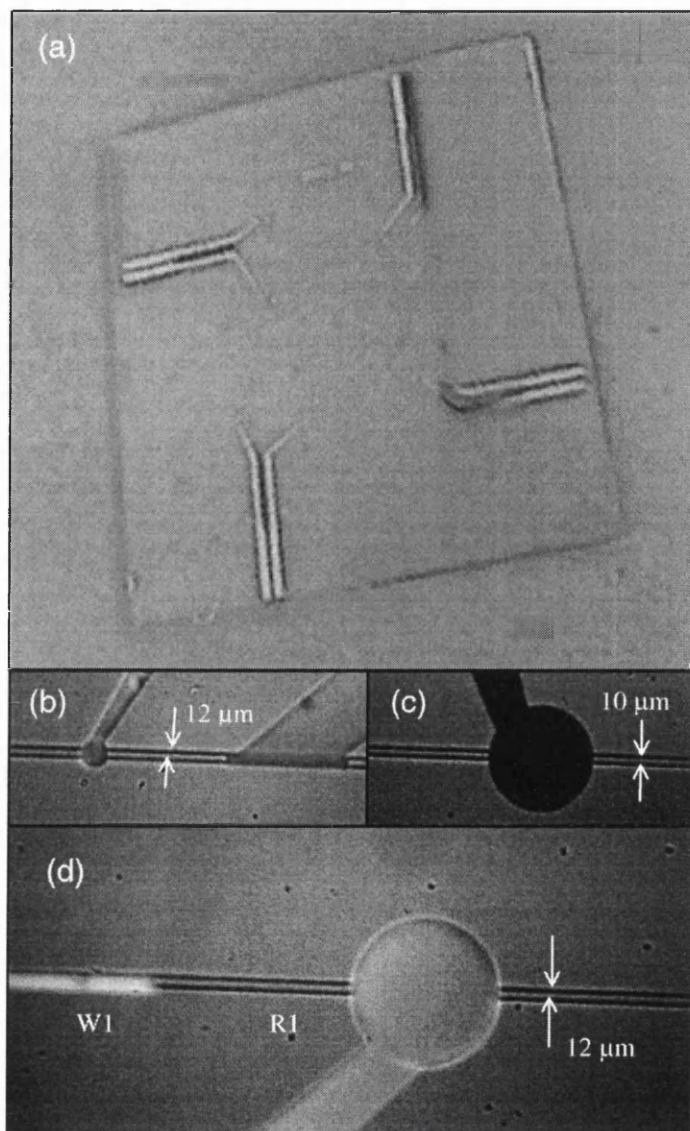


**Figure 6.5** Optical images of a microelectrode array and the microelectrodes within microchambers and microchannels. (a) Microelectrode array chip; (b) the working electrode (W1,  $\varnothing$  35  $\mu\text{m}$ ) and the reference electrode (R1, 12  $\mu\text{m}$   $\times$  200  $\mu\text{m}$ ) in the 1<sup>st</sup> pair of microelectrodes; (c) the working electrode (W2,  $\varnothing$  35  $\mu\text{m}$ ) of the 2<sup>nd</sup> pair of microelectrodes; (d) the working electrode (W3,  $\varnothing$  200  $\mu\text{m}$ ) and the reference electrode (R3, 12  $\mu\text{m}$   $\times$  5000  $\mu\text{m}$ ) in the 3rd pair of microelectrodes.

The microelectrode array chamber and channel were constructed using SU-8 resist due to it being non-toxic (Section 5.3.1) and transparent, thereby allowing

microscopic observation of the cells experiments in the future. The microchambers were completed with a height of 9  $\mu\text{m}$  so that cells would be able to adhere to the microelectrode under a glass cover. Microchannels were 10 or 12  $\mu\text{m}$  wide so that cells could be confined to the microchambers reducing the possibility of contact of the cells with the reference electrode. Figure 6.5 shows optical images of the microelectrode array and gives example images of the microelectrodes in microchambers and microchannels.

### 6.4.3 Rapid Fabrication of Microfluidic Systems Using PDMS

PDMS is an elastomeric material and can be molded at a scale suitable for many applications with feature sizes in the range of 0.1 ~ 10  $\mu\text{m}$ . It is optically transparent, chemically inert, non-toxic, commercially available and inexpensive. It has been developed for optical elements, optical systems [74,78] and microfluidic devices [79]. Here, we focus on developing non-traditional approaches, such as PDMS replica molding and oxidization bonding, which can yield rapid, simple and cost-effective routes to microsystems.

Before casting the PDMS prepolymer onto the SU-8 microchannels pattern, the mold was modified with a hydrophobic surface, which is useful for subsequent releasing. Processing of the mold with dimethyldichlorosilane causes hydrophobic ( $-\text{O}_2\text{Si}(\text{CH}_3)_2$ ) groups to replace polar ( $-\text{OH}$ ) groups on the surface of SU-8 and glass, thus creating a hydrophobic surface.

After curing at 75°C for 1 hour, a high resolution PDMS replica containing a negative relief of the channels was peeled away from the mold. The PDMS replica and a glass (or Si,  $\text{SiO}_2$ ,  $\text{Si}_3\text{N}_4$ , quartz) substrate were oxidized in an oxygen plasma discharge for 1 min and then were immediately brought into conformal press contact. For the substrate (ceramic material), the plasma removes organic contaminants on the surface and let the substrate expose plenty of polar functional groups of (SiOH); for PDMS, the plasma discharge converts ( $-\text{OSi}(\text{CH}_3)_2\text{O}-$ ) groups at surface to ( $-\text{O}_n\text{Si}(\text{OH})_{4-n}$ ) [78]. The formation of bridging, covalent siloxane (Si-O-Si) bonds occur via a condensation reaction between the PDMS and glass surface groups. Figure 6.6 shows optical images of PDMS replica and glass bonded together after plasma oxidation. A perfect bonding defined the channels as four walls (width 20  $\mu\text{m}$ , height 21  $\mu\text{m}$ ) were shown in Figure 6.6(a). This sealing method provides a rapid and simple way

to enclose microfluidic devices. Note, if the aspect ratio of a groove in PDMS is too low, it is easy to connect the glass to the bottom of the groove in the elastomer as shown in Figure 6.6 (b). Also, bonding should be completed immediately after removal from the plasma cleaner, otherwise, air pockets can form within the channel walls (width 10  $\mu\text{m}$ , height 9  $\mu\text{m}$ ), Figure 6.6 (c), causing bonding failure.

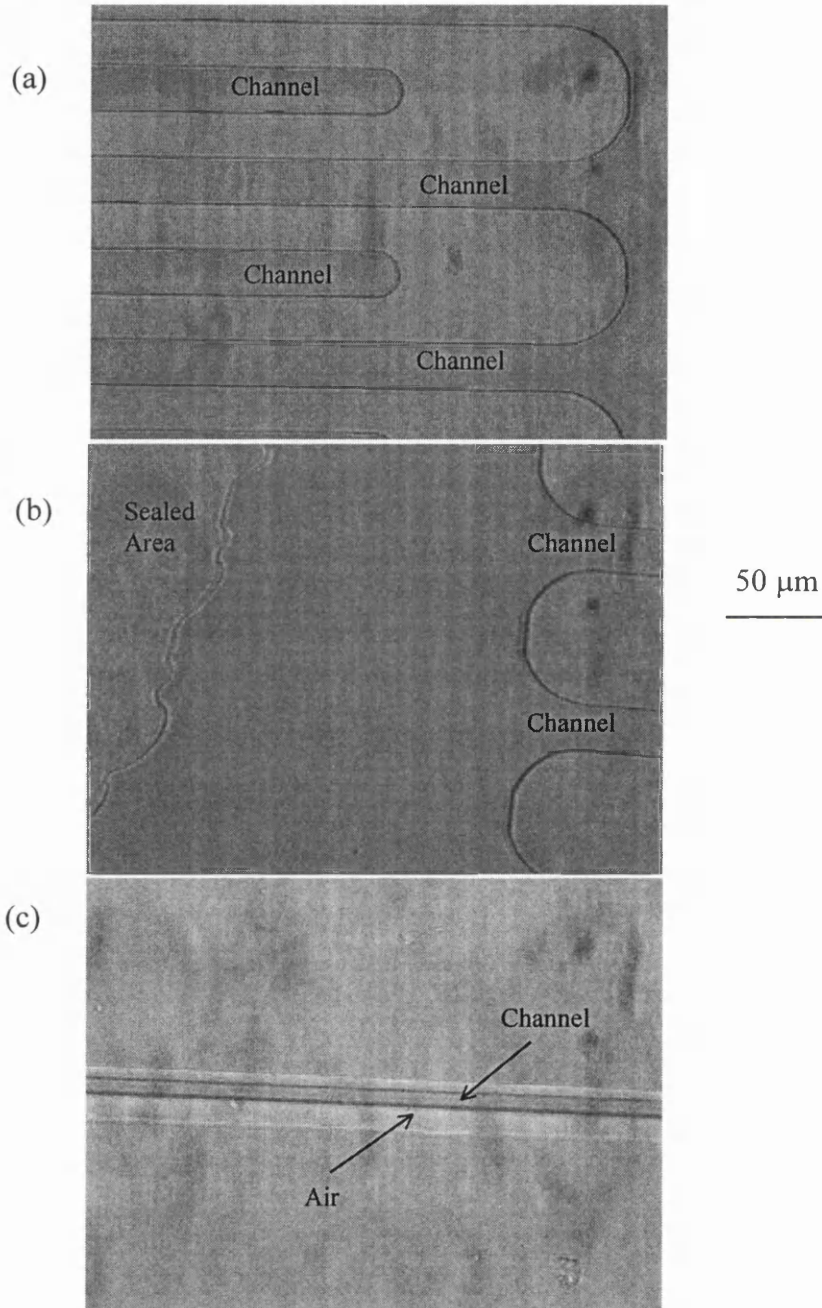


**Figure 6.6** Optical images of PDMS replica and glass bonded together after plasma oxidation: (a) perfect bonding defined the channels (width 20  $\mu\text{m}$ , height 21  $\mu\text{m}$ ); (b) sealing of part of a wide channel of PDMS to the glass; (c) after several minutes delay post-removal from the plasma cleaner, contacting the formed air pockets beside a channel (width 10  $\mu\text{m}$ , height 9  $\mu\text{m}$ ).

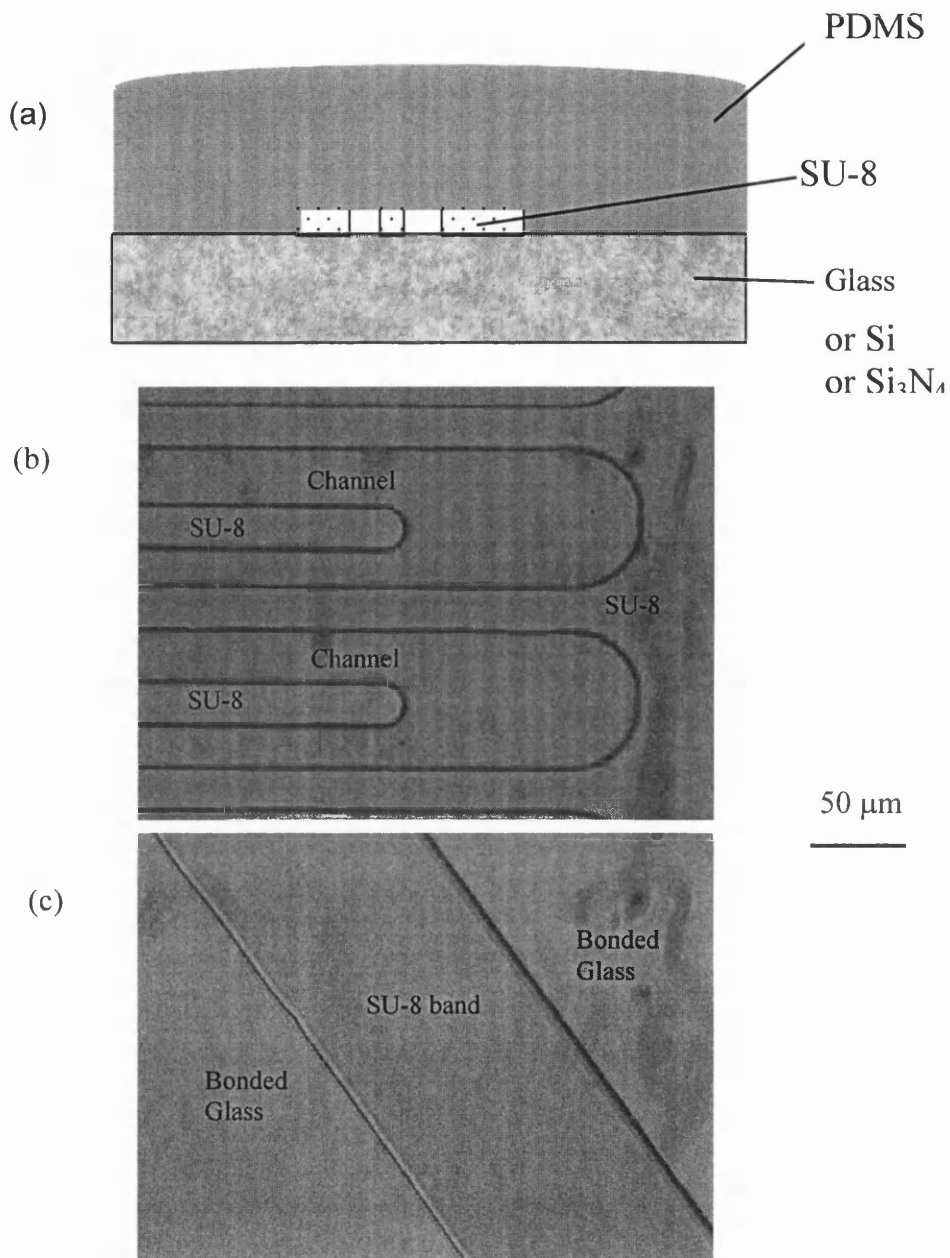


**Figure 6.7** The seal formed between PDMS and the substrate containing SU-8 patterns: (a) diagram depicting a glass slide (or Si, or Si<sub>3</sub>N<sub>4</sub> substrate) with an SU-8 pattern sealed using PDMS. An irreversible bond formed between the outside glass area (or Si, or Si<sub>3</sub>N<sub>4</sub> area) and the PDMS after plasma oxidation; (b) optical image of a glass slide with SU-8 microchannels sealed with a PDMS layer; (c) optical image of a glass slide with an SU-8 band sealed with the PDMS layer. The glass areas (bottom left and top right) beside the SU-8 band formed an irreversible bond with the PDMS covering layer.

As an elastomeric material, a flat PDMS adhered well to an SU-8 layer containing the microchannels. However it is difficult to bond PDMS and SU-8 and the seal between both leaked easily. However, since the potential of fabricating microelectrodes within various microchambers and microchannels using SU-8 photoresist could be useful, sealing PDMS and the patterned SU-8 should be investigated. Using the oxidation and bonding process described in Section 6.3.3.3, a glass slide with a specially designed SU-8 pattern was sealed with fresh PDMS flat. The outside of the SU-8 pattern was designed to include an area of glass. Irreversible bonding occurred between the outside glass area and the PDMS spontaneously (Figure 6.7a). After laminating, a seal formed between the top layer of elastomeric PDMS and the SU-8 layer containing the microchannels (Figure 6.7b). This seal formed without any air bubbles, with the additional benefit of the irreversible bonding, and could be tested by fluidic experiments in the future.

#### ***6.4.4 Integrated Microfluidic Biosensor Chip for On-line Flow Injection Analysis (FIA) Monitoring of Multi-Biomolecules***

On the basis of the techniques described in this work, an integrated microfluidic biosensor chip is proposed as shown in Figure 6.8. The device includes one common gold counter electrode (CE), one common reference electrode (Ag|AgCl) and one working electrode of platinum black without enzyme ( $WE_0$ , for differential output), the immobilized enzyme working electrode array of platinum black (two for representatives,  $ENWE_1$  &  $ENWE_2$ ) and SU-8 flow cell with PDMS top sealing. There are two layers of SU-8 (Figure 6.8a), one is a thin insulator layer ( $\sim 5 \mu\text{m}$ ) for the electrodes patterning and another one is thicker layer ( $\sim 200 \mu\text{m}$ ) for the flow chamber. The dimensions of the flow chamber are estimated less than  $2 \times 0.8 \times 0.2 \text{ mm}^3$  (Figure 6.8b) giving a total internal analytical micro volume of  $< 0.32 \mu\text{L}$ . The immobilization of various enzymes on the microelectrode array might be developed using microinjection processes.

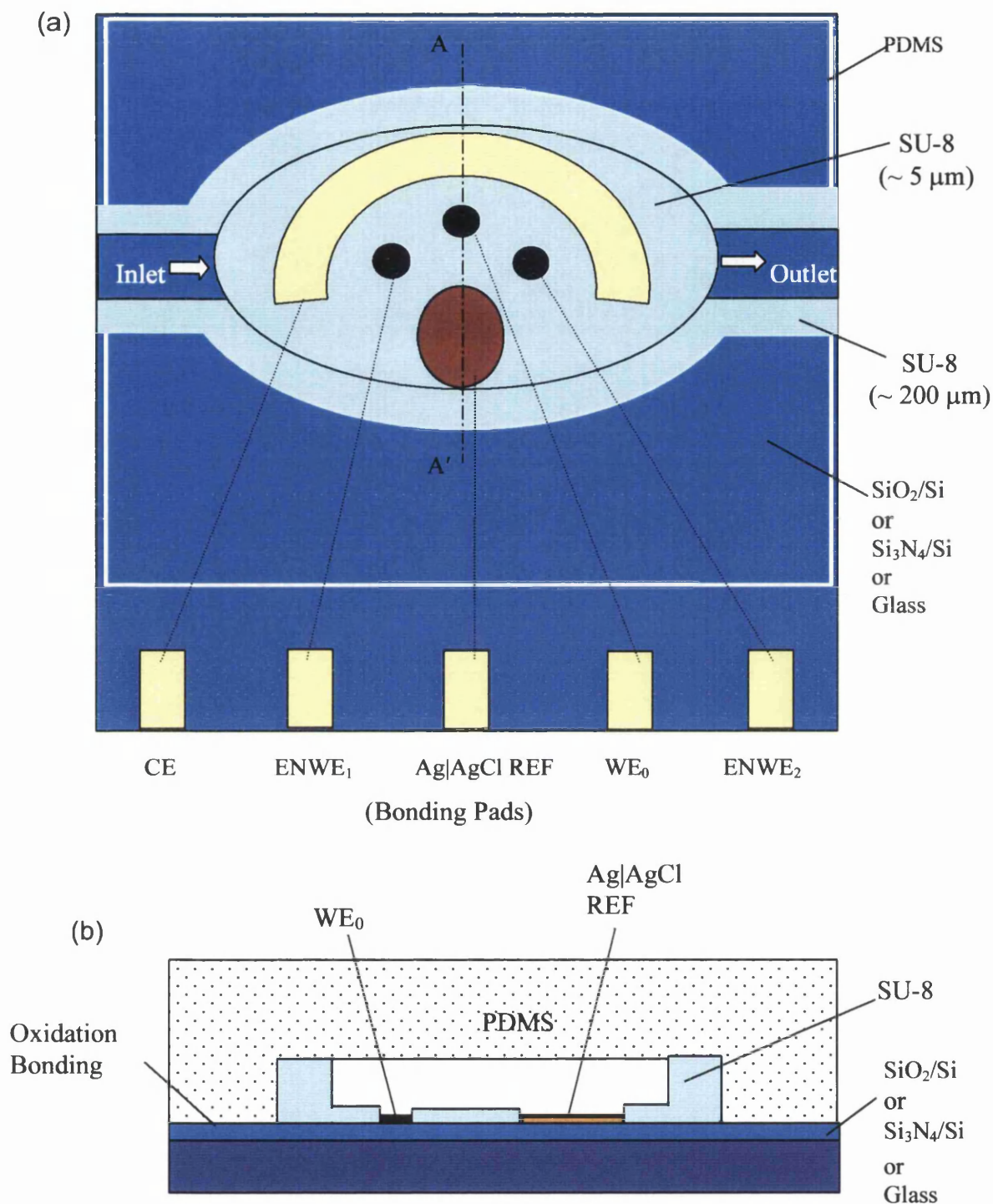


**Figure 6.8** A proposed integrated biosensor chip: (a) The schematic microfluidic chip shows two enzyme working electrodes of platinum black (ENWE<sub>1</sub> & ENWE<sub>2</sub>), one common gold counter electrode (CE), one common reference electrode (Ag|AgCl REF), one working electrode of platinum black without enzyme (WE<sub>0</sub>, for differential output) and SU-8 flow cell with PDMS top seal; (b) the cross-section (A-A') of (a) through a micro-flow cell (< 0.32  $\mu\text{L}$ ).

A proposed experimental set-up of on-line flow injection analysis (FIA) monitoring of multi-biomolecules using an integrated biosensor chip and microdialysis technique [80,81] is shown in Figure 6.9. A microdialysis probe is placed directly into the biological sample, which could be a fermentation bioreactor, or blood/serum tissue fluid. A syringe pump delivers a flow of the perfusion liquid (pure water) through the probe (Figure 6.9b) at a slow rate ( $\sim \mu\text{L min}^{-1}$ ) and the dialysate equilibrated with the surrounding sample fluid is transported to a six-port injection valve with a sample loop. Standard injections could be made possible by replacing the dialysate inlet to the injector with a syringe containing a standard mixture of biomolecules. The flow carrier of buffer is delivered by another syringe pump. The valve can be set either for loading sample or for injection. The biomolecules of the sample from the injector are simultaneously detected by the microfluidic biosensor array described above. The signal data from the multichannel potentiostat are then acquired and processed in a computer.

## 6.5 General Conclusions

This research has been concerned with micromachined sensors for lactate measurements from single heart cells. The general conclusions from this study are summarised below.

Micromachined sensors have been fabricated using photolithography to give a high aspect ratio analytical chamber with microelectrodes positioned within it. Besides the common 3-microelectrode sensor, a 2-microelectrode sensor has also been studied, consisting of a working microelectrode and an internal microreference of Ag|AgCl or Ag|Ag<sub>3</sub>PO<sub>4</sub> (which also acts as the counter electrode). The smallest width of the microband electrode achieved was 2  $\mu\text{m}$  and the lowest volume of the microchambers was 160 pL. After comparison, it has been shown that: SU-8 is more promising for this micromachining application than polyimide; Ag|AgCl is more stable than Ag|Ag<sub>3</sub>PO<sub>4</sub> microreference; and that chronoamperometry is a more reliable method than chronopotentiometry for the deposition of platinum black and Ag|AgCl.

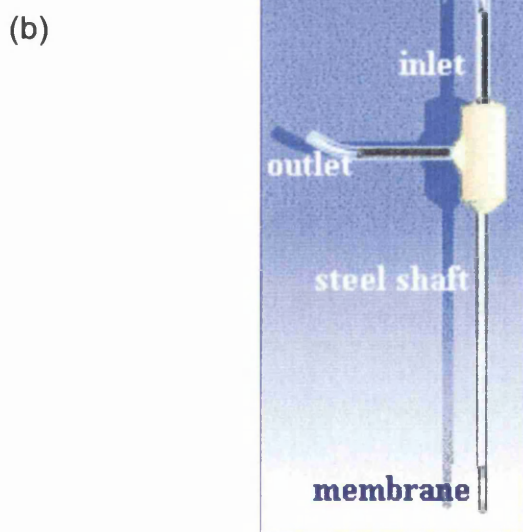
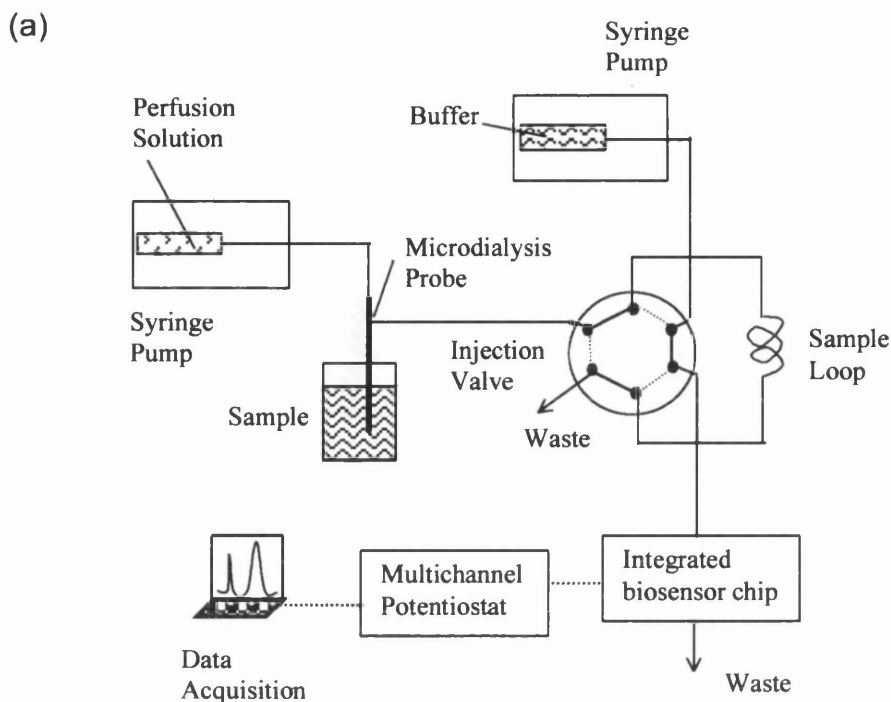


**Figure 6.9** A schematic diagram of the proposed experimental set-up: (a) on-line flow injection analysis (FIA) monitoring of multi-biomolecules using an integrated biosensor chip and microdialysis technique. The biological sample could be a fermentation bioreaction reservoir, or blood/serum tissue fluid; (b) a microdialysis probe.

The electrochemical characterization of a miniaturized sensor using a model redox compound of FMCA has been discussed. Meanwhile, the detection of hydrogen peroxide, the redox enzyme-linked electrochemical assay of glucose and the regeneration of the micro planar electrodes have been investigated.

'Bulk' and pL-scale lactate measurements using micromachined sensors have been carried out. The sensor was found to have a detection limit of 2  $\mu\text{M}$  for a model 'bulk' method. The resulting sensor, in 400 pL volume of FMCA, shows different cyclic voltammograms at a slow scan rate compared with a bulk response. The lactate sensor was characterised using a micro-injection system to dispense volumes as low as 6.5 pL producing a linear calibration curve between the charge transferred and the amount of injected lactate, in the range 65 to 266 fmol.

A study of lactate measurements from single heart cells has been presented, including a study of the biocompatibility of various materials of the electrochemical devices. The biocompatibility of a new material, SU-8, has been demonstrated. It has been shown that direct contact of the strongly oxidizing AgCl layer with a single myocyte can cause prompt death. The biocompatibility of AgI/AgCl can be improved greatly using a coating film of LOD/BSA. On the basis of the theory of lactate metabolism and an anoxia model, dynamic electrochemical measurements of lactate from healthy and anoxia single heart cells have been obtained. The lactate content after metabolic inhibition by injection FCCP at 15  $\mu\text{M}$  was approximately three times that in the unpoisoned cell. The efflux of high level lactate was measured in real time after the injection of FCCP at high concentration of 150 ~ 200  $\mu\text{M}$ . The lactate content of cells poisoned by AgI/AgCl was close to that of a healthy cell. The lactate signal produced upon piercing cells with an extruded pipette tip was higher than that for a quiescent or weakly contracting cell.

Besides photolithography techniques, new materials, namely SU-8 and PDMS, and "soft lithography" techniques have been explored for fabrication of microsensor arrays and microfluidics. An integrated microfluidic biosensor chip and on-line flow injection analysis (FIA) monitoring system has been proposed. Many benefits could be realized by incorporating these micro-components into an integrated analysis system.

In conclusion, this work described provides a generic method making a wide range of single cell sensors in pL-scale volumes, based on oxidase-reductase enzymes and microfluidics, applicable to a lab-on-a-chip format. Although extensive research work has been completed on the micromachined sensors, the enthusiasm and high expectations placed on such systems has not been fulfilled to date. Further work and technological breakthroughs are still necessary to advance the field. Decreased assay cost and time, along with improved throughput and reproducibility can be achieved by integrated systems. In addition, on-line measurements could be expected. Based on the research in this work, future work should be structured in the following way.

A multichannel potentiostat and its accompanying software are necessary for integrated sensor arrays measurements. An integration of individual enzyme sensor arrays and fluorescence sensors needs to be carried out for the detection of various biomolecules from one single cell simultaneously. A differential output between an enzyme-coated electrode and an electrode without enzyme would be advantageous for subtracting various disturbances from the signal. The immobilization of enzymes [82] on the microelectrodes, leading to improved stability but avoiding expensive enzyme strategies as a means to every response, would be a significant breakthrough.

A biocompatible of Ag|AgCl reference and elimination of polarisation should be a goal of future work. To this end, the production of a three-electrode configuration is suggested with a small Ag|AgCl reference in a separate small chamber, which is connected to the main chamber. Meanwhile, prevention of the degradation of Ag|AgCl and the direct contact with single cell using polymers [48,66,69,70,83], reducing the applied potential in order to attenuate polarisation problems in the two-electrode configuration should also be explored fully.

For on-line detection of biological sample, a fluidic biosensor array chip and on-line FIA system similar to that proposed in Section 6.4.4 should be realised.

## References

1. F. Palmisano, G.E. De benedetto and C.G. Zambonin, Lactate amperometric biosensor based on an electrosynthesized bilayer film with covalently immobilized enzyme, *The Analyst* **1997**, Vol.122, 365-369.
2. J. Wang, Amperometric biosensors for clinical and therapeutic drug monitoring: a review, *Journal of Pharmaceutical and Biomedical Analysis* **1999**, 19, 47-53.
3. P.C. Sundermeier, H. Hinkeers, H. Hinkers, O.M. Morell, W. Seifert, M. Knoll. Containment sensors for the determination of L-lactate and glucose, *Biosensors & Bioelectronics* **1999**, 14, 27-32.
4. Y.E. Korchev, Y.A. Negulyaev, C.R.W. Edwards, I. Vodyanoy and M.J. Lab, Functional localization of single active ion channels on the surface of a living cell, *Nature Cell Biology* **2000**, 2, 616-619.
5. J. Hartmann and M. Lindau, A novel  $\text{Ca}^{2+}$ -dependent step in exocytosis subsequent to vesicle fusion, *FEBS Letters* **1995**, 363, 217-220.
6. E.R. Travis and R.M. Wightman, Spatio-temporal resolution of exocytosis from individual cells, *Annu. Rev. Biophys. Biomol. Struct.* **1998**. 27, 77-103.
7. Q. Xin, R.M. Wightman, Release from Single Bovine Chromaffin Cells Using a Dual Microsensor Simultaneous Detection of Catecholamine Exocytosis and  $\text{Ca}^{2+}$ , *Anal. Chem.* **1998**, 70, 9,1677.
8. S. Jung, L.M. Kauri, W. Qian, and R.T. Kennedy, Correlated oscillations in glucose consumption, oxygen consumption, and intracellular free  $\text{Ca}^{2+}$  in single islets of Langerhans, *The Journal of Biological Chemistry* **2000**, 275(9), 6642-6650.
9. T.Vo-Dinh, G.D. Griffin, J.P. Alarie, D.W. Noid et al, Advanced Nanosensors and Nanoprobes, *The Sixth Foresight Conference on Molecular Nanotechnology* **1998**, Santa Clara, USA.
10. P.S. Cahill, Q.D. Walker and R.M. Wightman, Microelectrodes for the Measurement of Catecholamines in Biological Systems, *Anal. Chem.* **1996**, 68, 3180-3186.
11. K. Pihel, Q.D. Walker, and R.M. Wightman, Overoxidized Polypyrrole-coated Carbon Fiber Microelectrodes for Dopamine Measurements with Fast-scan Cyclic Voltammetry, *Anal. Chem.* **1996**, 68, 2084-2089.
12. C.D.T. Bratten, P.H. Cobbold and J.M. Cooper, Single-cell Measurements of Purine Release Using a Micromachined Electroanalytical Sensor. *Anal. Chem.* **1998**, 70, 1164-1170.
13. K.D. Kozminski, D.A. Gutman, V. Davila, D. Sulzer and A.G. Ewing, Voltammetric and Pharmacological Characterization of Dopamine Release from Single Exocytotic Events at Rat Pheochromocytoma (P12) Cells, *Anal. Chem.* **1998**, 70, 3123-3130

14. J.M. Cooper, Towards Electronic Petri-dishes and Picolitre-scale Single-cell Technologies. *Trends in Biotechnology* **1999**, 17(6), 226-230.
15. G. Chen, A.G. Ewing, Chemical Analysis of Single Cells and Exocytosis, *Critical Reviews in Neurobiology* **1997**, 11(1), 59-90.
16. D. Michael, E.R. Travis, R.M. Wightman, Colour images for fast-scan CV measurements in biological systems, *Analytical Chemistry News & Features* **1998**, 586A-595A.
17. R.A. Clark and A.G. Ewing, Characterization of Electrochemical Responses in Picolitre Volumes, *Anal Chem.* **1998**, 70, 1119-1125
18. C.D.T. Bratten, P.H. Cobbold, J.M. Cooper, Micromachined Sensors for Electrochemical Measurement in Subnanoliter Volumes. *Anal. Chem.* **1997**, 69(2), 253-258.
19. C.D.T. Bratten, P.H. Cobbold and J.M. Cooper, Enzyme Assay Using Ultra-low Volume Surface Micromachined Sensors. *Chem. Commun.* **1998**, 471-472.
20. Facts and figures about coronary heart disease and its prevention, <http://www.takeheart.co.uk/figs.htm>.
21. C.R.M. Grovenor, 2.4 Fabrication process for microelectronic devices, in *Microelectronic Materials*, Adam Hilger, Bristol and Philadelphia, **1989**, 76-83
22. J. Reche, Photolithography for thin film MCMs, [http://www.suss.com/sitemap/photolith\\_thin\\_film.htm](http://www.suss.com/sitemap/photolith_thin_film.htm).
23. Southampton Electrochemistry Group, *Instrumental Methods in Electrochemistry*. Chichester; Ellis Horwood, **1985**, 357-370.
24. F. D. Egitto, L. J. Matienzo, K. J. Blackwell, A. R. Knoll. Oxygen plasma modification of polyimide webs-effect of ion-bombardment on metal adhesion. *J. Adhesion Sci. Technol.* **1994**, 8, 411-433
25. K. Y. Lee, N. LaBianca and S. A. Rishton et al, Micromachining application of a high resolution ultrathick photoresist, *J. Vac. Sci. Technol.* **Nov/Dec 1995**, B 13(6), 3012-3016.
26. H. Lorenz, M. Despont, N. Fahrni, N. LaBianca et al, SU-8: a low-cost negative resist for MEMS, *J. Miromech. Microeng.* **1997**, 7, 121.
27. A.P.F. Turner; I. Karube and G.S. Wilson, The realization of electron transfer from biological molecules to electrodes. In *Biosensors: Fundamentals and Applications*, Oxford University Press: the U.S., **1987**, 257-275
28. A.C. Fisher, Voltammetry: the study of electrolysis mechanisms. In *Electrode Dynamics*, Oxford University Press: Oxford, **1996**, 27-50
29. A.J. Bard, L.R. Faulkner, Faradaic processes and factors affecting rates of electrode reactions. In *Electrochemical Methods: Fundamentals and Applications*, 2ns Ed.; John Wiley & Sons, INC: New York, **2001**, 1-43.

30. A.J. Bard, Basic electrochemical thermodynamics, in the *Electrochemical Methods: Fundamentals and Applications*, New York Chichester: Wiley, c1980, 44-82.
31. L. C. Clark, C. L. Lyons. Electrode systems for continuous monitoring in cardiovascular surgery. *Ann. NY Acad. Sci.* **1962**, 102, 29.
32. A.E.G. Cass, G. Davis, G.D. Francis, and H.A.O. Hill, Ferrocene-mediated enzyme electrode for amperometric determination of glucose. *Anal. Chem.* **1984**, 56, 667-671.
33. A.J. Bard, Kinetics of electrode reactions, in the *Electrochemical methods: fundamentals and applications*, New York Chichester: Wiley, **2001-B**, 87-136.
34. The different types of equilibrium constant,  
<http://www.compumart.ab.ca/plambeck/che/p101/p01104.htm>
35. Equilibrium and insoluble substances,  
<http://jcbmac.chem.brown.edu/baird/Chem221/lectures/Solubility/Solubility.pdf>
36. H. Suzuki, A. Hiratsuka, S. Sasaki and I. Karube, Problems associated with the thin-film Ag|AgCl reference electrode and a novel structure with improved durability, *Sensors and Actuators B* **1998**, 46, 103-113.
37. H. Suzuki, T. Hirakawa, S. Sasaki and I. Karube, An integrated three-electrode system with a micromachined liquid-junction Ag|AgCl reference electrode, *Anal. Chim. Acta* **1999**, 387, 103-112.
38. H. Suzuki, T. Hirakawa, S. Sasaki and I. Karube, Micromachined liquid-junction Ag|AgCl reference electrode, *Sensors and Actuators B* **1998**, 46, 146-154.
39. A.J. Bard, Double-layer structure and adsorbed intermediates in Electrode processes, in the *Electrochemical Methods: Fundamentals and Applications*, New York Chichester: Wiley, c1980, 511-549.
40. E. A. Hall, *Biosensors*, Wiley Publisher **1990**.
41. U. Spohn, D. Narasaiah, L.Gorton and D. Pfeiffer, A bienzyme modified carbon paste electrode for the amperometric detection of L-lactate at low potentials, *Analytica Chimica Acta* **1996**, 319, 79-90.
42. X. Liu and W. Tan, Development of an optical fiber lactate sensor, *Mikrochimica Acta* **1999**, 131, 129-135.
43. J. Perdomo, C. Sundermeier, H. Hinkers, O.M. Morell, W. Seifert and M. Knoll, Containment sensors for the determination of L-lactate and glucose, *Biosensors & Bioelectronics* **1999**, 14, 27-32.
44. H. Durliat, M. Comtat and J. Mahenc, A device for the continuous assay of lactate, *Analytica Chimica Acta* **1979**, 106, 131-135.
45. D.A. Eisner, C.G. Nichols, S.C. O'neil, G.L. Smith and M. Valdeolmillos, The effects of metabolic inhibition on intracellular calcium and pH in isolated rat ventricular cells, *Journal of Physiology* **1989**, 411, 393-418.

46. A.P. Halestrap and N.T. Price, The proton-linked monocarboxylate transporter (MCT) family: structure, function and regulation, *Biochem. J.* **1999**, 343, 281-299.
47. X. Wang, A.J. Levi and A.P. Halestrap, Kinetics of the sarcolemmal lactate carrier in single heart cells using BCECF to measure  $pH_i$ , *Am J. Physiol* **1994**, 267, H1759-H1769.
48. M. Kyrolainen, S.M. Reddy, P.M. Vadgama, Blood compatibility and extended linearity of lactate enzyme electrode using poly(vinyl chloride) outer membranes, *Analytica Chimica Acta* **1997**, 353, 281-289
49. L.C. Shriver-lake, Chapter 1, Silane-modified surfaces for biomaterial immobilization, in *Immobilized Biomolecules in Analysis*, edited by T. Cass and F.S. Ligler, published in the US by Oxford University Press, **1998**
50. B. Lillis, C. Grogan, H. Berney and W.A. Lane, Investigation into immobilisation of lactate oxidase to improve stability, *Sensors & Actuators B*, **2000**, 68, 109-114.
51. A.C. Rose and A.G. Ewing, Characterization of Electrochemical Responses in Picolitre Volumes. *Anal. Chem.* **1998**, 70, 1119-1125.
52. A.C. Giese, Chapter 12: The release of energy in cells in cell physiology, in *Cell Physiology*, Fifth Edition, **1979**, W.B. Saunders Company, Philadelphia.
53. M.K. Campbell, Chapter 12: Metabolism and electron transfer & Chapter 13: Glycolysis: Anaerobic oxidation of glucose, in *Biochemistry*, **1991**, Saunders College Publishing, Philadelphia.
54. L.H. Opie, Lactate Metabolism and Cardiac Muscle, in *Lactate Physiologic, Methodologic and Pathologic Approach*, edited by P.R. Moret, J. Weber, J.-Cl. Haissly and H. Denolin, Springer-Verlag, Berlin Heidelberg, New York **1980**, p174-180
55. A.P. Halestrap, X. Wang, R.C. Poole, V.N. Jackson and N.T. Price, Lactate transport in heart in relation to myocardial ischemia, *The American Journal of Cardiology* **1997**, 80, 17A-25A.
56. X. Wang, A.J. Levi and A.P. Halestrap, Substrate and inhibitor specificities of the monocarboxylate transporters of single rat heart cells, *Am. J. Physiol* **1996**, 270, H476-H484.
57. D.J. Hearse, Chapter 22: Protection of the ischaemic myocardium, in *Lactate Physiologic, Methodologic and Pathologic Approach*, edited by P.R. Moret, J. Weber, J.-Cl. Haissly and H. Denolin, Springer-Verlag, Berlin Heidelberg New York, **1980**, 230-246.
58. N. Krahenbuhl, Chapter 16: Blood lactate measurement in peripheral arterial disease, in *Lactate Physiologic, Methodologic and Pathologic Approach*, edited by P.R. Moret, J. Weber, J.-Cl. Haissly and H. Denolin, Springer-Verlag, Berlin Heidelberg, New York **1980**, p174-180.

59. R.G. Tiessen, R.A. Tio, A. Hoekstra, K. Venema, J. Korf, An ultrafiltration catheter for monitoring of venous lactate and glucose around myocardial ischemia, *Biosensors & Bioelectronics* **2001**, 16, 159-167.
60. I. Allue, O. Gandelman, E. Dementieva, N. Ugarova and P. Cobbold, Evidence for rapid consumption of millimolar concentrations of cytoplasmic ATP during rigor-contraction of metabolically compromised single cardiomyocytes, *Biochem. J.* **1996**, 319, 463-469.
61. C.D.T. Bratten, Chapter 4: Purine generation by single myocytes, in the thesis of *Micromachined electroanalytical device for single cell investigations* **1998**, 95-134.
62. M. Irving, Muscle-contraction ~ weak and strong crossbridges, *Nature* **1985**, 316, 292-293.
63. P. Connolly, P. Clark, A.S.G. Curtis, J.A.T. Dow and C.D.W. Wilkinson, An extracellular microelectrode array for monitoring electogenic cells in culture, *Biosensors & Bioelectronics* **1990**, 5, 223-234.
64. B.W. Kristensen, J. Noraberg, P. Thiebaud, M. Koudelka-Hep, J. Zimmer, Biocompatibility of silicon-based arrays of electrodes coupled to organotypic hippocampal brain slice cultures, *Brain Research* **2001**, 896, 1-17.
65. S.S. Stensaas and L.J. Stensaas, Histopathological evaluation of materials implanted in the cerebral cortex, *Acta Neuropathologica* **1978**, 41, 145-155.
66. F. Moussy and D.J. Harrison, Prevention of the rapid degradation of subcutaneously implanted AgI/AgCl reference electrodes using polymer coatings, *Anal. Chem.* **1994**, 66, 674-679.
67. A.M. Dymond, L.E. Kaechele, J.M. Jurist, P.H. Crandall, Brain tissue reaction to some chronically implanted metals, *Journal of Neurosurgery* **1970**, 33, 574-580.
68. G. Velho, P. Froguel, R. Sternberg, D.R. Thevenot, G. Reach, *Diabetes* **1989**, 38, 164-171.
69. D. Moatti-Sirat, F. Capron, V. Poitout, G. Reach, D.S. Bindra, Y. Zhang, G.S. Wilson and D.R. Thevenot, Towards continuous glucose sensor implanted for several days in rat subcutaneous tissue, *Diabetologia* **1992**, 35, 224-230.
70. D.S. Bindra, Y. Zhang and G.S. Wilson, Design and in vitro studies of a needle-type glucose sensor for subcutaneous monitoring, *Anal. Chem.* **1991**, 63, 1692-1696.
71. C.D.T. Bratten, Chapter 3: Nanolitrehydrogen peroxide and purine detection; Chapter 4: Purine generation by single myocytes, in the thesis *Micromachined electroanalytical device for single cell investigations*, the University of Liverpool, **1998**, 55-134.
72. G. Moores, Bioelectronics IV 1999-2000, Laboratory cell culture and biocompatibility, <http://www.elec.gla.ac.uk/groups/bio/biolab/biolab4b.html>.

73. S. Schmidt, K. Horch, R. Normann, Biocompatibility of silicon-based electrode arrays implanted in feline cortical tissue, *J. Biomed. Mater. Res.* **1993**, 27, 1393-1399.
74. D. Qin, Y. Xia, J.A. Rogers, R.J. Jackman, X. Zhao, G.M. Whitesides, Microfabrication, microstructures and microsystems, in *Microsystyem Technology in Chemistry and Life Sciences*, edited by A. Manz and H. Becker, Berlin: Springer, **c1999**, 1-20.
75. Y. Xia and G.M. Whitesides, Soft lithography, *Angew. Chem. Int. Ed.* **1998**, 37, 550-575.
76. A. van den Berg and T.S.J. Lammerink, Micro total analysis systems: microfluidic aspects, integration concept and applications, in *Microsystyem Technology in Chemistry and Life Sciences*, edited by A. Manz and H. Becker, Berlin: Springer, **c1999**, 21-49.
77. G. Fuhr and S.G. Shirley, Biological application of microstrucures, in *Microsystyem Technology in Chemistry and Life Sciences*, edited by A. Manz and H. Becker, Berlin: Springer, **c1999**, 83-116.
78. D.C. Duffy, J.C. McDonald, O.J.A. Achueller, and G.M. Whitesides, Rapid prototyping of microfluidic systems in poly(dimethylsiloxane), *Analytical Chemistry*. **1998**, 70(23), 4974-4984.
79. K. Hosokawa, T. Fujii, and I. Endo, Handling of picoliter liquid samples in a poly(dimethylsiloxane)-based microfluidic device, *Analytical Chemistry* **1999**, 71(20); 4781-4785.
80. E. Dempsey, D. Diamond, M.R. Smyth et. Al., Design and development of a miniaturised total chemical analysis system for on-line lactate and glucose monitoring in biological samples, *Analytica Chimica Acta* **1997**, 346, 341-349.
81. R.W. Min, V. Rajendran, N. Larsson, L. Gorton, J. Planas and B. Hahn-Hagerdal, Simultaneous monitoring of glucose and L-lactic acid during a fermentation process in an aqueous two-phase system by on-line FIA with microdialysis sampling and dual biosensor detection, *Analytica Chimica Acta* **1998**, 366, 127-135.
82. P. Yu, G.S. Wilson, an independently addressable microbiosensor array: what are the limits of sensing element density? *Faraday Discussions* **2000**, 116, 305-317.
83. G.S. Cha, D. Liu, M.E. Meyerhoff et al., Electrochemical performance, biocompatibility, and adhesion of new polymer matrices for solid-state ion sensors, *Anal. Chem.* **1991**, 63, 1666-1672.

## List of Tables and Figures

**Figure 1.1** Schematic of the experimental arrangement for single-cell measurements using the dual microsensor. The cylindrical microsensor was positioned touching a chromaffin cell that is attached to the floor of a Petri dish. A double-barrel microinjector was placed approximately 50  $\mu\text{m}$  from the cell to introduce reagents onto it. (Reproduced from reference [7])

**Figure 2.1** Diagrams of the two layers in a WAM file used to producing two masks for the electrochemical devices (scale, 2:1): (a) the electrode layer including contact bands; (b) the chambers/channels layer.

**Figure 2.2** Flow diagram briefly showing 16 steps for the fabrication of micro-electrochemical cell (using SU-8) devices. The figure aims to show the complexity of the fabrication, which should be considered in the context of overall yield (90%).

**Figure 2.3.** Schematic diagram of major fabrication steps: (1) exposure of positive photoresist through a mask, in order to define the template for microelectrode deposition; (2) development of exposed photoresist followed by; (3) evaporation of multilayers of metals to form the microsensor array; (4) lift off reveals the microsensor configuration; (5) deposition of the negative photoresist (e.g. polyimide or SU-8) and exposure through a mask; (6) development of the exposed resist to reveal the microelectrodes within an analytical chamber.

**Figure 2.4.** Photographs of 2-electrode or 3-electrode microelectrodes prior to the fabrication of the chambers, which sizes are shown in Table 2.1. The minimum width of the above microelectrodes is 2  $\mu\text{m}$ .

**Figure 2.5** Chronopotentialmetric and chronoamperometric curves for microelectrode platinisation. (a) Chronopotentiometry response to platinisation on a 1000  $\mu\text{m}^2$  microelectrode. The current density was fixed at  $-45 \text{ mA cm}^{-2}$  in curve (i) and  $-70 \text{ mA cm}^{-2}$  in curve (ii). (b) Chronoamperometry response to platinisation on microelectrodes of two different areas (500  $\mu\text{m}^2$  and 1000  $\mu\text{m}^2$ ). The applied potential was held at  $-1.00 \text{ V}$ .

**Figure 2.6** SEM micrographs of platinisation morphology: (a) micrograph of the platinized electrode; (b) magnified area of (a) to highlight platinum black morphology.

**Figure 2.7** Chronopotentiometric and chronoamperometric curves for Ag|AgCl deposition on microelectrodes: (a) chronopotentiometry responses to Ag deposition (at  $-40 \text{ mA cm}^{-2}$ ) and subsequent AgCl formation (at  $40 \text{ mA cm}^{-2}$ ) on a  $1200 \text{ }\mu\text{m}^2$  microelectrode; (b) chronoamperometry curves using a  $3125 \text{ }\mu\text{m}^2$  microelectrode. The potential was biased at  $-0.48 \text{ V}$  and  $-0.15 \text{ V}$ , for Ag and AgCl deposition respectively.

**Figure 2.8** SEM micrographs of Ag|AgCl morphology: (a) micrograph of the Ag|AgCl reference electrode; (b) magnified area of (a) to highlight the AgCl morphology.

**Figure 2.9** Chronopotentiometry response for time dependent deposition of Ag on a  $1200 \text{ }\mu\text{m}^2$  microelectrode from a solution of  $\text{AgNO}_3/\text{KI}/\text{Na}_2\text{S}_2\text{O}_3$  ( $0.2/2.0/0.5 \text{ M}$ ), and subsequent formation of  $\text{Ag}_3\text{PO}_4$  at a current density of  $33 \text{ mA cm}^{-2}$  in a solution of  $0.1 \text{ M H}_3\text{PO}_4$ .

**Figure 2.10** SEM Image (a) and photographs (b-c) of the devices fabricated with polyimide microchambers: (a) a 3-microelectrode with a polyimide microchamber ( $140 \times 140 \text{ }\mu\text{m}^2$ ); (b) a 2-microelectrode with a polyimide microchamber (diameter:  $160 \text{ }\mu\text{m}$ ); (c) a device with polyimide residue in its chamber bottom.

**Figure 2.11** Photographs (a, e) and SEM images (b-d) of the devices fabricated using SU-8: (a) a 2-microelectrode device (microchamber diameter:  $150 \text{ }\mu\text{m}$ ); (b) a 2-microelectrode device (microchamber diameter:  $150 \text{ }\mu\text{m}$ ); (c) a 2-microelectrode device (microchamber:  $140 \times 140 \text{ }\mu\text{m}^2$ ); (d) a 3-microelectrode device (microchamber diameter:  $150 \text{ }\mu\text{m}$ ).

**Figure 2.12** Typical profiles of microchambers fabricated using (a) SU-8 and (b) polyimide, obtained using surface profilometry. The electrode can be seen in the bottom of both chambers, whilst the lipped polyimide can be seen in Figure 2.13 (b). This latter feature can make micro-pipetting of cells into the chamber more problematical.

**Figure 2.13** shows some representative device: (a) the photograph of a typical two-microelectrode (left, working electrode; right, reference electrode) within SU-8

microchamber (150  $\mu\text{m}$  diameter); (b) the profile of the device in (a); (c) the photograph of a typical three-electrode (left, reference electrode; middle, working electrode; right, counter electrode) within SU-8 microchamber ( $140 \times 140 \mu\text{m}^2$ ); (d) the profile of the device in (c).

**Table 2.1** The sizes of the devices in Figure 2.4, where, CE: counter electrode; WE: working electrode; RE: reference electrode.

**Table 2.2** The sizes of the devices in Figure 2.11 (b,d), where, CE: counter electrode; WE: working electrode; RE: reference electrode.

**Figure 3.1** Schematic diagrams of (a) a two-electrode cell and (b) a three-electrode cell.

**Figure 3.2** Tafel plots for anodic and cathodic branches of the current-overpotential curve for  $\text{O} + \text{e}^- \rightleftharpoons \text{R}$  with  $\alpha = 0.5$ ,  $T = 298 \text{ K}$ , and  $j_0 = 10^{-6} \text{ A/cm}^2$ . (Reproduced from reference [8]).

**Figure 3.3** DC cyclic voltammograms for 0.5 mM FMCA cycled at  $100 \text{ mV sec}^{-1}$ , for different microanalytical devices, respectively: (a) a 2-microelectrode device with a  $500 \mu\text{m}^2$  working electrode area; (b) a 3-microelectrode device with a  $200 \mu\text{m}^2$  working electrode area; (c) a 3-microelectrode device with a  $500 \mu\text{m}^2$  working electrode area. Peak currents scale according to the area of the working electrode.

**Figure 3.4** Response of a two-electrode device to 1.0 mM FMCA in 10 mM PBS bulk solution: (a) the DC cyclic voltammograms at scan rates between  $5 \sim 1000 \text{ mV sec}^{-1}$ ; (b) the relationship between the peak current  $i_{pa}$  and  $\nu^{1/2}$  in (a), where  $\nu$  is the potential scan rate, indicating diffusion limited reactions. The surface area of the working electrode was  $500 \mu\text{m}^2$ .

**Figure 3.5** 2-electrode sensor responses to FMCA in 10 mM PBS bulk solution, at the scan rate of  $10 \text{ mVs}^{-1}$ : (a) DC cyclic voltammograms response to different concentrations of FMCA; (b) the plot of  $i_{pa}$  against concentrations of FMCA, each point was measured in triplet and the mean was taken, with error bars shown. The surface area of the working electrode was  $500 \mu\text{m}^2$ .

**Figure 3.6** “Macro-volumetric” test of microelectrode response to hydrogen peroxide at different applied potentials. A Pt-working electrode was held at the potentials indicated vs. internal Ag|AgCl reference. The microwell of the device was filled with 10  $\mu\text{l}$  of 2 mM PBS (pH7.4), and then 1.2  $\mu\text{l}$  of 5 mM  $\text{H}_2\text{O}_2$  was injected: (a) Plot of current against time; (b) Tafel plot of current peak against applied potential, obtained from the data of (a); (c) Plot of charge transferred against applied potentials over 150 sec., obtained from the data of (a). The surface area of the working electrode was 500  $\mu\text{m}^2$ .

**Figure 3.7** shows representative “macro-volumetric” responses of the 2-microelectrode sensor to hydrogen. 10  $\mu\text{l}$  supporting electrolyte of 10 mM PBS was injected over the microchamber of the device, and then: (i) 1 nmol; (ii) 2 nmol; (iii) 4 nmol; (iv) 6 nmol; (v) 8 nmol; and (vi) 10 nmol  $\text{H}_2\text{O}_2$  was injected into the microchamber. The potential was held at +640 mV vs. internal Ag|AgCl. The surface area of the working electrode was 500  $\mu\text{m}^2$ .

**Figure 3.8** Calibration curve of a 2-electrode sensor “macro-volumetric test” for the charge generated (Q) as a consequence of hydrogen peroxide, over a range of concentrations between 0.1 and 5 mM. Each point is measured as a mean of three readings.

**Figure 3.9** Repeated responses of 2-electrode sensor “macro-volumetric test” to (a) 0.1 mM, (b) 0.6 mM, (c) 3 mM and (d) 4 mM  $\text{H}_2\text{O}_2$ . The surface area of the working electrode was 500  $\mu\text{m}^2$ . (Raw data of Figure 3.8)

**Figure 3.10** ‘Macro-volumetric’ test of microelectrode response to glucose via the production of hydrogen peroxide. The sputtered Pt working electrode was held at 0.64 V vs. internal Ag|AgCl reference. At first, the microchamber was filled with 8  $\mu\text{l}$  244  $\text{Uml}^{-1}$  GOD in 2 mM PBS at pH7.4. Current values were then recorded upon addition of (a) 1  $\mu\text{l}$  50 mM glucose in 2 mM PBS to get the final 5 mM glucose; or (b) 2  $\mu\text{l}$  2 mM PBS. The surface area of the working electrode was 500  $\mu\text{m}^2$ .

**Figure 3.11** DC cyclic voltammograms, for a 2-microelectrode sensor, of 0.5 mM FMCA at a scan rate of 10 mV/s at pH7.4 with 10 mM PBS. (a) Addition of 50 mM Glucose to the solution, then further addition of (b) 200 unit  $\text{ml}^{-1}$  GOD ( $i_p/i_d = 1.3$ ) or (c)

10 mg ml<sup>-1</sup> (i.e. 781 unit ml<sup>-1</sup>) GOD ( $i_{ik}/i_d = 1.7$ ). The surface area of the working electrode was 500  $\mu\text{m}^2$ .

**Figure 3.12** Response to glucose via reaction involving ferrocene monocarboxylic acid. (a) Sensor response, when the microchamber was filled with 0.5 mM FMCA and 12.5 mg/ml (i.e. 977 Uml<sup>-1</sup>) GOD in the supporting electrolyte, upon addition of 10 mM glucose. The potential was held at 0.32 V vs. internal Ag|AgCl microreference. (b) Response using the same conditions as for (a), but without the addition of FMCA. The surface area of the working electrode was 500  $\mu\text{m}^2$ .

**Figure 3.13** DC cyclic voltammograms of 1.0 mM FMCA at 100 mV sec<sup>-1</sup> (The surface area of the working electrode was 500  $\mu\text{m}^2$ ), using either Ag|AgCl or Ag|Ag<sub>3</sub>PO<sub>4</sub> as a reference:

- (a) Stable electrochemistry of the microanalytical devices using an integrated Ag|AgCl reference.
- (b) Electrochemistry of FMCA, where the working potential was controlled with respect to an external Ag|Ag<sub>3</sub>PO<sub>4</sub> reference electrode. Ag<sub>3</sub>PO<sub>4</sub> was deposited onto an Au electrode using 0.03 M H<sub>3</sub>PO<sub>4</sub> at a current density of 10 mA cm<sup>-2</sup> for 7 seconds: (i) and (ii) describe a shift in the  $E_{1/2}$  values upon repeated cycling over 10 mins.
- (c) Working potential was controlled with respect to an integrated Ag|Ag<sub>3</sub>PO<sub>4</sub> within the microchamber. Ag<sub>3</sub>PO<sub>4</sub> was prepared using 0.1 M H<sub>3</sub>PO<sub>4</sub> at a current density of 33 mA cm<sup>-2</sup> for 10 seconds: scans (i) to (v) show the instability of the reference with respect to time.
- (d) Working potential was controlled with respect to an integrated Ag|Ag<sub>3</sub>PO<sub>4</sub>. Ag<sub>3</sub>PO<sub>4</sub> was prepared using 0.03 M H<sub>3</sub>PO<sub>4</sub> at a current density of 10 mA cm<sup>-2</sup> for 12 seconds: scans (i) to (v) show the instability of the reference with respect to time.

**Figure 3.14** D.C. cyclic voltammeteries for 1mM FMCA in 10 mM PBS (pH 7.4), ionic/compositions were equivalent in both experiments: (a) a micro working electrode's potential was scanned with reference to a micro integrated Ag|AgCl. The formal redox potential,  $E^0(\text{FMCA}/\text{FMCA}^+)$ , is estimated to be +270 mV vs. the micro quasireference; (b) a micro working electrode's potential was scanned with reference to a true reference electrode of Ag|AgCl (BAS),  $E^0(\text{FMCA}/\text{FMCA}^+)$  is estimated to be +315 mV vs. Ag|AgCl (BAS).

**Figure 3.15** Potentials of redox couple FMCA/FMCA<sup>+</sup> and reference electrodes in 10 mM PBS (pH 7.4 at 23°C). Potentials obtained vs. an integrated micro quasireference of Ag/AgCl are plotted on the left and potentials obtained vs. a true reference of Ag/AgCl electrode (BAS) are on the right.

**Figure 3.16** Variation of the DC voltammogram to 1 mM FMCA while the device was immersed in a supporting electrolyte of KRB with 129 mM Cl<sup>-</sup> for 17.6 hours. The voltammograms were measured using microelectrodes vs. a microreference of Ag/AgCl (2 ~ 3 μm thickness) with a scan rate of 100 mVs<sup>-1</sup>. Scans (a) to (h) show the responses with after 0, 0.3, 0.75, 1.08, 2.08, 3.08, 3.41, 17.6 hours.

**Figure 3.17** Stable half-wave potential ( $E_{1/2}$ ) vs. a micro reference of Ag/AgCl, obtained from Figure 3.17 for each test during 17.6 hours storage in KRB.

**Figure 3.18** Regeneration of a passivated sputtered Pt microelectrode swept successively in 0.5M H<sub>2</sub>SO<sub>4</sub> (the sweep number is given for each curve).

**Figure 3.19** DC cyclic voltammograms at 100mV/s with 1mM FMCA before and after regeneration of the working microelectrode using cycling in acid method: (i) voltammogram of a device immediately after reference deposition of Ag/AgCl; (ii) voltammogram of the same device with a passivated working electrode showing decreased redox currents; (iii) voltammogram of the same device with a regenerated working electrode after cycling in acid.

**Figure 3.20** A typical comparison of the device DC cyclic voltammogram, at 100 mVs<sup>-1</sup> in a solution containing 1 mM FMCA in 10 mM PBS, before (i) and after (ii) dry etching process. Prior to dry etching, the electrode had been “fouled” in cell culture medium.

**Figure 4.1** Schematic of the crosslinking of lactate oxidase to bovine serum albumin (BSA) using glutaraldehyde.

**Figure 4.2** Showing the measurement apparatus: (a) photograph of the measurement set-up; (b) a schematic diagram of the measurement set-up.

**Figure 4.3** Showing the microinjection system as a schematic diagram:

- (a) The microinjection system assembly, in which, R1 is the gas cylinder regulator assembly; R2 is a 0-60 psi pressure regulator; R3 is a 0-10 psi pressure regulator; V1 is a needle valve; V2 is a SMC 3-port valve that allows flow across selected ports; G1 is 0-60 psi pressure gauge; G2 is a 0-10 psi pressure gauge; C1 is a 3-way connector (which allows flow across 3 ports); C2 and C3 are 3-way connectors allowing flow across selected ports; S is a switch; ESV1 is an electric solenoid valve for left injection (timer pulse on: 1 ↔3) and balance (off: 2 ↔3); ESV2 is electric solenoid valve for right injection (timer pulse on: 1 ↔3) and balance (off: 2 ↔3). Port 1 and port 3 of electric solenoid valve (ESV1 or ESV2) are open for dispensation when timer pulse was set on; port 2 and port 3 of ESV1 or ESV2 are open for balance process when timer pulse was switched off. The left or right process was controlled by selecting left or right ports of C2 (for left or right dispensation) and C3 (for left or right balance), as well as left or right of S.
- (b) a photograph of the glass micropipette with fine tip for microinjection.

**Figure 4.4** Fluid moving (from a to e) in the fine tip of a filament pipette while it was being back filled with solution. The frame rate is 10 frames sec<sup>-1</sup>.

**Figure 4.5** A pulled pipette in the microinjection system for calibration of picolitre scale solutions: (a) insertion of a drawn micropipette into KRB in a microchamber covered with mineral oil, allowing the pipette to fill by capillary action, where,  $\alpha = 25^{\circ}\text{C}$ ,  $\Delta L =$  length change,  $\phi_i =$  inner diameter; (b) section diagram of the pipette tip at the position circled with the dotted line in (a).

**Figure 4.6** Calibration plot of injection volume vs. the shot time (calculated using the raw data in Table 4.1)

**Figure 4.7** Responses to fresh lactate and stored lactate. 20  $\mu\text{L}$  lactate (1 mM) was used to cover on the microchamber, then 2  $\mu\text{L}$  120 U  $\text{mL}^{-1}$  LOD was added to the solution from the time labelled by the arrow. (a) The response to lactate stored at 4°C for 3 days. (b) The response to fresh lactate prepared immediately prior to its use.

**Figure 4.8** Typical current-time responses to 10  $\mu\text{M}$ , 100  $\mu\text{M}$  and 1 mM lactate using a platinized electrode within the 3-electrode microstructure. The working potential was

held at +0.64 V vs. internal Ag|AgCl reference. The microwell device was filled with 9  $\mu\text{l}$  200 unit  $\text{ml}^{-1}$  LOD in 10mM PBS (pH 7.4) before each addition of lactate.

**Figure 4.9** Typical response to 2 ~ 10  $\mu\text{M}$  lactate using a platinized electrode within the 3-electrode microstructure. The working potential was held at +0.64 V vs. an internal Ag|AgCl reference. The microwell device was filled with 9  $\mu\text{l}$  200 units/ml LOD in 10mM PBS (pH7.4) before each addition of lactate: (a) the *i-t* response to lactate; (b) the normalization of charge transferred on the working electrode (for 70 sec) vs. lactate concentration.

**Figure 4.10** Typical response to successive additions of lactate using a 'bulk' solution method. The working potential was held at +0.64 V vs. an internal Ag|AgCl reference. The micro well device was filled with 126 units  $\text{ml}^{-1}$  LOD in 10mM PBS (pH 7.4), then 1  $\mu\text{l}$  aliquots of lactate were successively injected into it: (a) the current-time behaviour of additions of lactate made at points *i* to *v* for 2, 6, 10, 29, 63, 116  $\mu\text{M}$ ; (b) current peak output of the lactate sensor as a function of lactate concentration.

**Figure 4.11** Typical response to successive additions of lactate using the bulk method. The working potential was held at +0.64 V vs. an internal Ag|AgCl reference. The device was soaked in 50 units/ml LOD in 4.5 ml 10mM PBS (pH 7.4), then 50  $\mu\text{l}$  aliquots of lactate were successively injected into it: (a) the current-time behaviour of additions of lactate made at points (*i*) to (*xi*) for 4.4, 6.5, 8.6, 14.9, 27.0, 56.4, 122.4, 201.9, 368.6, 738.3, 1322.3  $\mu\text{M}$ ; (b) current peak output of the lactate sensor as a function of lactate concentration.

**Figure 4.12** Comparison of a 2-electrode sensor cyclic voltammograms of 1 mM FMCA in a low volume and a 'bulk' drop. The electrolyte is 10 mM PBS at pH 7.4. (a) in a 400 pL microchamber; (b) in a 'bulk' drop.

**Figure 4.13** Plot of the dependence of the peak current on the square root of the potential sweep rate according to Fig. 4.12(a).

**Figure 4.14** Injection of pL-scale lactate. The device microchamber was filled with 360 pL KRB containing 112 U/ml LOD. 1.5, 3.7, 6.5, 13.0, 20.0 and 26.6 pL volume aliquots of stock solutions of 10 mM lactate were injected and their responses recorded.

**Figure 4.15** Lactate calibration plot for the charge transferred vs. the injected lactate quantity. Each point was measured as a mean of three readings.

**Figure 4.16** Comparison of the response to lactate and the non-Faradic current, caused by injection pulse and perturbation of the electrode double layer. The device microchamber was filled with 360 pL KRB containing 112 U ml<sup>-1</sup> LOD: (a) response to the injection of pL-scale lactate. 10 mM lactate was injected for 30 ms (1.5 pL, n=3), 60 ms (3.7 pL, n=3), 100 ms (6.5 pL, n=3) and 200 ms (13.0 pL, n=2); (b) response to the injection of supporting electrolyte (buffer) under identical conditions.

**Figure 4.17** Location of lactate oxidase covalently linked in a bovine albumin gel membrane, indicating the rejection of interference (I) and the conversion of substrate (S) of lactate to electro-active product (P) of H<sub>2</sub>O<sub>2</sub>.

**Figure 4.18** Typical responses of a device with an immobilised LOD membrane. The working potential was held at +0.64 V vs. an internal Ag/AgCl reference. The device was soaked in 4.95 ml 10 mM stirring PBS (pH 7.4), then 50 μL aliquots of lactate were successively injected into it: (a) the current-time behaviour of additions of lactate made at points i to ix for final lactate concentrations of 5 μM, 13 μM, 37 μM, 85 μM, 181 μM, 298 μM, 531 μM, 994 μM and 1.910 mM; (b) calibration curve of lactate detection. conditions as for (a); (c) linear plot in the concentration range between 5 μM and 531 μM lactate, obtained from (b).

**Figure 4.19** shows the longitudinal study of a device with LOD immobilization for 1 mM lactate measurement using normal bulk method.

**Table 4.1** The length change ( $\Delta L$ ) of the fluid for dispensation (n=3) with different shot time ( $\Delta T_{inj}$ ).

**Table 4.2** Calibration table for different shot time dispensations, where,  $\Delta V_{inj}$  is the injection volume and  $\Delta T_{inj}$  is the shot time.

**Figure 5.1** Main metabolic pathways (a, b & c) of a muscle cell involving lactate transport across the plasma membranes.

**Figure 5.2** Photographs of various different shapes of rabbit single heart cells. Sizes (mean = 21 pL, Sd = 6 pL, n=8) vary accordingly: (a) volume = 9 pL; (b) volume = 11 pL; (c) volume = 24 pL; (d) volume = 22 pL; (e) volume = 19 pL; (f) volume = 25 pL; (g) volume = 30 pL; (h) volume = 31 pL.

**Figure 5.3** Experimental myocyte manipulation: (a) photograph of the glass micropipette with a 30 ~ 40 diameter tip for cell injection; (b) a single myocyte expelled from a pipette into the droplet over a device; (c) a fine tip pipette for drug microinjection positioned over a device microchamber, in which a myocyte is attached. Care was taken to avoid contact between the cell and the reference/counter electrode.

**Figure 5.4** shows BHKC13 cells attached and spreaded onto different substrate materials after 48 hours incubation at 37°C. (a) GaAs; (b) specially-treated polystyrene, *i.e.* tissue culture plastic; (c) gold; (d) silicon; (e) germanium; (f) indium-tin oxide; (g) SU-8.

**Figure 5.5** BHKC13 cell growth on different substrate materials after incubation at 37°C. Accordingly on: (a) SU-8 for 105 hours; (b) SU-8 for 161 hours; (c) gold for 161 hours.

**Figure 5.6** Optical microscope images of a single myocyte in contact with a AgI/AgCl pseudo reference within a microchamber, filled with 400 pL KRB solution (with 11 mM glucose): (a) a healthy rod shaped myocyte was just injected onto the AgI/AgCl reference electrode. This resulted in a fast beating and contracture; (b) the same myocyte, after 1 min beating and contracture, with a shortened length; (c) the same myocyte, after 2 min beating and contracture, with a further shortened length; (d) after 2 min 30 sec beating and contracture, the myocyte balled up rapidly.

**Figure 5.7** Optical microscope images of single myocyte cells inside a microchamber device, filled with 400 pL KRB solution (with 11 mM glucose): (a) a healthy rod shaped myocyte injected onto the platinum black electrode. After lying “dormant” for 8 min, it started a slow beating; (b) the same myocyte after slow beating for a further 3 minutes, moved onto the AgI/AgCl reference and started beating more quickly and contracture. The myocyte “balled-up” rapidly after 14 min.

**Figure 5.8.** A healthy “dormant” myocyte was permeabilised with saponin. The images show the length of the initially rod-shaped myocyte (i) prior to (ii) ~ (viii) after injection of the saponin (after 8 secs to a concentration of 80  $\mu\text{g/ml}$ ).

**Figure 5.9** A healthy beating single myocyte was permeabilised with saponin: (a) images showing the length of the myocyte (i) before and (ii) ~ (viii) after the addition of saponin (at 9 sec to a concentration of 80  $\mu\text{g/ml}$ ); (b) cell length is shown as a function of time.

**Figure 5.10** Lactate released from a single myocyte after direct contact with an Ag|AgCl reference, provoked fast beating and contractility. Chamber was filled with 400 pL 200 U/ml LOD in fresh KRB. Lactate calibration signal was obtained by injection of ~ 6.5 pL of 10 mM lactate. Platinised working electrode was poised at 0.64 V vs. an integrated Ag|AgCl pseudo-reference/counter. (a) to (c) are repeats of the same protocol (left) with the area of the graph around the lactate release magnified (right). The surface area of the working electrode was 1250  $\mu\text{m}^2$ .

**Figure 5.11** Lactate released from a single myocyte in a 400 pL chamber during cell shortening and balling up after piercing of the cell wall using the extruded tip (outer diameter < 1  $\mu\text{m}$ ) of a glass micropipette. A lactate calibration signal was obtained by injection of ~ 6.5 pL of 10 mM lactate. The platinised working electrode was held at 0.64 V vs. an integrated Ag|AgCl pseudo-reference electrode. The surface area of the working electrode was 1250  $\mu\text{m}^2$ .

**Figure 5.12** Differential output (see section 5.3.4) of lactate released from a single myocyte after the cell was permeabilised by the detergent saponin. The platinised working electrode was held at 0.64 V vs. integrated Ag|AgCl pseudo-reference electrode. Saponin was injected to ~80  $\mu\text{g ml}^{-1}$ , at which the cell immediately shortened and balled. Lactate calibration signal was obtained by injection of ~ 6.5 pL of 10 mM lactate. (a), (b) are repeats of the same protocol. The surface area of the working electrode was 1250  $\mu\text{m}^2$ .

**Figure 5.13** Electrochemical detection of lactate generation by a single rabbit myocyte (~ 25 pL) (in a 400 pL chamber) permeabilised after metabolic inhibition, imposed by injecting FCCP to ~ 15  $\mu\text{M}$ . A platinised working electrode was poised at 0.64 V vs. an integrated Ag|AgCl pseudo-reference electrode. During the metabolic inhibition, which

lasted 200 sec, the cell contracted a little. The cell membrane was then permeabilised using saponin to a final concentration of  $\sim 80 \mu\text{g ml}^{-1}$ , upon which the cell immediately shortened and balled. Lactate calibration signal was obtained by injection of  $\sim 6.5 \text{ pL}$  of  $10 \text{ mM}$  lactate. The lactate signal was obtained after the addition of saponin corresponds to a content of  $100.8 \text{ fmol}$ , at an intracellular concentration of  $4 \text{ mM}$ . The surface area of the working electrode was  $1250 \mu\text{m}^2$ .

**Figure 5.14** Lactate efflux from a single rabbit myocyte ( $25 \text{ pL}$ ) in a  $400 \text{ pL}$  chamber after metabolic inhibition, imposed by injecting FCCP to  $150 \mu\text{M}$ . A platinised working electrode ( $1250 \mu\text{m}^2$ ) was poised at  $0.15 \text{ V}$  vs. a Pt pseudo-reference/counter. Saponin was injected to a concentration of  $0.3 \text{ mg ml}^{-1}$ , at which point the cell shortened and balled. A lactate calibration signal was obtained by injection of  $65 \text{ fmol}$  lactate.

**Figure 5.15** Results obtained for a repeat experiment to that for Figure 5.14, apart from holding the platinised working electrode at  $0.29 \text{ V}$  vs. a Pt pseudo-reference electrode. (a) and (b) are repeats of the same protocol. During the metabolic inhibition of (a)  $13 \text{ min}$  or (b)  $16 \text{ min}$ , the cell shape did not alter significantly. The cell membrane was then permeabilised using saponin to a final concentration of  $\sim 80 \mu\text{g ml}^{-1}$ , at which the cell immediately shortened and balled. A lactate calibration signal was obtained by injection of  $\sim 6.5 \text{ pL}$  of lactate ( $10 \text{ mM}$ ).

**Figure 5.16** Summary of cytoplasmic concentrations calculated from the data values and the individual cell volumes. (A) Cells poisoned by AgI/AgCl ( $1.8 \pm 0.3 \text{ mM}$ ,  $n=3$ ); (B) cells inserted by tips ( $2.4 \pm 0.7 \text{ mM}$ ,  $n=2$ ); (C) healthy rod-shaped cells permeabilised by saponin ( $1.6 \pm 0.4 \text{ mM}$ ,  $n=4$ ); (D) cells after metabolic inhibition by FCCP ( $5.0 \pm 0.8 \text{ mM}$ ,  $n=3$ ).

**Figure 6.1** Schematic diagram describing the fabrication of an enclosed microscopic channel in oxidised PDMS. (a) An SU-8 mold was modified to produce a hydrophobic surface. (b) A prepolymer of PDMS was cast onto the mold and cured at  $75^\circ\text{C}$  for 1 hour. (c) The PDMS replica containing a negative relief of the channels was peeled away from the mold. (d) The PDMS replica and glass (or Si,  $\text{SiO}_2$ ,  $\text{Si}_3\text{N}_4$ , quartz) substrate were oxidized in a oxygen plasma discharge for 1 min and then were immediately brought into conformal press contact.

**Figure 6.2** UV absorption spectrum for a 60  $\mu\text{m}$  thick SU-8 film on a glass slide.

Transmission (T) =  $10^{-A}$ , where, A: absorbance.

**Figure 6.3** SEM and optical microscope images of SU-8 micromachined structures.

(a) SEM of SU-8 (500) microchamber with diameter of 100  $\mu\text{m}$  and depth of 60  $\mu\text{m}$ ;

(b) SEM of SU-8 (500) corner with straight walls; (c) an optical microscope image of

an SU-8 (SM1060) multi-channel with a channel width of 20  $\mu\text{m}$  and depth of 21  $\mu\text{m}$ .

**Figure 6.4** Four pairs of microelectrodes within four microchamber and microchannel systems.

**Figure 6.5** Optical images of a microelectrode array and the microelectrodes within microchambers and microchannels. (a) Microelectrode array chip; (b) the working electrode (W1,  $\varnothing$  35  $\mu\text{m}$ ) and the reference electrode (R1, 12  $\mu\text{m}$   $\times$  200  $\mu\text{m}$ ) in the 1<sup>st</sup> pair of microelectrodes; (c) the working electrode (W2,  $\varnothing$  35  $\mu\text{m}$ ) of the 2<sup>nd</sup> pair of microelectrodes; (d) the working electrode (W3,  $\varnothing$  200  $\mu\text{m}$ ) and the reference electrode (R3, 12  $\mu\text{m}$   $\times$  5000  $\mu\text{m}$ ) in the 3<sup>rd</sup> pair of microelectrodes.

**Figure 6.6** Optical images of PDMS replica and glass bonded together after plasma oxidation: (a) perfect bonding defined the channels (width 20  $\mu\text{m}$ , height 21  $\mu\text{m}$ ); (b) sealing of part of a wide channel of PDMS to the glass; (c) after several minutes delay post-removal from the plasma cleaner, contacting the formed air pockets beside a channel (width 10  $\mu\text{m}$ , height 9  $\mu\text{m}$ ).

**Figure 6.7** The seal formed between PDMS and the substrate containing SU-8 patterns: (a) diagram depicting a glass slide (or Si, or  $\text{Si}_3\text{N}_4$  substrate) with an SU-8 pattern sealed using PDMS. An irreversible bond formed between the outside glass area (or Si, or  $\text{Si}_3\text{N}_4$  area) and the PDMS after plasma oxidation; (b) optical image of a glass slide with SU-8 microchannels sealed with a PDMS layer; (c) optical image of a glass slide with an SU-8 band sealed with the PDMS layer. The glass areas (bottom left and top right) beside the SU-8 band formed an irreversible bond with the PDMS covering layer.

**Figure 6.8** A proposed integrated biosensor chip: (a) The schematic microfluidic chip shows two enzyme working electrodes of platinum black (ENWE<sub>1</sub> & ENWE<sub>2</sub>), one common gold counter electrode (CE), one common reference electrode (Ag|AgCl

REF), one working electrode of platinum black without enzyme ( $WE_0$ , for differential output) and SU-8 flow cell with PDMS top seal; (b) the cross-section (A-A') of (a) through a micro-flow cell ( $< 0.32 \mu\text{L}$ ).

**Figure 6.9** A schematic diagram of the proposed experimental set-up: (a) on-line flow injection analysis (FIA) monitoring of multi-biomolecules using an integrated biosensor chip and microdialysis technique. The biological sample could be a fermentation bioreaction reservoir, or blood/serum tissue fluid; (b) a microdialysis probe.

**Table 6.1** The sizes of the microelectrodes (in Figure 6.4), where, WE: working electrode; RE: reference electrode.

## Publications

1. Xinxia Cai, Andrew Glidle, Jonathan M. Cooper, Miniaturized electroanalytical sensor systems in micromachined structures, **Electroanalysis** 2000, Vol.12, No.9, pp.631-639.
2. Xinxia Cai, Norbert Klauke, Andrew Glidle, Peter Cobbold, Godfrey L. Smith and Jonathan M. Cooper, Ultra Low Volume, Real-Time Measurements of Lactate from the Single Heart Cell using Microsystems Technology Picolitre Scale Single Cell Lactate Measurements Using Microsystems Technology, submitted to **Analytical Chemistry**, in press.
3. Xinxia Cai, Norbert Klauke, Godfrey L. Smith, Jonathan M. Cooper Ultra low volume electrochemistry for single heart cell analysis, **Gordon Research Conference on Bioanalytical Sensors**, July 2000, Andover, USA.
4. Xinxia Cai, James Davis, Andrew Glidle, Jonathan M. Cooper, Micromachined sensors for bio-electrochemical measurement, **Butler Electrochemistry Meeting**, July 1999, University of St. Andrews.

